A New Metastable Helium Machine : An Investigation into the Attributes of Trapping, Cooling and Detecting Metastable Helium

Lynn Hoendervanger

INSTITUT D'OPTIQUE GRADUATE SCHOOL

ÉCOLE DOCTORALE ONDES ET MATIERE

Discipline: Physique

THÈSE

pour l'obtention du grade de Docteur en science de l'Institut d'Optique Graduate School
préparée au Laboratoire Charles Fabry

soutenue le 03/10/2014

par

Lynn HOENDERVANGER

A New Metastable Helium Machine: An Investigation into the Attributes of Trapping, Cooling and Detecting Metastable Helium

Directeur de thèse :	Chris Westbrook	–	Institut d'Optique Graduate School

Composition du jury :

Président du jury :	Philippe Roncin	–	Paris XI
Rapporteurs :	Hélène Perrin	–	Paris XIII
	Wim Vassen	–	Vrije Universiteit Amsterdam
Examinateurs :	Michelle Leduc	–	Ecole Normale Supérieure
	Chris Westbrook	–	Institut d'Optique Graduate School
Membres invités :	David Clément	–	Institut d'Optique Graduate School

Foreword

The thesis you have in front of you is the result of three and a half years of work at the Institut d'Optique Graduate School. In this time I have had the opportunity to learn and to grow both as a physicist and as a person. As the first student on a new experiment, I have had the unique opportunity to become a little bit of an expert in many different practical fields, from plumbing and vacuum technology to the design of laser cooling schemes.
The first person I have to thank for first of all, putting his trust in me, is my daily supervisor David Clément. David and I met when I was doing a small research project for my Masters at LENS in Florence, Italy. The first few years of my PhD it was mainly only me and him working in the lab, and without his continuing support, enthusiasm and guidance, I would have probably gone crazy. Of course I have to thank Chris Westbrook as well, for making the executive decision of actually hiring me, and for his interest and help in all my time here.

We started in a completely empty lab, and in a very reasonably fast pace this laboratory has been filling up with more and more added parts of the experimental apparatus, passing milestone after milestone and occasionally celebrating these with a nice champagne or prosecco. Now the time has come to gather all the knowledge I have gained over the years, to write it down and to defend it against a jury.

I want to give a special thanks to the members of my jury, and especially the two referees, Hélène Perrin and Wim Vassen. Wim has worked with metastable helium for more than twenty years, and was in the perfect position to ask me the most difficult questions during the defense. Hélène I owe a special thanks for taking the time to go over the manuscript with me again and pointing out to me the places where it could be corrected. I have greatly appreciated her involvement in this and I think it shows how committed she is to teaching and physics. As a side-note, Hélène is also very involved in programs for women in physics, and in programs that aim to encourage your girls to go into science. I find this a very important cause, and I am glad that she is putting her time and effort into it.
The president of my jury, Philippe Roncin I thank for his calm and gentle way of leading the discussion, as well as for his interesting insights into the workings of our detectors, a subject in which he is very well versed. Unfortunately my last jury member, Michèle Leduc was not able to make it to the actual defense, but I do thank her for reading through the manuscript and for her thoughtful comments. As the president of the IFRAF, the organization which has provided me with my scholarship, she has always been interested in the progress of my work and my general

well being, and I have always appreciated her concern.
In relation to my defense, the last person I have to thank, who although he was not directly involved in my defense, but who has been of great help with the administrative side of things, is Eric Charron from the doctoral school EDOM. Eric has been very helpful, and very responsive to all my panicked emails when I could not manage all the delicacies of the French administrative system anymore.

On the metastable helium experiment, the team has grown a bit over the years. I have enjoyed a lot working with Yami Fang, a student from China, who worked with us for more than a year. His way of looking at things and his genuine interest in people made it a joy to spend time with him and I wish him all the best, and I hope that if I have taught him one thing, it is that girls can carry heavy things just as well as boys !
In the past year, Quentin Bouton has started as a new PhD student, making our overlapping time not very long. I am however impressed with his capability to make things happen and I believe I can leave the experiment in his care without worry. There to help him is also Rockson Chang, who joined us from Toronto almost a year ago. I want to thank Rockson for going over my manuscript and picking out all the worst Dutchisms and general English mistakes, as writing in a second language can be tough at times. His help with preparing my presentation has been invaluable as well.
Over the years, Florence Nogrette has been there to help us with many technical aspects of the job, and she has always been a delight to have around, due to the combination of her knowledge and skills with the ever-present smile on her face. I hope my choice in music in the lab has not scared her too much.

In the atom optics group there are too many people to thank all individually, but know that I wish all of you nothing but the best. I have been impressed over the years by the consistently high levels of discussion, the curiosity and by the sheer brainpower available, but also by the willingness to help others and how everyone would always be ready to put aside their own work to help someone else understand better, it has been a great environment in which to do a PhD and I hope it will stay like this for many years to come, as I truly believe it is the group that shapes the progress that students make. Tough questions and criticism at your group presentations might be hard at the moment, but after it allows you to conquer the world.

A few people I want to mention by name: Kilian, Guilaume and Raphael, with whom I have shared an office for close to three years, clearly the best office in the whole building and Bess, with who I have done most of my gossiping and complaining about living in France (******* RER B). All have clearly a bright future ahead of them, in whatever career they choose, and I hope to stay in contact for a very long time.
All the other students and post-docs in the group I wish of course also a lot of happiness and many publications, Jérémie, Almaz, Lauriane, Aisling, Valentin, Guilhelm, Guiseppe, Vincent, you were all great.

In my personal life there are again too many people who deserve a big thank you. My parents for being so proud of me, and for all their support and help. My friends from university who hopefully will still recognize me when I return to The Netherlands, with a special thanks to Gwen, Keren and Tjebbe for driving all the way to Paris to see me defend my thesis.
Lastly, the most important person I have to thank, for his patience, help and love, Ralf, I would not be here in one piece if it had not been for you, and I thank you with all my heart for making me a better person and for standing by me.

Thesis

Introduction

Can you simulate a many-body quantum system with a classical computer? This is the question that Richard Feynman posed his public in his keynote speech at the very first international conference on physics and computing at MIT in 1982 [1]. The problem is twofold, it deals with limits of computational power of classical computers, but it also addresses the nature of quantum mechanics itself and whether a classical system, like a computer, can ever mimic some of its most remarkable features.

There are many reasons to want to simulate many-body quantum systems as they hold the key to many interesting physical phenomena, such as, but not limited to, high T_C superconductivity. However the computational power needed to simulate many-body system increases exponentially with the number of bodies involved. This makes it hard to give any meaningful information on systems of a size that would be relevant to everyday life and makes this method time and resource intensive.
Specifically, with Quantum Monte Carlo it is possible to get exact results from the Bose-Hubbard model for atoms in lattices [2, 3, 4, 5, 6]. At the moment, systems with up to 10^3 sites have been simulated [26], which starts to be reasonable compared to experiments.
For other systems, Quantum Monte Carlo is only able to say little to nothing.

Another complication of a different nature occurs when one is dealing with systems where entanglement has a large influence. Since we do not know how to quantify a level of entanglement of a system, making calculations or simulations with a non-quantum system, such as a classical computer, is difficult.
In some specific cases it is possible to quantify entanglement using the Von Neumann entropy [7], or other similar ones, but these cases are rare.

To be able to simulate system in which there are quantum mechanical effects such as entanglement, one has to use a simulator that has on its own already a quantum mechanical nature, one uses a quantum simulator.
It turns out that the best way to simulate a quantum mechanical many-body system, is by using a quantum mechanical many-body system.

One might think this is an obvious statement, but in fact it is not so straightforward, especially around the time that Feynman was giving his speech. Physicists are used to being able to calculate stuff, either with a machine as we do now, or with pen and paper as Feynman's peers were used to. When talking about quantum

mechanics though, the fundamental truth is that you cannot always calculate and predict everything, since the tools we use are not equipped to do so. To simulate entangled particles, one needs to use entangled particles.

So where does that leave us? If we want to know more about the true nature of the quantum mechanical world that we live in, how do we proceed? Or if we want to make simulations of systems that incorporate entanglement, how can we learn about those? All we need is to turn away from classical computers as the answer and find a different system to make the simulations, and this is where cold atoms come into play [8].

Cold Atoms as Quantum Simulators

In the mid-eighties the field of atomic physics started to bloom into what today is know as cold atoms. The development was mostly triggered by a big improvement in technology when by using lasers and magnetic fields, it was then possible to trap and cool ensembles of atoms. In the nineties this led to the first experimental realization of Bose-Einstein Condensates (BECs) [9, 10, 11] and later also to Fermi degeneracy [12, 13, 14]. The field of atomic physics had before these developments mostly dealt with single particle problems, these systems however have interactions and are in fact many-body.

When one works with cold atoms there is a degree of control over the system that is truly remarkable and unmatched anywhere else, and it is this that makes the field in essence a great toolbox to simulate many different systems.
As the field matured, so did the tools available and these days one can construct almost any customized Hamiltonian, by using optical lattices, Feshbach resonances and/or many other mechanisms to control interactions, geometries and topologies [15, 16, 17, 18].
With these tools it is possible to go from the weakly interacting systems cited above to more strongly interacting and more interesting ones. Not only have these systems been suggested as a great tool for simulating condensed matter [19] but the true influx of interest in the subject came from the suggestion that these systems could be useful to build a full-flegded quantum computer [20].

As a result, the superfluid to Mott transition with atoms in an optical lattice was first realized experimentally in 2002 [21] and kick-started the field of strongly correlated physics in cold atomic ensembles [22, 24, 23]. This system in particular is an example of a many-body system that has been exactly solved by quantum Monte Carlo simulations at finite temperature, both in 1D [25] and in 3D [26, 27], therefore rendering this system as a great starting point, which we can use to validate our experimental simulator.

Today the interest in using cold atoms as a quantum simulator is as large as ever, as we are able to simulate more and more complex Hamiltonians as technology improves and as new tricks and schemes for the manipulation and control of the atoms

are conceived, the era of the true quantum simulator is just around the corner.

Our Experiment

With the construction of a new experiment at the Institut d'Optique we throw ourselves into this field of using cold atoms to simulate interesting quantum many-body systems. The apparatus will be using the boson Helium-4, which will be addressed by a three-dimensional optical lattice in which we can do our simulations and experiments. We shall use a detector that is specifically suited to measure correlations between particles, by allowing three-dimensional single particle time-of-flight detection. Since the correlations between components of a many-body state drive the properties of the state, both ground state and excitations, the study of the correlations allows an in depth investigation of the many-body state.

A lot of atomic species have already been condensed to BEC or Fermi degeneracy, most recently Strontium [28], Helium has first been condensed into a BEC in 2001 [29, 30]. It is not per definition necessary to obtain a condensate to study the Hamiltonians we are interested in, however as one wants to be in the regime where we can really study the interactions and where the lattice effects are of a quantum mechanical nature, it is necessary to work with atoms that are in their ground state or at least very close to it. In practice this means that one starts by condensing the atoms into a Bose-Einstein Condensate as a first experimental step.

Working with helium offers exemplary opportunities, especially when wanting to study strongly correlated systems.

Helium in its ground state does not have any optically accessible transitions that can be used for laser cooling, as do all noble gases. This means that instead we work with the first electronically excited state, one that is metastable. The metastable state has a lifetime of > 1000 s, much longer than we could ever need in an experiment. It also has an internal energy of 19.8 eV, which is energy that can be used for detection by ionization after collision with for example a microchannel plate. This makes single atom detection possible and relatively efficient, and allows us to effectively study the correlations between particles.
The other strong point in favor of working with (metastable) helium, is that it is a relatively simple atom, it has only two protons, two neutrons and two electrons. This renders ab inition calculations actually possible, something which would be inconceivable with atomic species with a larger atom number. This means one can calculate the exact atomic structure and the potentials of interactions between particles.
The light mass of helium also allows us to reach the far-field regime much easier than with heavier atoms when doing time-of-flight measurements. This is especially useful when studying momentum space correlations, as it means it becomes possible to reach the Fraunhofer regime.
There is the small point to make that if one would add helium-3, which is a fermion, to the mix, there is a broad Feshbach resonance predicted which would allow very

nice tuning of the interaction strenght, an experimental tool that is highly useful. Although it is not easy (and cheap) these days to obtain any helium-3, we do foresee in the future to be able to add it onto our experiment.

To recapitulate, putting metastable helium-4 atoms into an optical lattice will allow us to study the correlations in momentum space in these strongly correlated systems. Adding helium-3 into the mix would allow us to control the interaction strength. By dropping the atoms on a microchannel plate we can do time-of-flight, single atom, and for the first time said momentum space correlations will be accessible for a three-dimensional system.

One Illustrative Example

A BEC at zero temperature will exhibit no thermally activated excitation. A BEC without interactions will at zero temperature have all its particles in the groundstate (or $k = 0$ when trapped). At zero temperature and with interactions present, atoms are kicked out of the condensate due to quantum fluctuations [31, 32, 33], this is know as the quantum depletion of a condensate and a first study we propose to do with the newly built apparatus.
In line with momentum conservation, these quantum fluctuations create pairs of correlated particles with equal but opposite non-zero momentum $-k$ and k, and the fraction of quantum depletion is dependent on the interaction strenght between the atoms. At finite temperature both thermal and quantum fluctuations cause depletions, but thermal fluctuations do not excite correlated pairs. In a homogeneous BEC the quantum depleted fraction is of the order of 0.1%, while around 90% in liquid helium systems.
In our experiment we can add a weak optical lattice to the BEC. This will have the effect of increasing both the interaction strength and the effective mass of the particles, both will have the effect of increasing the depleted fraction.

If the lattice is weak, the atoms will still be in the super fluid state and when we do time of flight detection, we will seperate the condensate fraction from the depleted fraction, thermal and quantum. We can seperate the two depletion mechanisms by searching for $(-k, k)$ correlations, something our experiment is designed for.

This is just a quick example of the sort of experiment that can be done with the new apparatus and it would demonstrate for the first time the microscopic mechanism of quantum depletion. Many other uses can be thought of, simulating condensed matter problems or doing tests on the nature of quantum mechanics.

This Thesis

In this manuscript the work I have done over the past three years will be documented. After I have just laid out the reasons for building the experiment, I will then guide you through the implementation of those ideas.

In the first chapter, we look at a study done on the detectors that are featured on the apparatus, the microchannel plates that are one of the primary reasons why helium has been chosen as the species to work with. We have tried and tested several methods to improve the efficiency and the accuracy of the detector system. An extra conductive gold layer on the input surface is tested, as well as the addition of a voltage between two plates in chevron configuration.

Next the focus shifts to the design and building of the experimental apparatus that is cooling and trapping the metastable helium. In the second chapter I describe the excitation of the ground state helium atoms into their metastable state in a plasma created with a high voltage. The resulting atomic beam has to be collimated transversely as well as being cooled longitudinally. The vacuum system and the lasers used for these purposes are described and I report on all the characterization of the apparatus.
The second chapter ends with the trapping of the atoms in a magneto optical trap. The narrative is picked up in the third chapter with a detailed description of the MOT, and the challenge to optimize and get as many atoms trapped as possible is documented. The final half of the chapter is dedicated to an original study of two-photon Doppler theory, for which our system turns out to be a very good place.

In the final chapter, another experiment done with the MOT is described. Penning ionization that is present in clouds of metastable helium if they are interacting with light, is studied. With the use of relatively new techonology that allows us to monitor the volume of the cloud in situ we measure the loss rate and compare it to literature.

With no further ado ...

Chapter 1

A Study on the Performance of Micro-Channel Plates

1.1 Introduction

1.1.1 Overview

This chapter is a description of the work done in [34]. Here a study on Micro-Channel Plates (MCPs) was presented, focusing on improving their performance with regards to the efficiency and the accuracy by adding an interplate voltage and a gold coating on the receiving surface.
In section 1.1.2 the proposed study is explained and we argue its significance. In section 1.2 a detailed explanation of the workings of the detection system are given. The MCPs are discussed, as well as the delay line anode and the influence of adding an interplate voltage. Subsequently the experimental setup is described in section 1.3 and the results are laid out in section 1.4.

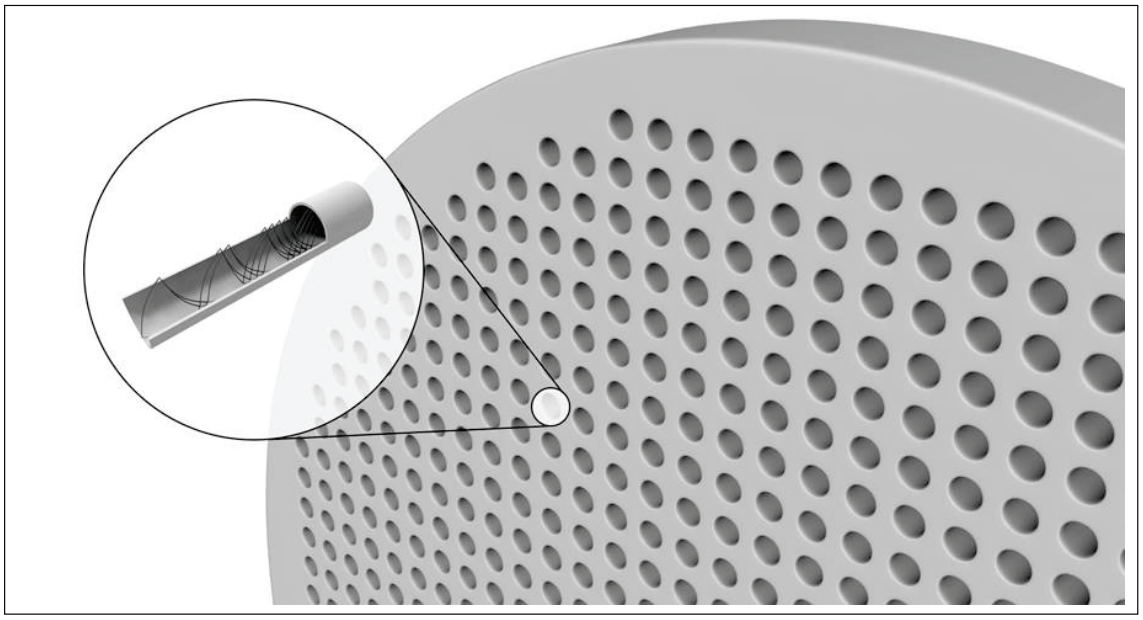

Figure 1.1: From www.Photonics.com. A Micro-Channel Plate consists of many μm scale electron multiplier tubes. An incident particle excites the first electron with a given efficiency leading to a cascade.

1.1.2 Introduction

Micro-Channel Plate (MCP) detectors are used widely for the detection of particles, in atomic and nuclear physics [35, 36, 37]. They can detect charged (> 0.2keV) and neutral (> 5eV) particles as well as UV photons ($\lambda < 150$ nm), and are for example used in night vision goggles. In cold atom physics, MCPs are used to detect metastable rare gas atoms, as their high internal energy allows the excitation of electrons on the MCP surfaces [38]. The detector is placed at a suitable distance (far enough so that detection is in momentum space) from a cloud of trapped atoms, which are then released and will fall onto the surface of the detector.
MCPs consists of an array of very small (μm) scale electron multiplier tubes. An incident particle can excite a first electron in s tube, leading to a cascade and an electron shower as output, see figure 1.1. A crossed delay line anode picks up this shower leading to three dimensional reconstruction of the distribution of the falling particles [39], see also figure 1.5. MCPs are in particular useful for the reconstruction of second (g_2) and third (g_3) order correlation functions along the three spatial axes, giving access to information related to the quantum statistics and coherence of a cold atom cloud [40, 41, 42]. The higher the order of the correlation function one wants to investigate, the higher the efficiency of the detector required. In the above cited experiments, the efficiency of MCPs with delay line anode detection system has been estimated to be around $10 - 20\%$ [43]. For many-body correlation studies, as planned with this new experimental apparatus, this is a rather low number and we would like to see it improved [44, 45, 46, 47, 48, 49].

The spatial accuracy of the detector is typically around ~ 150 μm, which is a figure

that could also do with improvement. Efficiency of detection and spatial accuracy are crucial quantities in the context of ion studies as well and they have been the object of recent work [50].

In this chapter we discuss a method for improving both the detection efficiency and the spatial accuracy of the detector. We are talking about accuracy instead of resolution, as they are not the same thing. Resolution deals with the ability to distinguish two separate events, whereas accuracy is the measure of precision of the detector. In other words, since we study single particle events, since we are working with dilute clouds of particles and events do not happen close to each other, we cannot talk about resolution, as there is no need to separate anything. However, the accuracy tells us how well we can determine the impact position of the particle. To improve the detection efficiency and the accuracy we will test adding a gold layer on the input surface of the detector as well as adding a voltage between two stacked MCPs. Adding a coating, whether it is gold, aluminium or Caesium Iodide (CsI), any material that has a higher conductivity than Nichrome but a similar work function, has been found to increase efficiency and maximum count rate [51, 52].
Seperating the MCPs and adding a voltage between the two faces will increase the energy of the electron showers. We shall see below the effect of this.

1.2 General Considerations

1.2.1 Microchannel Plates

MCPs consist of many single electron multiplier tubes. The surface of the plates and the tubes is coated with conductive material so that when a particle hits the MCP there is a given chance that the particle will excite an electron, coming from the work function of the conductive material, most commonly Nichrome or Inconel. The particle thus sets in motion a electron cascade in the multiplier tube. The tubes are at an angle with the surface, so that particles cannot just fall through the MCP without hitting a surface and to prevent particles (electrons and ions) from floating back up through the channels. When operating in the MCPs in pairs, single plates are put with their angles opposite to each other, in chevron configuration, see figure 1.2.
Therefore, to work an MCP has to be supplied with a voltage between the top and bottom surface. This supply voltage is usually in the order of a kilovolt. In this chapter we shall refer to the voltage we put over the faces of the MCP as V_{mcp}. If this voltage is not high enough, there will not be sufficient electrons excited in the tubes and after the excitation of the first electron the cascade will not escalate. When one increases V_{mcp}, the chance that the first induced electron excites secondary electrons is increased. When increasing V_{mcp} the gain of the detector will first increase exponentially (as the generation of secondary electrons is exponential), at a given voltage, the gain will saturate and will only increase linearly with V_{mcp}. This is due to the effect that too many electrons in the tube will start to screen the effect of increasing the voltage. The effect of V_{mcp} on the gain is the same no matter what the flux of incoming particles.

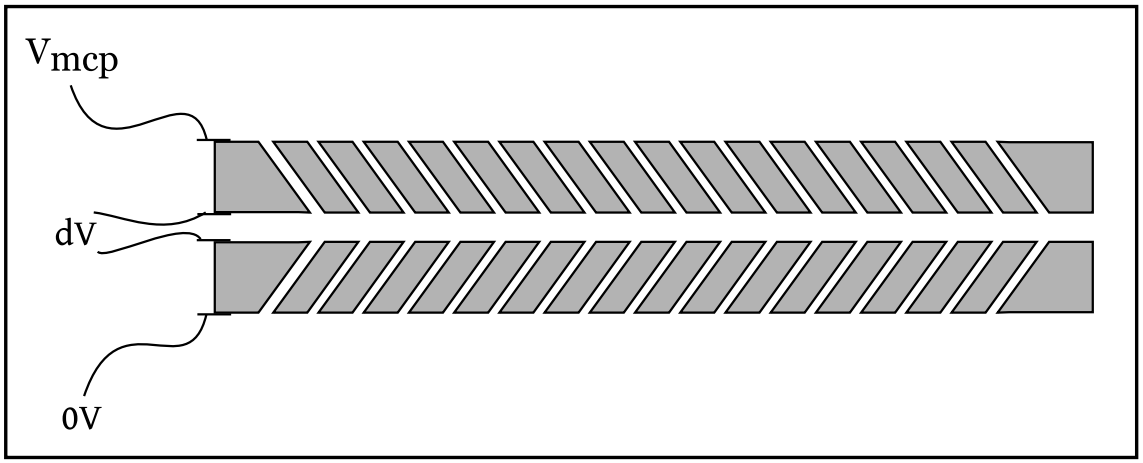

Figure 1.2: The MCPs are stacked in a chevron configuration to reduce the rate of ions flying up through the plate. The output of the lower plate is kept at 0 V and the top of the stack at V_{mcp}. Between the plates we can add a voltage dV.

When the electron shower cascades, the channel is temporarely emptied of electrons. Due to the voltage V_{mcp} over the plates, the electrons are replaced in a few nanoseconds. This sudden replacement of electrons after a discharge is a signal we can monitor. The signal is obtained by decoupling the high frequency signal from the supply voltage, as is shown in figure 1.3. The resulting signal gives us a measure of how many times a channel is fired in the MCP, it does not tell us anything about which channel it was that was activated.

In figure 1.4 a typical pulse generated by the impact of one particle is shown. The signal is take from the decoupler connected to the input plate of the top MCP. There are several rebounds visible, however the contrast with the first peak is big enough that we can easily distinguish between the signal peak and the rebound peaks.

At low flux the measured count rate will saturate, at a fixed discrimination level, as at some point all the particles that have excited the first electron will have generated a pulse that is above this level. At high flux, the count rate does not saturate with V_{mcp}, as increasing V_{mcp} allows faster replenishment of electrons in the multiplier tube.

When the flux gets large enough that pulses generated start to overlap in time; when the arrival time between two particles hitting the plate is shorter than the time it takes to reestablish the electric field after a discharge, the detector will show flux saturation. It will occur independent of the value of V_{mcp}, although the flux at which the saturation starts will be dependent on this voltage. When V_{mcp} is higher, it takes a larger flux before the detector shows flux saturation.

A gold coating on the surface of the MCP can improve the conductivity of the plate, as gold is more conductive than Nickel or Nichrome, and should allow faster replenishment of the electrons in the tubes. Therefore the coating is expected to help decrease flux saturation [51, 52].

When the voltage over the mcp V_{mcp} is large enough so that the gain has saturated,

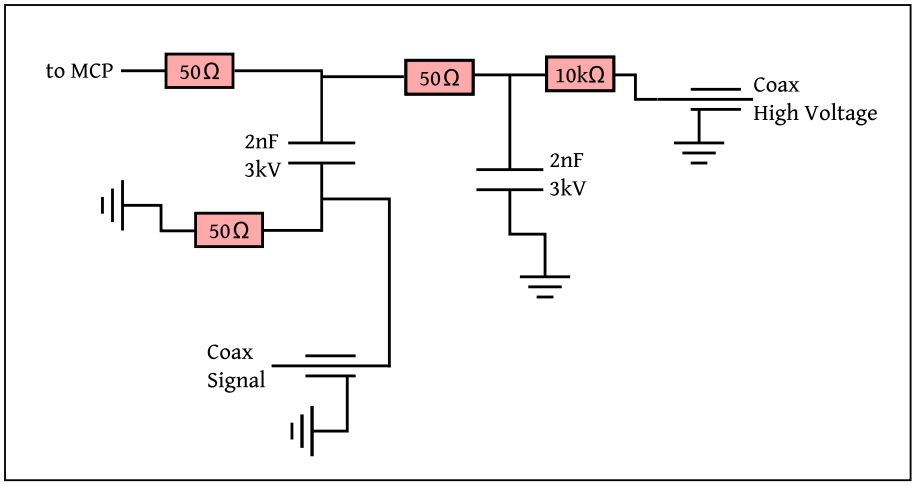

Figure 1.3: The electronics to decouple the high frequency pulse signal from the high voltage feed to the MCP.

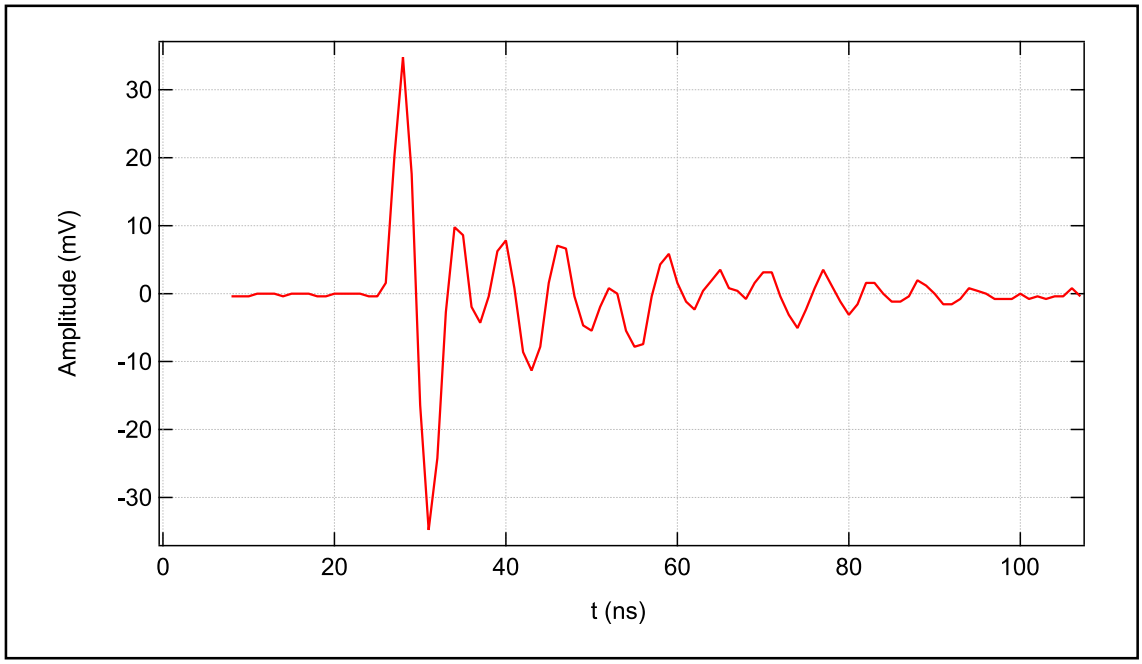

Figure 1.4: A typical pulse generated from the MCP. The primary pulse is $\sim$ 6 ns long, there are several rebounds that are easily distinguished from the first peak.

we can identify three flux regimes. At very low flux, when the detector is far from flux saturation, the count rate will increase linearly with the flux. The slope of the relation will be depending on the efficiency of the detector. If the flux keeps increasing, when the interval between particles becomes similar to the time it takes to recharge the channels, the count rate will start to saturate. There is a regime where the count rate still increases with increasing flux, but no longer linearly. The count rate completely saturates at a certain point, meaning that if the flux increases even more, the count rate will stay the same. In the saturated regime, the count rate is only dependent on V_{mcp} and no longer on the flux.

MCPs are usually operated in pairs, stacked on top of each other, either right on top of each other, or seperated by spacers, as in figure 1.2. The electron shower exiting the top MCP will spread out when it leaves the channel, as the electrons have different transverse kinetic energies [53]. When the electron shower hits the surface of the bottom MCP, the electrons will induce cascades in more than one of the channels of this plate, depending on the spreading of the shower and keeping in consideration that the bottom MCP also will show flux saturation. The excited channels in the bottom plate will have cascades of themselves and the result is a large electron pulse at the exit of the bottom plate.
Both MCPs need a voltage V_{mcp} to operate. To optimize conductive contact, we connect each face of each plate separately and operate the system in series. The output of the bottom plate is kept at 0 V, the input plate is connected to a negative voltage. This is another measure to prevent electrons from moving up through the channel, in combination with placing the two MCPs in chevron configuration. In this chapter we discuss the possibility of adding a voltage between the output plate of the top plate and the input plate of the bottom plate, which we shall refer to as dV. See below in section 1.2.3 for more details.

1.2.2 Delay Line Anodes

To obtain information on the position of the incident particle, the output electron shower can be captured in several ways. It is for example possible to visualize the output on a phosphor screen, as is done in night vision goggles. The phosphor screen can also be monitored with a camera.
We chose to capture the signal on a crossed delay line anode as its accuracy is far higher than the other methods.

To capture the amplified electron shower exiting the output surface of the MCP we use a two-dimensional delay line anode. Delay lines are transmission lines that are wound in one direction, like a helix. There are two delay lines, one for each spatial direction. When the electron shower hits the delay line, a pulse will be generated in both delay lines. The wires wrapped around the anode consist are paired, for each spatial direction there is a signal wire and a reference wire.
Due to the winding the speed of the signal in the winding direction, is much lower than the speed of the electrons in the wire it is possible, using the difference in arrival time between the two pulses, to determine the arrival position of the pulse.

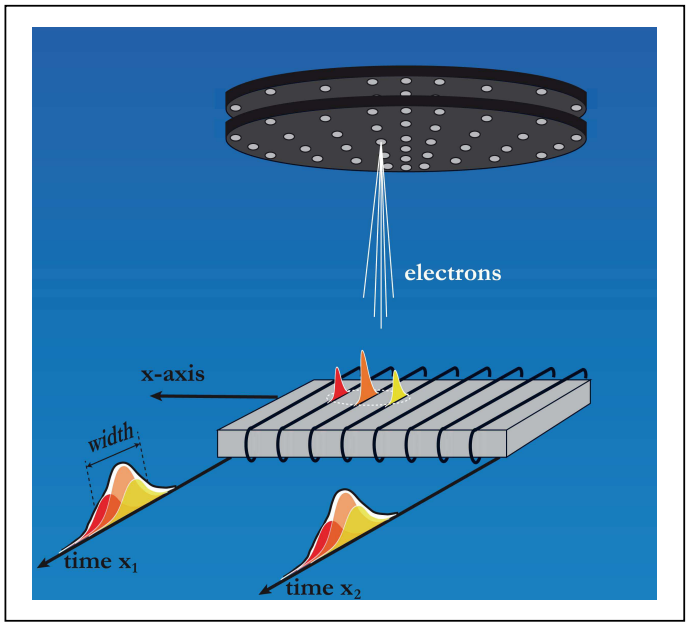

Figure 1.5: An electron shower exiting the second plate of the MCP pair is accelerated towards the delay line anode. During the time-of-flight the electron shower expands transversally and finally excites several loops of the delay lines. After propagation in the transmission lines, the pulses from the different loops overlap due to dispersion. A single broadened pulse is observed at the output of the delay lines.

The shower will hit more than one loop at the same time, however dispersion in the wire ensures that the pulses will overlap by the time they reach the end of the line. The center of the broadened pulse can be determined with greater precision than the spacing between adjacent loops. In figure 1.5 the principle of the delay line anode detection system is shown.

As with the pulses from the MCP, we can also look at a pulse shape from the delay line. In figure 1.6 we see a typical pulse from one of the four delay line outputs (in this case x_1). A typical pulse height distribution is also shown. The signal is negative because the amplifier works only with negative signals, there is an inverter between it and the delay line. The middle of the pulse in determined by a constant fraction discriminator (CFD). We use the pulse height distribution to set the level of the CFD to discriminate between noise and signal. Since there is a clear distinction between the two in figure 1.6 in this situation it is an easy discrimination to make, and we put the discriminator level at -5 mV.

The size of the shower hitting the wires depends on the kinetic energy of the electrons. A large longitudinal velocity will reduce the time of flight and therefore the size of the shower, assuming the transverse velocity distribution stays fixed. A larger transverse velocity will lead to a larger expansion of the electron shower and to a larger size on the delay line anode.

When the electrons generated in the MCPs are accelerated towards the delay line, by increasing V_{mcp} or by adding a voltage dV between the plates, both the transverse and longitudinal kinetic energy of the electron shower exiting the final plate

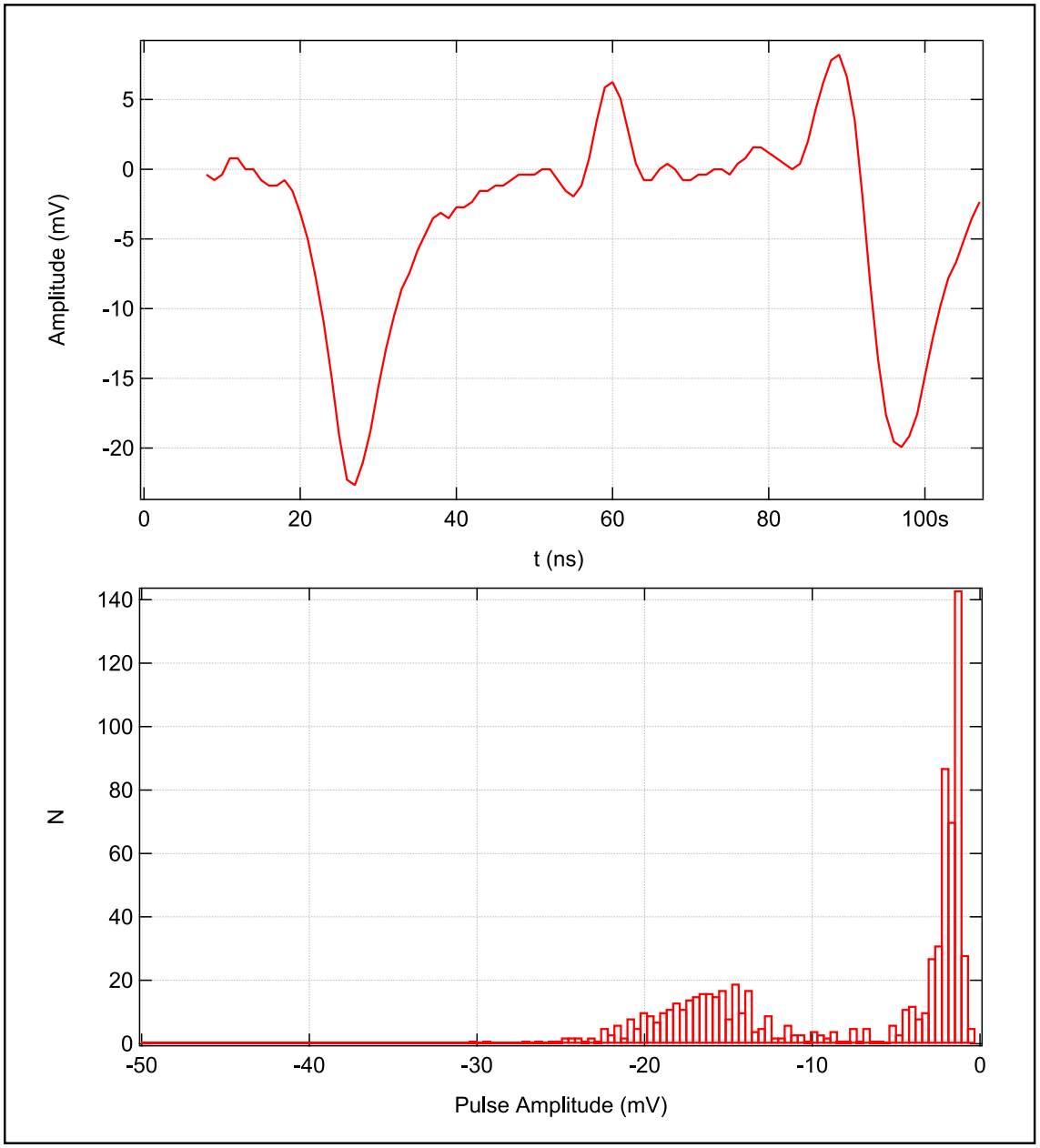

Figure 1.6: Top: A sample pulse from the delay line x_1. A second event is visible. Bottom: A typical pulse height distribution from the delay line output of the gold coated MCP, both for $V_{mcp} = 1000$ V and $dV = 0$ V. Pulse amplitudes are negative due to the CFD. The discriminator will be set at -5 mV.

are increased [53]. There is thus a competition between the two effects described above and it is not straightforward to determine whether the spot size increases or decreases.

The delay line wires are kept at a voltage of 300 V, a voltage we shall refer to as V_{sig}. If V_g is the difference between the output of the MCP and the delay line and eV_n and eV_t respectively the longitudinal and transverse electron energies then from the electrostatic force we can derive the time of flight [55]:

$$t_{tof} = \sqrt{\frac{2m}{e}}\ \frac{d}{V_g}\ \left(\sqrt{V_n + V_g} - \sqrt{V_n}\right) \tag{1.1}$$

This gives a spot size increase of:

$$\Delta_t = \sqrt{\frac{2eV_t}{m}}\ t_{tof} \tag{1.2}$$

Assuming that V_n and V_t increase the same way with the voltage V_{mcp} applied on the MCPs, one finds that the larger the voltage V_{mcp} the larger the electron shower size Δ_t on the delay lines.

Coordinate Determination

The effective velocity of the signal travelling in the delay line anode, is perpendicular to the direction of the flow of the current in the wires. The velocity is equal to the ratio of the distance between two adjacent loops and the time it takes for the pulse to pass through one loop.
The speed of an electron in a copper wire is estimated to be c and the time it takes the pulse to propagate through one loop has been measured by Roentdek to be 0.73 ns [54]. This gives an effective velocity along the axis of measurement, which has loops that are 1 mm apart, of $v_x = 1$ mm/0.73 ns$\sim 1.36 \times 10^6$ m/s. The delay line system has 100 loops in total, spread in an array of 10×10 cm.

To get the coordinates of the arrival position of the incoming particle, there are four arrival times, two four each dimension. Taking the middle of the delay line as the origin of the coordinate system, the arrival times of the pulses $t_{x,1}$ and $t_{x,2}$ at the end of the delay line are related to their incoming position x_0 and time t_0 as:

$$t_{x,1} = t_0 + \frac{L}{2v} - \frac{x_0}{v_x} \tag{1.3}$$

$$t_{x,2} = t_0 + \frac{L}{2v} + \frac{x_0}{v_x} \tag{1.4}$$

With L the length of the delay line, v the speed of the pulse in the wire and v_x the effective velocity in the direction of measurement.
It follows that the $x-$coordinate can be extracted:

$$x_0 = \frac{1}{2}\left(t_{x,2} - t_{x,1}\right) v_x \tag{1.5}$$

The $y-$coordinate is found in the same way.

The Accuracy

As mentioned above, we talk about the accuracy of the detector instead of the resolution. To determine the accuracy we need to know in what measure an identical event yields identical results.
To measure the accuracy with which the position is detected from the four arrival times t_{x1}, t_{x2}, t_{y1} and t_{y2}, whose fluctuations limit the detector accuracy, we take the quantity D:

$$D = (t_{x_1} + t_{x_2}) - (t_{y_1} + t_{y_2}). \tag{1.6}$$

Here, $t_{x1}+t_{x2}-2t_0$ and $t_{y1}+t_{y2}-2t_0$ are the total time it takes to propagate through the whole respective wires (t_0 being the arrival time of the incoming particles on the delay line. If the $x-$ and $y-$wire are the same length, a measurement of D should always give 0. In reality the wires are not exactly the same length, meaning D should have a constant, finite value that can be measured.
Due to fluctuations in the arrival times of the pulses however, the quantity D fluctuates per witnessed event around its mean value. We define the accuracy of our detector from the standard deviation σ_D of the statistical distribution of D.

We assume that for the time measurements $t_{x,1}$ and $t_{x,2}$ the errors are uncorrelated and that their standard deviation in the measurement results is equal:

$$\sigma_{t_{x,1}} = \sigma_{t_{x,2}} = \sigma_t \tag{1.7}$$

See also the thesis of M. Schellekens [56]. This leads to:

$$\sigma_D^2 = 4\sigma_t^2 \tag{1.8}$$

The standard deviation in x is:

$$\sigma_x^2 = \frac{1}{2} v_x^2 \sigma_t^2 \tag{1.9}$$

And this quantity σ_x is related to σ_D as:

$$\sigma_x = \frac{\sigma_D \; v_x}{2\sqrt{2}} = \frac{\sigma_D}{2\sqrt{2}} v_x \tag{1.10}$$

In spatial units, the accuracy is therefore given by:

$$d_x = \frac{\sigma_D}{2\sqrt{2}} v_x \tag{1.11}$$

With d_x in units of meters.

It is important to note that previous theses have written $v_x = c/300$ with c the speed of light in vacuum. While the numerical approximation is correct, there is no physical reason to write v_x this way, as the value comes from the ratio between the length of wire in one loop and the distance between adjacent loops. The speed of electrons in a wire is c, the speed of a waveguide in vacuum.

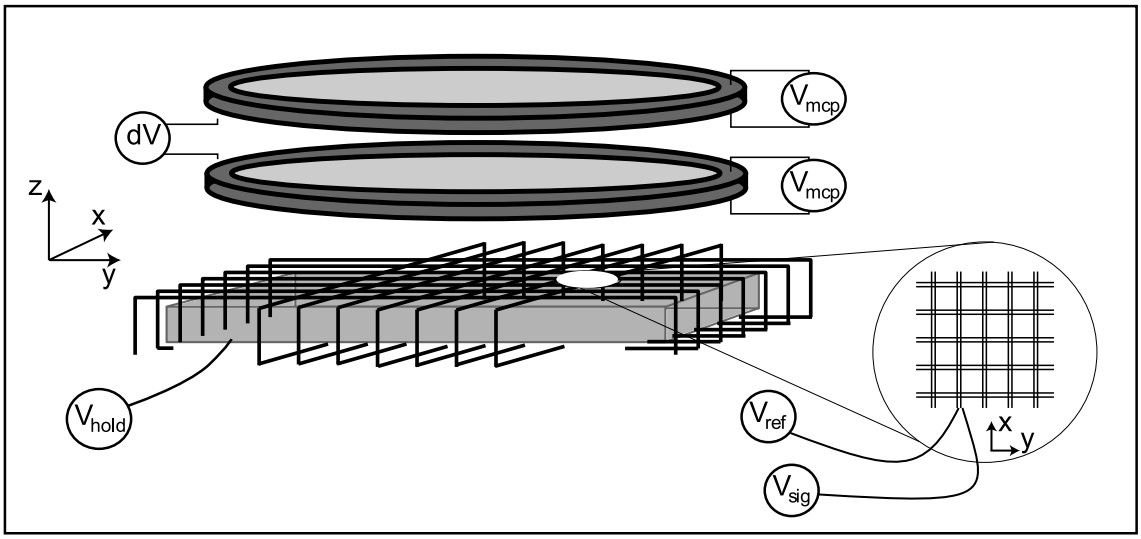

Figure 1.7: Details of the micro-channel plate mountings. Each plate is provided with a variable voltage V_{mcp}. The output face of the second plate is set to 0 V. A variable voltage dV is applied between the two MCPs. Finally, the delay line anodes are supplied with fixed voltages $V_{\mathrm{sig}} = 300$ V and $V_{\mathrm{ref}} = 250$ V for the transmission lines and $V_{\mathrm{hold}} = 150$ V for the anode holder.

1.2.3 Interplate Voltage

An overview of the detector is shown in figure 1.7. As mentioned above, V_{mcp} is the voltage over the MCPs and there is the possibility to add a voltage between the output of the top plate and the input of the bottom plate, this voltage is referred to as dV.
Up until now we have not addressed the situation in which there is a voltage dV applied between the two MCPs. The added voltage will have the effect of accelerating the electrons towards the second plate. This both collimates the electron shower and transfers (longitudinal) energy to the electrons. An interplate voltage will therefore increase the chance that the electrons induce a cascade in the second plate. An increase of dV should therefore have a positive effect on the efficiency and the signal-to-noise ratio of the detector.

When the electron shower is collimated it will excite fewer channels in the second MCP. The size of the spot on the delay line depends on the initial size (the number of channels excited in the second plate) and transverse expansion of the shower between the second plate and the delay line, as described above. The interplate voltage decreases the former, as there are less channels excited in the second MCP, but increases the latter as the increase in energy will result in a larger transverse velocity. The net effect of dV is therefore non trivial and it is worth being investigated. Adding dV should raise the efficiency and increase the accuracy of the detector [55, 57], but not all workers have observed such improvements [58].

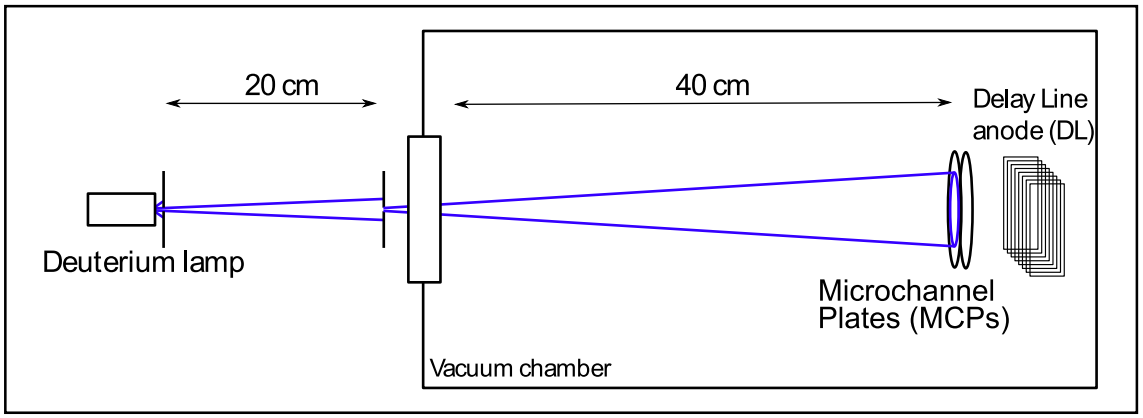

Figure 1.8: A deuterium lamp emitting photons in the range 185 nm to 400 nm is shone onto the MCPs. The light passes through two pinholes which control the flux. Inside the vacuum chamber the photons hit the MCPs.

1.3 Experimental Setup

To test our MCPs directly with metastable Helium atoms is impractical, as the vacuum will need to be opened often to change the plates and the vacuum requirements for ultra-cold gases are more stringent than the requirements of the MCPs. The MCPs need only 1×10^{-6} mBar to operate, whereas for obtaining a magneto-optical trap with Helium the vacuum needs to be at least 1×10^{-8} mBar.
We choose instead to work with ultraviolet photons. This allows us to work with a simple vacuum chamber that can be opened easily and pumped back to operating values within 12 hours, as opposed to several weeks.
The energy of an UV photon is comparable to that of a metastable Helium atom (19.8 eV for Helium and of the order of 10 eV for the UV photons) and both will in general only excite one starting electron in the multiplier tubes. This does not hold true for ions, which can release more than one primary electron. What we learn from working with photons will be applicable for metastable Helium.
The photons are emitted by a deuterium lamp L6301-50 from Hamamatsu, with a spectrum ranging from 185 nm to 450 nm. This lamp uses the vibrational transitions of deuterium to generate a broad spectrum of UV photons.

We study two different pairs of MCPs. Both pairs are new, Nichrome MCPs from Photonis USA, Inc. with a diameter of 1.245 inches and were matched by the manufacturer. The micro-channels have a diameter of 10 μm, a center-to-center spacing of 12 μm and a bias angle of 12°. All technical specifications are given by the manufacturer and we have found no discrepancies in the resistances of the plates with the ones provided. One pair has a layer of 10 μm of gold deposited on the input surface of the first plate. In this work we have not considered the alternative mounting consisting in using the gold surface as the input one of the second plate. In the following we will refer to the non-coated MCP pair when using two Nichrome coated MCPs and to the coated pair when using the pair with the gold coating. The setup of the tests is show in figure 1.8. The detector setup is placed in a vacuum chamber

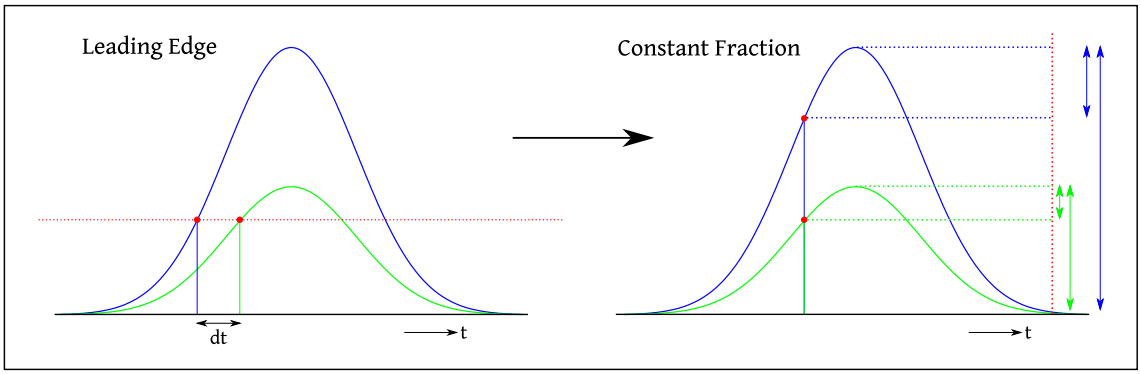

Figure 1.9: Left: A leading edge discriminator triggers as soon as the signal reaches a certain level. When the pulses have different amplitudes, while having the same center position, this leads to an unwanted offset. Right: a constant fraction discriminator triggers when the signal reaches a certain fraction of its maximum value. This gives the same output timing signal for pulses with different amplitudes.

with a pressure of 10^{-6} mBar. We mount the two plates with a circular spacer in between them, with conducting surfaces to allow the application and adjustment of dV. Even when we keep $dV = 0$ V, the spacing is still there to ensure the same environment for every test. In the usual chevron configuration the two plates are mounted on top of each other.
We can vary the voltage dV from 0 V to 250 V. Below the MCPs is the aforementioned delay line anode that picks up the emitted electron showers from which we get a three-dimensional reconstruction of the signal.
The pulses we obtain from the delay line are decoupled from the reference voltages by a Roentdek FT12-TP feed through and decoupler. The pulses are subsequently amplified and discriminated by a Roentdek ATR-19 Constant Fraction Discriminator/Amplifier.

The pulses we get from the delay line will not always have the same size, as we know from the pulse height distributions. We can cut off the noise by setting a discriminator level, but to determine the position of the pulse, we cannot just use a fixed 'trigger level'. This method, known as leading edge discrimination, does not work when the pulses have different heights, see figure 1.9. As a solution, the Constant Fraction Discriminator (CFD) triggers when the signal reaches a certain fraction of its maximum amplitude, giving always the same result for the identified time of the pulse, no matter what the amplitude of the pulse.
To get this result, the CFD takes the original pulse and duplicates it. One of the two pulses gets divided by a certain, adjustable fraction, and delayed by a certain, adjustable time. The two signals are then substracted and the zero crossing of this final pulse is taken as the time signal for this pulse, and is outputted as a NIM (digital 0 at 0 V, digital 1 between -0.8 and -1 V) signal, see figure 1.10.
The settings of the electronics are fixed throughout the study with the CFD level threshold set at 5 mV. The amplified pulses are then processed by a Time to Digital Converter (CTNM4, IPN Orsay) with a coding step of 250 ps. For counting the

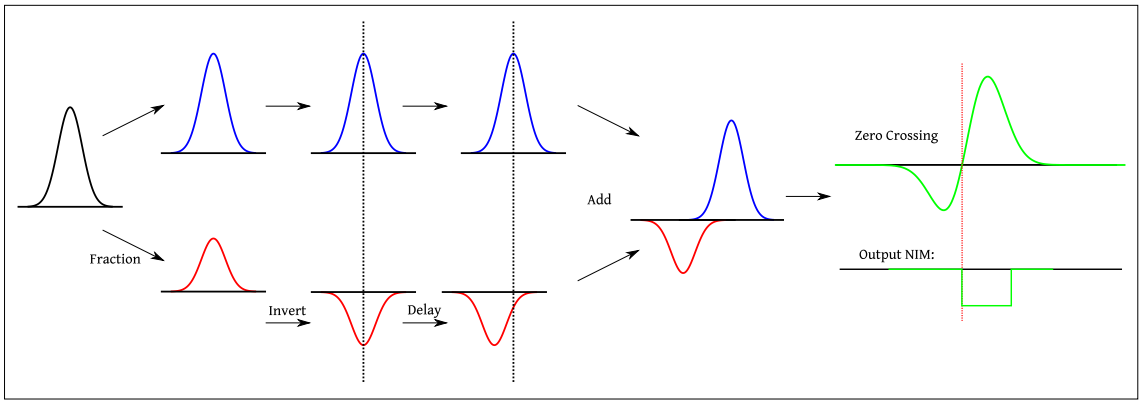

Figure 1.10: The operation of a constant fraction discriminator. The original pulse gets duplicated, after which in one of the branches the pulse is made smaller by a constant fraction, which is adjustable. The smaller pulse gets a certain time delay, and the two pulses are added. The point at which the total signal crosses zero is taken as the start of the NIM signal. This timing is always the same compared to the center of the pulse, not dependent on the amplitude of the original signal.

pulses from the delay line we take the pulses after the CFD/Amplifier and count them with a counter. The pulses from the MCP are taking directly from the high voltage signal as described before. We will use the pulses from the delay line for our subsequent measurements, therefore any mention of the count rate assumes counting pulses from one of the delay lines. All four delay line outputs are always checked for consistency.

The photons emitted by the lamp pass through two pinholes, the first right after the lamp to reduce the amount of harmful radiation in the lab, the second just before the window of the vacuum chamber. The size of the first pinhole can be varied from 0.5 mm to 2 mm, allowing us to change the flux of photons on the MCPs. To obtain a absolute number for the flux we have measured the intensity of the lamp with the different pinholes, with the use of an interference filter at 410 nm and extrapolating using the spectrum provided by the manufacturer of the MCPs. The window of the vacuum chamber is made of magnesium fluoride, which has a cut-off wavelength at 100 nm. The spectrum of the lamp is broad, but do not expect all the photons at all wavelengths to contribute equally to the excitation of primary electrons on the MPC. The effiency of multiplier tubes in detecting UV photons decreases sharply from 10^{-5} at 180 nm to 10^{-9} at 250 nm [59]. In fact, when we operate the system with a Kodial glass window that has a cut-off at 250 nm, we barely register any counts on the detector. We therefore only detect the photons with the lowest wavelengths, close to 200 nm, with an energy of $6 - 7$ eV.

To create the voltage dV F. Moron has designed and constructed a divider box for us. In figure 1.11 we see the electronics. This box allows us to change dV manually with a potentiometer and to measure both dV as well as the two V_{mcp}. Due to the design of the box, changing dV also changes V_{mcp} and to keep the voltages over

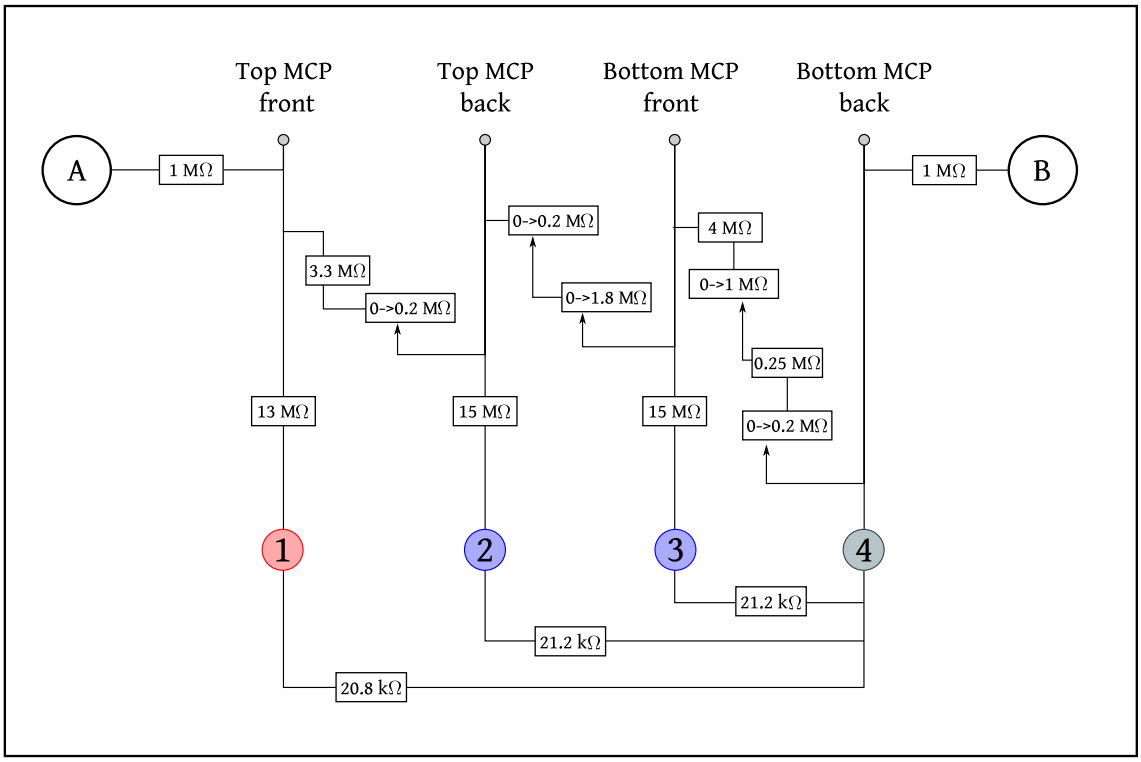

Figure 1.11: The electronics designed by F. Moron, that allow us to divide the total voltage into dV and V_{mcp}. The total voltage is put over A and B, the high voltage going to the MCPs are indicated. The numbered red, blue and black points are where we can measure the voltage over the respective channels. The measured voltage is 1/100 of the true signal, for safety reasons. The electronics are put in a plastic box.

the two MCPs the same, their potentiometers also have to be adjusted.

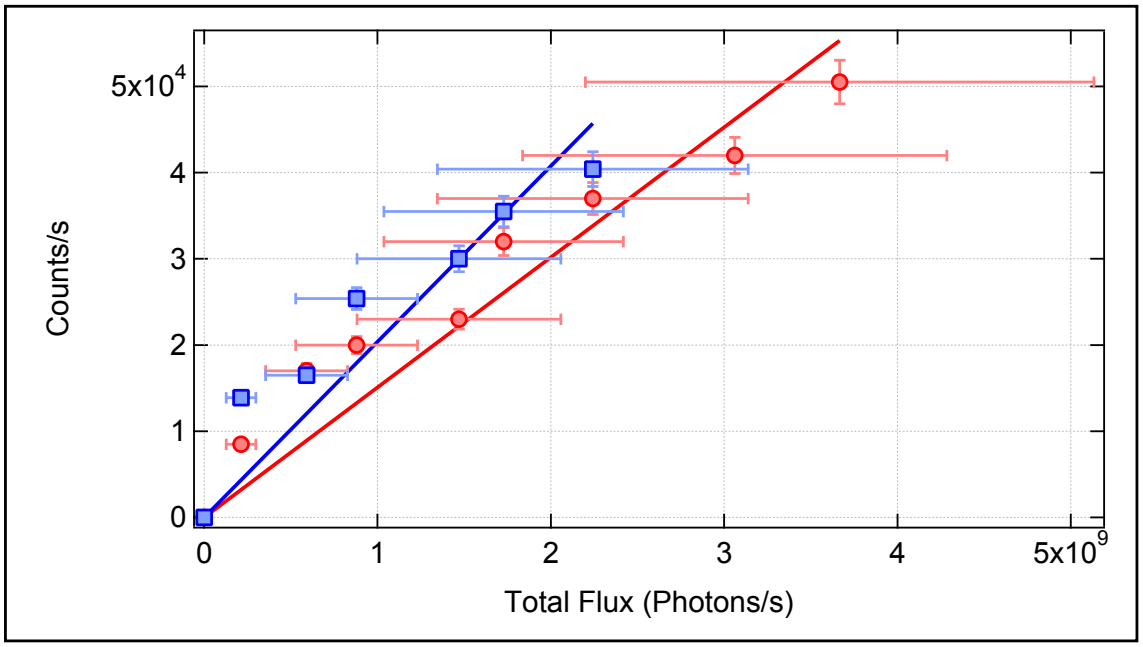

Figure 1.12: The count rate from the delay line output y_2 as a function of the incoming flux for the low flux regime, where the relation is linear. Blue squares: Gold coated MCP. Red circles: MCP without coating. Both pairs: $V_{mcp} = 1000$ V, $dV = 0$ V. Lines are linear fits crossing the origin.

1.4 Experimental Results

1.4.1 Count Rate vs Flux

As a start to the study of the two different pairs of MCPs we measure the count rate from the MCPs as a function of the flux. This will tell us whether the gold coating has indeed the expected positive effect of reducing the flux saturation. The photon flux plotted here is the number of photons emitted by the lamp and passing through the pinhole in a spectral range of $\sim$ 1 nm at the wavelength 200 nm, which is slightly underestimating the total number of photons. The count rate is measured from pulses from the delay line, after the constant fraction discriminator and amplifier. Without the amplifier the counter does not register the counts.
From figure 1.12 we see that for low flux the count rate goes up linearly with the intensity of the lamp. The slope at low flux is 2.0×10^{-5} counts/photon for the gold coated MCP and 1.5×10^{-5} counts/photon for the MCP without coating, values comparable to [59] for photons with a wavelength of 200 nm. For larger fluxes the linear relation no longer holds up. As we see in figure 1.13 the flux deviates from the linear regime and starts to saturate. Shown here are curves for the two sets of MCPs with a small interplate voltage $dV = 25$ V. The gold coated MCP exhibits slower flux saturation than the non-coated plate, even with a non-zero dV present. For comparison also the non-coated plate with $dV = 0$ V is plotted (for the gold coated pair dV does not have a big influence, see figures 1.14 and 1.15). The gold coated pair showing less flux saturation is related to its lower surface resistance compared to the pair without coating. The gold allows faster replenishment of the input plate

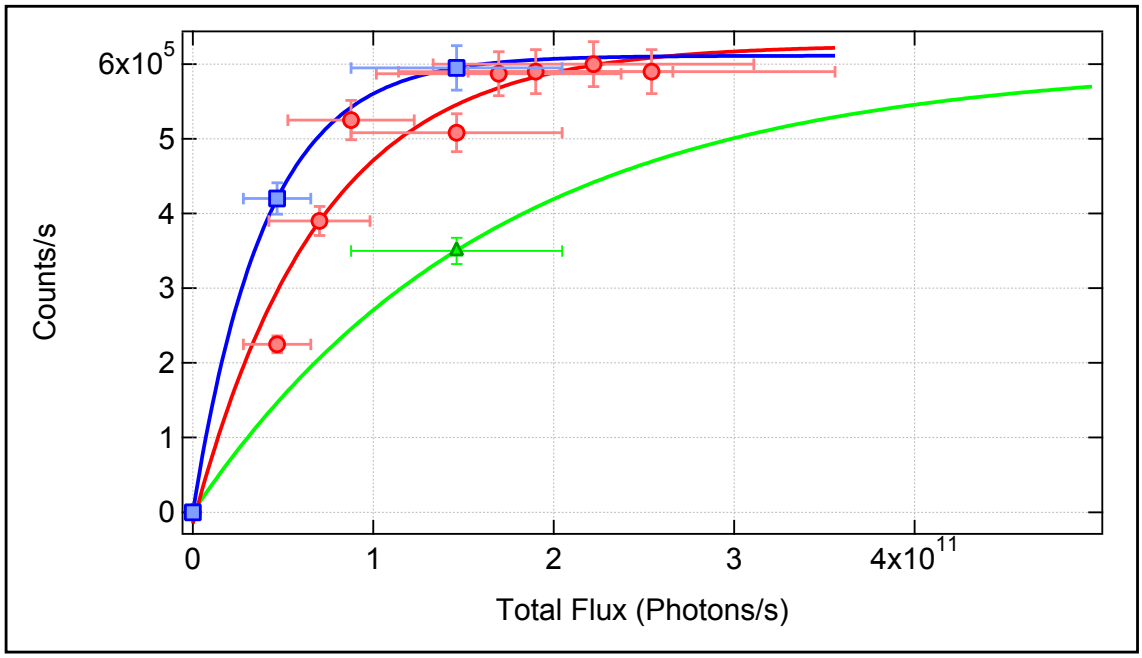

Figure 1.13: The count rate at higher flux. The count rate for the gold coated pair (blue squares) hardly changes with dV (plotted is $V_{mcp} = 1000$ V, $dV = 25$ V). dV has a strong influence on the non-coated pair: Green triangle: $V_{mcp} = 1000$ V, $dV = 0$ V / Red circles $V_{mcp} = 1000$ V, $dV = 25$ V. Lines are exponential fits.

[52]. The level at which the flux saturates is determined by the properties of the channels, which are the same for both pairs.
The work function for gold is 5.1 eV and for nickel 4.6 eV. The quantum efficiency of the input plate is therefore expected to be the same for both pairs of MCPs.

1.4.2 Count rate

Further characterization of the difference between the two pairs is done by monitoring the response of the count rate from the delay line to an increase of V_{mcp}. As mentioned before, MCPs need a certain voltage to start working, if the voltage is too low there will not be any secondary electrons generated. We increase V_{mcp} and measure the count rate, the result is seen in figure 1.14. These measurements are done at a photon flux of $\sim 1.5 \times 10^{11}$ photons/sec, near the saturated regime. The gold-coated MCP exhibits gain saturation at a lower total voltage V_{mcp} than the non-coated pair.
To systematically investigate the influence of dV on the performance of the MCP we keep V_{mcp} constant and increase dV, results are shown in figure 1.15. As mentioned above, for the pair of MCPs with the gold coating on the input surface, adding the interplate voltage dV does not have much effect. This is because the gain is already saturated. However for the pair with no coating on the input, this is not the case and adding a finite dV improves the gain of the detector. The effect saturates at $dV \simeq 50$ V.
This increase of the gain with dV that we find differs with findings in the literature

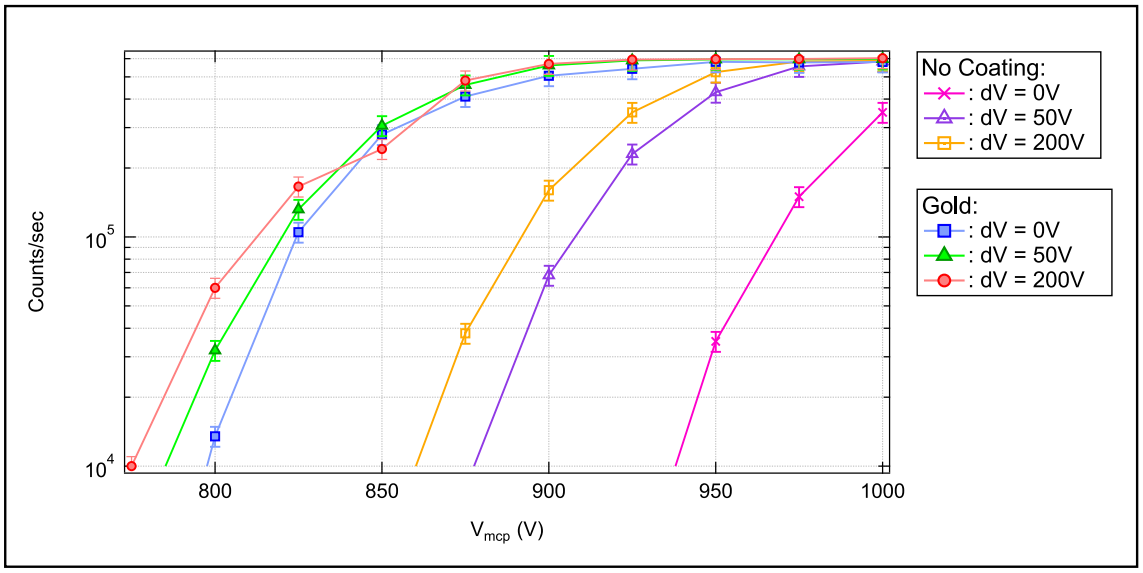

Figure 1.14: Count rates as a function of V_{mcp} for the two pairs of MCPs and for different voltage differences dV. Incoming flux $\sim 1.5 \times 10^{11}$ photons/sec.

[58]. We believe this to be because even at $dV = 0$ we are working with a spacing between the two plates. The distance between the two plates is crucial to the effect of dV [55], it is for instance possible that if the two plates are very close together, that adding dV can have a negative effect on the gain, because the electron shower gets collimated too much. We have seen that pressing the plates closer together results in a drop in the count rate by a factor $5 - 10$. The MCPs in our experiment are spaced $\simeq 0.2$ mm apart, a distance that is defined by the thickness of the two spacers separating the two plates.

These measurements show, that although the gold coating has a positive effect on the gain of the detector, it is possible to get the same result without a coating by adding an interplate voltage dV. The final level of flux and gain saturation depends on the channels of the detector and is therefore the same for both MCP pairs.

1.4.3 Pulse Shapes

Since we have seen the effect of the gold coating and dV on the gain of the detector we turn to an investigation of the shapes of the pulses registered from the delay lines and the MCPs. The final three-dimensional reconstruction of the particles falling on the MCP comes from the four arrival times of the signals from the four delay lines, t_{x1}, t_{x2}, t_{y1} and t_{y2}. Our ability to accurately determine the incident coordinates will depend on the shape of these pulses. Their amplitude and width determine how well we can determine the center of the pulse.
A study into the accuracy of the detector system must therefore start with an investigation of the pulse shapes, to increase our understanding of the working of the system.

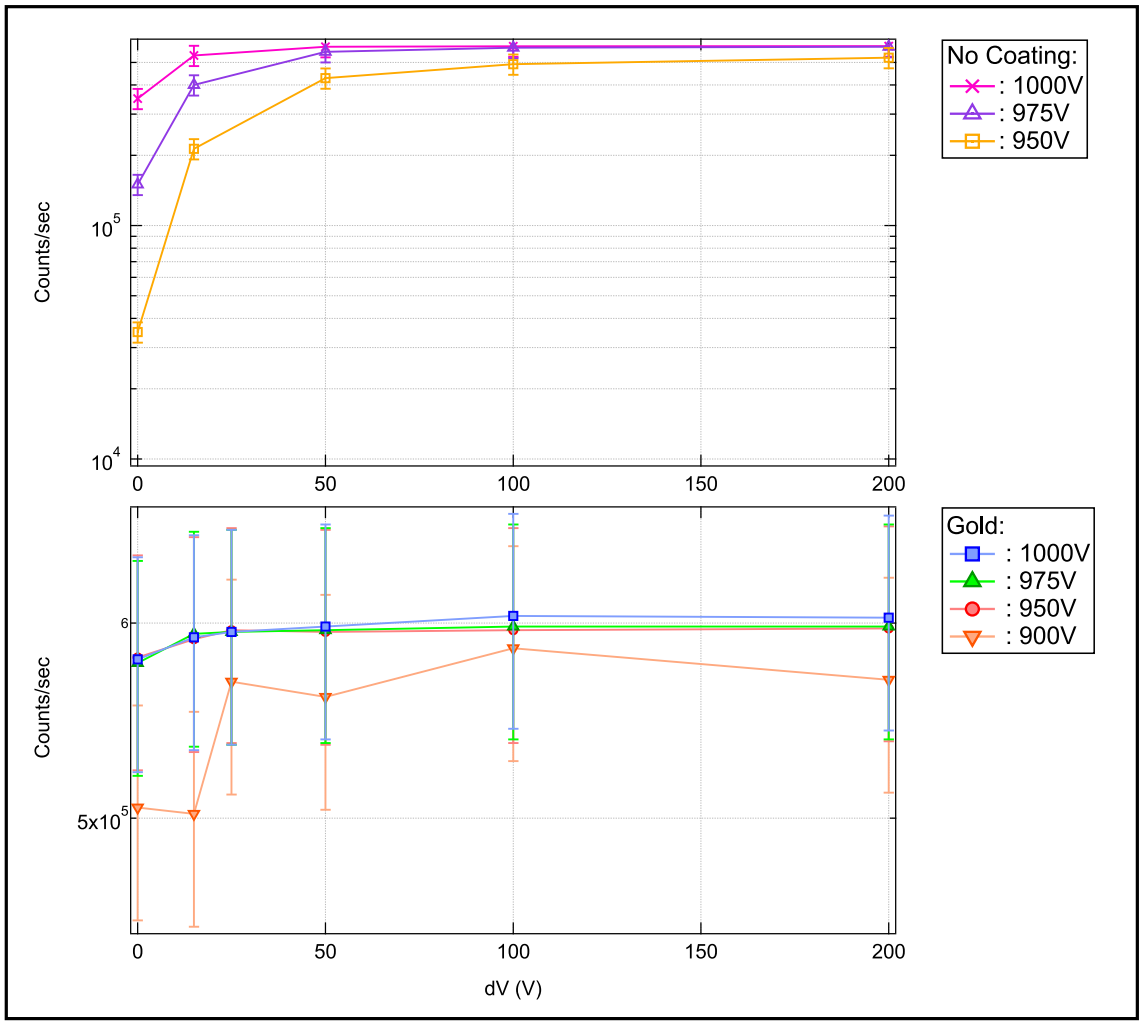

Figure 1.15: Top: Count rates measured with the non-coated MCP pair as a function of dV. Bottom: Count rates measured with the gold coated MCP pair as a function of dV. Incoming flux in both cases is $\sim 1.5 \times 10^{11}$ photons/sec.

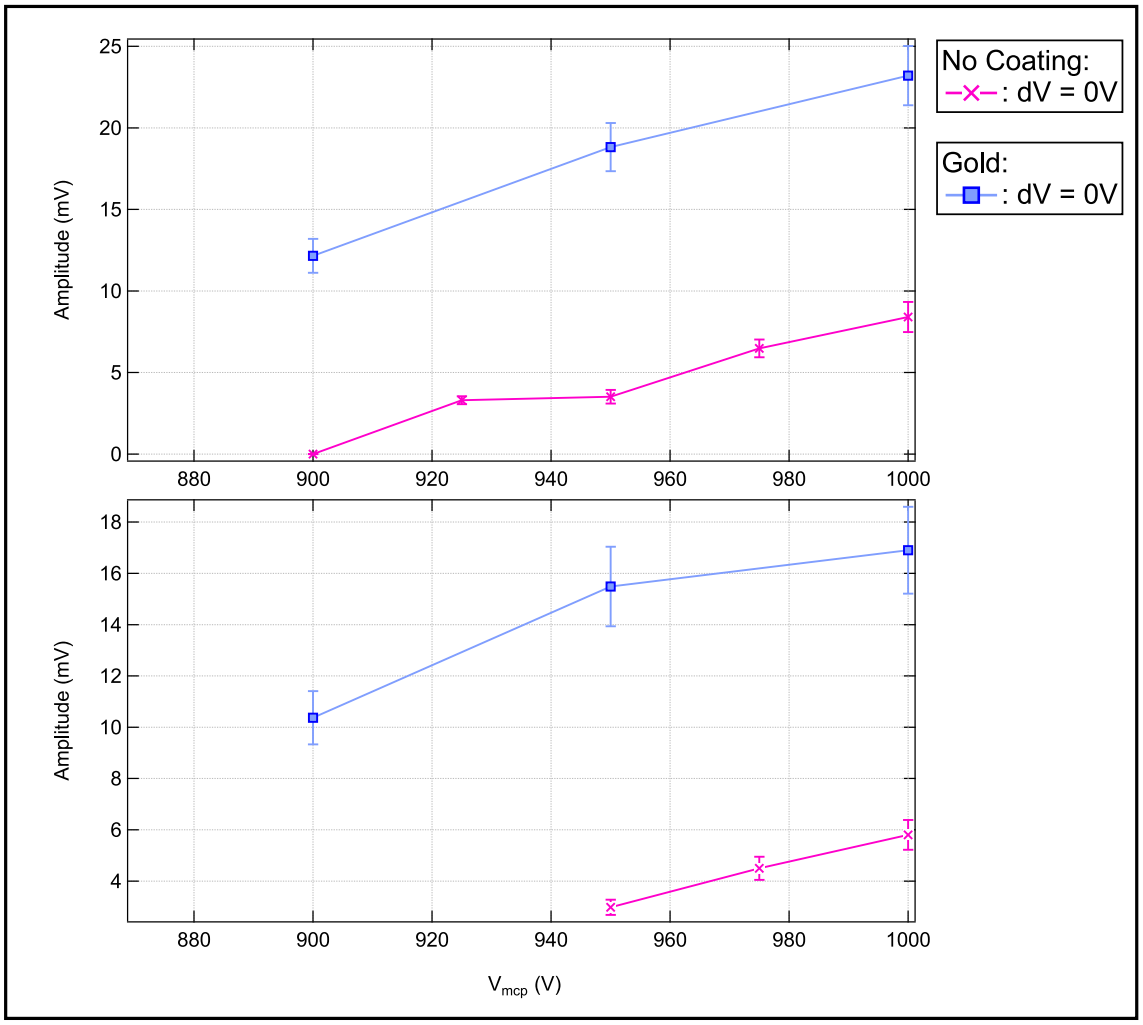

Figure 1.16: The mean amplitude taken from the pulse height distributions of the pulses for $dV = 0$ V and as a function of V_{mcp}. Top: The amplitude of the pulse from the input plate of the MCP. Bottom the amplitude of the pulses from the delay line, averaged over all four channels.

Amplitude

In figure 1.16 it is shown how the amplitude of the pulses from both the MCP and the delay line changes when V_{mcp} is increased. The displayed amplitude is the fitted mean of the pulse height distributions. The first thing that we note from this results is that without any interplate voltage $dV = 0$ the amplitudes of the pulses from the MCP are higher for the pair with gold coating. This is consistent with our previous results of the higher count rates observed for this MCP pair.
As expected, the higher V_{mcp}, the more electrons are used in a channel, which results in a larger amplitude of the pulse from the MCP. This effect follows through in the amplitudes of the delay line, as they are in principle the same electrons, and more electrons in the MCP channels will mean a larger electron shower and a larger number of electrons on the delay line. The amplitude measurements as a function

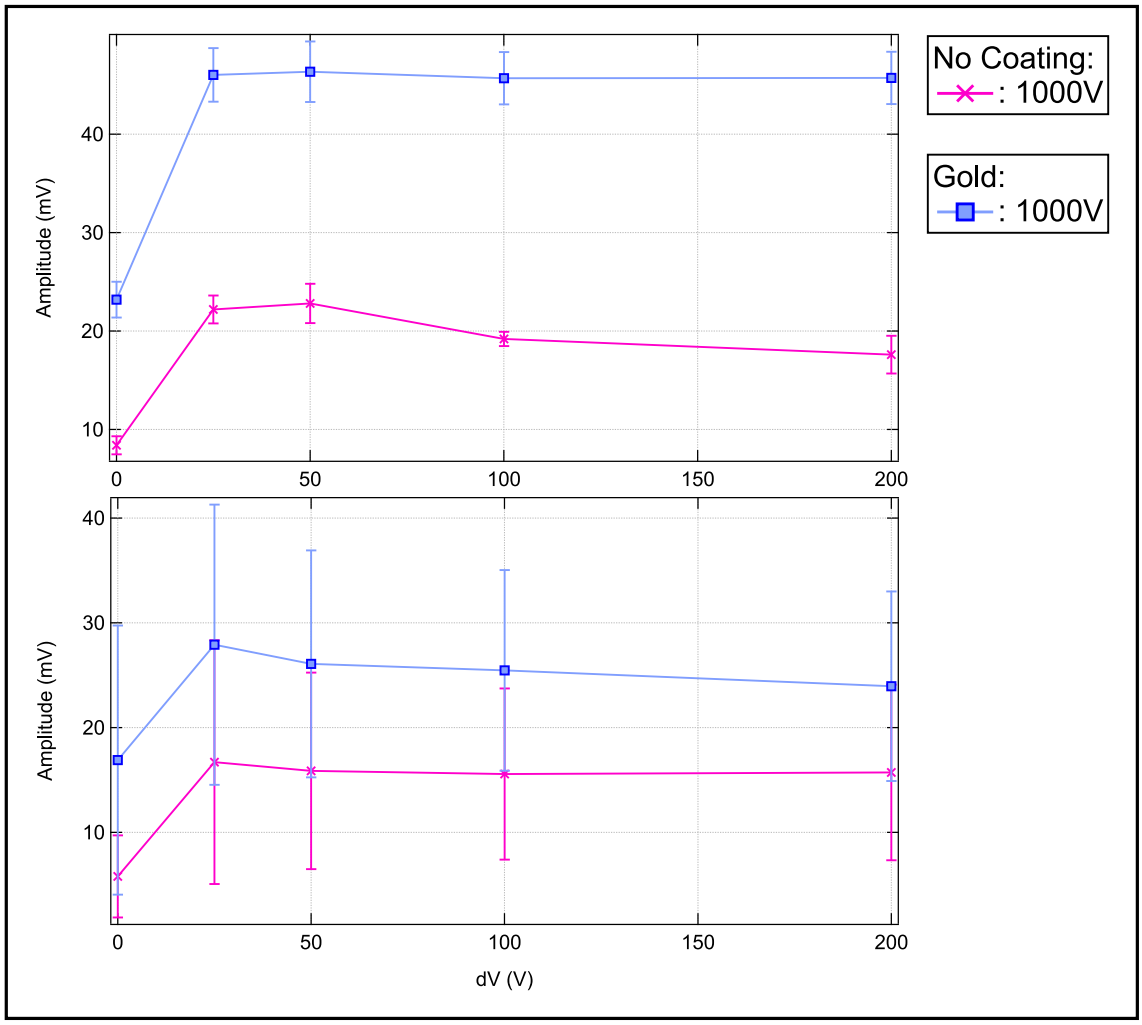

Figure 1.17: The amplitude of the pulses for $V_{mcp} = 1000$ V and as a function of dV.Top: The amplitudes of the pulses from the input plate of the MCP. Bottom: The amplitude of the pulses from the delay line, averaged over all four channels.

of changing dV are shown in figure 1.17, for $V_{mcp} = 1000$ V.
When dV is increased there is a clear effect on the pulse amplitudes, as the electrons gain energy by being accelerated. We see that while the amplitude of the pulses from the MCP are saturating and keep the larger amplitude, the amplitude of the pulses from the delay line have a maximum. This is due to the competing effects introduced in section 1.2.3, the electrons get both more transverse and longitudinal kinetic energy and a too large increase in one without a proportional increase in the other will result in a spreading out of the electron shower. In that case, more electrons in the pulse will not mean a larger amplitude, only a larger width.

Width

The widths of the pulses from the delay line are plotted in figure 1.18, for both pairs of MCPs and as a function of dV and V_{mcp}. The width is in the order of

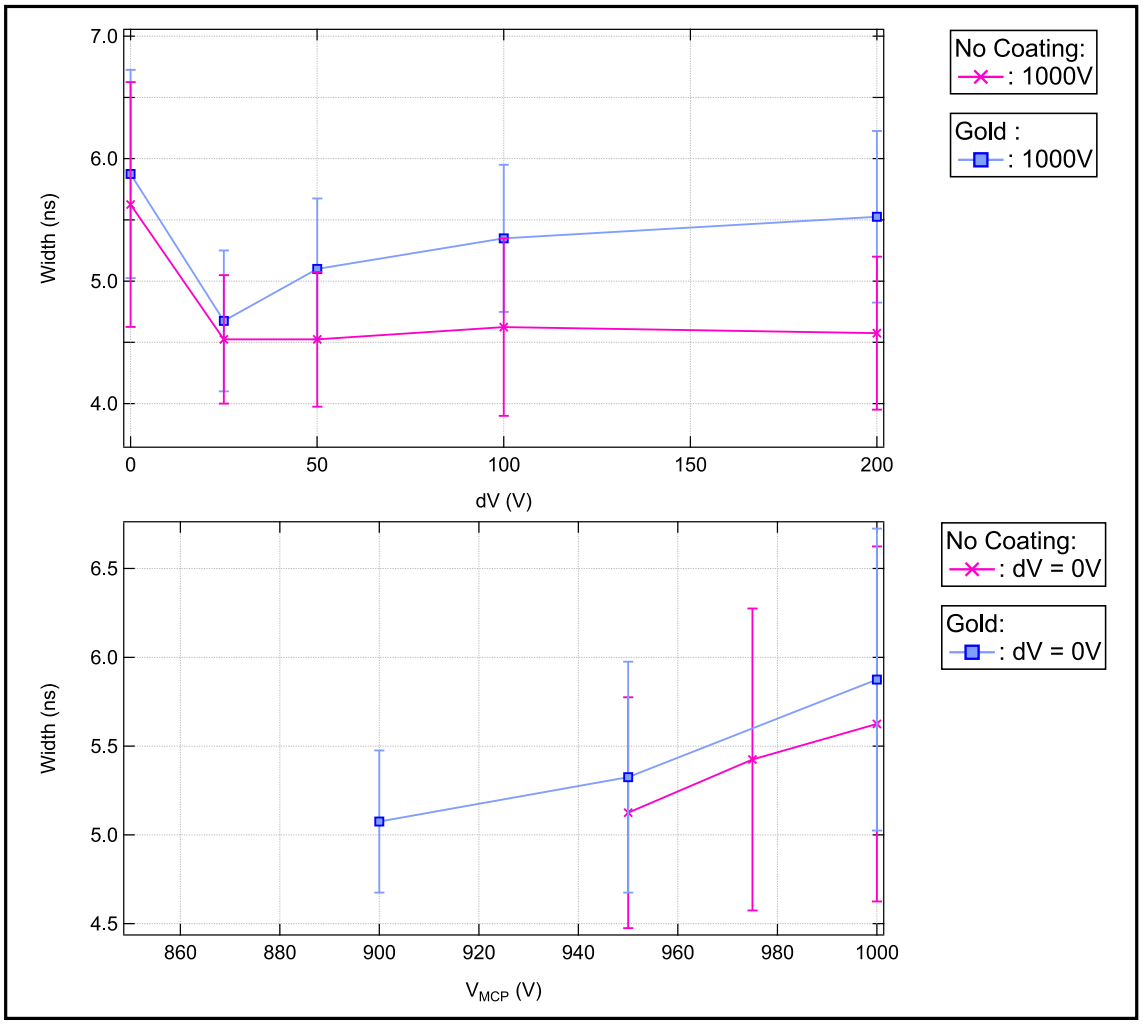

Figure 1.18: Top: The width of the timing pulses, averaged from all four delay lines, as a function of dV. Bottom: The width of the pulses with $dV = 0$ V and increasing V_{mcp}.

~ 5 ns, as predicted above, which has to do with the dispersion in the delay lines. When $dV = 0$ V, the width increases with V_{mcp} for both of the pairs of MCPs. As the pulses consist of more electrons which have larger kinetic energy with increased V_{mcp}, both the amplitude and the width increase (compare with figure 1.16).
The width of the pulses from the MCP are always the same and of the order of 1 ns. Increasing V_{mcp} or dV has no influence on this width.
Increasing dV to a small value has the effect of shrinking the size of the electron shower from the first to the second plate, resulting in hitting only a minimal number of channels in the bottom plate. After this minimum has been reached, increasing dV more has only the effect of adding kinetic energy to the electrons, and the width of the pulses on the delay line grows. The smallest pulse width is reached at an interplate voltage $dV \simeq 25$ V.
Since the width is dominated by dispersion in the transmission lines, its decrease with dV can only be of order of several percent, as it is observed experimentally

(about 10 %).

These results seem to indicate that we should be working with a voltage between the MCPs of 25 V.

1.4.4 Accuracy

In the same configuration as above, with varying dV and V_{MCP}, we test the accuracy of the detector. We suspect that the width of the pulses on the delay line is correlated with our ability to correctly determine the position of the incoming particle. In section 1.2.2 it is described how we quantitatively determine the accuracy of the detection system. We can only measure the accuracy of the detection system as a whole, the MCPs, the delay line and the electronics, as there is no way for us to separate the signals. The main source of noise is believed to come from the electronics used for the signal processing [56].

The first thing we note, is that D from equation 1.6 is not equal over the whole plate. An example of the distribution over the non-coated MCP can be see in figure 1.19. Here the mean of D is plotted for many events, usually a few thousand. To get a map like this, for every event where there are four arrival times we calculate the spatial coordinates and as well as D. There will be more than one event for every coordinate, so more than one D. The mean of this quantity D is then plotted for every coordinate. The Time-To-Digital converter has a coding step of 250 ps. This means that the pixel size and the theoretical maximal accuracy are equal to $0.25ns/2\sqrt{2} \times v_x = 88$ μm.
Not for every even we recover a pulse from all four delay lines. Sometimes one or more get lost somewhere in the chain of data processing. We do not use these events, we only use the ones that have four pulses to reconstruct the arrival position.
We see that the mean of D varies from around -30 in the upper left, to around -20 in the bottom right. This behaviour has also been observed by the other Helium experiment in the laboratory [56] and the consensus is that it is an effect that has to do with the geometry of the delay line. If one only looks at the x part of D $(t_{x_1} + t_{x_2})$ the mean will have a gradient in the x-direction, and $t_{y_1} + t_{y_2}$ has a gradient in the y-direction. As the mean of D is of no real influence on the accuracy, but rather the variation around the mean is, we shall not concern us with this gradient.
For every pixel of 250 ps by 250 ps from figures like figure 1.19 we get a distribution of the values of D for every event. We can look at the mean, but we can also derive the standard deviation σ_D.
We have found the distribution of σ_D in space, over the surface of the MCP, to be random (isotropic and homogeneous) and have therefore taken the mean of every D of every event, regardless of the pixel, as σ_D of the detector. This removes the dependence on the number of events per pixel.
We have treated the distributions as Gaussian, analyzing the accuracy in different situations. For an example of the distribution of D for the non-coated detector at $V_{mcp} = 1000$ V and $dV = 25$ V see graph B in figure 1.20.

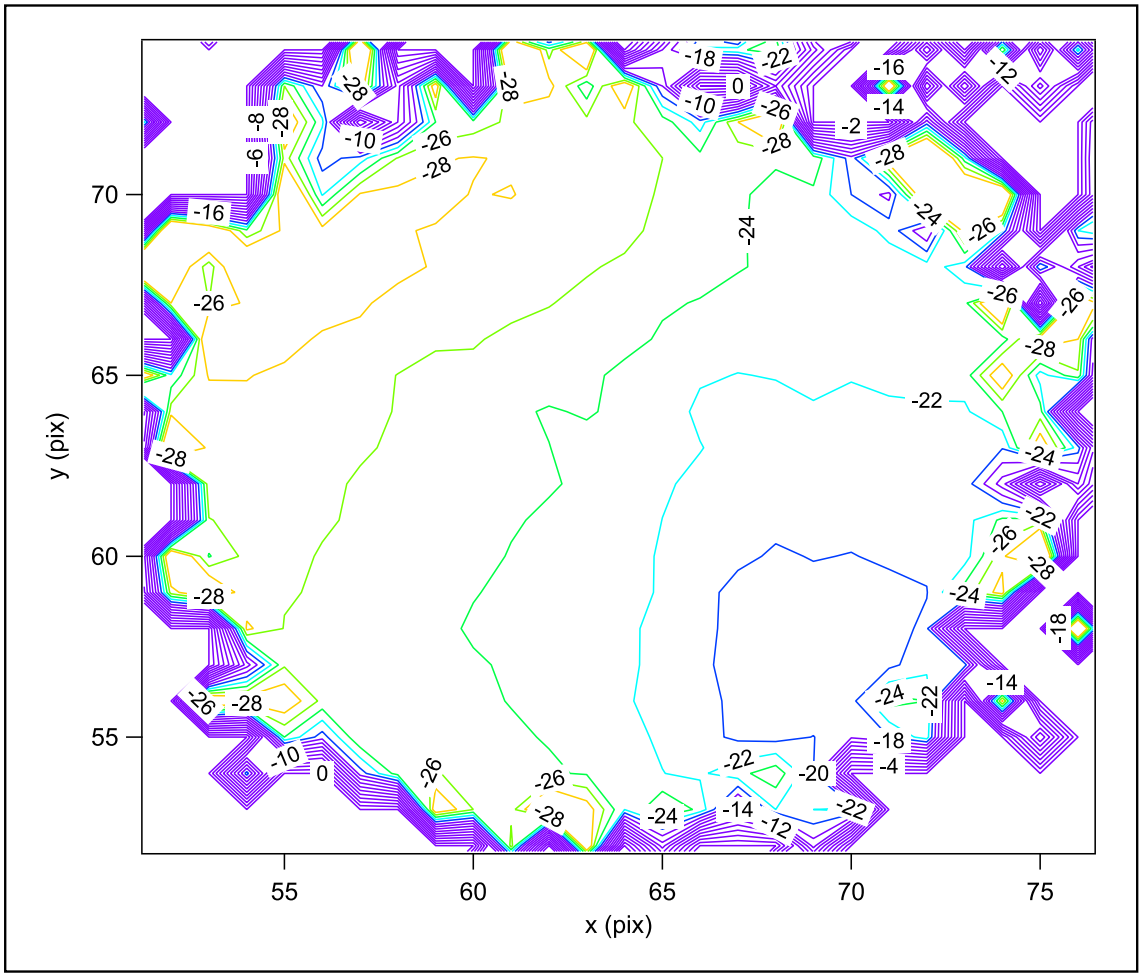

Figure 1.19: The map of the mean of the quantity D over the surface of the MCP. This image is for the non-coated MCP with $V_{mcp} = 1000$ V and $dV = 0$ V. The pixel size is 88 μm, with the size of the MCP equal to 1 inch.

In figure 1.20 we plot the mean spatial accuracy d_x as given by equation 1.11. There are a few observations to be made from this data. First, we see that for a given (high) flux, the accuracy of the detector without coating is 50% better than the accuracy of the gold coated detector. The accuracy of the gold coated pair gets better when the flux is lower. This may be due to a broadening of the pulse height distribution at higher flux as discussed in [51], leading to a smaller signal-to-noise ratio. We do not observe a great difference between different voltages V_{mcp}
Secondly, we observe a dependence of the accuracy on the interplate voltage dV. The behaviour is similar to the behaviour of the width of the timing pulses from the delay line observed in figure 1.18. The optimum value for the accuracy for dV of ~ 25 V corresponds to the minimal width and maximal amplitude of the pulses. However, the increase in accuracy is around 20%, much larger than the decrease of the width of the pulses. Therefore we believe the improvement of the accuracy to be mostly due to the increase in amplitude, as seen in the bottom graph of figure 1.17. The amplitude has an increase of $\sim 20\%$, just as the accuracy. A larger amplitude of the pulse will lead to a better signal-to-noise ratio, increasing the accuracy.
To test this hypothesis, we have mounted a phospor screen, instead of a delay line system, behind a pair of MCPs. We observe that the spot size of the electron shower decreases when increasing dV from 0 V to ~ 100 V, at which point only one channel in the second pair is excited and the focussing saturates. However we observe a large increase in the spot intensity in the range of 0 V to 50 V, with a small decrease for larger values.
In the first regime, the electrons between the two MCPs gain energy and are more likely to excite channels in the second plate. We believe this mechanism to be responsible for the increase in accuracy. The decrease in width will most likely have a positive effect on the accuracy, however the effect is small.
The increase of d_x at values of $dV > 50$ V is attributed to the slight amplitude decrease which gives a lower signal-to-noise ration.

To note, the accuracy in the z-direction is not dependent on the delay line system as the one in the x- and y-direction. It depends on how accurately we can assign a time to the arrival of the particle, and this is in essence the ration between the angle of the channels of the MCP and their diameter, see figure 1.21. There will be a different arrival times for particles hitting the side of the channel at different heights, due to the angle, even though they arrive at the surface of the MCP at the same time.
For the MCPs used in our tests, the angle is 12° and the diameter of the channels is 10 μm. This leads to an accuracy in the z-direction of $d_z = 47$ μm.

1.5 Conclusion

We have compared the performance of two different pairs of MCPs in chevron configuration, one with a gold layer and one with an usual Nichrome surface. We have tested these plates by using UV light, as it has a similar chance of exciting a primary electron.
We found the gold plated MCP to have a higher gain than the pair without coating

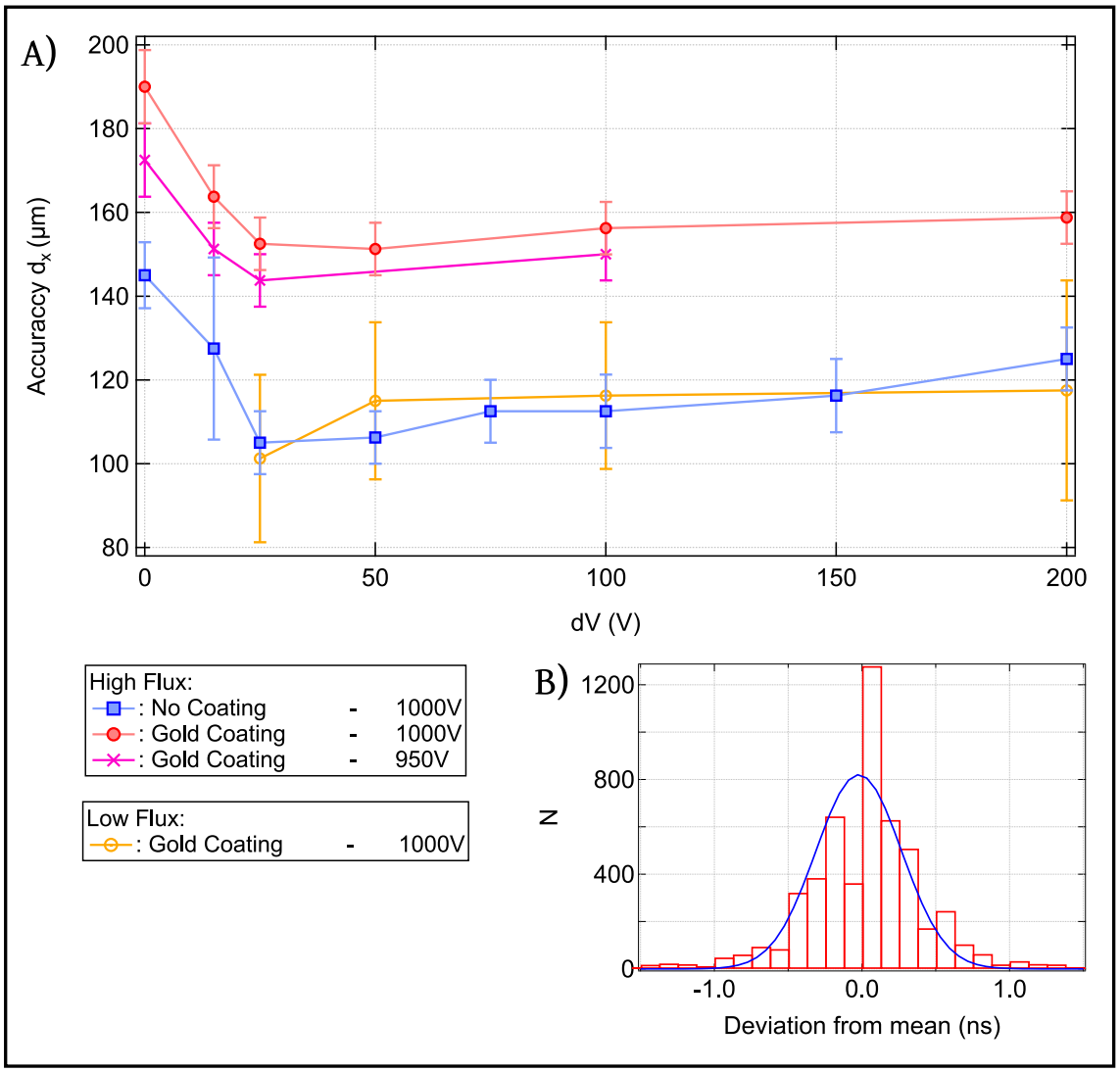

Figure 1.20: A) The accuracy of the detector in μ m for different configurations of the detector. B) The distribution of σ_D for the point at $dV = 25$ V for the non-coated MCP.

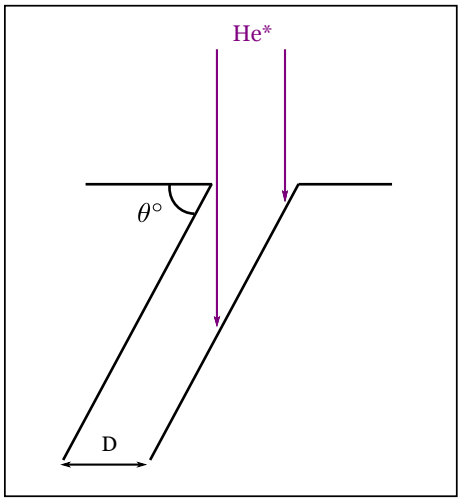

Figure 1.21: The accuracy in the z-direction is determined by the angle θ of the channels of the MPC and the diameter D: $d_z = D/\tan\theta$. Particles hitting on the left will get a different arrival time as particles hitting the channel on the right, even though their z-coordinate is the same.

Adding a gold layer on the input plate will increase the quantum efficiency of the detector by a factor 1.5. We also found that the gain of the non-coated pair could be improved by adding an interplate voltage dV between the two MCPs. The gain saturation level of both pairs is the same.
The gold layer has a negative effect on the accuracy of the detector, which is crucial for the 3D reconstruction of the cloud of particles falling on the detector. At a given flux, the accuracy of the detector is up to 30% better for the MCP without coating.

The interplate voltage dV not only increases the gain of the non-coated pair, it also leads to better accuracy by increasing the amplitude of the pulses collected on the delay line system and increasing the signal to noise ratio. The width of these pulses is also reduced, but not by a large enough factor to explain the increase in accuracy of $\sim 20\%$.
At a voltage of ~ 25 V the accuracy of the detector is ~ 100 μm.

For an experiment working at low flux, it can be interesting to use an MCP with a gold coating, as at lower fluxes the accuracy is better. However an experiment that deals with larger fluxes and is heavily dependent on the accuracy of their measurements, such as our experiment will be, is better off using a non-coated pair with an interplate voltage. This allows high gain with good accuracy.

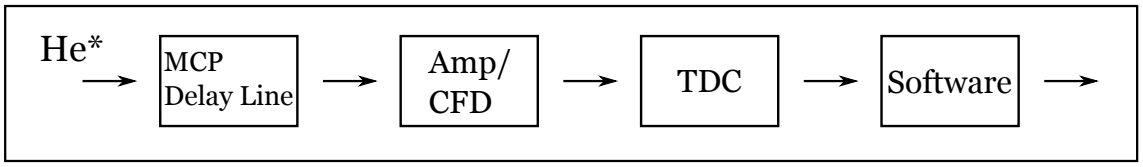

Figure 1.22: The incident particle excites an electron shower and electronic pulses in the MCP and delay line. Those signals are amplified and the position of their maximum determined by the Surface Concept amplifier. The pulses are assigned a time by the TDC, and the data is transferred to the computer, where there is specialized software to analyze it.

1.6 Outlook

The MCPs that were used for the tests done in this chapter are not the ones that are put on the experiment to detect the metastable helium atoms. For this we have bought larger MCPs with the following characteristics:

Useful Plate Diameter	78.0 mm
Plate Thickness	0.96 ± 0.03 mm
Bias Angle	$20 \pm 1^\circ$
Channel Diameter	12μ m
Z-direction Accuracy	33μ m
Gain	minimum 8×10^3

In figure 1.22 the path that the signal takes is shown. The delay line is the same as the one used in the rest of the chapter, from Roentdek. After the delay line is an amplifier/constant fraction discriminator from Surface Concept, corrected by A. Villing for input resistance and offset problems.
Extensive tests and characterization of the detection system have been done by F. Nogrette. The time-to-digital converter is an updated version of the one used in this chapter. It can be used with five channels, one for each delay line and one for the MCP surface pulses. The data from the five channels is retrieved with the same probability (multiplexing), and the system operates on a first-in-first-out basis. It is therefore continuously sending data to the computer, and the technological limit of the card is 18 MWords/s, it can be limited though by the writing speed of the data onto the PC.
F. Nogrette has also written software in CVI to analyze quickly incoming data from the detection system. A more extensive program to analyze correlations still has to be written.

Chapter 2

An Atomic Beam of Metastable Helium

2.1 Introduction

In this chapter we will discuss methods to achieve an atomic beam of metastable helium-4, its longitudinal velocity slow enough so that it can be captured by a Magneto Optical Trap (MOT). We are starting this description from the very beginning and in great detail, as this is the first thesis written about the experimental setup. This chapter is therefore partly intended to serve as a guide and a reference about the apparatus, as well as a documentation of the work done during the PhD.

With this in mind, we will start the chapter in section 2.2 by describing the vacuum system and the pumps, to give the reader a picture of the general layout of the experiment and to provide the overview needed to understand the rest of the chapter. To complete the overview, we will discuss the laser system used and the saturated absorption spectroscopy that locks the laser to the atomic transition in section 2.3.

In our experiment we use a newly available near-infrared InGaAs camera. The description and calibration of this camera can be found in appendix B.

The rest of the chapter deals with the creation of an atomic beam of metastable helium-4 and its slowing. We describe the method used to excite the metastable particles in section 2.4. The method of transverse collimation is described in section 2.5, which is necessary for the atomic beam to pass through the longitudinally slowing Zeeman slower, discussed in section 2.6.

This chapter aims to explain what it means experimentally to work with metastable helium-4, in the context of a laser cooling cold atom experiment.
The description of the experimental apparatus will continue in chapter 3 which focusses on the trapping and subsequent cooling of the atoms.

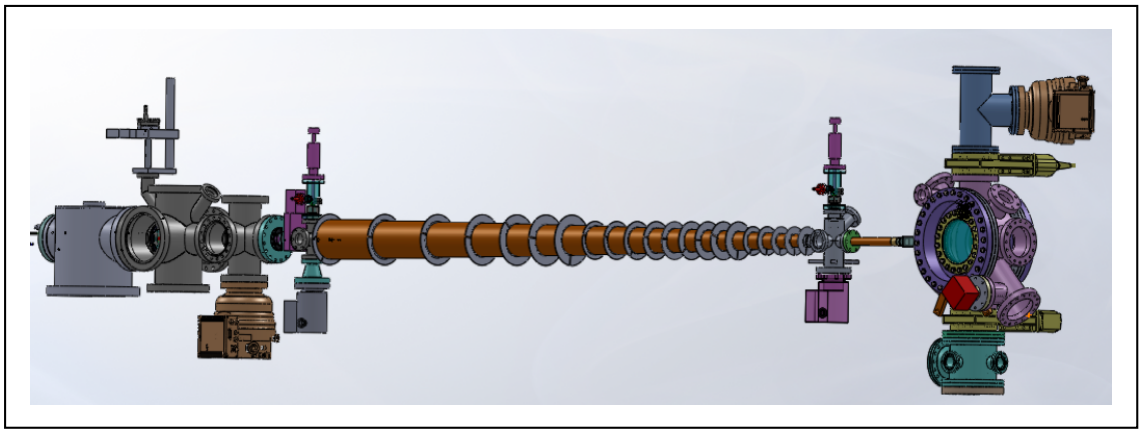

Figure 2.1: A drawing of the total vacuum system. The source on the left is where the metastable helium atoms are excited, afterwards they are collimated transversely and slowed longitudinally by the two Zeeman slowers. The end of the slower is connected with bellows to the science chamber, the glass cell which would allow the 2D MOT is no longer on the system.

2.2 The Vacuum System

2.2.1 Source Chamber and Zeeman Slower

To start with the description of the experimental apparatus that we built, we will first describe the vacuum system. In this section we focus on the description of the vacuum system in which we create, collimate and cool the atomic beam of metastable helium. The vacuum of the science chamber will be discussed in section 2.2.2.

The main point objective we have to keep in mind is that the vacuum in the science chamber in which we will trap and cool the atoms has to be as high as possible. The background gas is the limiting factor of the lifetime of a trapped gas as $\tau \sim 1/P$, and we aim for a pressure in the range of 10^{-11} mBar, which will be adequate for our needs. The whole vacuum system is designed for this purpose. However, the excitation of ground state atoms to the metastable state, the details of which are discussed below in section 2.4, requires a pressure in the source chamber of the order of 10^{-5} mBar, due to the very low efficiency of the process.
To maintain a high enough vacuum in the science chamber, there will need to be a significant pressure gradient from one end of the experiment to the other. In figure 2.1 an overview of the entire apparatus is given, from the source in which the atoms are excited, to the science chamber where they are trapped and cooled.
In figure 2.2 we see the vacuum system of the source chamber and the Zeeman slower. The figure is not to scale, as the size of the Zeeman slowers has been reduced. In reality the larger Zeeman slower is around 2 m long and the shorter one is another 50 cm.
To pump the ground state helium needed for the metastable excitation we need a large pump of 2300 l/s, this pump is water cooled. Pumping helium or other light

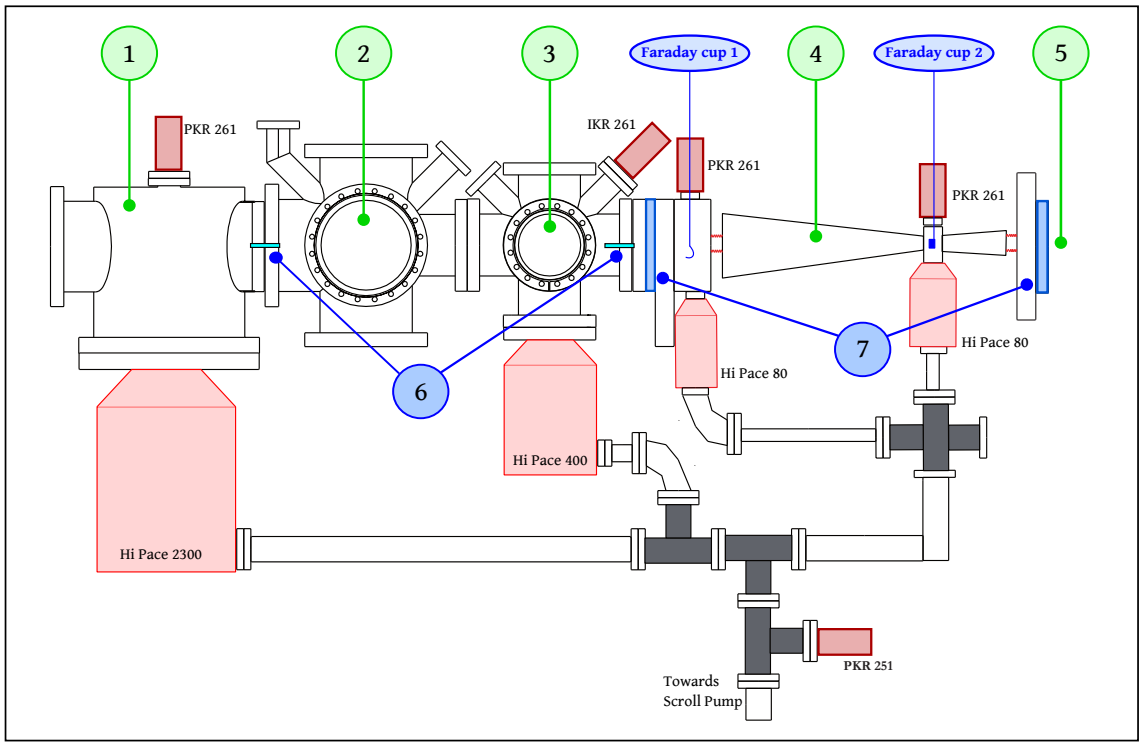

Figure 2.2: Schematic overview of the vacuum system. The atomic beam moves from left to right. Pumps and gauges are indicated in red and named. 1) Metastable Helium source 2) Optical molasses chamber 3) Observation chamber 4) Zeeman slower 5) Towards the science chamber. 6) Small (5 mm) differential tube separate chambers 7) At these places the system can be closed off by pneumatic valves. Two Faraday cups are shown, the first one has a non-insulated copper wire to collect atoms, the second one has a metal plate of 5×21 mm.

particles is notoriously difficult, the best option as for pumps are turbo (short from turbomolecular) pumps, which consists of a turbine-like rotor that rotates in a housing.

Between the source chamber with low vacuum there is a tube with a diameter of 5 mm and a length of 5 cm, separating this chamber from the next one, allowing a large difference in pressure between the two, since the conductance C of a pipe in the molecular flow regime goes as $C \propto d^3/l$ l/s, with d the diameter and l the length of the tube (Knudsen's Equation). This tube gives us low conductance between the source chamber and the next. In this next chamber there is optical access to transversely cool the atoms coming out of the source. There is a $CF100$ flange connecting it to another chamber, intended for observation purposes, in which there is another pump, to keep the vacuum in this part of the system high.
This turbo pump, which is also water cooled, has a pumping speed of 400 liters/hour. This chamber will be connected to the Zeeman slower, described in section 2.6. Between the slower and this chamber there is both a pneumatic valve capable of sealing off the connection, as well as another low conductance tube with diameter of 5 mm and length 5 cm to keep the pressure gradient in the system high. In the collimation and observation chambers the pressure is a factor ~ 15 lower than in the source chamber when the source is running, giving usual pressures of 1×10^{-6} mBar.

At the beginning and in the middle of the Zeeman slower there are two 80 liters/hour turbo pumps. These two smaller pumps have no water cooling, but fans. On the far end of the Zeeman slower there is another pneumatic valve.
Knudsen's Equation is also valid for the Zeeman slower, the larger one which has a diameter of 3 cm and a length of 2 m. The pressure at the beginning of the slower is in the order of 10^{-8} mBar and in the middle it is 10^{-9} mBar. The small slower has the same diameter, but is only 50 cm long.
All are made by Pfeiffer and are connected at the back to a primary scroll pump, specifications can be found in [60]. The pressure at the back of the pumps is around 10^{-2} mBar.

The pressure gradient that is thus created in the system will allow us, with the appropriate pumps in place to have the desired ultra high vacuum in the science chamber. It would not be possible to reach pressures in the order of 10^{-11} mBar there if the rest of the vacuum system was not designed to accommodate this.

The atomic beam starts at the left of figure 2.2 from a source in which ground state helium is excited into its metastable excited state and travels to the right. At several points in this journey we have the possibility to monitor the atomic beam. First there is the dedicated observation chamber, with glass windows which allows to observe the atomic fluorescence with a camera. There are also two Faraday cups that collect atoms and ions on their surface and convert these to electrons. The measured electrical current corresponds directly to the number of particles captured on the surface of the cup. The first Faraday cup is a copper wire with the insulation scraped off, the second Faraday cup is a metal plate with dimensions 5×21 mm,

with the long side parallel to the ground, and another small plate of 5×5 mm. These tools let us measure the qualities of the atomic beam at several points in its trajectory and will prove to be invaluable for the understanding of the workings of the experiment, and we will look at them in more detail later on in this chapter.

2.2.2 The Science Chamber

Overview

As mentioned before, the requirements for the vacuum in the science chamber are more stringent than in the rest of the system, as the presence of a background gas is the limiting factor for the lifetime of a trapped cloud of atoms. The lifetime due to collisions with the background is related to the pressure as $\tau \propto 1/P$ [61, 62].

The challenge of creating an as high as possible vacuum comes in two steps. There is the initial problem of pumping the chamber after it has been opened to air, to get all the water and air molucules that have collected on and in surfaces out. This process of outgassing can take months if one does not do anything to speed up the desorption from the surfaces. With heating (baking) the walls of the chamber we can get the time needed down to a few days. The other issue is to have a good enough continuous pumping to pump the helium atoms we put in the system while we are running the experiment.
We need to design a system that can deal with both aspects of ultra high vacuum generation.

In figure 2.3 a schematic overview of the vacuum system in which the experiments will be performed is shown. On the left side of the picture one can see the end of the Zeeman slower, with its light coming in from the right. Four of the six MOT beams are at a 45° degree angle with the floor. The other two are going in and out of the frame. There are two large windows that allow us a lot of optical access, not only for the MOT light, but also for the dipole trap and the optical lattice.

Pumps

To maintain ultra high vacuum there are two pumps besides the ones discussed in the previous chapter. First there is a 300 l/s turbo pump from Pfeiffer Vacuum [60]. Turbo pumps are not as efficient for light particles such as helium as they are for heavier ones such as water, but they are the most efficient pumps for helium available. For example, the 300 l/s pump only has a pumping speed of 255 l/s for helium-4, which is not a too large difference. The turbopump has a vacuum limit of 10^{-10} mBar, so for the pumping of the very low pressure background (permeating the walls of the chamber) we have a different pump, which is a new model from the Seas Group, the NEXTorr 500-5 which combines an ion pump with a non-evaporable getter (NEG) pump [99]. The ion pump pumps continuously with a pumping speed of 6 l/s.
The NEG section of the system consists of 114 cm^2 of porous sintered getter disks (St 172) that can sorb (absorb or adsorb plus retaining) gases very efficiently. To

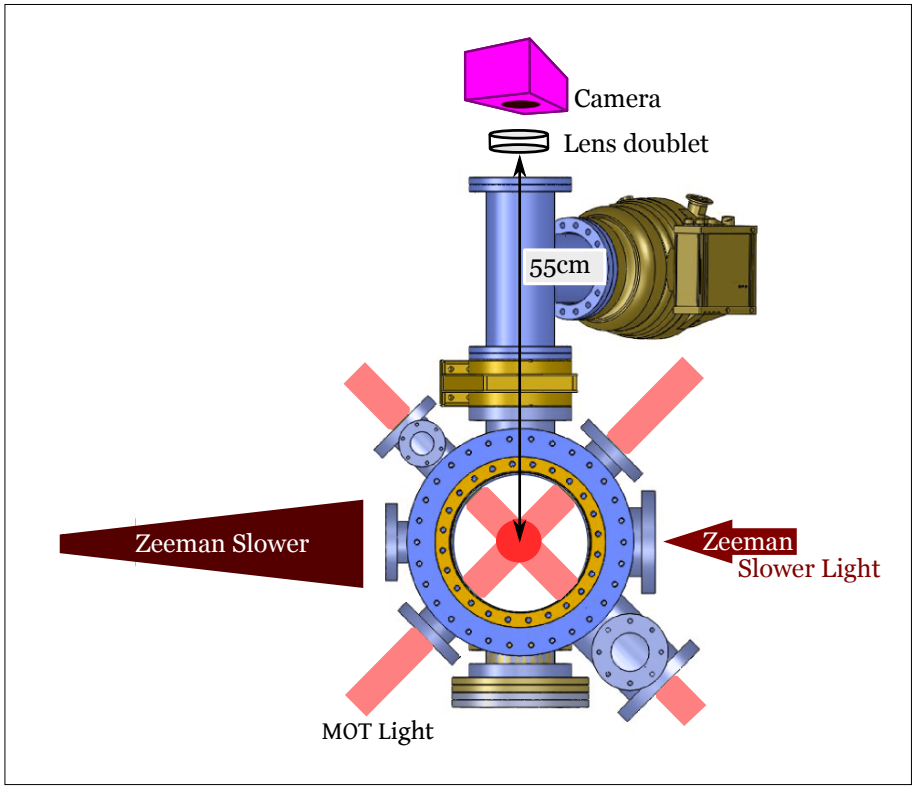

Figure 2.3: An overview of the science chamber. The slowed atoms come out of the Zeeman slower. The magneto-optical trap is centered in the vacuum chamber, where the six beams overlap. The two beams that are not shown are in and out of the plane of the graphic. Coils for the creation of the magnetic field gradient of the MOT will be placed around the windows. To monitor the MOT the camera is placed at the top, and to improve the imaging there is a doublet made of two lenses with $f_1 = 200$ mm and $f_2 = 130$ mm. The microchannel plates will in the future be placed at the bottom of the chamber, but are not in place at the moment. To pump the vacuum, there is a 300 l/s turbo pump and a combined ion and NEG pump, with a continuous speed of 6 l/s.

activate the NEG pump it has to be heated to 500°C, since exposure to air leaves a protective layer on the getter disks. When the module is heated to high enough temperatures, the layer evaporates and the getter material can start sorbing. After it is activated the NEG pump can reach speeds of 500 l/s, this speed depending on saturation as the particles that are pumped will also leave a layer on the getter material. To speed the pump up again, reheat it to evaporate this layer.

Baking

To go from a chamber open to air to ultra high vacuum, what usually is done is baking the system. Exposed to air, the walls of the vacuum chamber, usually stainless steel, will adsorb a variety of particles but mostly water. While pumping vacuum to

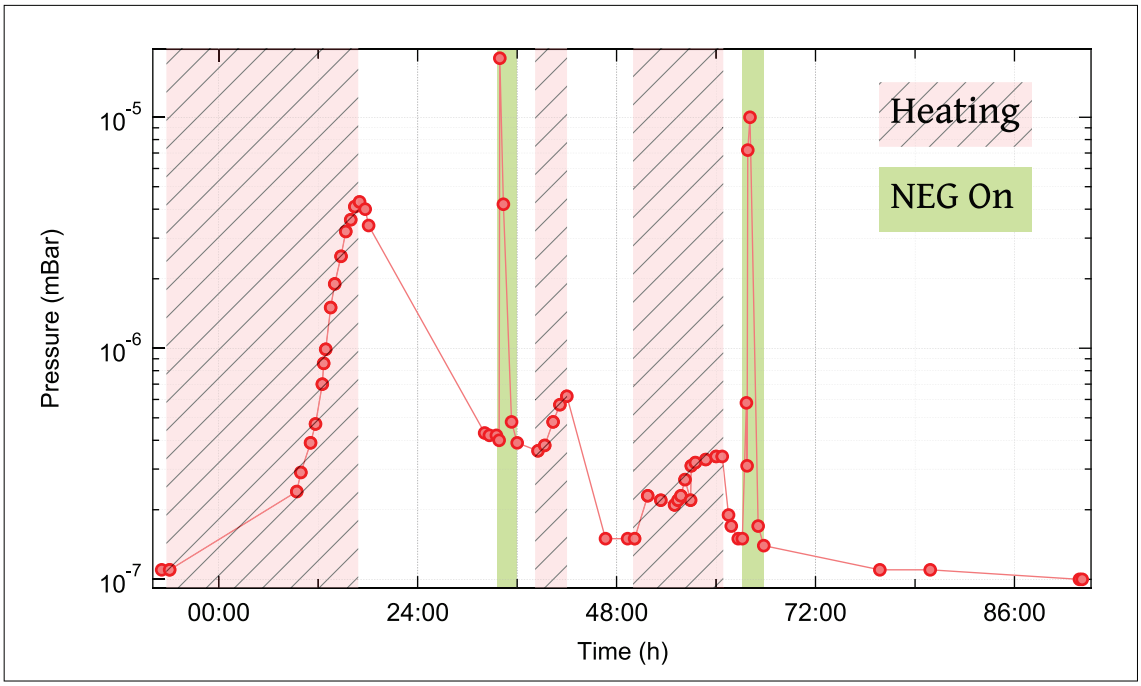

Figure 2.4: The pressure as a function of time during the heating of the baking process. Times when the temperature is increased gradually are shown in red. At the end the temperature of the chamber is 170° C. The activation of the NEG is shown in green.

low pressures, the amount of adsorbed material in the surfaces will be higher than the background of particles. The adsorbed gas will slowly come out of the surfaces, causing the vacuum to stay lower than it could be. This phenomena is known as outgassing. Without any solutions, this process can take up to several months to close to a year. Very light particles such as helium can also penetrate the stainless steel from the outside, and travel trough the walls into the vacuum. This process can be slowed by cooling the walls down, but can never be really stopped. The effect is very small though and it is possible to reach ultra high vacuum notwithstanding the penetration.
To speed up the desorbtion and outgassing process, we heat up the stainless steel. This will make the surfaces release the adsorbed gases more quickly.
In practice, the vacuum chamber is heated to $\sim 180°$ C. We will bake the science chamber, the small Zeeman slower and the small chamber with the Faraday cup, as the requirements on the vacuum of rest of the system are less, for example 10^{-9} mBar in the source chamber, is reachable within a few days of pumping without baking the walls. When the larger Zeeman slower is being used, it also heats up to 80° C, effectively speeding up outgassing every time it is in operation. As the non-baked pressures are satisfactory for us, we will no longer concern us with those parts of the vacuum. There is a valve between the part of the vacuum we bake and the part we do not.

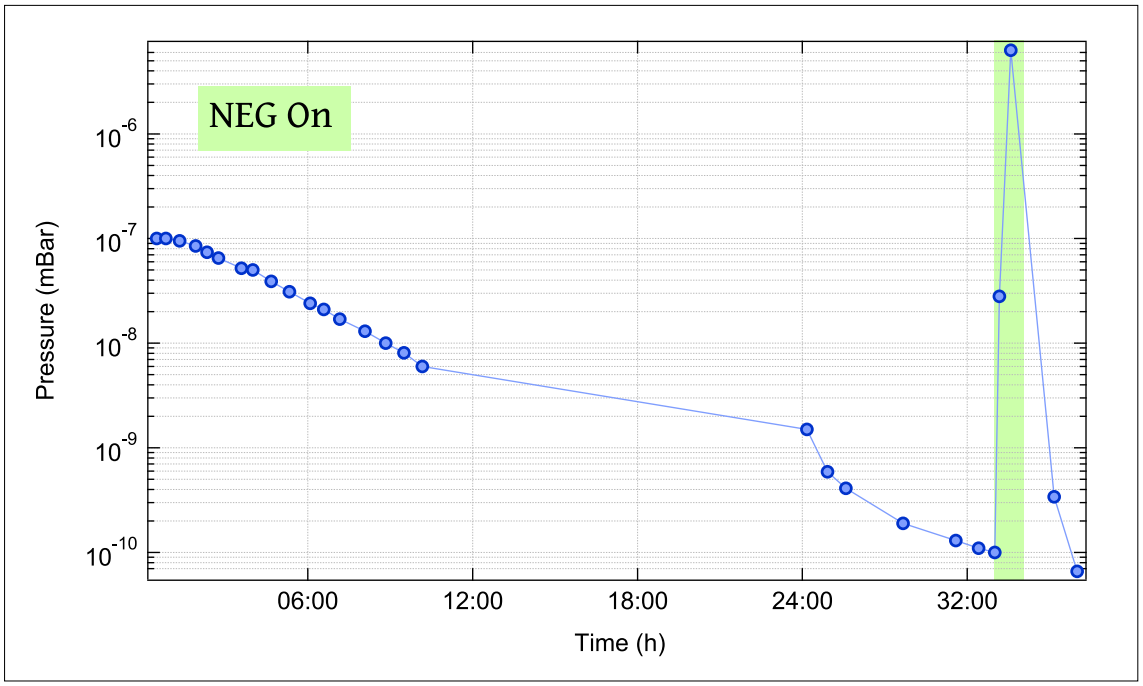

Figure 2.5: The pressure in the science chamber during the cooling down phase of the baking. At $t = 0$ the chamber is gradually cooled back to room temperature. The activation of the NEG is show in green. The final pressure in the science chamber at room temperature is 6.6×10^{-11} mBar.

After closing the vacuum chamber from air, we start pumping with the turbo pump and the ion pump. Without baking we can within a few hours get to a pressure of 1×10^{-7} mBar. We start baking as soon as the pressure has stabilized to this value. The temperature is increased slowly, as to not put a shock on the system. When the temperature goes up, more gases will be desorbed from the surfaces, causing the pressure to rise to about 5×10^{-6} mBar. However, when most of the outgassing is done, the pressure will decrease. At this point one can start to activate the NEG pump to speed up the baking. The NEG pump does not work for pressures higher than 10^{-6} mBar. Using the NEG pump will also make the pressure go up, since the layer on the getter strips is evaporated.
Now one needs to wait for the outgassing of the surfaces to be finished. This will cause the pressure to stabilize at around 5×10^{-8}mBar, not much lower than the previous pressure, however when we start to cool down the system the pressure goes down to 1×10^{-10} mBar.

During the process of baking and during the cooling down, it is possible that the NEG becomes saturated, there will be a layer on top of the sorbing material that will prevent the pump from working. To get rid of the layer, one can heat up the pump again to activation temperature (500° C). This will evaporate the layer and make the pump start sorbing again. There are no lasting negative effects of heating up the NEG pump again to activate it, so when one suspects the pump does not

work as well as it could, one can try to re-activate it.
We reactivate the NEG pump three times, the last time after the system has finished cooling down. With this last activation the pressure in the science chamber goes down to 6.6×10^{-11} mBar. In figure 2.4 the pressure as a function of time is shown for the heating and outgassing. The points at which the NEG pump is activated and re-activated are indicated. In figure 2.5 the pressure is shown as we cool down the vacuum chamber from 170° C back to room temperature.

For the running of the experiment the 500 l/s NEG pump and the 250 l/s turbo pump (speed for helium) will pump leftover helium quickly and efficiently. When the source is on, the pressure in the science chamber goes up to $\sim 10^{-10}$ mBar, which goes back down to 10^{-11} mBar within a second as soon as the atomic beam is shut off.

Conclusion

This concludes the section on obtaining the high vacuum needed for ultra cold atoms experiments. By using a turbo pump and a new NEXTorr ion and NEG pump, we have created a vacuum of 6.6×10^{-11} mBar in a vacuum chamber that is specifically designed for our needs. The chamber is baked at temperatures around 180° C and the NEG pump is activated several times during the baking process, to speed up the pumping and to increase the final vacuum.

2.3 The Laser System

In this section we will discuss the laser, the amplifier and optics. We will only discuss the main laser here that is tuned close to an atomic transition (2^3S_1 to 2^3P_2) of metastable Helium-4 at 1083 nm. This is a wavelength that lies in the infrared and is therefore not visible by eye.

The main laser used for the experiment is a NKT Photonics Adjustik Y10 single frequency fiber laser. We have a custom made system at a central wavelength of 1083 nm, which gives an output power of 100 mW with a FWHM linewidth of maximal 10 kHz and a fast piezo-electric tuning option [63].
The output of the Adjustik laser is coupled into a Ytterbium doped fiber amplifier from the Keopsys CYFA-BO series, it amplifies up to a power of 33 dBm, or 2 W [64]. The output of this amplifier is fibered again and sent to an optical table, whose layout is shown in figure 2.6. The light coming out of the fiber coupler is linearly polarized. To protect the amplifier and to prevent fluctuations due to back reflection an optical isolator (OI) from Toptica is installed. After the isolator, we take part of the beam to lock the laser. The locking scheme will be described in detail below in section 2.3.1. The light is locked at -350 MHz off the 2^3S_1 to 2^3P_2 resonance, so the light is red detuned. From the remaining beam we take a part to go to the Zeeman slower, whose light therefore will be also be -350 MHz red detuned. For the fibers taking the light for the Magneto Optical Trap (MOT) and the Optical Molasses, Acousto-Optical Modulators (AOMs) are used to tune the light back to resonance. The AOMs are from AA Optoelectronics, have a center wavelength of 200 MHz and a dynamic range of 60 MHz. The AOMs are detuned with the same

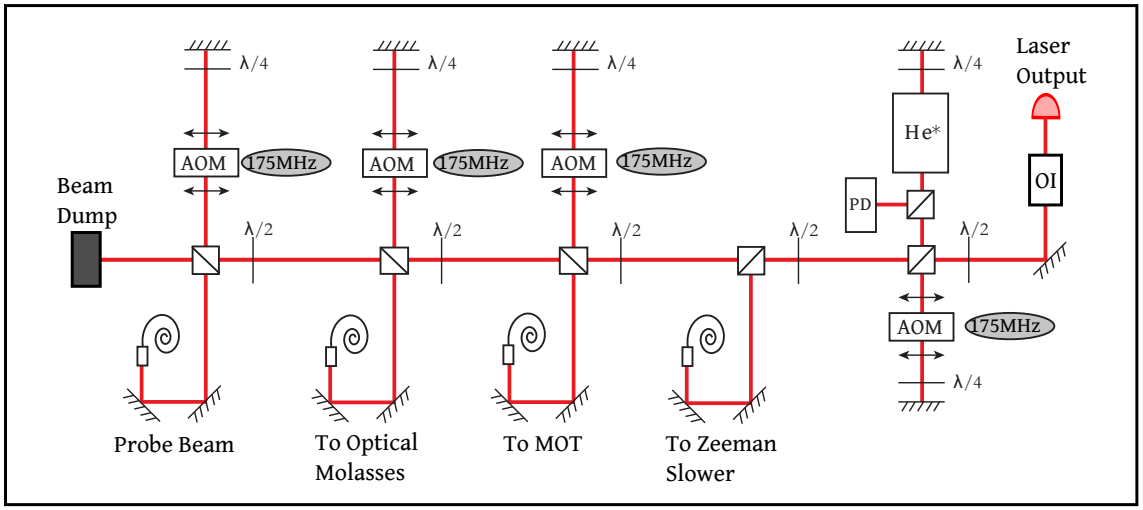

Figure 2.6: The manipulation of the laser light on the optical table. The laser light is locked -350 MHz off the 2^3S_1 to 2^3P_2 resonance. The light for the Zeeman MOT is therefore also -350 MHz detuned. The AOMs for the light of the MOT and optical molasses shift the light back on the transition. There is a multipurpose probe light fiber and the remaining light is dumped.

frequency as the AOM for the locking, giving us on-resonance light, with the ability to tune several tens of MHz.
Besides the light reserved for the MOT and optical molasses we have an extra fiber set up to use as a probe for various detection schemes.

Let us now look at the saturated absorption spectroscopy needed to lock the laser.

2.3.1 Saturated absorption spectroscopy

The following chapter is an overview of the work described in [65].

Introduction

To lock a laser system, one needs a reference frequency, in most cases the atomic transition frequency. Usually an absorption cell is used, through which with saturated absorption the signal is obtained.
In the case noble gases, things can get slightly more complicated, as one does not work with the ground state atom, but an excited, metastable state. We use the word 'meta'stable, because the lifetime of the exited state is for all intents and purposes infinite (> 1000 s, much longer than any experiment one could ever do with it). So although when working with the metastable atom, one does not have access to it without exciting it first.

Generally speaking there are two ways in which one can create metastable Helium-4 from ground state atoms. The first way, which we shall discuss more in section 2.4, is to create a plasma of positive He ions and electrons, by putting a DC high voltage over a gas of ground state atoms [66][67]. This way is not very suitable for a saturated absorption cell, because of the need for metal parts in the vacuum, which means that a sealed glass cell is not an option and one ends up with rather large vacuum chambers, for which an experimentalist might not have room in his/her lab. The good thing about the direct current technique is that there is little radiation leaking towards the rest of the experiment.

The other way to create metastable atoms is using an radio frequency (rf) discharge, and this method has somewhat the opposite characteristics [68][69][70]. Because the rf discharge can be created outside of a cell, it is possible to use smaller, sealed glass cells filled with low-pressure ($\sim$ 1 mBar) helium gas. This is ideal for a locking scheme, as it does not take up too much space. However, the rf signal can easily leak to the rest of the room, and there are many parts of the experiment that are sensitive to this kind of radiation. As the locking is a continuous process, it is not possible to turn off the rf signal.
In this section I will describe a new electrical scheme for the creation of metastable helium atoms, which is small enough so that it can be housed in a metal box that protects the rest of the experiment from the rf signal. The rf signal can be controlled by a potentiometer, since the power needed to create the initial discharge is higher than the power one needs to keep it going. So when turning on the cell, we increase the signal and as soon as the discharge is on, we can decrease it. Both

the electronics and the helium cell are enclosed by the metal box. After all, it is the rf signal generated around the cell that we want to prevent from leaking into the labroom. There are two small holes in the box to let the laser beam for the saturated absorption through.
Let us have a look at the electronics, newly designed and implemented by F. Moron:

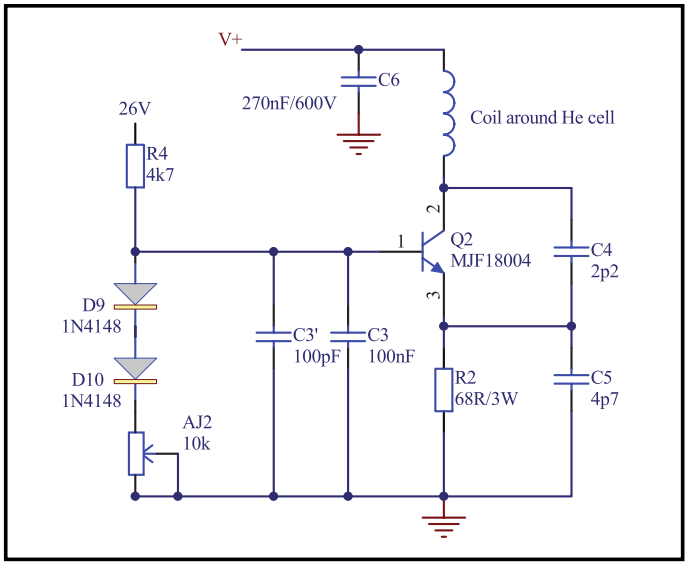

Figure 2.7: The electrical circuit of the Collpits generator that creates the radio frequency signal necessary to initiate and maintain the discharge for the saturated absorption cell.

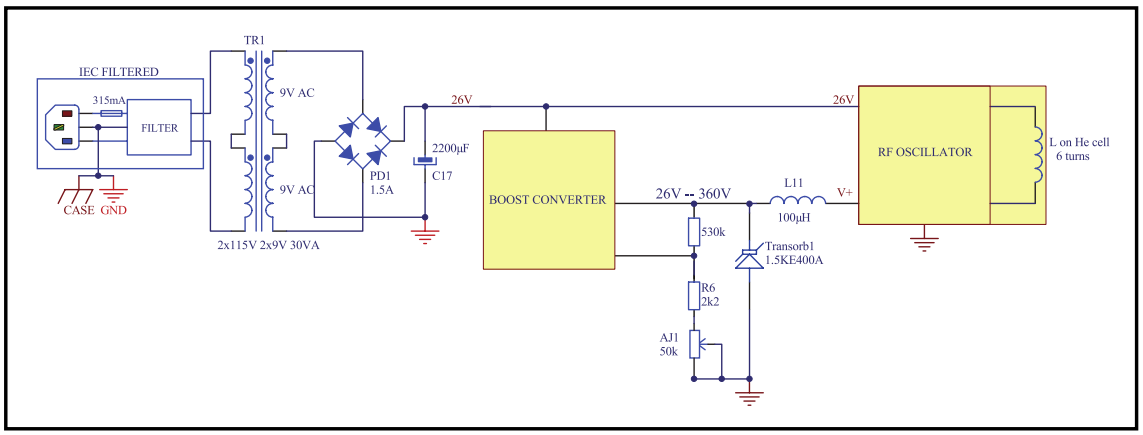

Figure 2.8: The total electrical scheme that is inside the box. The voltage $V+$ is controlled with the potentiometer, allowing us to manually adjust it.

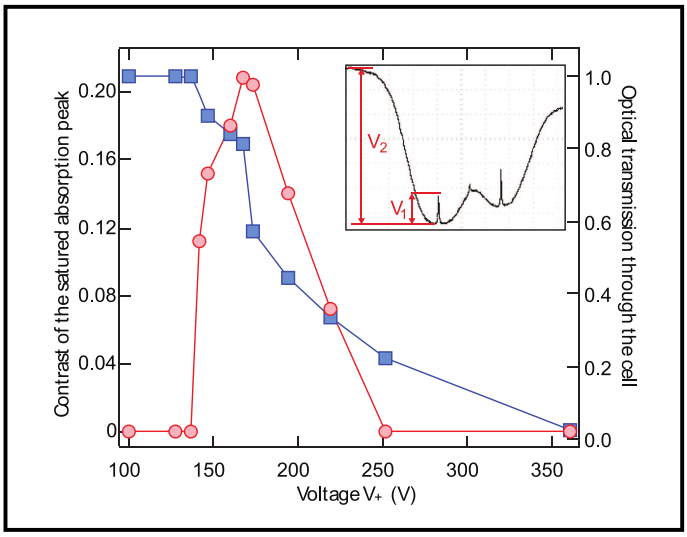

Figure 2.9: The contrast of the saturated absorption peak as a function of the adjustable voltage $V+$ (red circles, left scale) and the optical transmission through the cell (blue squares, right scale). At a voltage below 130 V there is no plasma at all. Inset: absorption spectrum of metastable helium. The contrast is defined as the ratio of V_1 and V_2 of the 2^3S_1 to 2^3P_2 transition. Also visible is the 2^3S_1 to 2^3P_1 line.

The Electronics

In figure 2.7 the electronics needed to create the rf signal are shown. The circuit is in a so-called Collpits configuration, which is a type of LC oscillator that produces an oscillation at a certain frequency that is determined by the inductance of the coil wrapped around the cell. This circuit generates a rf signal ranging from 12 to 21 MHz, with varying amplitude $V+$ of 160 to 360 V. In figure 2.8 all the electronics put inside the box are shown.

To use these electronics on a day to day basis is extremely easy, as one can adjust the amount of helium-4 that is excited to the metastable state in the cell by adjusting the voltage $V+$ with the potentiometer. To check whether everything works as expected we monitor the contrast of the saturated absorption peak, as shown in figure 2.9. The measurement is done with a diode laser and the spectrum shown in the inset is an usual frequency modulated (fm) spectroscopy, where the fast modulation is done by the AOM and the slower modulation by the diode control.

Attenuation

As mentioned before, a higher voltage is needed to start the discharge then to keep it on afterwards. We find that an even higher voltage is needed when the metal box around the electronics and the glass cell is closed. We believe this is because of negative coupling of the rf generator to the housing which decreases the rf signal. We check whether the rf signal gets attenuated by the protective box by measuring

the signal being picked up by a loop of copper wire with a diameter (the loop) similar to the diameter of the coils around the glass cell. At the point where there is a small hole in the box to let the laser light through, which is on the long axis of the cell and the coil, the attenuation of the rf field is 100, but on the side of the box where there is no hole it is 300. This last figure is more indicative for conditions in the lab, as the hole is small (5 mm) and is not pointing towards anything vital.

Conclusion

The electronic circuit is inexpensive and uncomplicated to construct, while staying small enough to be put in a metal enclosing. The attenuation provided by this enclosure is more than adequate for average laboratory use.

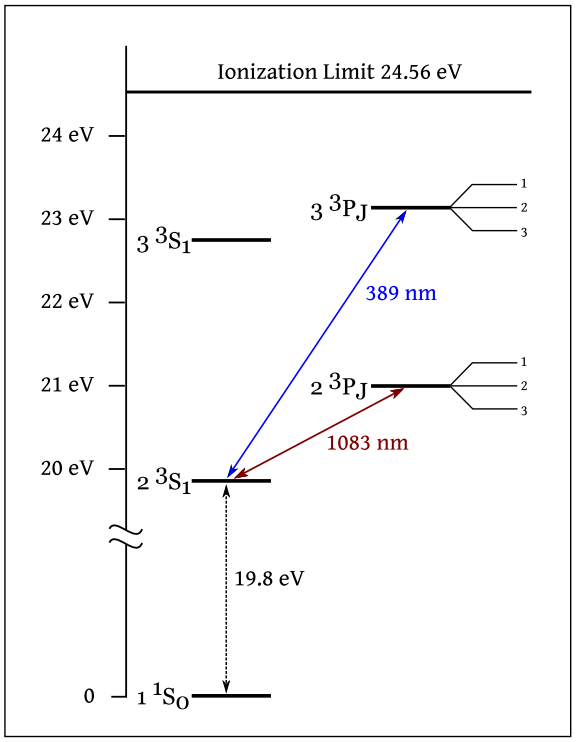

Figure 2.10: The energy structure of helium-4. The groundstate is not optically accessible, the metastable first excited state is the de facto groundstate for laser cooling experiments.

2.4 A Source for Metastable Helium-4

Let us look at the methods of excitation of helium-4 from its groundstate to its metastable excited state. The electronic structure of helium is shown in figure 2.10. The excitation into the metastable ground state is shown, as well as the subsequentely accessible optical transitions that can be used for cooling.

Two methods of creating metastable particles from ground state particles have been discussed in section 2.3.1. For the saturated absorption cell we used microwave radiation to excite the atoms. For the experiment we will create a plasma by setting a high voltage over a gas of helium-4.

For the excitation of metastable helium atoms, we inject ground state helium-4 into our source. The flux of ground state atoms is controlled by an EVN 116 gas dosing valve from Pfeiffer [78], values used in the experiment (see details below in section 2.4.2) range from 310 (0.8×10^{-4} mBar) to 350 (2.7×10^{-4} mBar) on the display.

To create the high voltage there is an anode, the needle, which is connected to a voltage of $\sim$ 3 kV and a cathode, which is the skimmer, as seen figure 2.11. Because of the high voltage, a current of positive ions and electrons is established between the needle and the skimmer (the red dotted line in figure 2.11). In this

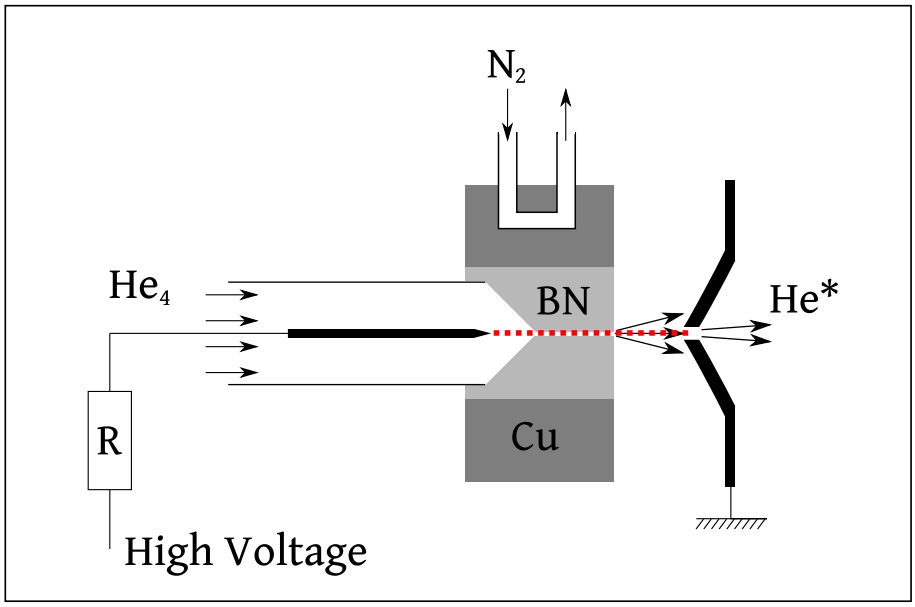

Figure 2.11: Schematic overview of the source where the helium is excited into the metastable state. There is high voltage between the needle (anode) and the skimmer (cathode). Between these two a plasma of helium-4 ions and electrons is created, which recombine into the metastable state with an efficiency of $\sim 10^{-4}$. The atoms go through a small hole in the Boron Nitride which is held in a copper mount, and is continuously cooled by liquid nitrogen.

plasma, sometimes a positive ion and an electron recombine in the metastable 2^3S state. The whole process has an efficiency of $\sim 10^{-4}$. In between the anode and the cathode the atoms are in contact with a cooled piece of boron nitride, which is imbedded in a copper block. The copper is continuously cooled by liquid nitrogen, fed through the vacuum chamber in pipes from a refillable tank which can hold up to 100 l of liquid. This tank is filled from a big 1000 l tank outside. A full small tank will last around a day in the lab.
Boron nitride (BN) is chosen because of its remarkable properties. It is an electrical insulator while being thermally very stable. This means it will not interfere with the plasma creation or the high voltages, but it will transfer the heat from the atoms to the liquid nitrogen.
The skimmer is put on a 3D translation stage, so we can direct the beam and change the distance between the skimmer and the needle. The mechanics of the translation stage have been designed and built by F. Nogrette.

In figure 2.12 we see a technical drawing of the metastable helium source. The needle and the skimmer are visible, as is the piping for the liquid nitrogen. The skimmer is mounted on bellows, to ensure that the only connection between the two chambers is the hole of the skimmer. This allows the pressure in the next vacuum chamber to be lower than the one in the source chamber, as discussed before in section 2.2.

The characteristics of the created beam of metastable helium will be described in the following.

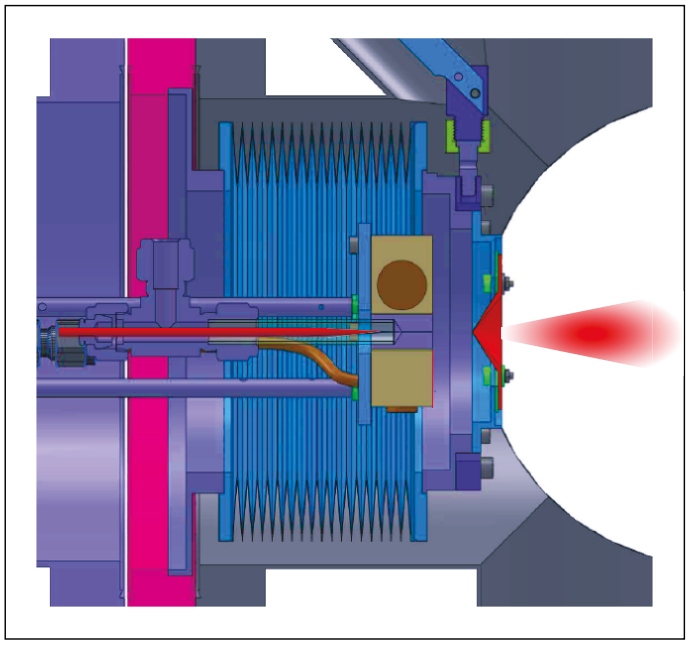

Figure 2.12: The source in the vacuum, where the atomic beam of metastable helium is created. The needle and the skimmer are highlighted in red, as is the beam of atoms shooting towards the right side of the picture. The copper pipe feeding the liquid nitrogen is visible in brown.

2.4.1 Velocity Dependent Spectroscopy

After the source the atoms are collimated by transverse molasses and afterwards decellarated in a Zeeman slower (and then captured in the MOT), which will be the subject of following sections and chapters. At first however, we investigate what the metastable helium beam looks like before it enters the slower.
For our purpose a few parameters are important, namely the velocity of the atoms along the direction of the beam (the longitudinal velocity v_L), the velocity of the atoms perpendicular to the direction of the beam (the transverse velocity $v_\perp$) and the flux, the atoms per second per steradian.

To explain why these parameters are crucial, one should realize that for the collimation of the atoms by the optical molasses there is a range of transverse velocities which can be addressed and if $v_\perp$ is too large, the atoms will not be interacting with the optical molasses and will not be collimated. Non-collimated atoms will not be able to pass through the small tube before the Zeeman slower and will be lost to us. Furthermore, a Zeeman slower is designed with a certain starting longitudinal velocity in mind and if v_L of the atoms is too large, the atoms will not be slowed down by the Zeeman slower.

We want to capture as many atoms in the MOT as quickly as possible, so the flux of the atoms is important. We are looking for the best setting for the source, for which we get the most atoms, but with their velocities still in the range so we

can collimate and slow them.

We have control over just a few adjustable parameters when working with the source. First of all, we can change the voltage which we put over the needle, thus influencing the plasma operating regime. Secondly we have access to the translation stage for the skimmer, so we can change the distance between the anode and cathode by several centimeters. Besides changing the conditions of the plasma, this can also influences the transverse velocities allowed to pass through the hole of the skimmer. Last, we control the amount of ground state helium that we put into the source by adjusting the dosage valve that connects our supply canister to the source.

Measuring the transverse and longitudinal velocity

We aim to measure the above mentioned quantities by looking at the fluorescence of the beam of metastable helium atoms right after they pass through the skimmer. In figure 2.13 the setup of the fluorescence measurement is shown. The probe light hits the atoms in two places, the mirror on the other side is at an angle of θ°, so the first beam is perpendicular to the atomic beam, and the reflected light is at this slight angle. With an InGaAs camera (see appendix B) we capture the fluorescence photons emitted by the metastable helium atoms. To make sure that we always send the same intensity of light onto the atoms, we monitor it at the output with a power meter.
The probe beam is detuned from the atomic transition by the use of the AOM before the fiber. By changing the frequency of the light we can control which velocite class of atoms we address, since they will have a Doppler shift due to their velocities. The first pass of the probe through the atomic beam is to the best of our abilities perpendicular to the longitudinal direction. This means that by changing the detuning of the probe we look at different classes of transverse velocities. For finding then the transverse velocity spread of the atomic beam, we make a series of measurements while changing the detuning, which gives use the transverse velocity profile. In our case 1 MHz corresponds to 1.083 m/s ($v = 2\pi \times \delta/k$).
To obtain the longitudinal velocity of the atom, we add an angle to the probe light. This angle means that there will be an element of the longitudinal velocity in the Doppler shift. Since $v_{long} \gg v_\perp$ the Doppler shift comes predominantly from v_{long}. So then:

$$v_{long} = 2\pi \times \delta \times \frac{k}{\sin\theta^\circ} \tag{2.1}$$

Measuring the flux

By summing the total number of photons collected (integrating over all the detunings of the probe light) we can get a clear picture of how many atoms there are in the beam. Let us discuss how to construct the number of atoms from the number of collected photons.

The number of photons emitted by one atom in the time that it is in the probe

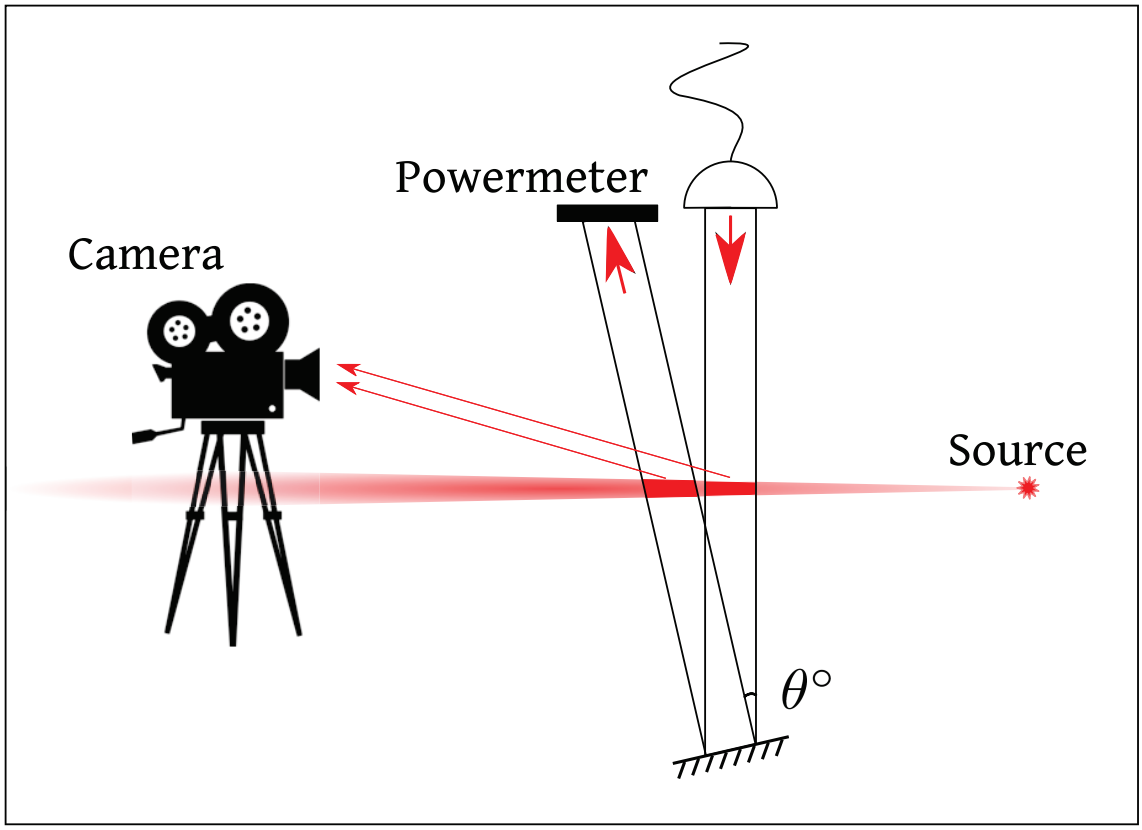

Figure 2.13: The schematics of the velocity dependent fluorescence measurement. The probe beam passes through the atomic beam twice, first perpendicular and then at a slight angle. By detuning the laser and using the Doppler effect, we can determine v_L and $v_\perp$.

light, with $R_{sc}(I, \delta)$ the rate of emission in Hz:

$$N_p = R_{sc}(I, \delta) \times \frac{L_{int}}{v_{long}} \tag{2.2}$$

The scattering rate of one atom is:

$$R_{sc}(I, \delta) = \frac{\Gamma}{2} \frac{I/I_{sat}}{1 + 4\left(\frac{\delta - kv}{\Gamma}\right)^2 + (I/I_{sat})} \tag{2.3}$$

Here Γ is the natural linewidth of the transition ($2\pi \times 1.6$ MHz for He*), I_{Sat} the saturation intensity (0.16 mW/cm^2 for He*) and δ the detuning of the light from the transition. This scattering rate is for a two-level system with the Clebsch-Gordon coefficients assumed to be equal to 1. When one deals with a multilevel system, the saturation intensity can be replaced with a de facto $I'_{Sat} = I_{Sat}/C$ with C a constant of the order of 0.7. We sum over the detunings and assume the light is on resonance ($\delta = kv$) for the velocity class it addresses, as well as that the spread in velocities is far larger that the linewidths, for the total flux of atoms per second this gives us [81, 71]:

$$\Phi^* = A \times \left(\frac{\pi}{2} \eta \frac{\Omega}{4\pi} h\nu \frac{\Gamma}{2} \frac{I/I_{sat}}{1 + I/I_{sat}} \frac{L_{int}}{v_x} \frac{\Gamma}{2\pi} \sqrt{1 + I/I_{sat}} \right)^{-1} \tag{2.4}$$

With A the camera signal in ADU, η the conversion to photons which depends on the gain model used, Ω the solid angle, L_{int} the interaction length with the probe beam and v_x the longitudinal velocity of the atomic beam.

With these tools we can now calculate transverse and longitudinal velocities as well as the total flux of atoms.

2.4.2 Characteristics

We set up the equipment as described in figure 2.13 right after the skimmer where the atomic beam exits the source. We monitor with the camera the fluorescence of the atoms as a function of the detuning of the laser. We use the camera to distinguish the fluorescence coming from the perpendicular beam and the fluorescence from the retro reflected beam at an angle, since they are spatially separated by the angle.
For the velocity measurements we look at the maximum fluorescence per measurement point, since this does not influence peak position. For the flux measurements we take the average fluorescence of all the atoms. In figure 2.14 an example result of such a measurement is shown. As we change the detuning of the probe laser, we are addressing atoms with different velocities because of the Doppler shift. The width of the transverse velocity distribution is extracted from a Lorentzian fit on the fluorescence from the probe beam perpendicular to the atomic beam. The longitudinal velocity comes from the difference of the peaks of the fits of the two distributions. The distributions has a Lorentzian shape due to the large velocities present (kv in formula 2.3 is large).

To get the total flux we sum the photons from all the different transverse velocity classes (the red curve), as this measurement automatically already includes the whole longitudinal velocity spread.

Source pressure

We investigate first how the pressure of ground state helium in the source influences the properties of the atomic beam. In figure 2.15 we see how the longitudinal and transverse velocities as well as the total flux changes when we increase the pressure. We vary the pressure from 8×10^{-5} mBar (EVN 315) to 26×10^{-5} mBar (EVN 360). At values below that the discharge in the source does not start.
We see that the longitudinal velocity gets larger when the pressure gets higher, as does the transverse velocity spread, due to the changed properties of the plasma. Also the flux of atoms increases with the pressure, since there are more ground state atoms to excite.

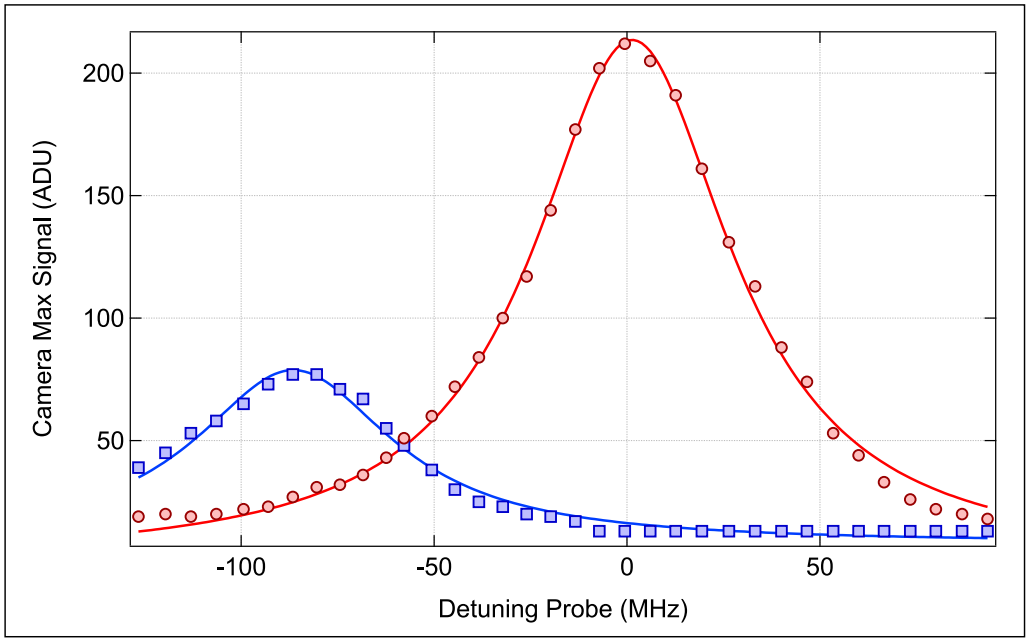

Figure 2.14: A measurement of the transverse and longitudinal velocities $v_\perp$ and v_L. As the detuning of the laser is changed, the light addresses a different velocity class due to the Doppler effect. The first beam is perpendicular to the atomic beam (red circles) and gives us a width 31(7) MHz which means $v_\perp = 34(8)$ m/s. The reflected beam (blue squares) has an angle $\theta = 4.6(2)^\circ$ with the atomic beam. The difference between the two peaks is 88(1) MHz which gives $v_L = 1185(14)$ m/s. Fits are Lorentzian. These curves are taken for $V_{source} = 3kV$ and $P_{source} = 1.67 \times 10^{-4}$ mBar.

Source voltage

The next variable we look at is the applied voltage between the anode and cathode to start and maintain the plasma. In the previous measurements on the source pressure we have kept the voltage at 2.7 kV. The voltage is varied, while keeping the pressure at $P_{source} = 1.67 \times 10^{-4}$ mBar. In figure 2.16 we see how the voltage influences the properties of the atomic beam.
We see that for a low voltage of 2 kV the longitudinal velocity is slightly lower, but the transverse velocity spread seems to be barely influenced. The flux is also lower for low voltage, but does not seem to be very sensitive for higher voltages. As long as the voltage is high enough to start the discharge, the properties of the plasma do not change by much when varying the voltage.

Distance anode and cathode

The final variable that is checked in our investigation of the source is the distance between the needle (anode) and the skimmer (cathode). The needle is fixed so we move the skimmer. In figure 2.17 we see the dependence to the skimmer position. The longitudinal velocity goes up the further the two are away from each other, while the transverse velocity goes down as expected (the hole in the skimmer cuts off larger transverse velocities). The flux is highest for short distances. We choose to work from now on at a distance of 14 mm, as it is a good compromise between the conflicting criteria. As for the pressure, we keep it at $P_{source} = 1.67 \times 10^{-4}$ mBar and we choose to work at a voltage of 2.4 kV for now. These parameters give a good compromise between a large flux of atoms with a not too large transverse velocity spread and a longitudinal velocity that is in line with the starting conditions of the Zeeman slower (see section 2.6).

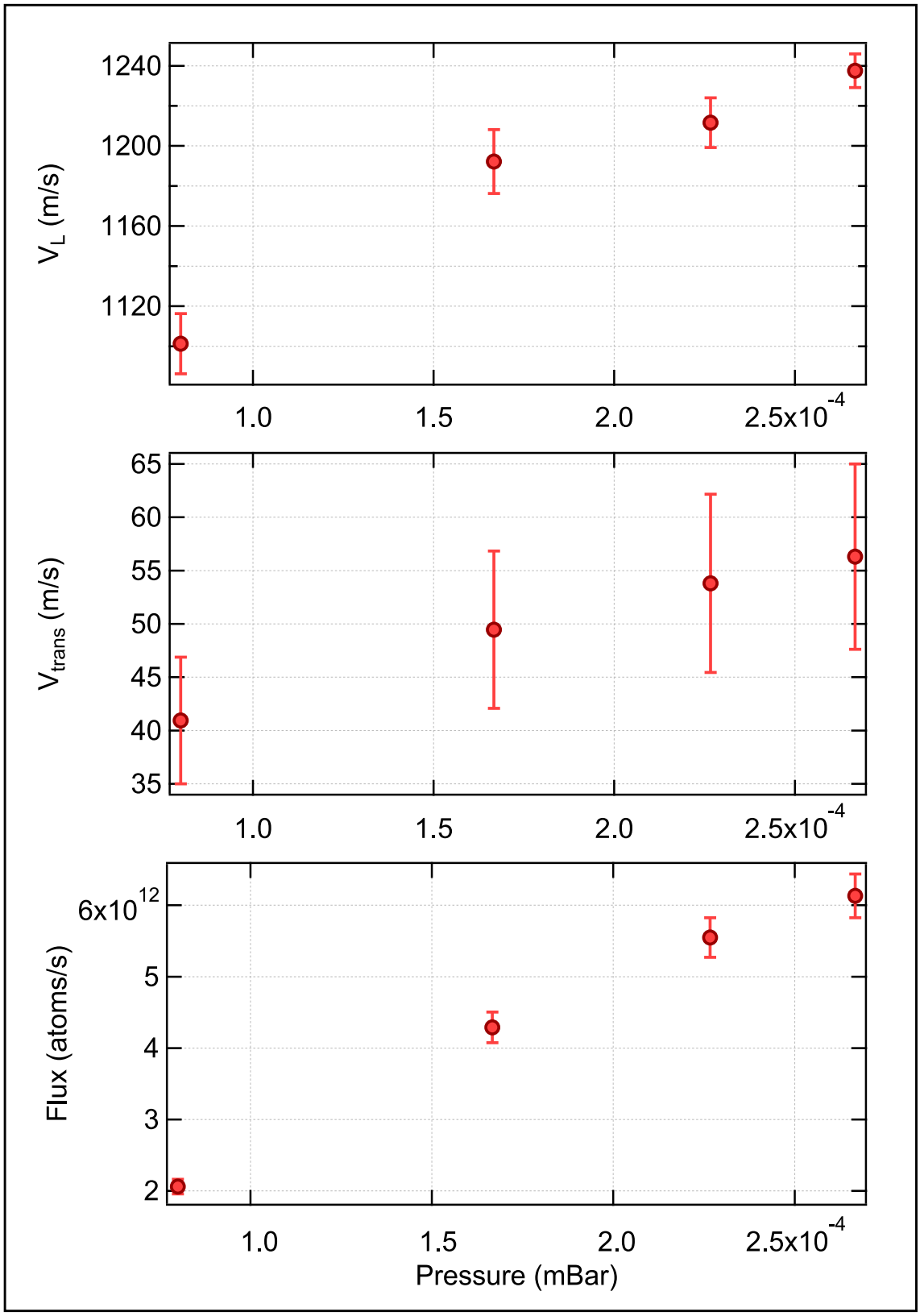

Figure 2.15: The longitudinal velocity (top), the transverse velocity spread (middle) and the total flux of atoms per second (bottom) as a function of the pressure of ground state helium in the source. The values for the EVN dosage valve are 315, 340, 350 and 360.

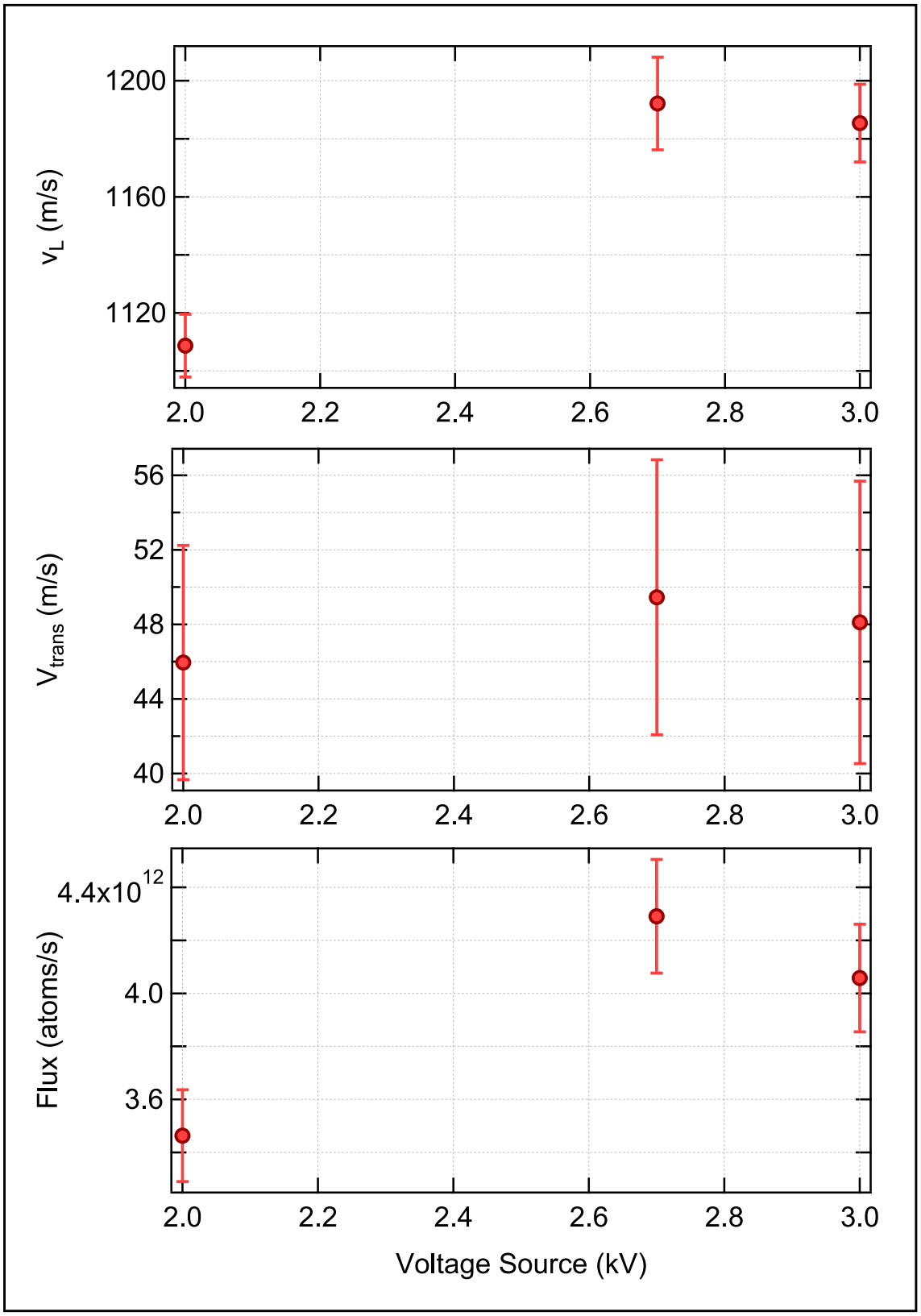

Figure 2.16: The longitudinal velocity (top), the transverse velocity spread (middle) and the total flux of atoms per second (bottom) as a function of the voltage over the anode and the cathode that creates the plasma. The pressure is $P_{source} = 1.67 \times 10^{-4}$ mBar.

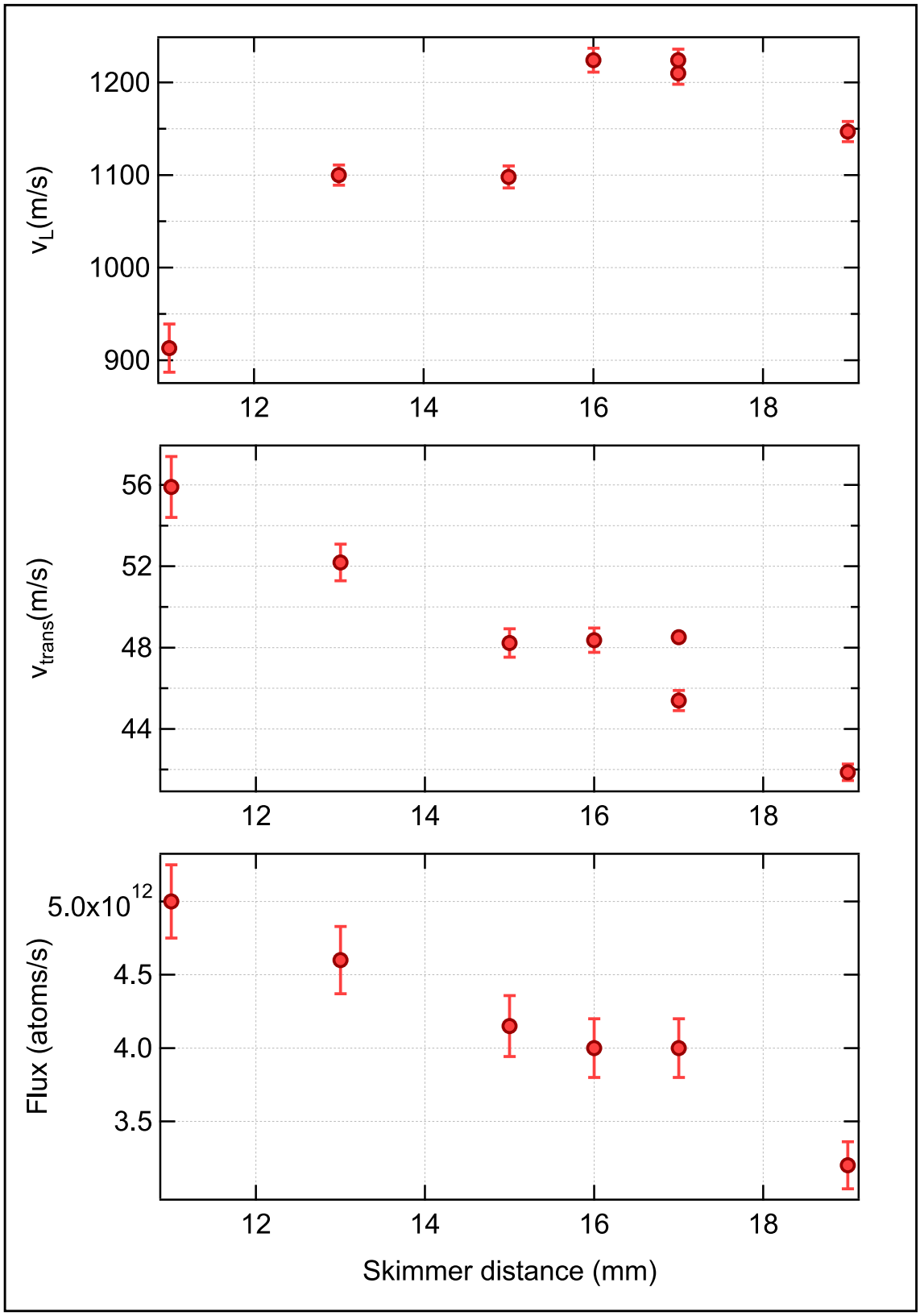

Figure 2.17: The longitudinal velocity (top), the transverse velocity spread (middle) and the total flux of atoms per second (bottom) as a function of the distance between the anode and the cathode that create the plasma. The anode is fixed, so it is the cathode that is moving. The voltage over the plasma is 2.7 kV and the pressure is $P_{source} = 1.67 \times 10^{-4}$ mBar.

2.5 Transverse Optical Collimation

2.5.1 Introduction

After the atoms exit the source, they have a given transverse velocity, as seen in the previous section 2.4.2. Since the distance to the science chamber is more than 2.5 m long, atoms with a large transverse velocity will not pass through the full length of the Zeeman slower and will not be captured in the MOT. In fact, if the beam is not transversely collimated, hardly any atoms will reach the capture site of the MOT (only $\sim 5\%$).
To start there is already the small tube (diameter 5 mm and length 5 cm) before the slower through which almost no atoms would pass if the beam is not collimated before. We therefore collimate the atomic beam by two-dimensional optical molasses right after the skimmer.

The principle of the optical collimation is based on the scattering force of photons. However, the capture range of the transition is equivalent to only 1.5 m/s, this is not large compared to the spread of ~ 50 m/s. To get a larger capture range, we do two things. First of all, we power broaden the transition, increasing the width with about a factor 3.5. Secondly, we use a curved wavefront, as seen in figure 2.18. The curved part of the beam will address the atoms with a certain Doppler shift because of the transverse velocity spread. The atom interacts with the molasses if:

$$\delta = kv_{\perp} \times \cos\beta \tag{2.5}$$

Since the angle β between the photon and the atom changes over the wavefront, we now address a much large range of transverse velocities.
From this it follows that if the detuning of the laser is small, the flattest part of the beam will interact with atoms moving perpendicular to it, and the curved part of the beam will interact with atoms with a larger transverse velocity [79, 80].

Since the scattering force cannot exceed the centrifugal force, the minimum curvature of the molasses is:

$$R_{min} = \frac{2Mv_L^2}{\hbar k\Gamma} \tag{2.6}$$

Which, for us with $v_L = 1200$ m/s, gives us a $R_{min} = 3.1$ m.

2.5.2 Implementation

To obtain a curved beam profile discussed above, we take the light coming trough the fiber from the optical table with the laser (described in section 2.3), which has passed through an AOM with the same frequency shift as the locking beam, so the light is near the atomic transition. The beam is first enlarged by a telescope and then there are two cylindrical lenses that elongate the beam along one axis, with $f_1 = 50$ mm and $f_2 = 400$ mm, see figure 2.19. The resulting beam is roughly 1×11 cm.

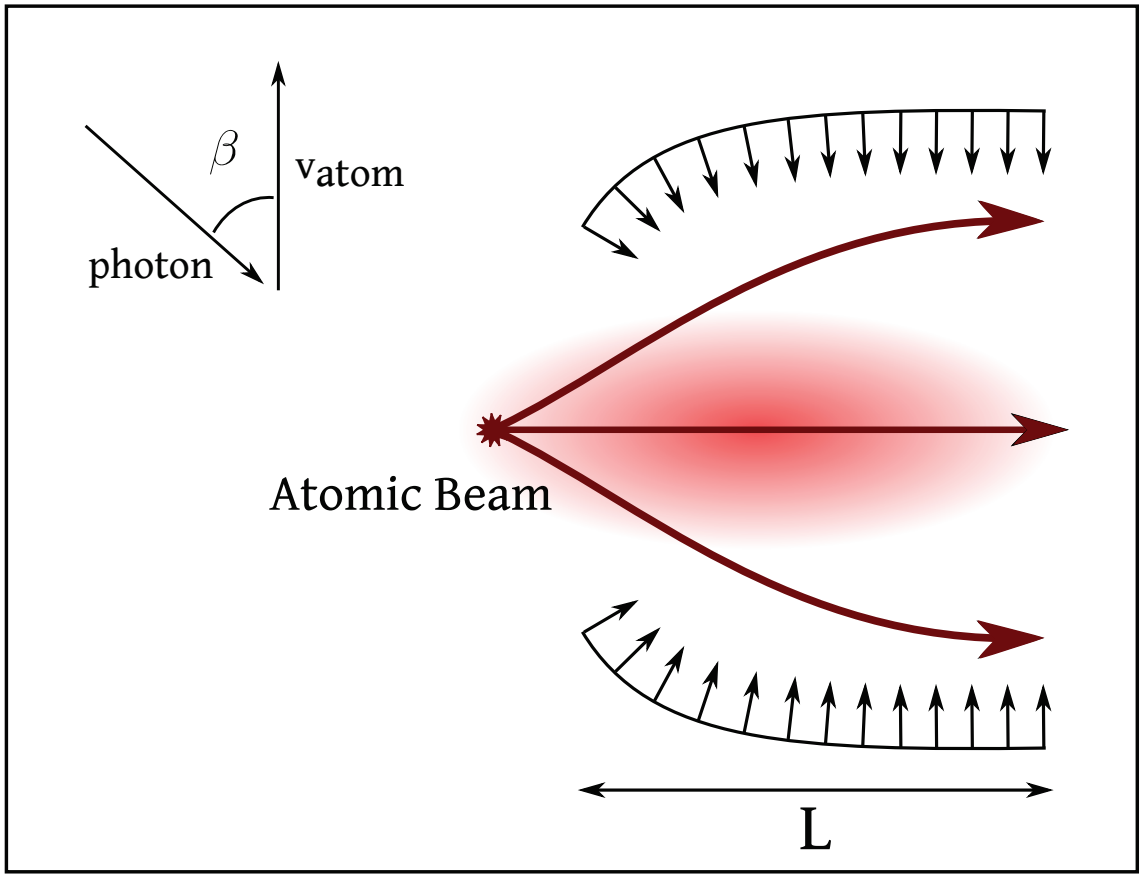

Figure 2.18: The principle of optical molasses: The curvature of the collimating beam counteracts the Doppler shift that occurs because of the transverse velocity spread, and ensures to collimate the maximum number of atoms. Here L is the interaction length of the optical molasses and β the angle between the vector of the photon and the transverse vector of the atom.

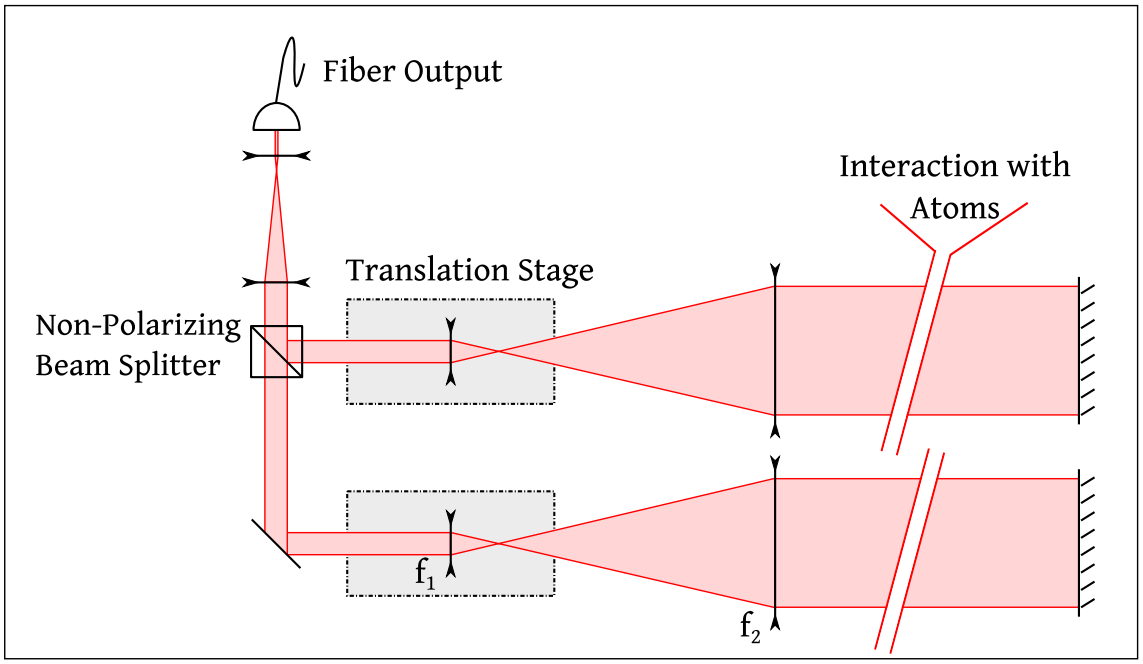

Figure 2.19: The optics that created the curved wavefront needed for the collimation by the optical molasses right after the atoms exit the source. On the other side of the atomic beam the light is reflected by a mirror as to get collimation from all four directions. The first lenses are placed on translation stages to change the curvature easily.

If the distance between the lenses is exactly equal to the sum of the focal points, the beam will be collimated ($R = \text{inf}$). If the lenses are closer together than the sum of the focal points, the beam is divergent ($R < 0$), and if they are further apart, the beam is convergent ($R > 0$), which is the situation we want.
From this picture we can calculate the (theoretical) curvature of the beam based on the distances of the lenses:

$$R_{calc} = \left(\frac{1}{f_2} + \frac{1}{f_2 + D_c} \right)^{-1} \tag{2.7}$$

Where D_c is the extra distance between the lenses $D_c = D - f_1 - f_2$.
In practice, the theoretical curvature is not always exactly the same as the real curvature as optics can be not perfectly aligned. To measure the curvature therefore we measure the distance between the focal points of the beam going towards the atoms and the beam coming back:

$$R_{meas} = 2 \times d + f_2 \times \left(\frac{f_2}{f_1 + f_2 + D_m - D} - 1 \right) \tag{2.8}$$

Where, d is the distance between the last lens and the retro-reflecting mirror and D_m the measured distance between the focal points.
The curvature is very dependent on the distance between the lenses, even a millimeter difference in distance results in a rather large difference in curvature. Unfortunately we cannot measure D very well (not better than 5 mm). For the measured

curvature, D is also important, so what we do is measure as well as we can D_m and d (the dependance on d is not very strong) and set the two equations to equal to find the most probable D and then the most probable R.

To align the beams:

1. Set a certain curvature (not too big, not too small, you have to start somewhere)

2. Make sure that the beams are not tilted horizontally

3. Make sure that the edge of the beam is hitting the atoms right as they exit the skimmer, one can make the edge of the light hit the skimmer

4. Make the flat part of the beam. Put a pinhole on the very side of the beam, on the side that is furthest away from the skimmer. Now make sure that this part is propagating straight through the entire path of the beam

5. Once we have created the flat part which is propagating straight, overlap the reflected beam on this part. This means that the reflected light will also be flat

6. For the last part you need to look with atoms. We look at the Faraday Cup in the middle of the Zeeman slower and optimize the signal there. This is done by blocking the reflected beam, adjusting the mirrors slightly, unblocking and adjusting slightly on the other side as well. Note that the alignment should be done with the other of the 2D molasses not blocked, since they influence each other and if you block the other direction, you will not find the optimum, but create an abberated atomic beam with two or more peaks.

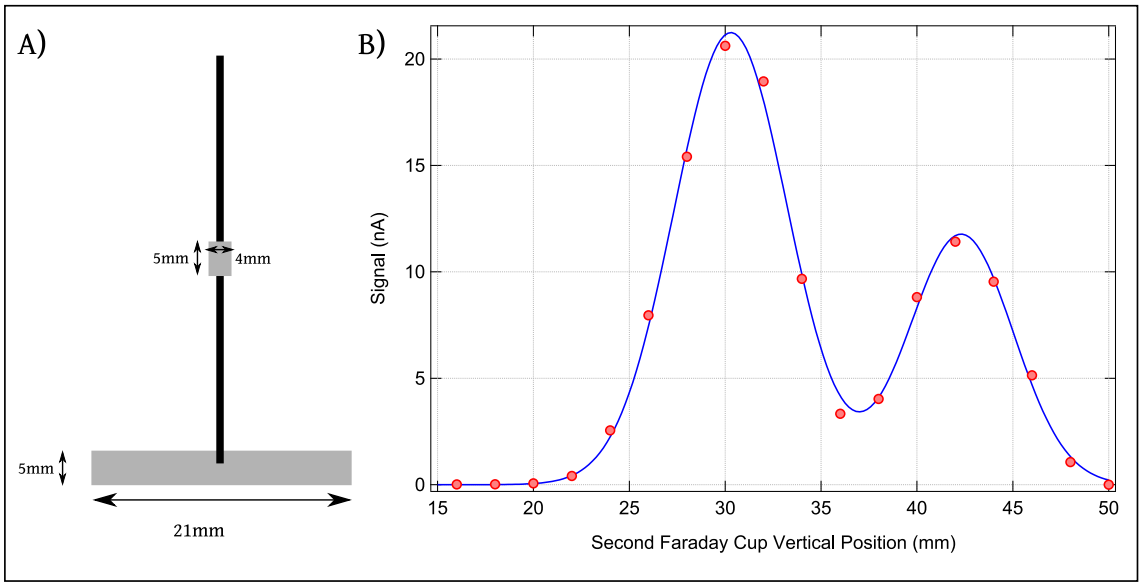

Figure 2.20: A) Schematic view of the second Faraday cup in between the two Zeeman slowers. The small plate is 5 mm by 4 mm, whereas the large plate at the bottom is 5 mm by 21 mm, the wire in between the plates is coated and non-conductive. B) Example measurement taken with the Faraday cup by moving the instrument in the vertical direction. The line is a double Gaussian fit. The lower maximum peak comes from particles collected by the small plate, and the total maximum peak from the particles collected by the larger plate.

2.5.3 Calibration

Besides the curvature of the beams, there are as well the intensity and the detuning of the light to consider. We have already mentioned that the detuning should not be far from resonance, as the flat part of the beam should be interacting with atoms that have small to very small transverse velocities.
To determine how good the collimation of the atomic beam is, we look at the total flux of the atoms in the small chamber behind the first Zeeman slower, and at the width of the beam, both with the Faraday cup that is located there. Since it is so far away from the source (more than 2 m), we measure in momentum space and the width measured corresponds to a velocity distribution. This is the reason we use this Faraday cup and not the one closer to the source.

Determining the flux of atoms with the Faraday cup

A Faraday cup works by collecting particles on a conducting surface. When a particle hits, an electron is extracted with a certain probability. When a continuous flux of particles hits, this results in a measurable current.
The Faraday cup between the two Zeeman slowers has two conducting okates, the largest part that collects atoms is 5 mm wide and 21 mm long, as seen in figure 2.20. There is also a small part, which is 4 mm by 5 mm. From changing the height

of the cup you get a distribution, which you can fit with a normalized Gaussian:

$$f(x) = \frac{A_m}{\sqrt{2\pi}\sigma_m} e^{-\frac{x^2}{2\sigma_m^2}} \tag{2.9}$$

With amplitude A_m and width σ_m, which gives us a width of the atomic beam, from the convolution of the width of the beam (gaussian) and the width of the Faraday cup (square):

$$\sigma = \sqrt{\sigma_m^2 - (a^2/12)} \tag{2.10}$$

And a flux:

$$\Phi = \frac{A_m}{a} \times \frac{1}{0.7 * e} \tag{2.11}$$

Where A_m is the fitted amplitude, a the vertical size of the cup (5 mm), 0.7 an efficiency factor for the extraction of electrons by the metastable helium and e the elementary charge.

With these tools we can start to make a characterization of the optical molasses. We will look at the flux of atoms on the Faraday cup as well as the width of the distribution in the vertical direction (as the Faraday cup moves vertically we do only have access to this width).

Fluorescence measurement

To measure the velocity spread we also use the velocity dependent fluorescence measurement technique described in section 2.4.1. An example of the influence of the optical molasses on the atomic beam can be seen in figure 2.21. We see the difference between the uncollimated and collimated atomic beams. When the optical molasses are on, they take atoms from a the velocity class that corresponds to $\delta = kv_\perp \times \cos\beta$ and collimate them. This picture is taken in the vacuum chamber just before the Zeeman slower, therefore the atomic beam has not passed through the small tube and we can see the non-collimated part of the beam.

Characterization

It is important to mention again here that the non-collimated beam, as seen in figure 2.21, will not at all pass through the 5 mm tube. Having optical molasses is therefore not a luxury but a necessity, as without it we will not be able to let the atoms pass through the tube to the Zeeman slower.

At this point we are interested in two main parameters, the flux and the size of the beam far away from the source. We perform all the measurements with the Faraday cup at 2 m. In figure 2.22 the influence of the curvature of the molasses on the atomic beam is shown. We know from reference [80] that the width of the beam depends on the curvature R as:

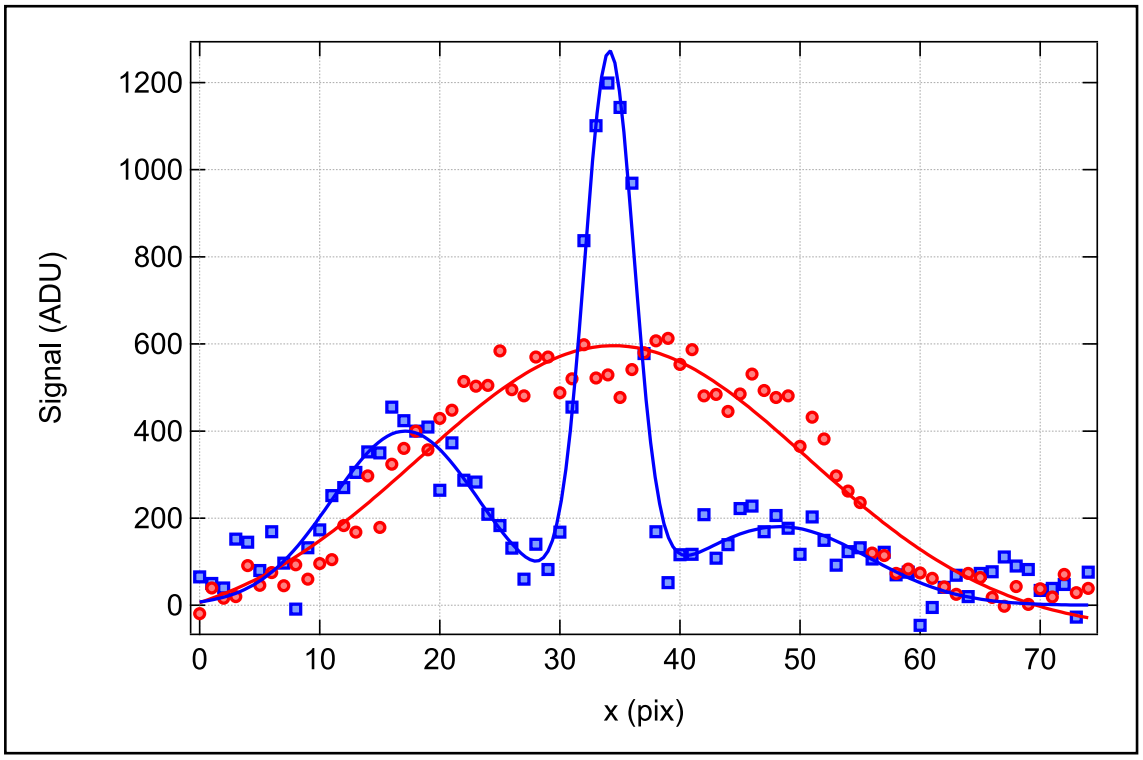

Figure 2.21: The effect of the optical molasses, taken with the camera in the chamber before the Zeeman slower. The uncollimated (red circles) atomic beam has a broad transverse profile, whereas the collimated (blue squares) beam has a smaller width.

$$\sigma = \sigma_i + \frac{L^2}{R} \tag{2.12}$$

Where σ_i is the transverse width of the atomic beam at the beginning of the collimation by the optical molasses; the initial size of the atomic beam and L is the interaction length of the molasses with the atomic beam. The fitted values as shown in figure 2.22 of $L = 7.2$ cm and $\sigma_i = 2.1$ mm are within the expected range, however the above formula is for a 1D molasses and as we know the two directions influence each other, so it is possible that there is a difference for the 2D case. Since this measurement is taken at 2 m from the source, a width of 1 mm at this point means a velocity spread of 0.6 m/s, since the atoms have a longitudinal speed of 1200 m/s. We have to keep in mind that optimizing the optical molasses by looking at the Faraday cup will focus the atomic beam on the position of the cup. Therefore the best alignment of the molasses for the Faraday cup is not the same as the best alignment for MOT loading. The transverse velocity spread measured here is thus underestimating the velocity spread one gets when one optimizes the optical molasses for the MOT.

The flux of atoms saturates with the curvature of the molasses. Only for small curvature (in this case $R \sim 2 \times R_{min}$) the flux is significantly lower, but at larger curvatures the influence of the curvature seems less important. This is consistent

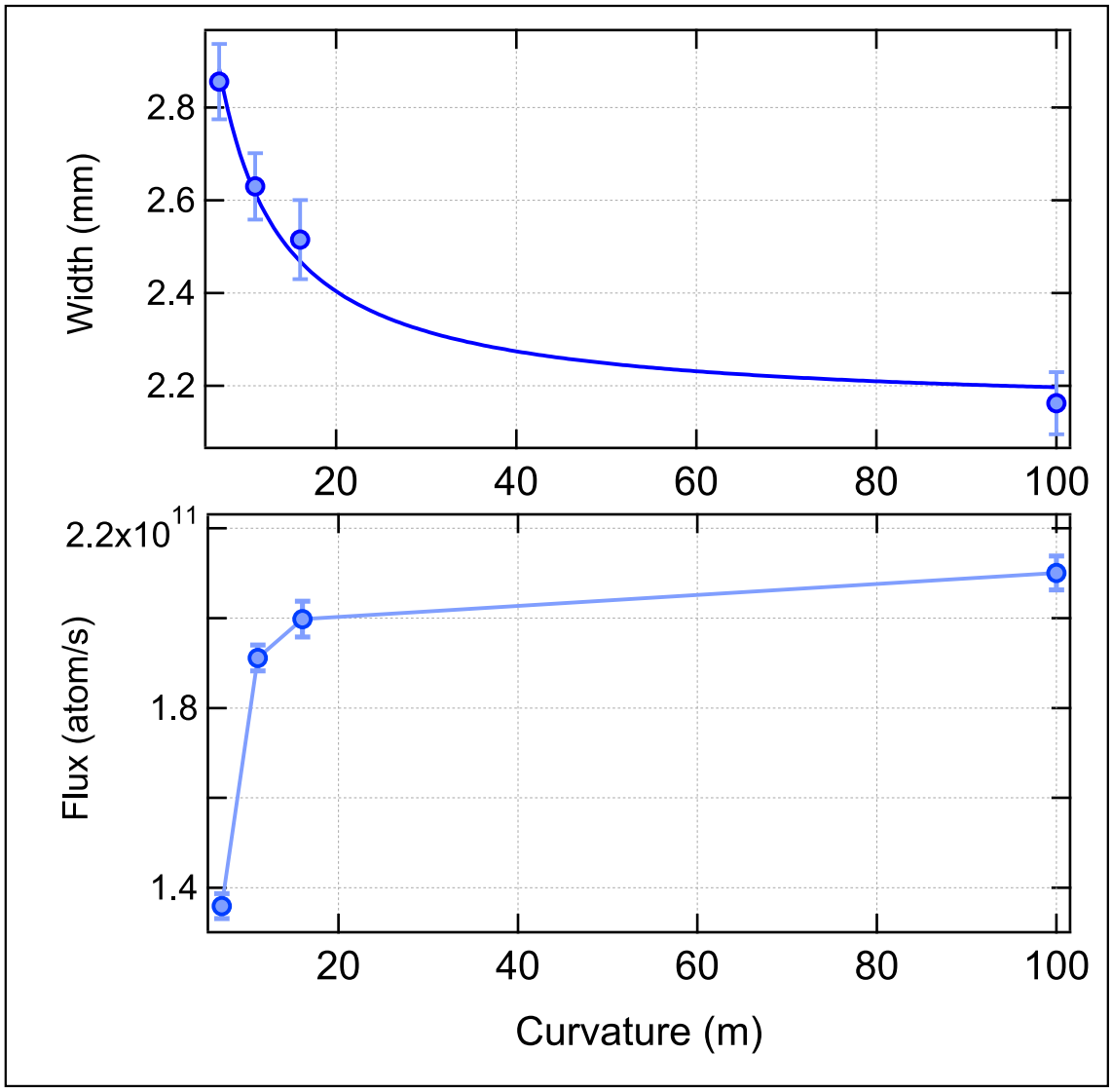

Figure 2.22: The width of the atomic beam (top) and the flux of atoms (bottom) as a function of the curvature of the molasses for an intensity of 150 mW in total (so 75 mW per beam) and a detuning of $\delta = 0$ MHz. The fit gives us an interaction length of $L = 7.2$ cm and an initial size of $\sigma_i = 2.1$ mm.

with findings in the thesis of G. Labeyrie [81].

In figure 2.23 we see how the optical power in the molasses beams influences the collimation of the atomic beam for two curvatures, $R = 16$ m and $R = 100$ m. For the larger curvature the width decreases slightly with higher power, whereas for $R = 16$ m the power does not seem to influence the width so much. The smaller final width of the larger curvature is in accordance with equation 2.12.
The flux increases with higher power, because of the power broadening of the tran-

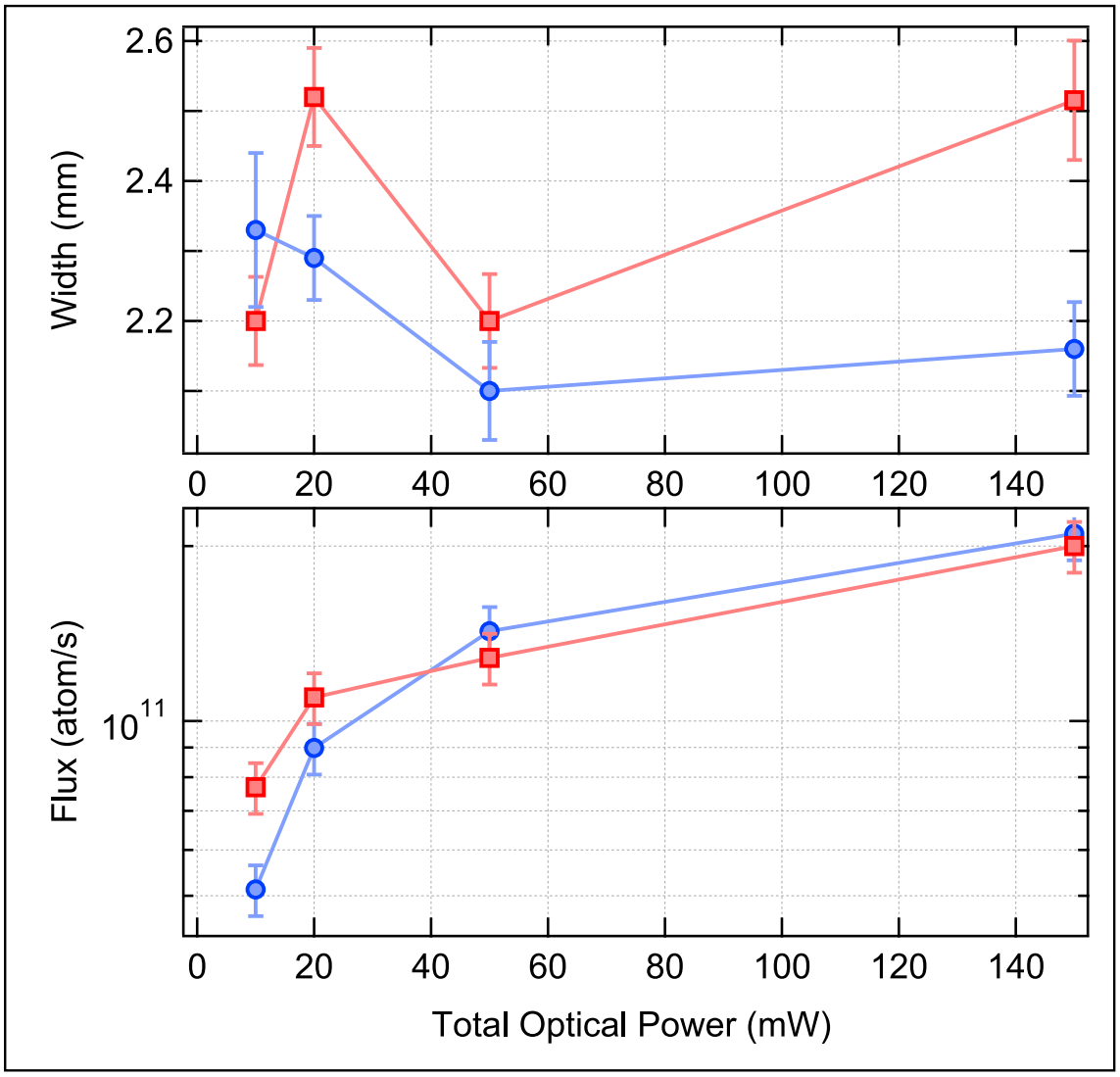

Figure 2.23: The width of the atomic beam (top) and the flux of atoms (bottom) as a function of the total power in the optical molasses. Red squares: $R = 16$ m, blue circles: $R = 100$ m.

sition, which allows us to capture larger velocity classes at a fixed angle β:

$$\Gamma' = \Gamma\sqrt{1 + \frac{I}{I_{sat}}} \tag{2.13}$$

We can conclude from this that at low powers it is beneficial to have a certain curvature to the optical molasses beams, as it increases the flux by a little less than a factor 2, but at higher power the power broadening clouds this advantage and it is favorable to have a larger curvature as it delivers a larger total flux with a smaller width. We have no shortage of optical power and therefore opt to work at high power and large curvature.

We have also compared different detunings for the optical molasses light. In table 2.1 we see some numbers for the performance of the optical molasses for $R = 10$ m,

Power (mW)	Detuning (MHz)	Flux (atom/s)	Width (mm)
30	0	2.4×10^{11}	3.1
	-2	1.9×10^{11}	3.0
50	0	3.0×10^{11}	3.3
	-2	2.4×10^{11}	3.3

Table 2.1: Difference in flux and width of the collimated atomic beam as a result of the detuning of the molasses light. Numbers are given for 0 MHz and -2 MHz, for two different powers and a small curvature of $R = 10$ m.

a relatively small curvature. Given are numbers for 0 and -2 MHz. The small detuning of the light does not have a big influence on the flux, although it is slightly higher for no detuning than for -2 MHz detuning. The width of the atomic beam barely changes with the detuning. A detuning of several Γ' would have a greater effect.

Conclusion

As we have seen, the optical molasses right after the source work efficiently to collimate the beam after it exits the source. We have determined the best parameters to get the highest number of atoms in a beam with a width as small as possible. Since we have enough optical power available, we decide to make use of the power broadening effects of the optical molasses beams, and work at a large curvature with high power.
We will work from now on with the molasses with a total optical power of 100 mW, with a very large curvature ($R >> R_{min}$) and no detuning.

2.6 The Zeeman Slower

After the atoms come out of the source and are collimated transversely by the optical molasses described in the previous section, we slow them down longitudinally by the use of a Zeeman slower, an apparatus first described by W. D. Phillips and H. Metcalf in 1982 [82], for which (among other contributions) W. D. Phillips was awarded the Nobel Prize in Physics in 1997 [83].
When wanting to slow down neutral atoms that have large velocities with light, one runs into the problem that the Doppler shift of the atoms soon shifts the transition out of resonance of the photons that are used to slow them down. This holds especially true for helium with its low mass and small natural linewidth.
A Zeeman slower uses the Zeeman shift by a magnetic field to compensate for the Doppler shift of the atoms. There are many other ways to try and compensate for this shift [84][85][86], but among these it has been the use of the Zeeman shift that has stood the test of time and is now most widely used.

I will describe the basic design considerations that went behind the construction of our Zeeman slower and I will discuss the construction and the tests done on the slower.

2.6.1 Design

The Zeeman slower uses the Zeeman shift to keep a decelerating atom in resonance with a slowing light beam. As the atom slows, the Doppler shift of the light with respect to the moving atom becomes less, and the Zeeman shift has to be adjusted. The length z of the slower from basic kinematics is:

$$z = \frac{\delta v^2}{2a} \tag{2.14}$$

With $\delta v = v_{start} - v_{end}$ the change in velocity from start to finish, and a the acceleration due to interaction with the photons.
The minimal length of the slower assumes the atom absorbs photons in the maximum rate Γ. Every photon transfers a momentum of $\hbar k$ to the atom. The scattering force is:

$$F_{sc} = \frac{\hbar k \Gamma}{2} \tag{2.15}$$

Therefore the acceleration due to the scattering force:

$$a = \frac{F}{m} = \frac{\hbar k \Gamma}{2m} \tag{2.16}$$

Combine the above to get the minimum length z_0 for a Zeeman slower, with an experimental efficiency parameter η:

$$z_0 = \frac{1}{\eta} \frac{m\ \delta v^2}{\hbar k \Gamma} \tag{2.17}$$

From this length z_0 we can now calculate the optimal field. An important thing to remember is that one wants the magnetic field at the end of the slower to be unequal to zero, for if it was, atoms exiting the slower will be in resonance with the light at zero magnetic field, so the light of the slower would be resonant to atoms in the trap. We also do not want the field at the end to be too large, since at the place of the trap, the magnetic field of the slower should be negligible.
This means that we can choose a magnetic field for the end of the slower and a detuning for the light. The total magnetic field will be the changing field plus this final field:

$$B_Z = B_{final} + B_t\sqrt{1 - z/z_0} \tag{2.18}$$

$$B_{final} = \frac{\hbar}{\mu_B} \times (\delta_L + kv_{final}) \tag{2.19}$$

$$B_t = \frac{\hbar}{\mu_B}(k\delta v) \tag{2.20}$$

With the field at the beginning of the slower:

$$B_{start} = \frac{\hbar}{\mu} \times (\delta_L + kv_{start}) \tag{2.21}$$

This means that when designing a Zeeman slower, one has two parameters that are important, the velocity of the atoms entering the slower v_{start} and the desired velocity of the atoms at the end of the slower v_{final}.
The last point to keep in mind is that due to the bias field B_{final} there will be a zero-crossing in the middle of the slower which will take up space, longitudinally, since we will construct the two slowers separately and there is the pump and the Faraday cup in between them. This length will give the atoms more space to expand transversely (the transverse velocity is never zero). The slower the atoms are moving during this zero-crossing, the more they are able to expand.
We thus have to balance our need to keep the magnetic field not too high and not too low and the end of the slower, and our need to keep the zero crossing at not too low longitudinal velocities of the atoms.
We put the detuning of the light at first at 400 MHz, which gives us the following parameters:

$$\delta_{zeeman} = 400MHz \tag{2.22}$$

$$B_{start} = 505G \tag{2.23}$$

$$B_{final} = -240G \tag{2.24}$$

$$v_{start} = 1200m/s \tag{2.25}$$

$$v_{final} = 60m/s \tag{2.26}$$

$$L = 2.43m \tag{2.27}$$

$$t = 4.2ms \tag{2.28}$$

$$v_{Zero} = 433m/s \tag{2.29}$$

The calculated form of the magnetic field of the Zeeman slower can be seen in figure 2.24. We can shift the bias field and the detuning of the Zeeman light together, this will not affect the performance of the slower.

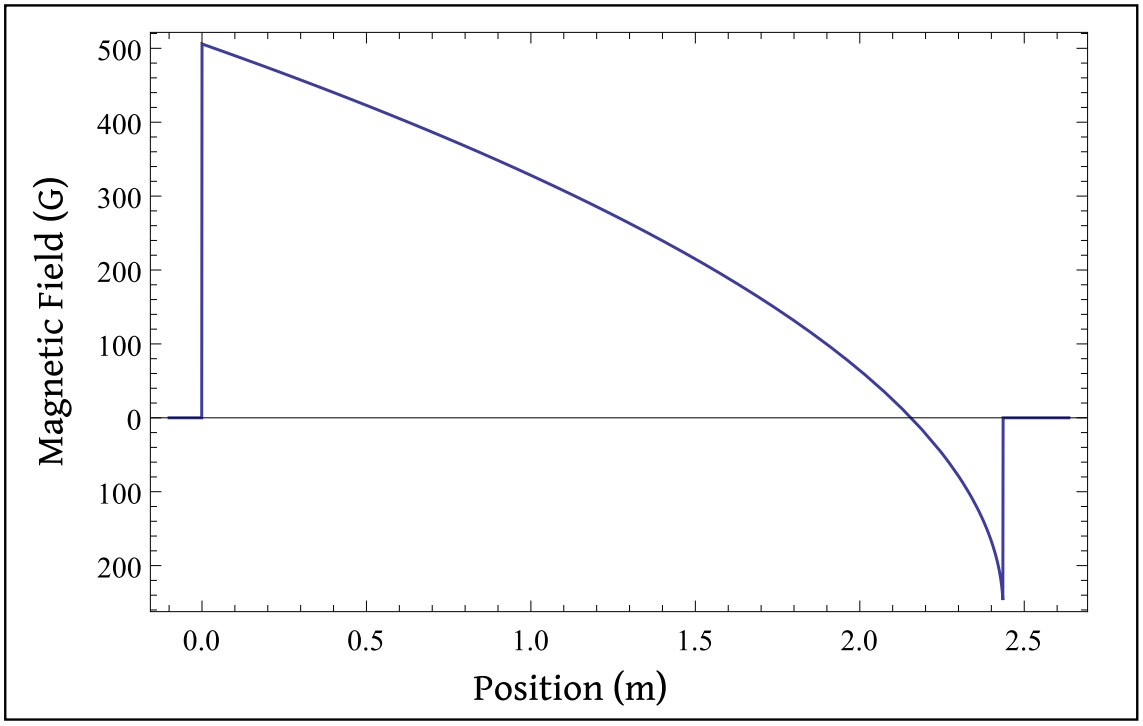

Figure 2.24: The shape of the magnetic field when applying the calculated parameters the shape of the magnetic field of the Zeeman slower, for a detuning of the Zeeman light of 400 MHz.

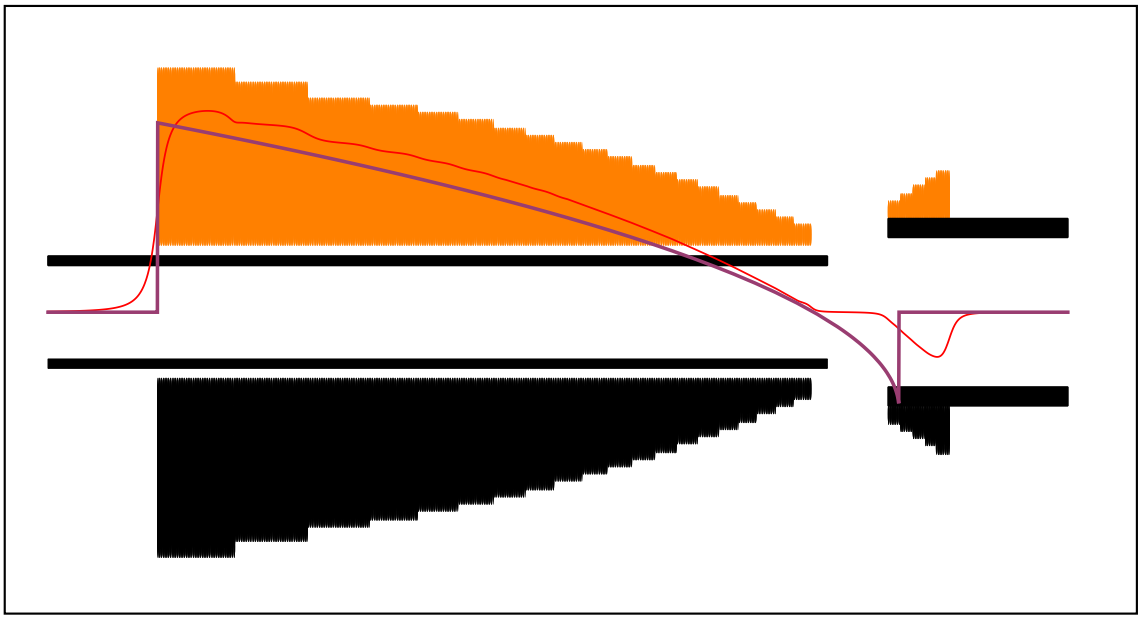

Figure 2.25: The design for the coils of the Zeeman slower and the resulting magnetic field, compared to the previously designed optimal magnetic field. There are 20 coils in the big slower and 5 coils in the small slower.

2.6.2 Characterization

We look now at the physical Zeeman slower we have constructed. In practice, we make the magnetic field with a range of coils, as this is easier to construct than making the Zeeman slower out of one long wire and it also leaves us the freedom to replace or adjust separate coils. The coils are independent, but connected in series. We can choose how many loops we use to create the coils, and we control the current going through the wire, resulting in a given magnetic field. In figure 2.25 the coil design for the slower and the expected magnetic field resulting from them are shown. We construct two Zeeman slowers, one for the positive field (the first, longest part) and another one for the negative field (the second, smaller part). For the longer one, the coils are produced and assembled commercially, the small one is made in-house. For the biggest coils we have put a potentiometer in parallel, so we have a measure of control over the magnetic field they create. To measure the magnetic field, we construct a Hall probe on a piece of plastic, with a rope to each side to pass it through the length of the slower. The result of this measurement with the probe can be seen in figure 2.26. We find that the profile is not as smooth as we expected, the field goes down faster than expected between coils, even though the coils are only 0.5 cm apart. Even when using the potentiometers to level out the magnetic field the profile remains uneven. A magnetic field profile that is not smooth will reduce the efficiency of the Zeeman slower and should be avoided.
The reason for this behaviour could not be determined. To counteract the effect, we put some extra windings on the ends of the bigger coils, the result of this addition is also shown in 2.26. With the additional windings the profile is smoother and more suitable for slowing the atoms.

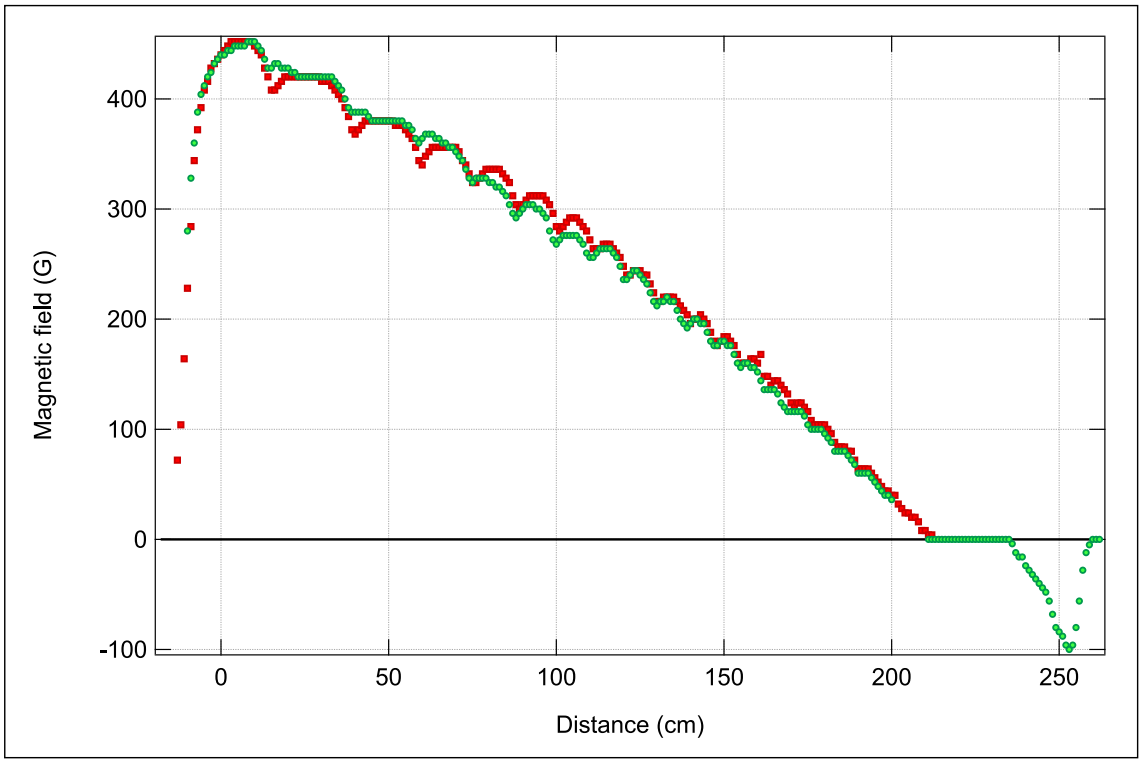

Figure 2.26: The measured magnetic field of the Zeeman slower, with (red squares) and without (green circles) compensation with the potentiometers and the added compensation coils. The current through the slower is here 4 A.

For the light of the Zeeman slower we use a fiber coupler from Schäfter Kirchhoff [114] which outputs a beam with a waist of 15.8 mm. We focus the beam onto the skimmer for best results. There is some space in between the slowers where the Faraday cup mentioned in the previous chapter is located. We cannot use the cup for evaluating the slower since it would block the light. Instead we use the same fluorescence detection methods with the camera as described earlier in section 2.4.1, for measuring the flux and longitudinal velocities.

An example of a measurement like this is shown in figure 2.27. One can see the atoms that are not slowed down by the Zeeman slower, as well as the atoms that are only slowed by the first slower, and then there are the atoms that are slowed down by both. It is important to note that in this picture, the area under the curves does not represent a number of atoms, as it is the fluorescence that is shown, and slow atoms have more time to fluoresce while in the probe beam. By depicting the graph in this way we can better show the difference between the smaller peaks, which would wash out when converting to flux.

A quantatative evaluation of the performance of the first Zeeman slower is found in figure 2.28, where the total atomic flux slowed by the big Zeeman slower and the width of the velocity distributions are shown. Independent of the current, the final

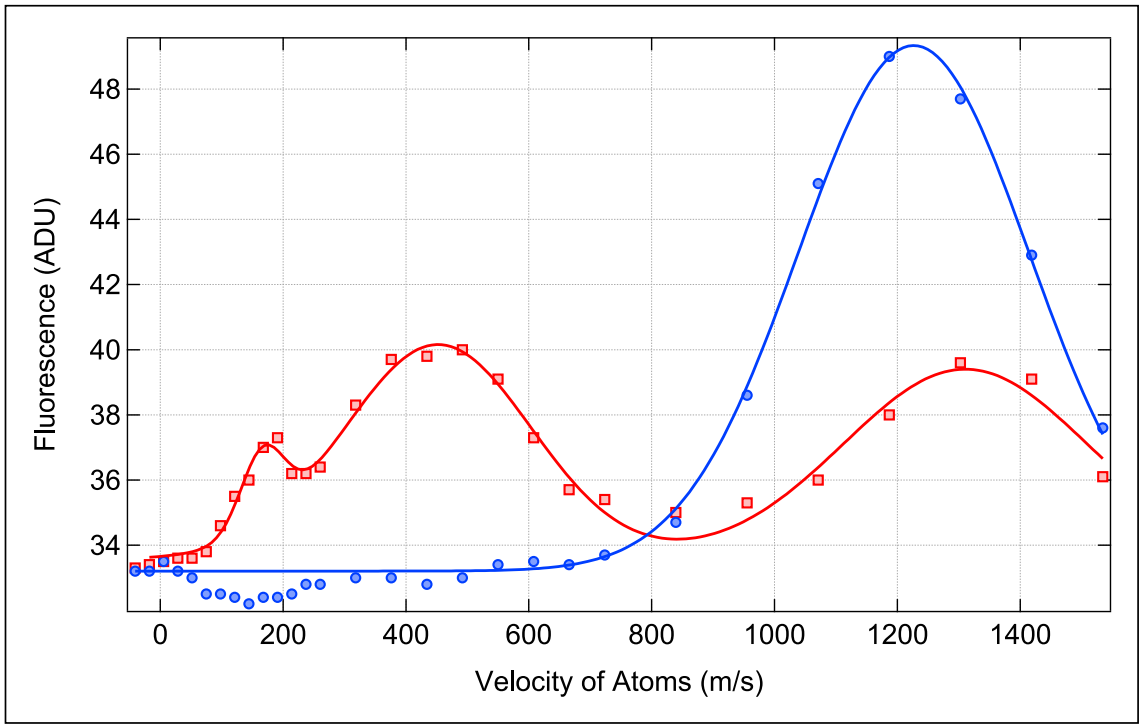

Figure 2.27: An example measurement of the velocity distribution of atoms going through the slower. Red squares: Zeeman slower on. Blue circles: Zeeman Slower off. Pictured here is the amount of fluorescence detected by the camera.

velocity of the atoms slowed by only the large slower is 465(15) m/s.
From the data we see that there is an optimum for slowing atoms the maximum number of atoms, at a current of 4 A, at this point the efficiency of the slower is ~ 50 %. The width of the longitudinal velocity distribution, shown in the bottom graph, is in principle not of big concern to us. However, the second Zeeman slower also has a designed $v_{start} = 430$ m/s and if a too large portion of the atoms slowed down by the first slower have a velocity larger than that, the efficiency of the second slower will be worse. At present, a bit less than half of the atoms satisfy this condition.

Presently we turn to the performance of the second Zeeman slower. For the second slower the alignment of the light is much more important, since the atoms are much more spread out transversely. For the big slower the atomic beam is smaller than the light, so one has some leeway. Therefore we optimize the alignment for every different current when making this measurement.
We have found that at a detuning of $2\pi \times 400$ MHz the efficiency of the small Zeeman is not very good, the flux of slowed down atoms is lower than expected and the final velocity is too high for the atoms to be captured in the MOT. This is most likely due to a too large magnetic field gradient in the small slower, leading to losses and inability to reach the lowest velocities.
To increase the efficiency, we have changed the detuning of the Zeeman light from $2\pi \times 400$ MHz to $2\pi \times 350$ MHz. This means that the first slower slow the atoms down to lower velocities and v_{start} for the second slower is lower. In figure 2.29 the

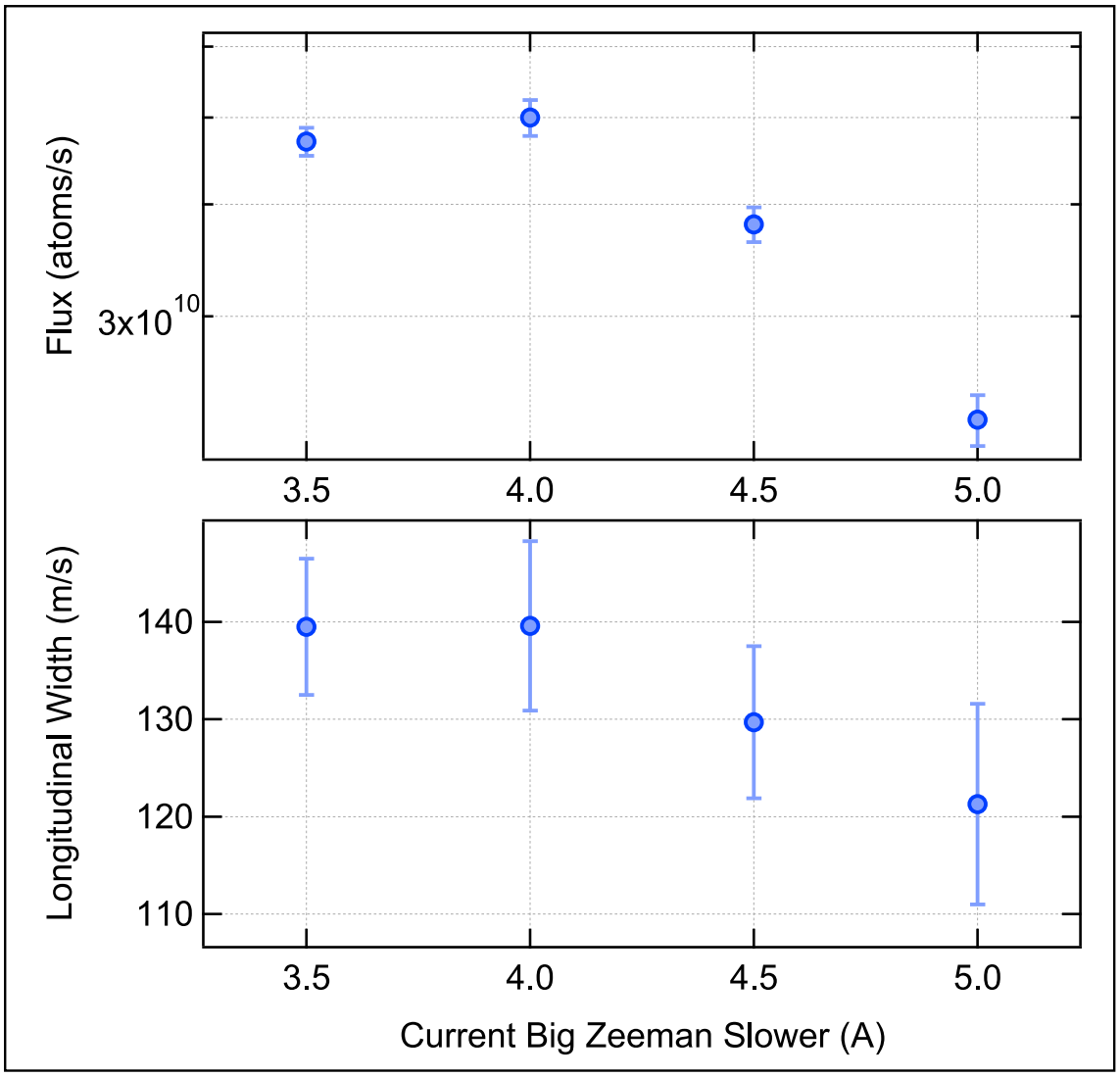

Figure 2.28: Top: The flux of atoms after being slowed down by the big Zeeman slower. This part of the slower has an efficiency of ~ 50 %. Bottom: The longitudinal velocity spread of the slowed down atoms. The final velocity of the slower is 465(5) m/s, independent of the current.

two situations are compared. As one can see the flux when having a detuning of $2\pi \times 350$ MHz is higher than at $2\pi \times 400$ MHz, and this effect is more noticeable at higher currents of the slower. At $I = 5.5$ A the difference between the two is almost a factor 10. With $\delta = 2\pi \times 350$ MHz we get at this current a flux of 3×10^{10} atoms per second.
From the bottom of the figure we see that we need to be at a current of around 6A to get a velocity of ~ 50 m/s for $\delta = 2\pi \times 350$ MHz, whereas for $\delta = 2\pi \times 400$ MHz the required magnetic field would mean a current of closer to 7 A. At 6 A for $\delta = 2\pi \times 350$ MHz the flux will also be lower than the above mentioned 3×10^{10}, but we cannot directly measure it as the signal is too low. We will see when loading the MOT in the next chapter how many atoms are captured.
From these results we decide to keep working with a detuning of the light at $2\pi \times 350$ MHz and work with the first Zeeman slower at 4 A and the second Zeeman slower at 6 A to get the desired final velocity with the highest possible flux.

These measurements have been done with a slightly smaller collimator, the later replacement with a waist of 15.8 mm makes the total effect of the Zeeman slower about 3 to 4 times more effective, which gives us a flux of several 10^{10} atoms per second at ~ 50 m/s to be loaded into the MOT.

We had planned to add a 2D MOT stage after the Zeeman slower to transversely cool the slow atoms before they would be captured in the MOT. Unfortunately there were technical difficulties with installing the glass chamber which was designed for this purpose. More information on the 2D MOT can be found in appendix A.

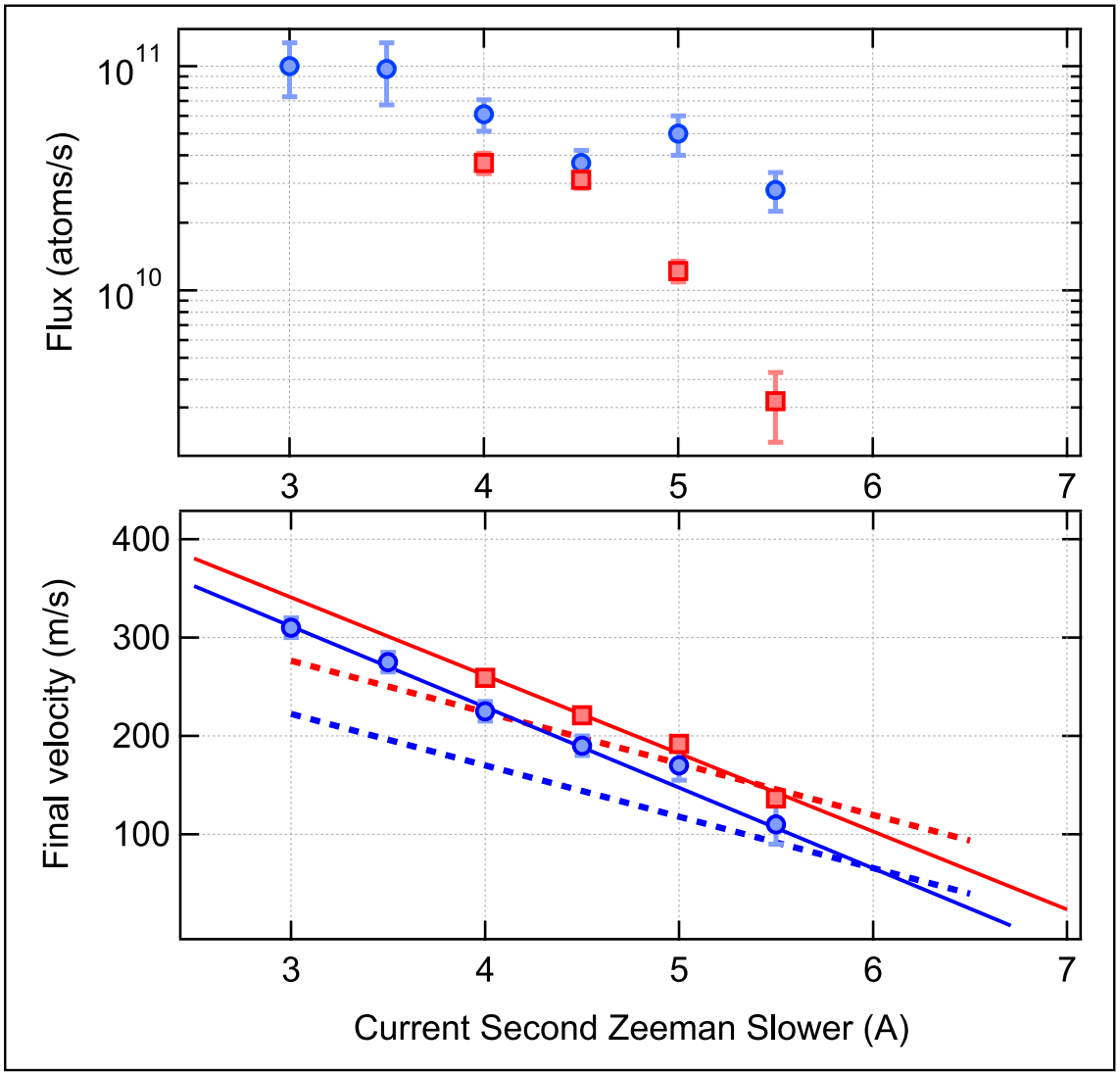

Figure 2.29: The difference between $\delta_{Zeeman} = 2\pi \times 400$ MHz (red squares) and $\delta_{Zeeman} = 2\pi \times 350$ MHz (blue circles). Top: The flux of atoms at the end of the second Zeeman slower as a function of the current in the second slower. Bottom: The velocity of the atoms at the end of the second Zeeman slower (v_{final}), with the dotted lines the calculated v_{final}.

2.7 Conclusion

At the end of this chapter it is time to make a small summary of what we have discussed so far. We have talked about the physical systems present in our experiment, the laser system and its optics, as well as the vacuum system in which the experiments will be performed. We know how to detect metastable helium atoms, not only by the fluorescence with the new camera, but also how to collect atoms on a Faraday cup and how to calculate properties like the flux and the width of a velocity distribution.

We have explained how metastable helium is created from ground state atoms in our source which is cooled with liquid nitrogen. We have seen that the atoms coming out of the source with a flux of several 10^{12} atoms per second have a longitudinal velocity of $\sim$ 1200 m/s and a transverse velocity spread of $\sim$ 50 m/s. Since with these parameters the atoms will never be trapped in a MOT, we collimate them with optical molasses until we get a large flux of atoms that have a small enough velocity spread so that they can travel the whole distance of the Zeeman slower to the science chamber. With no slowing happening we report a flux of 10^{11} collimated atoms per second on the Faraday cup.
To cool the above flux longitudinal there are two Zeeman slower that have been described extensively. After the first slower we have a flux of 5×10^{10} atoms per second, which are still travelling at 500 m/s, which is still too fast. After the second slower we have atoms with a longitudinal velocity of $\sim$ 50 m/s and we still have a flux of several 10^{10} atoms per second.

We are content with these results and believe with an atomic beam such as the one described in this chapter, one can load a MOT in sufficiently short time to run an efficient experiment. More details on why a high loading rate is important will be discussed in the next chapter, as will the progression of the experiment. The next chapter will deal with the trapping and subsequent cooling of the metastable helium atoms.

Chapter 3

Doppler Cooling of Metastable Helium

3.1 Introduction

The previous chapter dealt with the creation of a slow atomic beam of metastable helium-4. It was created specifically with the purpose of trapping and cooling the metastable helium atoms down to ultra-cold temperatures.

In this chapter we will discuss the cooling and trapping of metastable helium in a magneto-optical trap. The subject is placed into context and an overview of the atomic physics at hand is given in sections 3.2, 3.3 and 3.3.1.
Subsequently we will describe the experimental steps taken to obtain the trapped and cooled cloud of atoms in the lab. In section 3.4 the hardware necessary is introduced and in section 3.5 the results of the characterization and the comparison to theory are made.

The control of the experimental sequences that are described in this chapter have been made and executed in a fairly new environment named *Cicero*, a graphical interface developed at the MIT Center for Ultra Cold Atoms in the United States. A description of the hard- and software and the way it works is given in C.

Nostalgia

In the evening of the 26th of June 2013 we trapped for the first time a cloud of metastable helium atoms in a MOT. The resolution of the camera was quite bad (the lens system had not been installed yet), all the fluorescence from the alleged MOT was captured in a number of pixels that could be counted on one hand. Our first reaction was disbelief (after trying for so long, it suddenly felt too easy), but soon we started to disprove all the other possible sources of the fluorescence.
How do you know the fluorescence light you see is a cloud of trapped atoms ? We had already had several false alarms at this point and were hesitant to announce yet another one, and deal with the disappointment again.
There are two tests: When you block one of the six MOT beams, the spot should dis-

appear and when you switch the polarization of the magnetic field, the spot should also disappear. Those two conditions combined, makes it definitive that the spot of fluorescence, however small it might be on your camera, is in fact a cloud of trapped atoms. It turned out we had no other option but to accept our success.
In the following months we installed the better magnifying objective for the camera, allowing us to characterize the MOT. We have optimized not only the internal parameters of the trap but also the loading by the Zeeman slower and the collimation from the optical molasses.

A MOT works twofold, it traps the atoms and it cools them at the same time. The trapping stems from a position dependent force resulting from a magnetic field gradient combined with detuned counter propagating beams of light, forcing the atoms to the center of the trap. The cooling comes only from the light, and only works if the light is red-detuned. Let us have a closer look at the mechanics of the trapping and the cooling.

3.2 Trapping in Magneto-Optical Traps

The first magneto-optical traps (MOTs) were realized in the middle of the 80's [90, 110]. The trap combined at the time known optical molasses [111] with a small magnetic field to add a position dependent force. Since then, for basically all cold atom experiments trapping atoms in a MOT is the benchmark starting point to further cooling processes [108, 109].

In a MOT the atoms are trapped by a position dependent force that directs them back to the center of the trap. When a (static) magnetic field acts upon a neutral atom, there is a level splitting know as Zeeman splitting. A MOT has a magnetic field gradient which gives a position dependent Zeeman splitting, see figure 3.1. To get a force that pushes the atoms to the center of the trap, the magnetic field gradient is combined with circularly polarized counter propagating beams of light, such that the Zeeman shift and the detuning put the atoms in resonance with the light. However, since the beams have, from the atoms point of view, different polarizations, only the beam that has an opposite momentum sign from the atoms has the right polarization to excite the atom ($m = 0$ to $m = 1$ for σ^- and $m = 0$ to $m = -1$ for σ^+), as shown in figure 3.1.
This condition is met when:

$$\delta_L = \mu B(x) = \mu B' x \tag{3.1}$$

With B position dependent and μ the magnetic moment of the particle, neglecting the nucleus part, since it is several orders of magnitude smaller than the electronic part of the magnetic moment, makes $\mu = -\mu_B g J/\hbar$, with μ_B the Bohr magneton, J the total electronic angular momentum and g the Landé g-factor.
When the atom absorbs this photon, it gets a (small) kick towards the center. Emission is random and not associated with a net average change in momentum for the atom. The resulting average force is therefore in the direction of the center. In the figure the process is shown in 1D, with only two counter propagating beams, a real-life MOT for trapping atoms has 6 beams. In a MOT the atoms are not only trapped but the light also cools them. This cooling is independent from the trapping, as it also happens without the magnetic field gradient present. The simple scheme presented above of trapping of the atoms in the MOT could in principle work with both red and blue detuned light, one just has to choose which transitions one wants to address.
However, the real picture is though that the atoms themselves are not static, but they are moving around in the MOT. This adds a Doppler detuning to the picture. As long as $\mu B >> kv$, the trapping can still be done with blue detuned beams, but in that case there will not be any cooling, when with red detuned light there is Doppler cooling present.

3.3 Cooling in a Magneto-Optical trap

The mechanism that is responsible for the cooling was first introduced in 1975 when an idea for the cooling of neutral and charged atoms with light was simultaneously

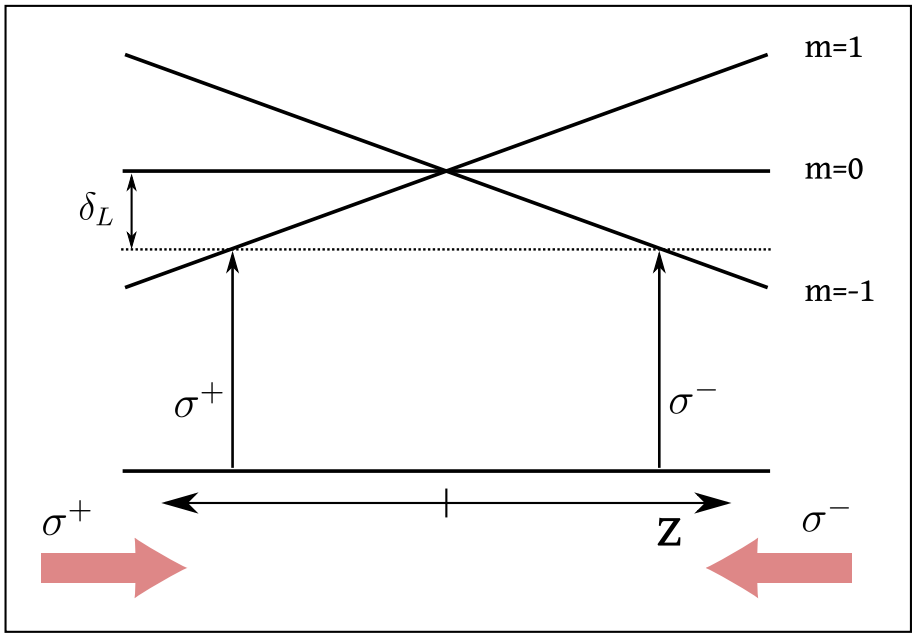

Figure 3.1: How a Magneto-Optical Trap works. A magnetic field gradient creates a position dependent Zeeman shift. Circularly polarized red-detuned beams interact with the atoms and push them back to the center of the trap. At the same time the Doppler effect creates a molasses-like cooling force. This picture is one dimensional, but applies in all three dimensions.

proposed by two groups [88, 89]. The principle uses low-intensity opposing beams with a small red-detuning from the atomic transition. The Doppler shift of the transition of an atom that is moving, leads to an imbalance in the radiative pressure of the two beams, for that atom, and results in cooling. A moving atom is more likely to absorb an atom from the light that has a velocity opposite to its own, since the light is red-detuned. Emmission is random, meaning this process is a momentum transfer from the photon to the atom. Three orthogonal pairs of opposing beams will cool the atoms in all dimensions.

3.3.1 Two-Level Systems

When one only has to consider one transition, a so called two-level system, one can get a clear picture of the dynamics of a MOT.
For a two-level system the absorbtion/emission rate of an atom in a near-resonant light field is given by [120]:

$$R = \frac{\Gamma}{2} \frac{I/I_{sat}}{1 + I/I_{sat} + \left(2\left(\delta_L - kv\right)/\Gamma\right)^2} \tag{3.2}$$

Where Γ is the natural linewidth of the transition, $I_{sat} = 2\pi^2\hbar c\Gamma/3\lambda^3$ the saturation intensity, I the intensity and δ_L the detuning of the laser beam light.

Temperature of a MOT for a two-level system

The lowest temperature a cloud of atoms in a MOT can reach is an equilibrium between the constant absorbing and emitting of photons, with rate Γ. The capture velocity is the largest velocity that can be cooled down by two-level Doppler cooling, $v_c^D \simeq \delta/k$.
A two-level atom in a MOT will feel a force from the beams corresponding to the momentum of the photon times the rate of absorbtion [108, 109]:

$$\vec{F}_{\pm} = \pm\frac{\hbar\vec{k}\Gamma}{2}\frac{I_{tot}/I_0}{1+(I_{tot}/I_0)+(2\delta_{\pm}/\Gamma)^2} \tag{3.3}$$

With the detuning $\delta_{\pm}$ for each laser beam and $I_0 = C \times I_{sat}$, an effective saturation intensity:

$$\delta_{\pm} = \delta_L \mp \vec{k}\cdot\vec{v} \pm \mu B/\hbar \tag{3.4}$$

Where the minus and plus signs depict the two opposing beams. For atoms in a low intensity light field ($I \ll I_{sat}$) and with low velocities ($|kv| \ll \Gamma$ and $|kv| \ll \delta$) the average force on one atom is $F_{av} = F_+ + F_-$ and can be written as [92]:

$$F_{cooling} = 4\hbar k\frac{I_{tot}}{I_0}\frac{kv(2\delta/\Gamma)}{(1+I_{tot}/I_0+(2\delta/\Gamma)^2)^2} \tag{3.5}$$

For red detuned light ($\delta < 0$) the above formula depicts a friction force and can be written as:

$$F_{cooling} = -\alpha \times v \tag{3.6}$$

With:

$$\alpha = 4\hbar k^2\frac{I_{tot}}{I_0}\frac{(2\,|\delta|\,/\Gamma)}{(1+I_{tot}/I_0+(2\,|\delta|\,/\Gamma)^2)^2} \tag{3.7}$$

This force is always damping, as the atoms will absorb photons out of the beam with opposing v more than the other, it is linear in $|kv| < |\delta|$.
The work done by this force on an atom is:

$$\left(\frac{dE}{dt}\right)_{cool} = Fv = -\alpha v^2 \tag{3.8}$$

The absorbtion and subsequent emission happens at random times, and there is a heating associated with this randomness, which gives a kinetic energy increase of:

$$\left(\frac{dE}{dt}\right)_{heat} = \frac{\hbar^2k^2\Gamma}{m}\frac{I_{tot}/I_0}{1+I_{tot}/I_0+(2\delta/\Gamma)^2} \tag{3.9}$$

With m the mass of the atom. Put $\left(\frac{dE}{dt}\right)_{cool} + \left(\frac{dE}{dt}\right)_{heat} = 0$ to get an expression for v^2:

$$v^2 = \frac{\hbar\Gamma}{4m}\frac{1+I_{tot}/I_0+(2\,|\delta|\,/\Gamma)^2}{2\,|\delta|\,/\Gamma} \tag{3.10}$$

This is the mean square velocity of the atoms in the MOT, it is the average of all the velocities squared of all the atoms. Taking the thermal energy $k_B T/2 = m v_{rms}^2/2$, this gives for the temperature of the cloud of atoms in a MOT:

$$k_B T = \frac{\hbar \Gamma}{4} \left(\frac{1 + I_{tot}/I_0 + (2\delta/\Gamma)^2}{2\,|\delta|\,/\Gamma} \right) \tag{3.11}$$

With I_0 the adjusted saturation intensity and I_{tot} the total power in the six MOT beams. From this we see that the lowest possible temperature for the MOT is:

$$k_B T_D = \hbar \frac{\Gamma}{2} \tag{3.12}$$

Which is reached for $2\delta/\Gamma = -1$ and $I_{tot} \ll I_0$.

Size

In the two-level scheme, and when there is no multiple scattering of the photons, the size of the cloud of atoms trapped in a MOT is only governed by the equilibrium of the forces, the same as the temperature, see equation 3.11. Multiple scattering would introduce another repulsive force from the center of the cloud, which would increase cloud size, as photons emitted by particles will be absorbed by other particles. When this regime is reached, the density of the cloud becomes uniform instead of Gaussian [119, 120]. The density at which multiple scattering starts to occur is dependent on factors such as the detuning of the light, the magnetic field gradient and the number of atoms [121, 122].

A MOT of metastable helium is less dense than MOTs filled with other species of atoms, due to light induced collisions that prevent high densities, see section 3.3.3 for a more detailed description. This means we are not in the multi-scattering regime, and allows us to study Doppler theory in a very clean environment.

When we assume not to be in the multiple scattering regime, we can write the forces that act on an atom trapped in a MOT as follows:

$$F(x, \vec{v}) = -\alpha \vec{v} + \kappa x \tag{3.13}$$

Here α is the friction coefficient from equation 3.7. A spring constant κ is introduced and is written as:

$$\kappa_i = \alpha \frac{\mu B_i'}{\hbar k} \tag{3.14}$$

With the index i to denote the different spatial dimensions and B_i' the magnetic field gradient in that direction.
If one combines this with the equipartion theorem, we get an expression for the size of the trapped cloud:

$$\frac{1}{2} \kappa_i \sigma_i^2 = \frac{1}{2} k_B T \tag{3.15}$$

We shall verify these predictions in experiment.

3.3.2 Multi-level Systems

Sub-Doppler Cooling

When experiments with laser cooling started in the 1980's, used were mostly alkaline atoms [90, 92]. It was found that the temperatures found in these clouds were much lower than the Doppler temperature that was calculated [118].
The solution to this question is that the transitions that were used for the cooling scheme were not perfect two-level systems [91][123]. Doppler theory does not take into account the sublevels of the atomic states such as the hyperfine structure or Zeeman splitting. When there is such a non-degeneracy of the ground state, there is cooling present that goes beyond the Doppler theory, known as sub-Doppler cooling. In the case of alkalines, there is the hyperfine ground state splitting, due to the atom having a nuclear spin $I \neq 0$, which leads to the sub-Doppler cooling. Alkaline-earth species promised a cleaner test of Doppler theory as their groundstate has $I = 0$, however there turned out to be additional heating present, giving the cooled clouds higher temperatures than the expected Doppler temperature [93, 94].

The question is then whether metastable helium atoms are different from the above. There is a hyperfine structure of the ground state, since the state has a total angular momentum $J = 1$, so this could potentially lead to sub-Doppler mechanisms.

The multi-level system introduces different Clebsch-Gordan coefficients for the different sublevel transitions. To deal with this we write the scattering rate as:

$$R = \frac{\Gamma}{2} \frac{C_1 I / I_{sat}}{1 + C_2 I / Isat + \left(2\left(\delta_L - kv\right)/\Gamma\right)^2} \tag{3.16}$$

The constants C_1 and C_2 are averaged Clebsch-Gordan coefficients, which account for the multi-level structure of the transition. In practice $C_1 = C_2$ and having these constants is equivalent to treating the system with an effective saturation intensity $I_0 = C_1 I_{sat}$. As there are in helium no loss channels the excitation rate is the same as the decay rate.

Mechanisms of Sub-Doppler Cooling

When you take into account the atomic sublevels, it follows that there is a time delay of the atom reacting to the internal sublevel state shifts, which occur because the atom is moving through the light field, to the motional reaction of the atom. This means that by the time the internal states of the atom have adjusted to any changes in the light field, the atom has moved and the light field has changed again.

Sisyphus Cooling Two counter propagating waves with linear polarization create a ellipticity gradient, which induces a position dependent light shift in the magnetic sublevels of the ground state. The atoms moving through the light field repeatedly 'climb' the potential hills after which they are optically pumped back to the bottom of the hill, in the process giving the excess energy to the emitted photon. Note

that the retardation effect mentioned above is responsible for the atom being able to move from the bottom of the hill to the top before being optically pumped in the other sublevel. Another way to look at it is that the photon that is absorbed will be red-detuned and the photon emitted by stimulated emission will be blue detuned from the transition. It follows that if the laser is on resonance, the atom will absorb photon from the beam that is countering its motion, and will emit in the beam that is in the same direction, leading to slowing.
The process continues until the atom has not enough energy left to climb the hill, unlike Sisyphus himself. This leads to a cloud of atoms with a temperature well below the Doppler temperature. In principle, the process is conservative, however since the retardation time is finite, the atoms will on avarage see more uphill than downhill trajectories.

Orientational Cooling In the case for the σ_+, σ_- configuration, there is a different underlying mechanism from Sisyphus cooling, as the polarization of the resulting standing wave is always linear, therefore not resulting in a ellipticity gradient like above and there is no positional dependence of the light shift. The mechanism at work here is also known as orientational cooling. If the atom is at motion, the changing polarization leads to an effective magnetic field in the frame of the atom, resulting in a reducing of the energy of the Zeeman level and an effective higher population of this state. The atoms will accumulate in the sublevel with m_F values with opposite sign of the velocity, meaning that they then will primarily absorb photons from the light beam with shares the sign of m_F, leading to damping. Unfortunately, this only works when the Zeeman sublevels are coupled, which is only the case for a very small velocity class. Therefore only atoms that are already moving very slow will be slowed even more.

Capture Velocities

The capture velocities of these sub-Doppler mechanisms come from these new mechanisms. For Doppler cooling, the limitations are set by how fast we can pump from the ground state to the excited state, so we are limited by the timescale Γ. For sub-Doppler processes the new timescale is dependent on how fast we can pump between different ground state levels [96]. This new timescale has to be of the same order of magnitude as the time it takes an atom to travel the distance of one wavelength for the sub-Doppler mechanism to be efficient.
We call this pumping rate between ground states Γ' and we can write:

$$\Gamma' = \frac{s}{1+s}\Gamma \tag{3.17}$$

Where s is the saturation parameter. This leads to a capture velocity:

$$v_c = \frac{\Gamma}{2k}\frac{s}{s+1} \tag{3.18}$$

This capture velocity is valid for both mechanisms of sub-Doppler cooling at detunings $\delta \sim \Gamma$, which is the detuning at which the capture range is the largest [97].

It would seem like one can increase the capture range by increasing the intensity of the molasses, however the friction coefficient α changes sign at large s [98]. The flip comes from the contribution of multi-photon processes and occurs generally around $s \sim 1$. An upper limit for the capture velocity can be found at $s_0 = 1/2$ at $\delta = \Gamma/2$. The upper value of the capture range becomes then:

$$\frac{v_c^{max}}{v_D} = \sqrt{\frac{1}{6}\frac{T_{Doppler}}{T_{Recoil}}}\frac{s}{1+s} \tag{3.19}$$

For metastable helium this ratio is 0.59, whereas for example rubidium it is 3.87 and for cesium 5.12. Because of this small ratio in metastable helium we expect no efficient sub-Doppler cooling schemes, as the two regimes (Doppler and sub-Doppler) do not overlap enough in temperature. This holds true for both sub-Doppler mechanisms and we shall verify this hypothesis in experiment.

3.3.3 Penning Collisions

We have talked about the differences between a MOT of metastable helium and that of other species of atoms. The 'perfect' two-level structure of the cooling transition in addition to the relative small difference between the recoil and the Doppler temperature removes additional cooling or heating.

When working with helium atoms, in the presence of light, light-induced Penning collisions [112] limit the density of a cloud of atoms to around $< 10^9$ atoms/cm^3. Light-induced Penning ionization is a process in which one excited and one ground state metastable helium atom collide and ionize:

$$He^*(2^3S, 2^3P) + He^*(2^3S) \rightarrow He(1^1S) + He^+(1^2S) + e^- \tag{3.20}$$

$$\rightarrow He_2^+ + e^- \tag{3.21}$$

The light induced collisions are dependent on the population of the excited state, as one needs one excited and one groud state atom to collide. If one wants to get a high number of atoms trapped in the MOT, and if one forgets for a moment about what this means for the temperature, it is neccessary to work at a high detuning of the light [75]. It also follows that a MOT with light that is far detuned needs to have a large magnetic field gradient to optimize the number of atoms, and the resulting cloud will have a large size.
As the ionization rate is as well dependent on the density of excited state atoms in the cloud, it is therefore suppressed by decreasing the density. In the MOT with large size, we will be able to fit more atoms until we reach the saturation density.

3.3.4 Calibration of Atom Number and Size

A quick word on how we measure the parameters of our cloud such as the number of atoms, the volume and the temperature of the cloud, by using fluorescence measurements with the camera described in section B.

Number of Atoms

To determine the number of atoms from merely fluorescence is a not a straightforward case, which we have already partly discussed in section 2.4.1.
As we know, finding the number of atoms from a fluorescence probe measurement can be done by:

$$N_{atoms} = N_{counts} / \left(\eta \times NA \times L \times R_{sc}(I, \Delta) \times \tau\right) \tag{3.22}$$

Here N_{counts} is number of counts registered on the camera, η is the conversion factor from counts to photons, τ is the time the camera is acquiring data, NA the numerical aperture and L the losses due to reflection. We measure the losses to be less than 1% since all the optics are coated for the used wavelength. The numerical aperture is found from the geometry.
The scattering rate $R_{sc}(I, \Delta)$ of an atom is expressed as usual as in equation 3.2, with the C_1 and C_2 constants to compensate for the real multilevel structure of the transition:

$$R_{sc}(I, \delta) = \frac{\Gamma}{2} \frac{C_1 I / I_{sat}}{1 + C_2 I / Isat + \left(2\left(\delta_L - kv\right)/\Gamma\right)^2} \tag{3.23}$$

With δ_L the detuning of the probe and no magnetic field present. For helium, for the $J = 1 \rightarrow J' = 2$ transition, I_{sat} is 0.16 mW/cm^2 (for Clebsch-Gordon coefficients set to 1) and Γ is $2\pi \times 1.6$ MHz.

To find the number of atoms we take a series of pictures of the cloud with the camera. We use the MOT beams as the probe, but we put the light on resonance with the transition with the AOM. The formula above is assuming the Clebsh-Gordon coefficient is 1.
We have to be careful of the presence of the magnetic field influencing the fluorescence due to the Zeeman shift of the transitions. To properly do the measurements we have to do them with the magnetic field turned off. Using a home build switch we can switch the coils off in ~ 0.5 ms. To be sure that the magnetic field is completely off everywhere, we wait 1.5 ms until taking the picture. The cloud will expand during this time, but the number of atoms stays the same. After this time we give a probe pulse of 400 μ s with the MOT beams on resonance, the fluorescence activated with this we record with the camera.

With our way of locking the laser to the transition (see section 2.3.1), we are not able to estimate the central frequency better than to one linewidth Γ, this is due to collisional broadening of the transition in the saturated absorbtion cell. To circumnavigate this issue we take a resonance curve measurement using the cold MOT cloud as a probe, to precisely determine the atomic transition frequency. An example is shown in figure 3.2, here the resonance frequency can be found up to a factor $\Gamma/5.3$.
We increase the intensity I of the probe beam for every picture, until the transition saturates. The reason for this is: helium has a rather narrow natural linewidth of only $2\pi \times 1.6$ MHz and in addition MOTs of helium are relatively hot, as they

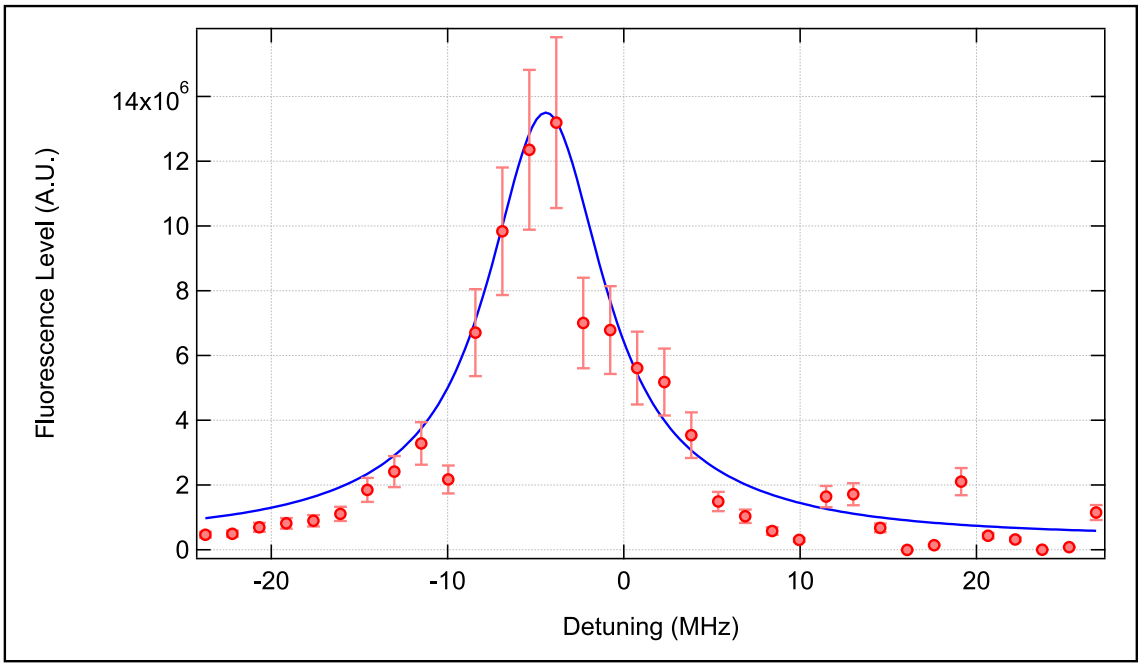

Figure 3.2: Fluorescence level of a time of flight picture of a MOT as a function of the frequency of the probe beam. The fit is a simplified Voigt profile ($\eta \sim 0.5$) and gives the resonance frequency to $\delta_{res} = -4.4(3)$ MHz.

need to be large to keep the light-induced losses to a minimum. This leads to a Doppler broadening of the linewidth that is not negligible in comparison to the natural linewidth. For example, for a MOT with a temperature of 1 mK the Doppler width of the transition is $2\pi \times 4.16$ MHz, that is 2.5 times larger than the natural linewidth. This Doppler broadening can be seen as an effective increase of the saturation intensity I_{sat}.
The saturation method eliminates uncertainties on the saturation intensity by making it a fit value:

$$N_{calc}(I) = N_{true} \times \frac{I}{B + I} \tag{3.24}$$

Where N_{calc} is the calculated number of atoms by fitting every picture by treating it as though $I >> I_{sat}$ and N_{true} is the fitted number of atoms. In figure 3.3 an example of the saturation method of detecting the number of atoms is shown. As one can see, even if we do not reach the saturation regime completely due to the Doppler width, we can still fit the data to find the number of atoms.

This method of atom number calibration is fast and reasonably accurate. However we have made the assumption that the Clebsh-Gordon coefficient is 1, which is an approximation. Therefore we estimate that this method can reliably give us the number of atoms up to a factor of 2.

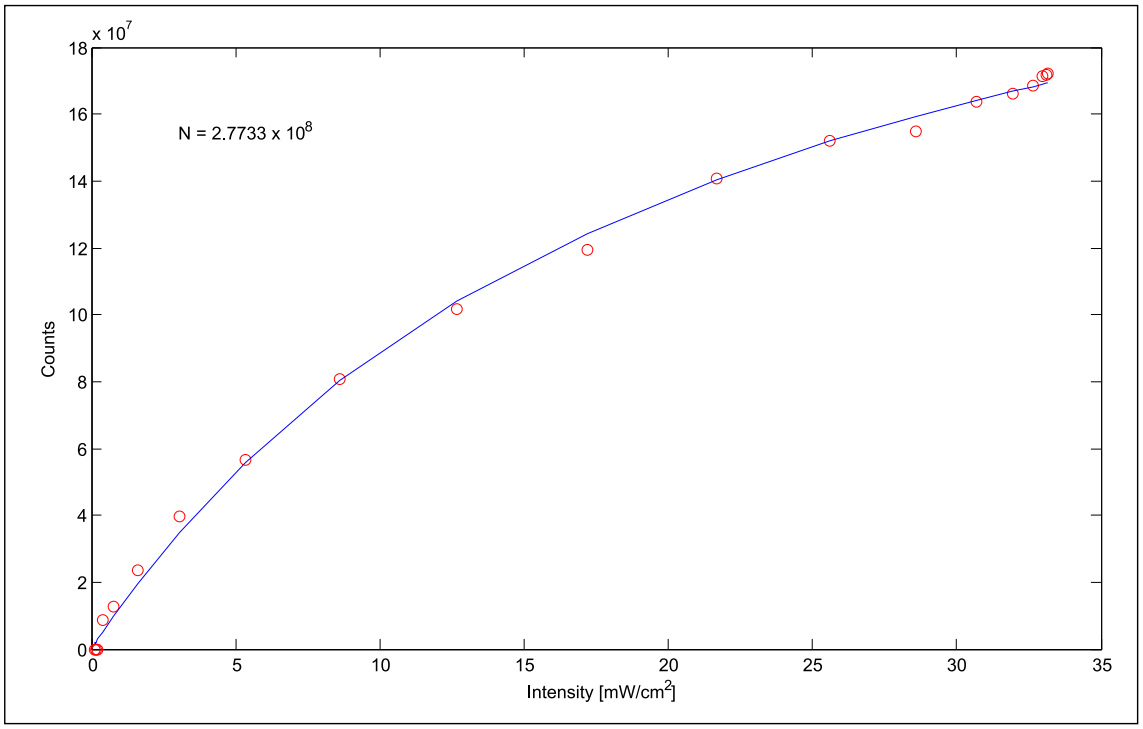

Figure 3.3: The saturation curve of fitted number of atoms versus the intensity of the probe, for a MOT of metastable helium, fitted to give $N_{atoms} = 2.77 \times 10^8$ atoms. Pulses of 400 μ s are taken after 1.5 ms time of flight.

Temperature and Initial Size

The other parameters of the MOT that we are interested in are its temperature and its size. The complications due to the magnetic field presence, mentioned above, are valid whenever we measure the fluorescence of the MOT. Therefore when we take a picture in situ, we cannot determine the size with certainty, as the presence of the magnetic field distorts the fluorescence. However, we do want to know what the actual size of the trap is. To work around this problem we do time of flight measurements. Since the temperature of the MOT is related to its expansion speed when we release it from the cloud, we take a series of pictures, each with a increasing time of flight. Fitting the obtained curve will give us both the temperature and the initial size of the cloud, since the size at time t from the three dimensional Maxwell-Boltzmann distribution:

$$\sigma^2(t) = \sigma^2(0) + \frac{k_B T}{m} \times t^2 \tag{3.25}$$

In figure 3.4 we see an example time of flight picture, where the σ^2 is plotted against t^2. Since we measure a two dimensional picture, we measure the size in two directions, which gives us two measurements of the temperature. This particular picture is from a cloud that has been trapped in a MOT and afterwards cooled by red molasses.

To make sure the magnetic field does not disturb our measurements, we do not take

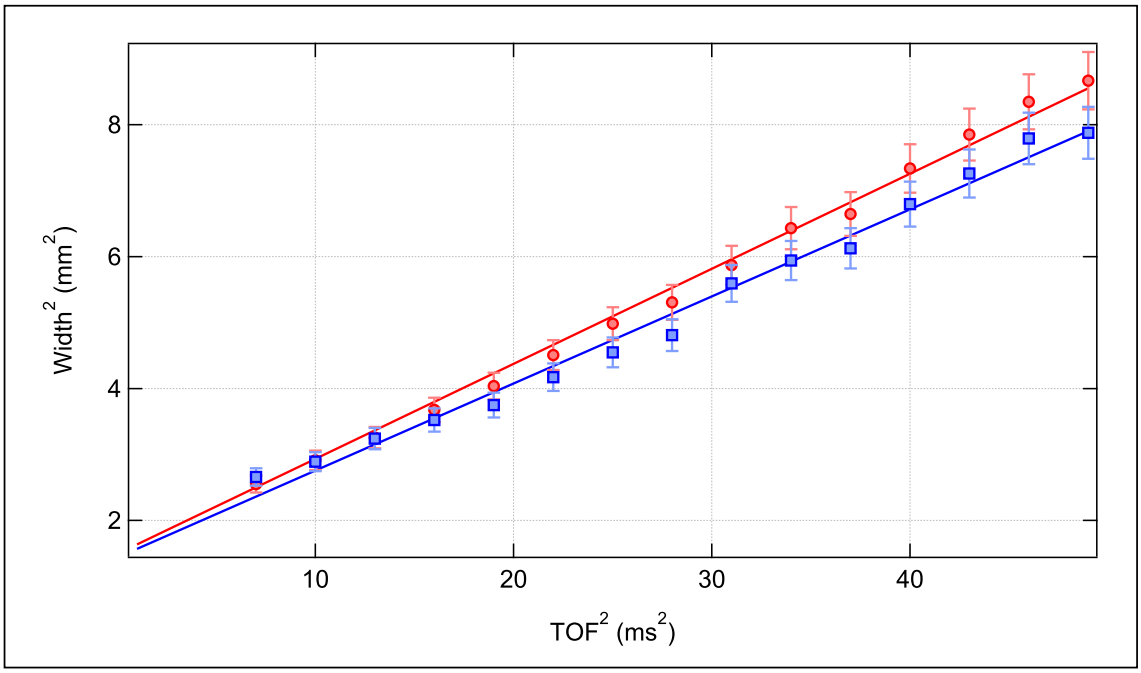

Figure 3.4: A time of flight picture after red molasses. The fit gives a $T_x = 134.7 \pm 3.7$ μK and $T_y = 111,6 \pm 4.6$ μK. For the initial size this gives $\sigma_x = 2.4 \pm 0.2$ mm and $\sigma_y = 2.5 \pm 0.2$ mm.

TOF pictures with a expansion time lower than 1 ms into account. We also monitor the number of atoms and as long as the number stays constant, we use the size values in the TOF fit. When the number starts to drop, we stop the measurement. The size and the temperature of the cloud are extracted only in this way. With these measurement techniques we are ready to start evaluating and optimizing the MOT.

3.4 Hardware

As we have seen above, to construct a cloud of metastable helium-4 atoms trapped in a MOT, there are four things one needs. First is a suitable environment, the science chamber with ultra high vacuum discussed in section 2.2.2. For a MOT a vacuum of 10^{-11} mBar is not strictly necessary, the first helium MOTs were made in vacuum of 10^{-9} mBar. Our vacuum is more than suitable for the creation of a MOT, so the first requisite is completed.
The next thing we need, are atoms to fill the trap. In the previous chapter we have talked about the creation of a slowed atomic beam of metastable helium that is ready to be caught in a trap.

There are two more things that we need to trap the atoms, we need a magnetic field gradient and we need light. Let us have a look at those, starting with a brief description of the coils we have to make the magnetic field and finishing with the optics.

Magnetic Field

To create an magnetic field suitable not only for the magnetic gradient necessary for the MOT, but also magnetic fields employed for following magnetic trapping stages, we have designed and commissioned a pair of coils. The coils are installed on on the sides of the science chamber, around the windows, in an anti-Helmholtz configuration. This means that the magnetic gradient in the axis that is orthogonal with both the atomic beam and with gravity will be twice as high as the other two directions.

Some numbers on our coils:

Inner diam.	Outer diam	N_{turns}	Tube	R_{theory}/R_{meas}	L_{theory}/L_{meas}
180 mm	250 mm	500	1×5 mm	0.28/0.30 Ω	$7 - 20/11$ mH

The two coils are in parallel to reduce the inductance, as it goes as $L = \frac{\mu N^2 A}{l}$ where μ is the magnetic permeability, N the number of turns, A the surface of the coil and l the length of the coil, so a parallel construction reduces the inductance with a factor 2.
Our design run with a current of 100 A gives us a theoretics gradient of 1.52 T/m, when measured it is 1.41 T/m, the conversion factor us 1.41 A per G/cm.

A problem that occurs is that the coil is heating up much more than expected. The coils are held in to place and in surface contact with a metal construction, which is water cooled. In figure 3.5 one can see a graph showing the heating of the coils as a function of the time that they are on, for a current of 30 A, while the water cooling is on. For the MOT we will be working with lower currents (see section 3.5), but for the magnetic trap we will need currents exceeding 30 A by far. New coils will be needed at that point.

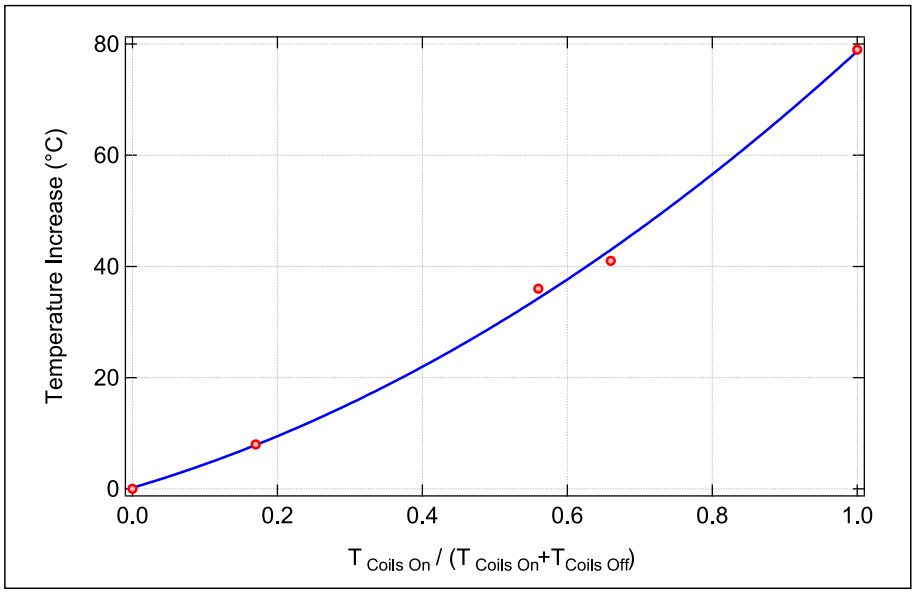

Figure 3.5: The heating of the coils as a function of downtime for a current of 30 A, while being water cooled on the surface. The fit is a third order polynomial.

Optics

The light is the final piece of the puzzle. We have seen the laser being amplified and locked in section 2.3, up until where we inject it into a fiber. We pick up the light at the end of this fiber and inject it into a Schäfter Kirchhoff cluster that splits the light into six beams [113]. A detailed look at the optics inside the cluster can be seen in figure 3.6.
This cluster outputs six linearly polarized fibers which we connect to six Schäfter Kirchhoff fiber collimators that have built-in $\lambda/4$ plates to change the light to circular helicity [114]. These collimators have a gaussian shape and a beam waist of $w_0 = 15.8 \pm 0.1$ mm as measured with the knife edge method.

The light is subsequently put on the atoms as three pairs of counterpropagating beams, as shown before in figure 2.3. Four beams are put at a 45° angle with the ground as there is no optical access from below, that is where the micro-channel plate will be located. One has to be mindful that the polarization of the atomic transition is defined by the axis of the magnetic field. This leads then to the two counterpropagating beams having the same helicity when they come out of their respective collimators. It also means that the two beams parallel to the ground are at the opposite helicity as the other four beams, as the atomic transition is defined oppositely in this direction compared to the other one.

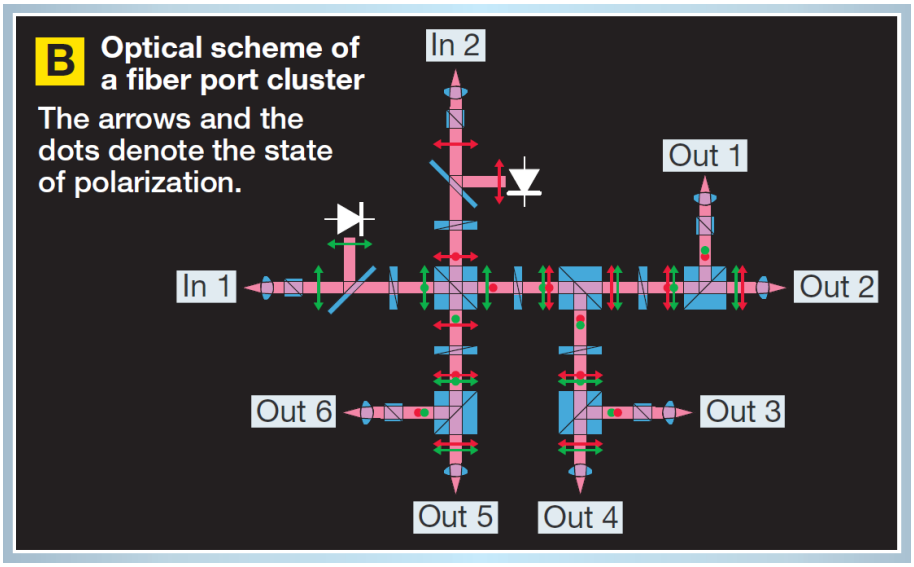

Figure 3.6: From [113], the optics inside the Schäfter Kirchhoff cluster. There are two inputs and six outputs. To measure the intensity of the light 1% of the light is split off and measured by a photodiode. The outputs are all balanced, but can be changed by hand if desired. Output is linearly polarized.

3.5 Experimental Results

3.5.1 Optimization

Let us have a look at the characteristics of our MOT. We have to remind ourselves what our goals are for the continuation of the experiment. We want as many atoms in the MOT as we can, and we want them as cold as possible. With this in the back of our head we look at the behavior of the MOT.

The number of atoms in a MOT is an equilibrium between atoms coming in and atoms going out. Loss mechanisms for the MOT are the previously mentioned light assisted Penning collisions and collisions with background atoms. The MOT is loaded with atoms from the slowed atomic beam discussed in chapter 2. We shall discuss below internal MOT conditions, optimized to keep its density and therefore its light-induced collisions low, and external conditions to make the loading rate as high as possible.

From 3.11 we know that working at a higher detuning leads to higher temperature as well. Since we can put additional cooling stages after the MOT stage to lower the temperature, but we cannot add more atoms whenever we want, our main focus will be to get as many atoms as possible in the trap.

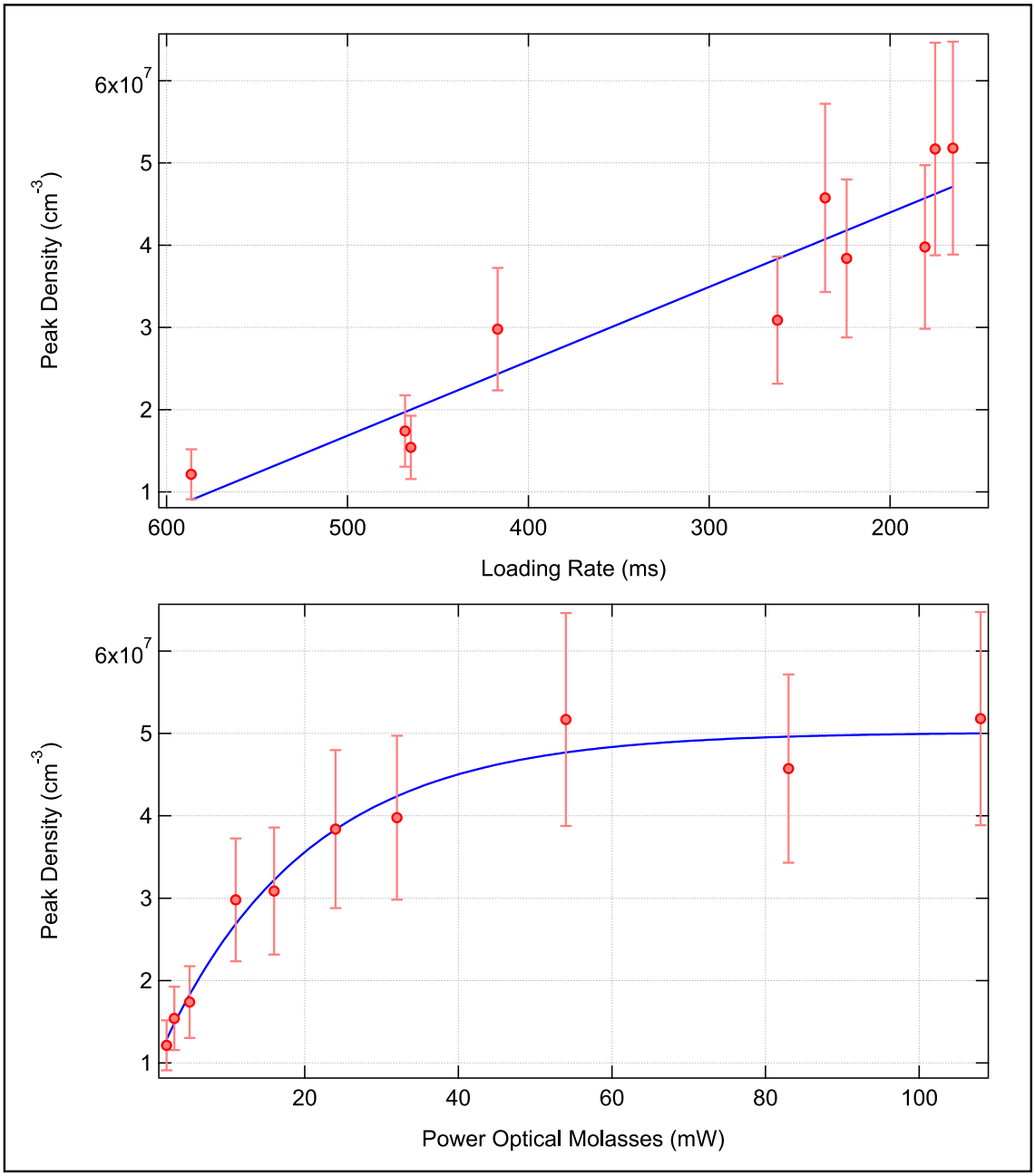

Figure 3.7: Top: The equilibrium peak density as a function of the loading rate. Bottom: The equilibrium peak density as a function of the total power in the optical molasses.

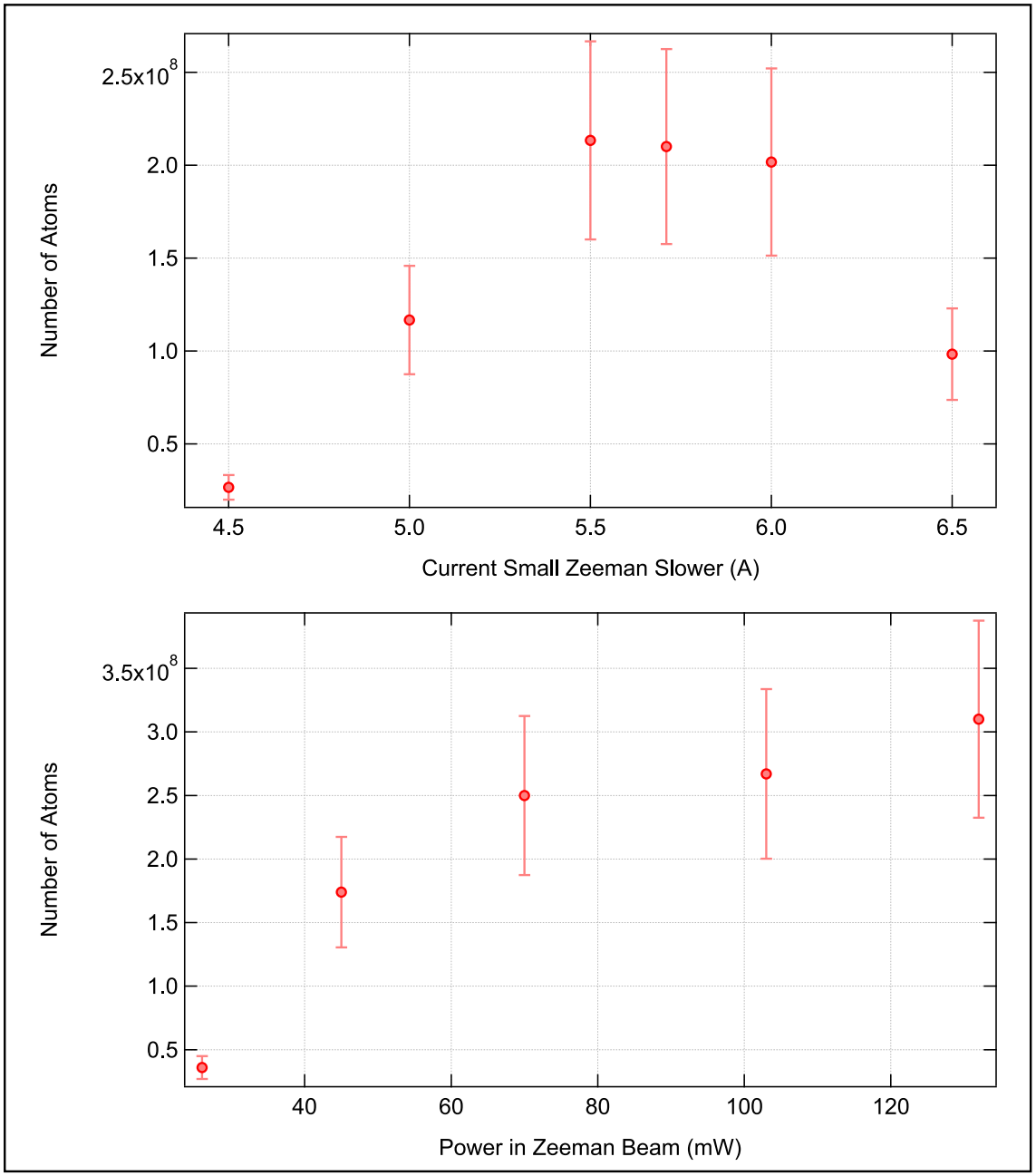

Figure 3.8: Top: The number of atoms in the MOT as a function of the current in the small Zeeman slower. Bottom: The number of atoms as a function of the power in the Zeeman beam.

Loading Rate Optimization

While the loading rate also depends on the MOT parameters such as the detuning, gradient and intensity, as they influence the capture range of the trap, the optimization of those parameters is done separately from the external loading rate optimization. To get the highest number of atoms from the internal parameters does not necessarily mean that the capture range is optimized, as one is balancing loading and losses.
It is therefore imperative, to maximize the atoms that are able to be caught in the MOT. The loading rate depends on the flux of atoms, as well as their velocity and spread. As we know, these things are governed by the optical molasses and the Zeeman slower.
We can see how the loading rate of the MOT depends on the power in the optical molasses in graph 3.7. We at first see that indeed the equilibrium density is dependent on the loading rate, the higher the loading rate, the higher the peak density. The relation looks linear for our parameter range, we would expect this to continue for a large range of values, until time scales would become so short we can no longer reach equilibrium. The peak density as a function of the power in the molasses reaches saturation for powers > 80 mW. This is consistent with findings in section 2.5, for the flux in the vacuum chamber.

The effect of the Zeeman slower on the equilibrium number of atoms is shown in figure 3.8. The current in the second slower is related to the final velocity. We see that there is a definite maximum for the number of atoms at ~ 5.5 A. The number of atoms saturates at around 100 mW in the slower beam. This is an interplay between the efficiency of the slower getting worse at higher currents (loading rate $\downarrow$), but the final velocity getting lower (loading rate $\uparrow$).

These measurements are done after there has already been quite some optimization of internal and external MOT parameters, as the two play off each other. For a certain set of internal parameters there might be a different set of external parameters than for another and vice versa. So to optimize the loading rate we have first set the internal parameters to those of our choosing.

Internal Parameter Optimization

The parameters over which we have control when working with the MOT are the detuning and intensity of the light, as well as the magnetic field gradient. As mentioned above, the internal parameters optimization mainly focus on keeping the losses due to light induced collisions low. We achieve this by keeping the detuning of the MOT light far from the transition. This ensures both that there will be a smaller population of excited atoms available for collisions with (metastable) ground state atoms, as well as a larger cloud size, see section 3.3.3.

From the description of the MOT (equation 3.1) we know that for different detunings of the light there will be a different optimal magnetic field gradient to get the largest number of atoms, as the Doppler shift of the light has to be compensated

by the Zeeman shift of the magnetic field, or the other way around.
It leads then that the larger the detuning, the larger the magnetic field gradient needed to trap the maximum number of atoms. A large detuning and a large magnetic field gradient leads to an increased size of the MOT, from equation 3.15.

Detuning and Magnetic Field Gradient For characterizing the MOT we want to figure out what the best parameter set is to get the largest number of atoms. We determine this by setting the detuning to a certain value and subsequently vary the magnetic field gradient and the intensity, in that order, to obtain the largest number of atoms.
In figure 3.9 we see the results of this parameter optimization, which gradient and which intensity give us the largest number of atoms for a given detuning. We see that for smaller detunings, the atom number is highest when the intensity is not too high, since too many photons can lead not only to heating and evaporative losses, but will also increase the light-induced Penning ionization, as the Rabi frequency increases with intensity. For larger detunings, as the density and the Rabi frequency are lower, a larger intensity is tolerated before light-induced collisions limit the density.
The relationship between the optimal magnetic gradient and detuning is linear, as we expect from the collaboration of the Doppler shift and the Zeeman shift.

In figure 3.10 the maximum obtained number of atoms for a given detuning is shown, with optimized gradient and intensities. We see that the maximum number of atoms is reached at 50 MHz, but this is possibly because for larger detunings we cannot reach the intensities needed to optimize the number of atoms, as the AOM shifting the frequency of the light is no longer within its most effective range at this detuning. Of course, at some point the number of atoms should no longer increase with higher detunings, due to increasing temperatures.
In the bottom graph of figure 3.10 the size of the cloud for the same situations as the top graph is plotted. As we expected the size of the cloud goes up with larger detuning/gradient. The x- and the y-sizes of the clouds are not the same, due to a difference in the magnetic field gradient in the two directions (for definition of x and y see section 3.4)
This observation that the largest number of atoms in a metastable helium MOT occurs when the MOT is large complies with our expectations from the Penning collisions. In figure 3.11 we see that the density of the cloud has indeed a maximum and therefore a larger cloud means a larger number of atoms. As the light-induced collision rate depends on the detuning and the intensity of the light, the maximum density is different for each configuration, this is what is show in the graph in figure 3.11.

We will work from now on with the optimal gradients and intensities for a given detuning. The final MOT has 7×10^8 atoms and a measured temperature of $\sim$ 1.2 mK.

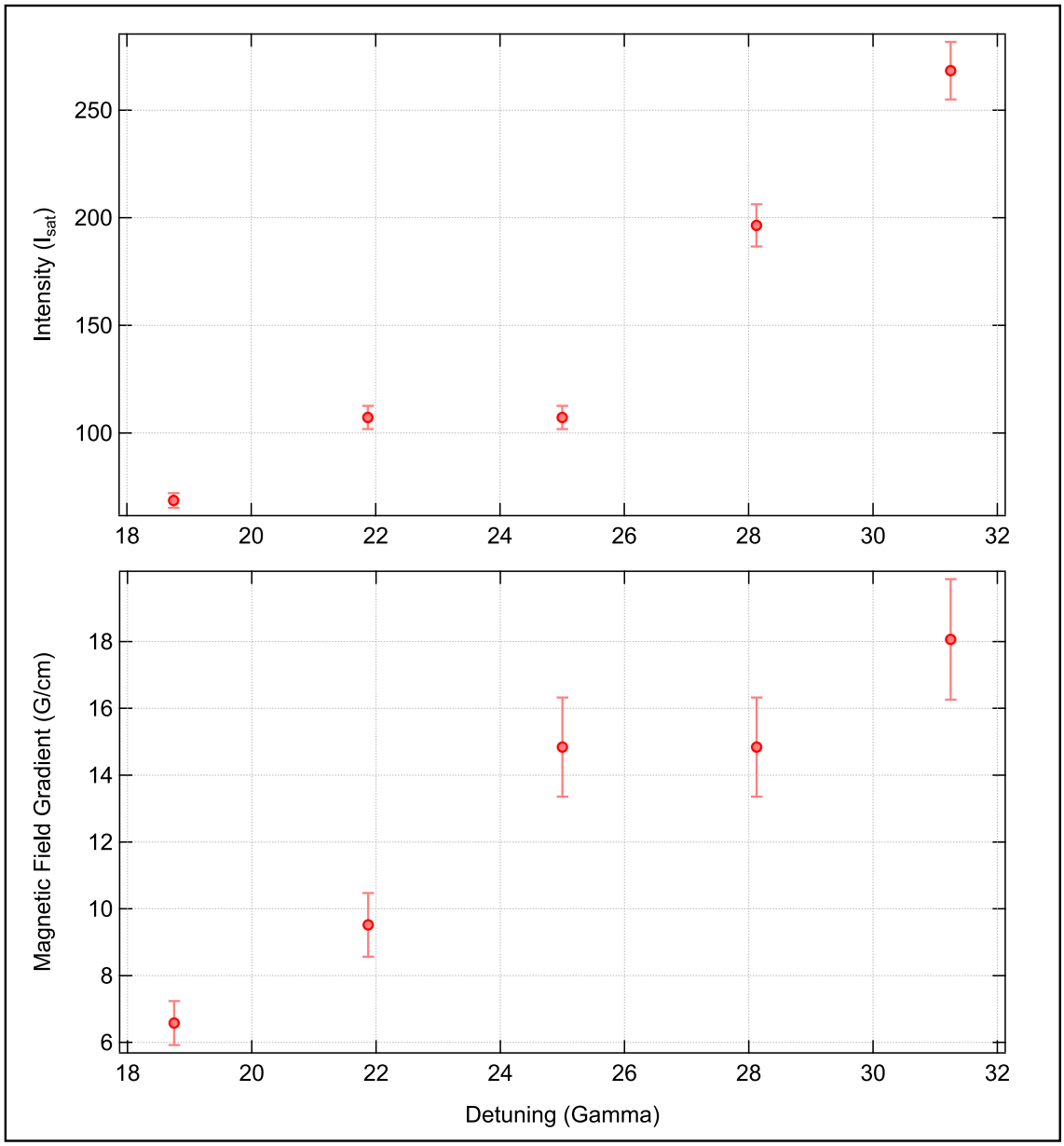

Figure 3.9: Top: The total intensity for six beams that gives the largest number of atoms in the MOT for the detuning of the MOT light. Bottom: The magnetic field gradient that gives the largest number of atoms in the MOT versus the detuning of the MOT light.

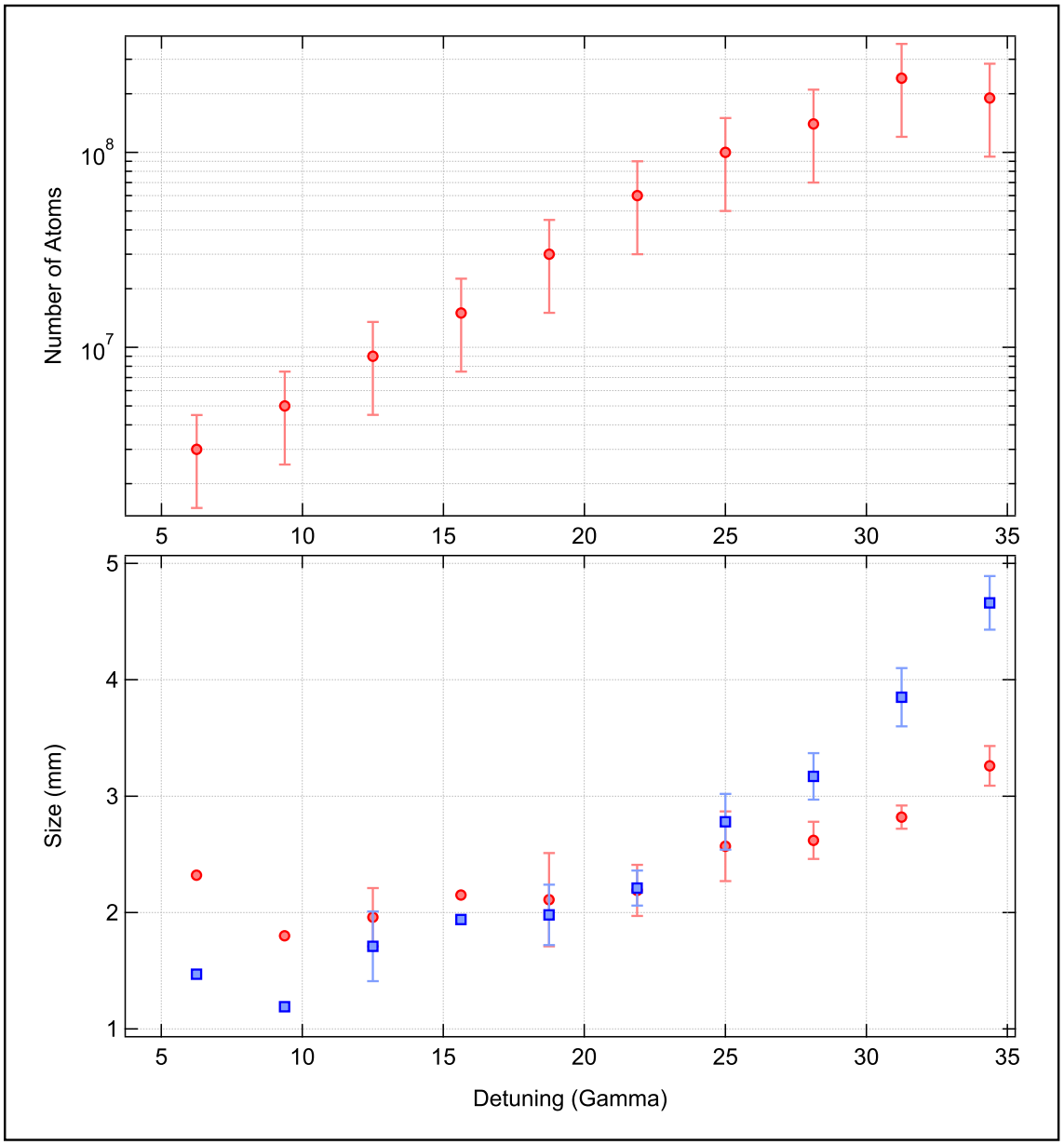

Figure 3.10: Top: The number of atoms as a function of the detuning, with for every detuning the magnetic field gradient and the intensity optimized for maximum number of atoms. Bottom: For the same situations as the top graph, the size of the MOT. Red circles: x-direction; Blue squares: y-direction.

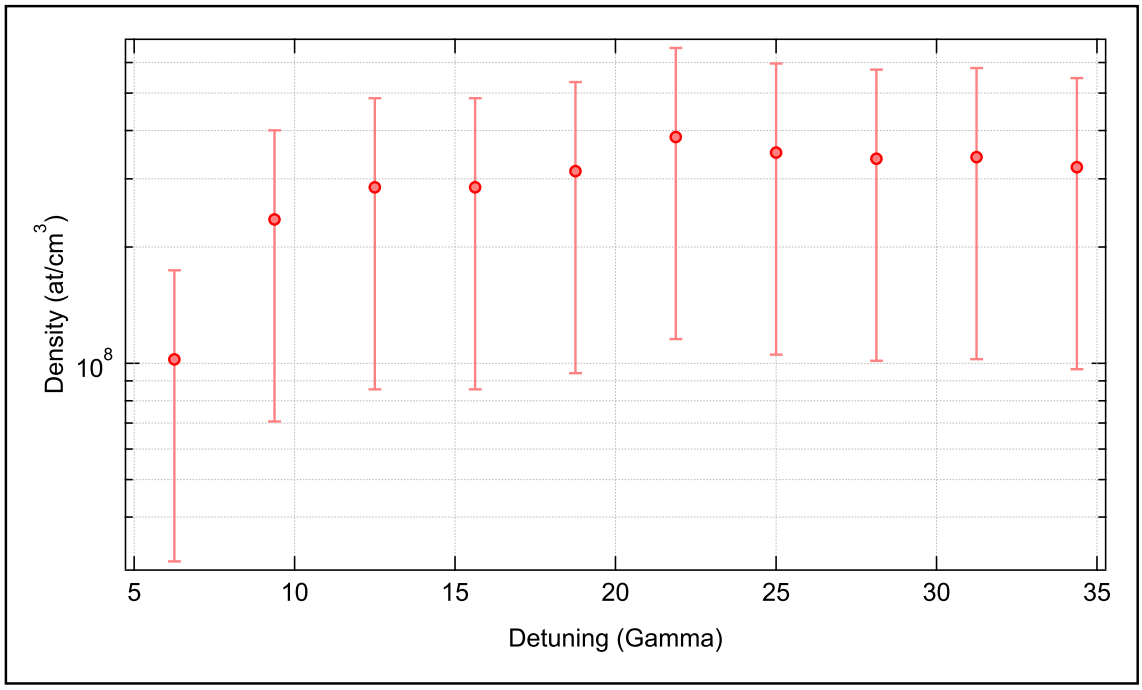

Figure 3.11: The density of the cloud of atoms trapped in the MOT as a function of the detuning. Due to light-induced collisions the density has a threshold at a certain value, depending on the detuning and intensity of the light.

3.5.2 Doppler Cooling Regime

As mentioned at the beginning of the previous section, the main objective of the magneto-optical trapping of metastable helium atoms is to get as many atoms as possible trapped. The process on how to construct a MOT, how to trap the atoms and how to optimize the trap has been described in the previous section.
The temperature of the cloud at the end of the molasses phase and in the magnetic trap will determine the efficiency of the later transfer to the optical dipole trap [125]. For a more detailed simulation of the cloud temperatures in relation to the loading, see the master thesis of R. Bodedda [115].

We know from equation 3.12 that we should be able to reach a temperature of $T_D = 38.4\ \mu$K with Doppler cooling of metastable helium at a detuning of $\Gamma/2$. While having the atoms trapped in the MOT we have measured the temperature of the cloud with time-of-flight imaging, it is shown in figure 3.12 for an intensity of $I = 100 I_{sat}$ for all six beams, compared with equation 3.11. The measured temperatures follow the two-level Doppler theory very well [120]. In systems where there is sub-Doppler cooling present, the temperature scales inversely with the detuning of the light. This is a good first indication there are no such schemes present in our system, we shall now try to conclusively prove this hypothesis.
First of all we want to verify the scaling of the MOT size with the magnetic field gradient and the detuning, as put in equation 3.15. In the top of graph 3.13 the size of the cloud as a function of the detuning is shown, along the magnetic axis

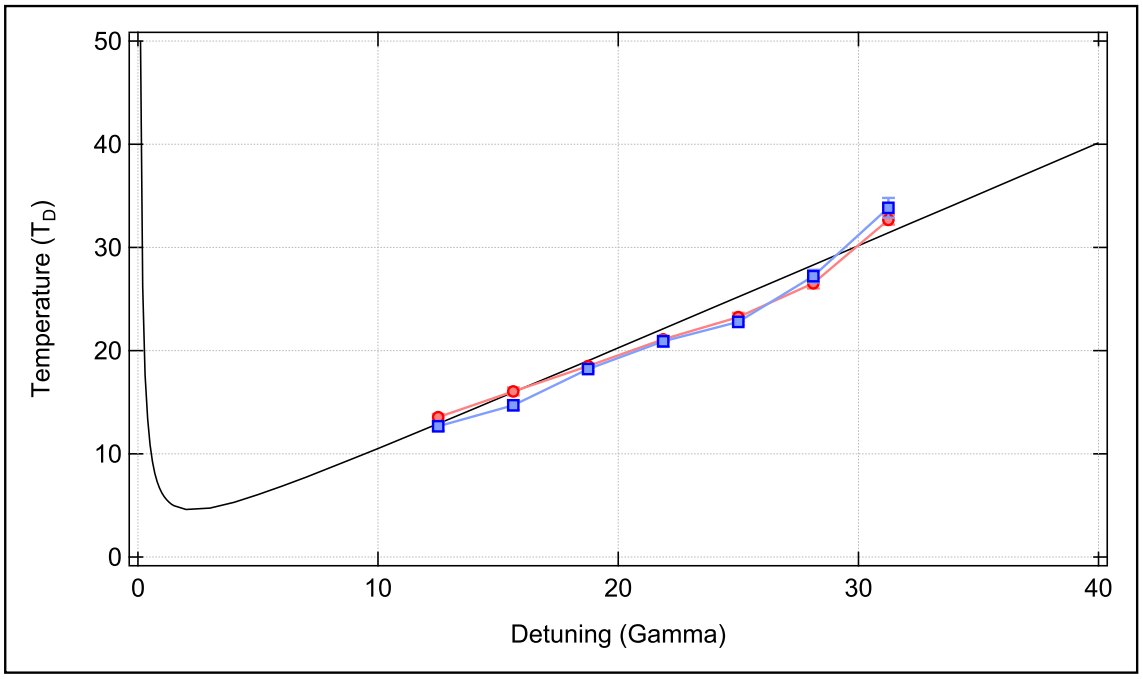

Figure 3.12: The temperature of the cloud of atoms in the MOT for different detunings of the light with $I = 4I_{sat}$ per beam. Red circles: x-direction; Blue squares: y-direction. The line is two-level Doppler theory with the used experimental parameters.

(x-direction) and the orthogonal direction (y). The measurements fall in line very well with the theory and confirm that there is no multiple scattering in our system, as its presence would increase the size and equation 3.15 would no longer be valid. To verify the scaling with the magnetic field gradient we keep the detuning of the MOT light constant at $\delta_L = 31.3 \times \Gamma$ and an intensity of $I = 100I_{sat}$ with an estimate error of 5 % in the calibration, per beam and vary the magnetic field gradient. As we see in the bottom graph of figure 3.13 the size of the MOT squares indeed as the square root of the detuning and the data matches the theory curve (with no adjustable parameters) very well, further validating the assumption we are working with a perfect two-level system. In the inset of figure 3.13 we see that the temperature stays constant as we vary the magnetic field for constant detuning and intensity of the light, also in accordance with equation 3.15.

Graph 3.12 only shows the temperatures of the MOT down to a detuning of $\delta_L = 12.5\Gamma$. Going any lower than that and we end up with a MOT that contains very little atoms. So little that we have trouble accurately doing the time of flight measurements and determining a temperature.

To test Doppler theory down to lower detunings we use a molasses phase, on the same transition and with the same laser frequency as the MOT beams. We make a MOT at the $\delta_L = 31.25\Gamma$ and after the MOT phase we switch off the magnetic coils. It takes 0.6 ms to switch off the current and eddy currents persists with half life $\tau = 5.3(1)$ ms. The intensity and detuning of the laser are ramped down to the

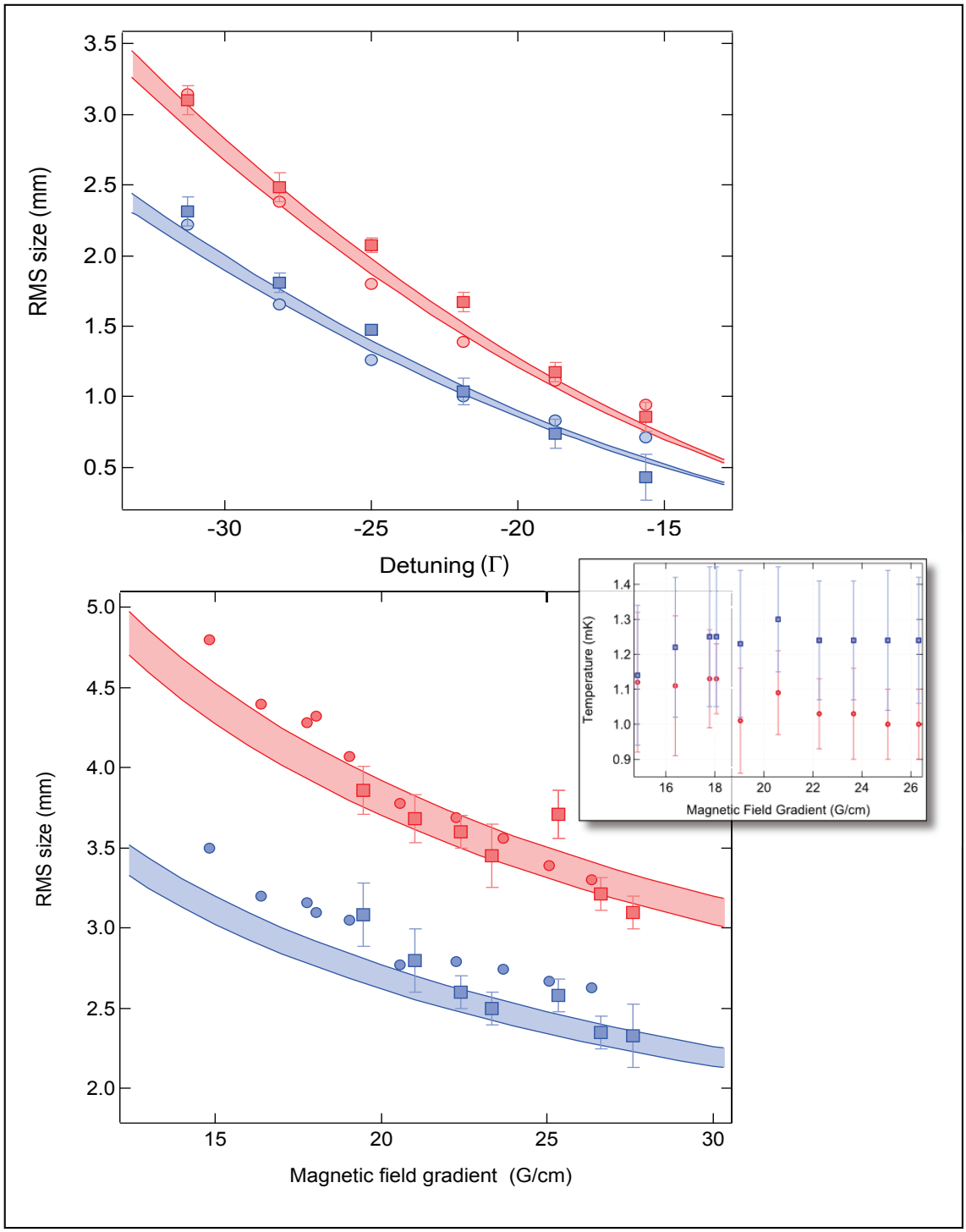

Figure 3.13: Top: The rms size of the cloud trapped in the MOT as a function of the detuning of the light. Red circles: x-direction; Blue squares: y-direction. Lines are the theory (no adjustable parameters) with an error of 5 % in the calibration of the intensity of the light. Bottom: The rms sizes of the trapped cloud as a function of the magnetic field gradient with theory curves (no adjustable parameters) from equation 3.15. Inset: Temperature of the cloud as a function of the magnetic field gradient.

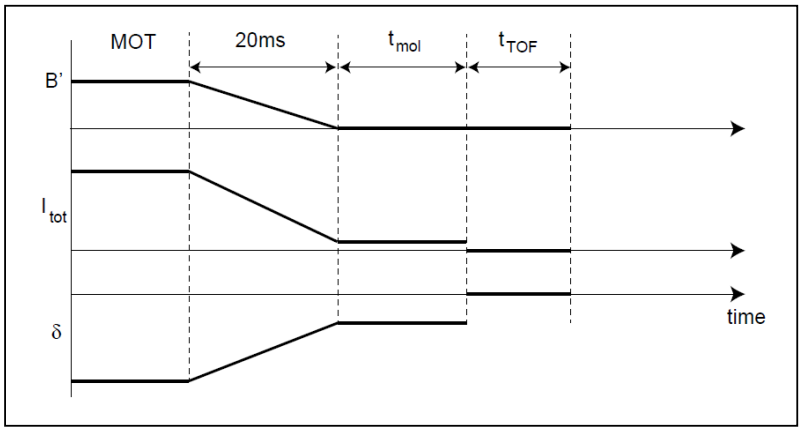

Figure 3.14: The time sequence used to obtain the temperature measurement at lower detunings. After the initial MOT stage the magnetic field gradient, intensity and detuning are ramped down to their desired values in 20 ms. The cloud is left for $t_{mol} \simeq 20$ ms to equilibrate. Afterwards we take TOF pictures to get the temperature.

molasses values within 20 ms, as we use the same beams and optics as for the MOT we have still circularly polarized light. We let the atoms equilibrate for up to 25 ms before taking temperature measurements. If we wait much longer we start to lose atoms, since the molasses are not strictly trapping the atoms, see section 3.3.2. To cool as much as possible though we want to wait as long as we can before we start to lose atoms, therefore using all the time possible.
The temperature is measured with the same time of flight methods as the MOT, see section 3.3.4. The time sequence used to do this measurement is shown in figure 3.14.
In figure 3.15 the temperature as a function of the detuning is shown for different intensities of the molasses beams. We observe a minimum temperature of $T = 1.3T_D$ at a detuning of $\delta_L = \Gamma/2$ and an intensity of $I = 0.1I_0$. The measurements follow Doppler theory for two-level systems very nicely.

We have found that the temperature of the cloud at low intensities is very dependent on the balance between the molasses beams. When the beams are not properly balanced, the temperature far exceeds the temperatures predicted by Doppler theory. The effects of the imbalances can be compensated with a properly set magnetic bias field. However since the imbalance depends on the absolute photon difference between the beams, the bias field has to be set differently for all different intensities. In figure 3.16 an example of a temperature measurement with unbalanced beams is presented. For larger intensities the measurements follow Doppler theory well, however at lower intensities there is a definitive heating.
Indeed, when the first molasses were created, researchers were surprised by the lack of instabilities, something that turned out to be a feature of sub-Doppler cooling. The presence of these instabilities in our experiment again confirms that we are truly working in a regime where there is only two-level Doppler cooling.

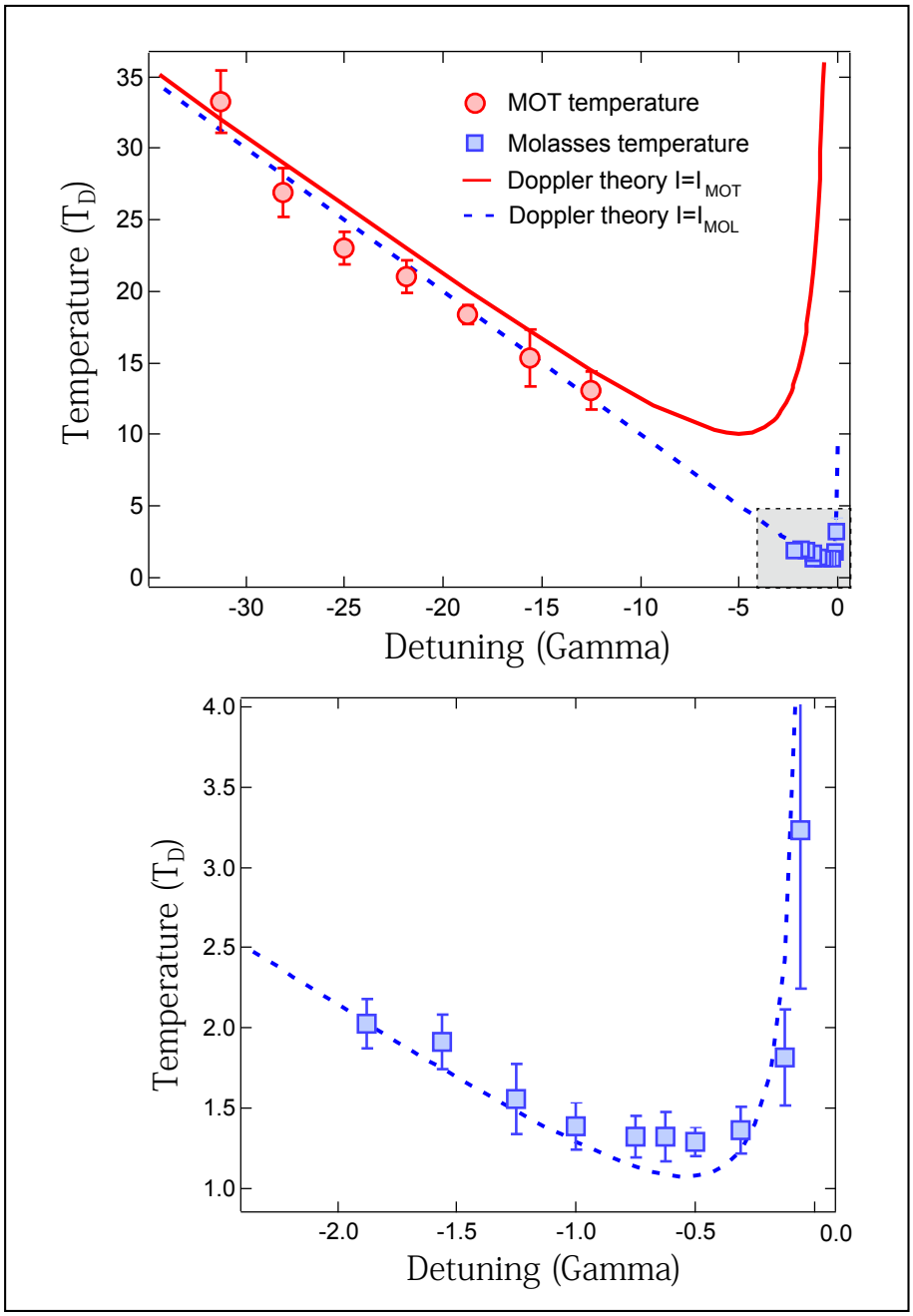

Figure 3.15: The temperature of the molasses for different intensities of the molasses beams with the comparison to two-level Doppler theory (solid lines).

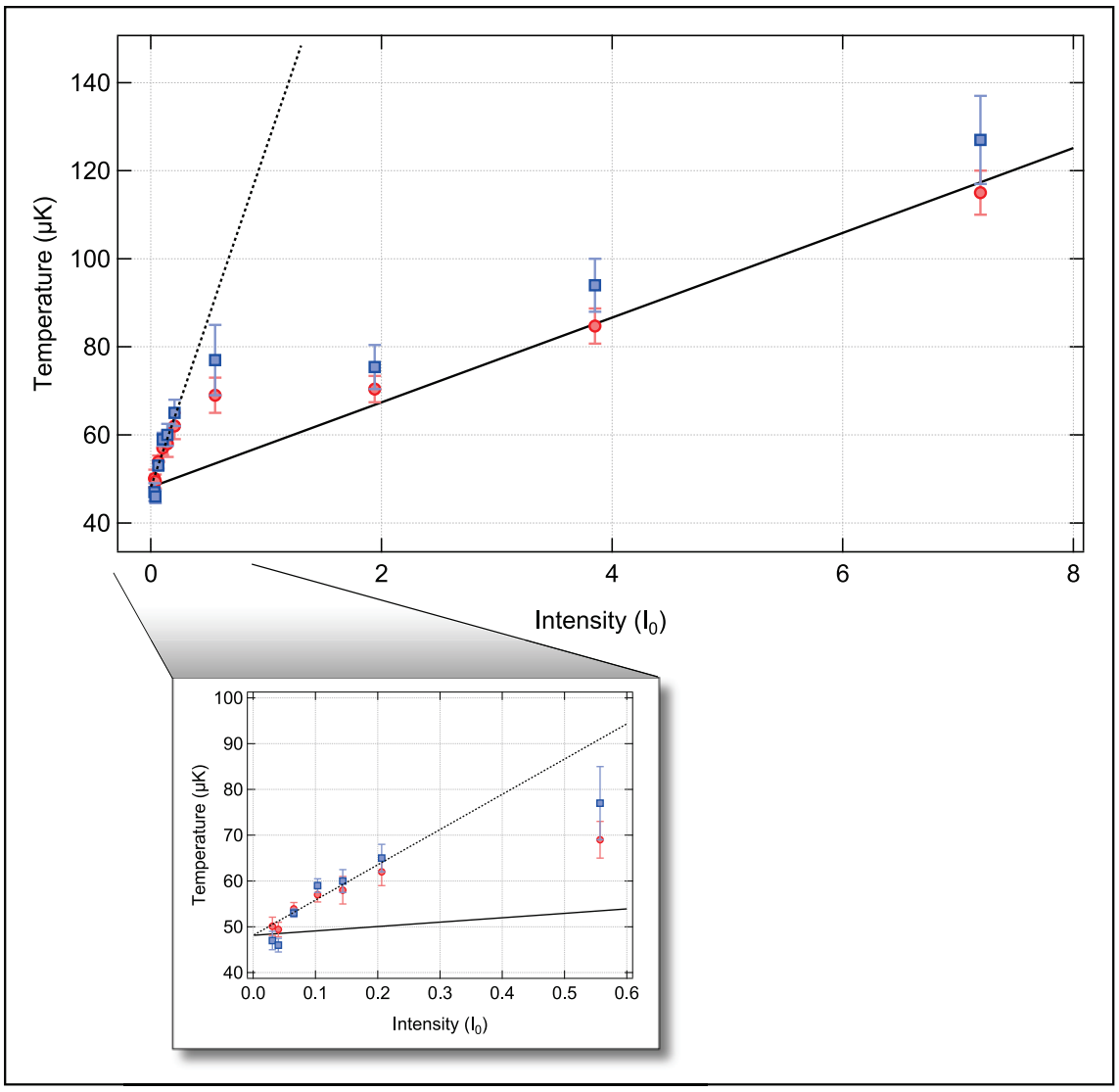

Figure 3.16: The temperature after the molasses stage for different intensities of the molasses light. This measurement is for $\delta_L = \Gamma$. The solid line is the Doppler theory for $I = I_{tot}$ and the dotted line for $I = 8I_{tot}$. Inset: Closer look at the lowest intensity measurements.

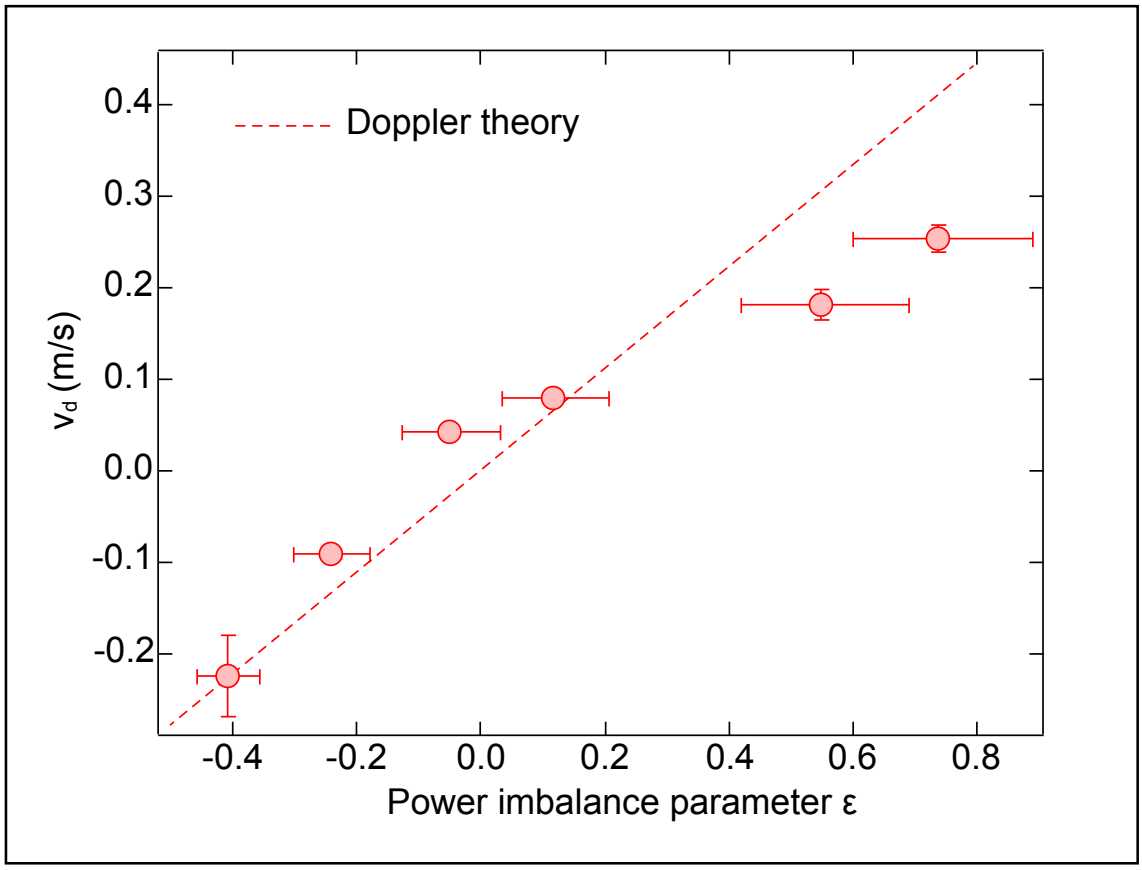

Figure 3.17: The drift velocity v_d as a function of the imbalance between two opposing molasses beams. Dashed line is the Doppler theory.

To investigate the beam intensity imbalance ϵ we evaluate the drift velocity, a quantity which can be derived from Doppler theory when one allows a imbalance between opposing beams [92]:

$$v_d = \frac{\epsilon\Gamma}{8k}\frac{1 + I_{tot}/I_{sat} + 4\delta^2/\Gamma^2}{2|\delta|\Gamma} \tag{3.26}$$

We have put artificially an imbalance between the beams and measure v_d as a function of ϵ, results are shown in figure 3.17. The drift velocity is subsequentely measured by varying the duration of the molasses t_{mol} and measuring the displacement of the cloud after a short time-of-flight of 0.1 ms.
As we see the results correspond convincingly with two-level Doppler theory. This confirms again that on the$2^3S_1 \rightarrow 2^3P_2$ cooling transition of metastable helium there are no efficient sub Doppler cooling mechanisms at work.

3.6 Conclusion

In this chapter we have explained how we were able to trap a cloud of metastable helium atoms and how we cooled them down.
We have shown how we have created a cloud of atoms trapped in a magneto-optical trap, and after optimization we have trapped 7×10^8 atoms, at a temperature of ~ 1.5 mK. This has been done by optimizing both the loading rate and by minimizing the light induced collision rate, by working at low density and relatively far detuned light. A closer study of light induced collisions will follow in the following chapter.

With our system we have been able to test the theory of two-level Doppler cooling. In most systems studied before there are either sub-Doppler mechanisms at play due to multi-level influences or there is multiple scattering of photons due to high densities of atoms.
We have found working in a molasses stage after the initial trapping stage that these mechanisms are absent and the system presents itself as a perfect playground for two-level Doppler cooling. The absence of any loss channels allows effective molasses stages and here heating due to multiple Zeeman levels will be absent as well. There is no sub-Doppler cooling due to the small relative difference between the recoil temperature and the Doppler temperature.
The molasses stage cools the atoms down to $T = 1.3T_D$ at a detuning of $\delta_L = -\Gamma/2$. We have found that the temperature of the cloud at very low intensities is very dependent on the balance between opposing beams in the molasses stage. This dependence has been tested and found to follow two-level Doppler theory and has strengthened our conclusion that there are truly no efficient sub-Doppler cooling mechanisms in our metastable helium system.

Chapter 4

Light Induced Collisions

4.1 Introduction

After having created a MOT of metastable helium and getting to know our experiment while investigating Doppler cooling, we take the time to try and shed some light on an old and slightly controversial issue that has been around since the first metastable helium cooling experiments.

In ultra cold atomic gases there is a loss of atoms from a trap associated with the population of the excited state as in many cases the low temperatures surpress collisions between ground state atoms [126]. Ever since the first trapped atomic gasses this loss rate has been the subject of theoretical [127, 128, 129] and experimental investigation. The loss rate has been measured in many different species of atoms, ones that can be trapped in their groundstate such as for example sodium [130, 131], cesium [132, 133], rubidium [134, 135, 136], litium [138, 139], potassium [137] or even mixtures [140].
For species that are trapped in their metastable state (such as helium), light induced collisions give rise to Penning ionization of one of the colliding atoms and a decay into the ground state for the other atom, as the internal energy of the metastable state is large enough. Loss rates are subsequently larger than in non-metastable ultra cold gases and their investigations are of great practical interest, since the loss rates determine experimental condition.
The ionization rates have been studied again for a wide range of species, not in the least helium [75, 141, 142, 143, 144] as in this thesis, but also for example krypton [145], neon [146], argon [147] and xenon [148].

These loss rates are dependent on the density of the gas, the intensity and the frequency of the light. In this chapter our attempt to contribute to the discussion started 15 years ago will be described. Not all the measurements performed at that time have reported the same outcome and at the same time they did not have access to the possibilities that come from the use of the efficient InGaAs camera that we do. It will be interesting to see if we can illuminate the issue.

4.2 Description

4.2.1 Penning Ionization

The process in which a collision between two particles results in the creation of one positive ion has been briefly discussed in section 3.3.3. In 1927 F. M. Penning described for the first time the process [149], saying that if atom A^* has an internal energy (denoted by the *) higher than the ionization potential of atom B, ionization can occur when they collide in the following ways:

$$A^* + B \Rightarrow A + B^+ + e^- \tag{4.1}$$
$$A^* + B \Rightarrow AB^+ + e^- \tag{4.2}$$

The first reaction is commonly know as Penning ionization whereas the second reaction is usually referred to as *associative ionization*. Both of the processes result in a loss of both initial atoms to the trap. With metastable atoms, the internal energy of the two particles is by itself enough for the processes described above. The processes are not limited to metastable atoms however.
In the case of metastable helium in a MOT, one is in a regime where there is only s-wave scattering, as collisional energies in a MOT are around 100 neV (at $T_{MOT} = 1$ mK $kT = 86$ neV) , whereas the limit for the s-wave regime is 10 μeV, the centrifugal barrier $l(l+1)\hbar^2/m_r r^2$ for $l = 1$ angular momentum, see for example [150] or [151]. Because of this two particles both in the metastable ground state 2^3S have only a very small probability to collide. However, if one of the two is excited by a photon to the 2^3P state, there is no rotational barrier anymore and there is nothing preventing a collision between the metastable atoms, and subsequent ionization and loss from the trap.
Therefore, when we talk about Penning ionization with metastable helium, the collisions are light-induced.
In figure 4.1 a simplified model for light induced collisions of two metastable helium atoms is shown [152]. The full picture is a bit more complex, as for inter-atomic distances smaller than $R_\lambda = \lambda/2\pi$ the excitation has the character of a molecular excitation (SS to SP), as opposed to a single particle excitation at larger distances. For a full theoretical description of the optical collisions, see the Julienne-Vigue generalization of the Gallagher-Pritchard model [127, 128, 129, 153, 154].

In the most simplest terms, the rate of light induced collisions is dependent on the fraction of the atoms that are in the excited state. The loss rate due to light induced ionization is called β and we can write this as [155, 144]:

$$\beta = K_{ss}\pi_s\pi_s + 2K_{sp}\pi_s\pi_p + K_{pp}\pi_p\pi_p \tag{4.3}$$

In this equation, the terms K_{ss},K_{sp} and K_{pp} are the constant rate coefficients, and π_p and respectively π_s the populations of the p and s state. From experiments [141, 75] and theory [142, 156, 157] we know that K_{sp} is several orders of magnitude larger than its counterparts, K_{pp} and K_{ss}.

As we see, the chance of a particle being ionized by a light induced collision is

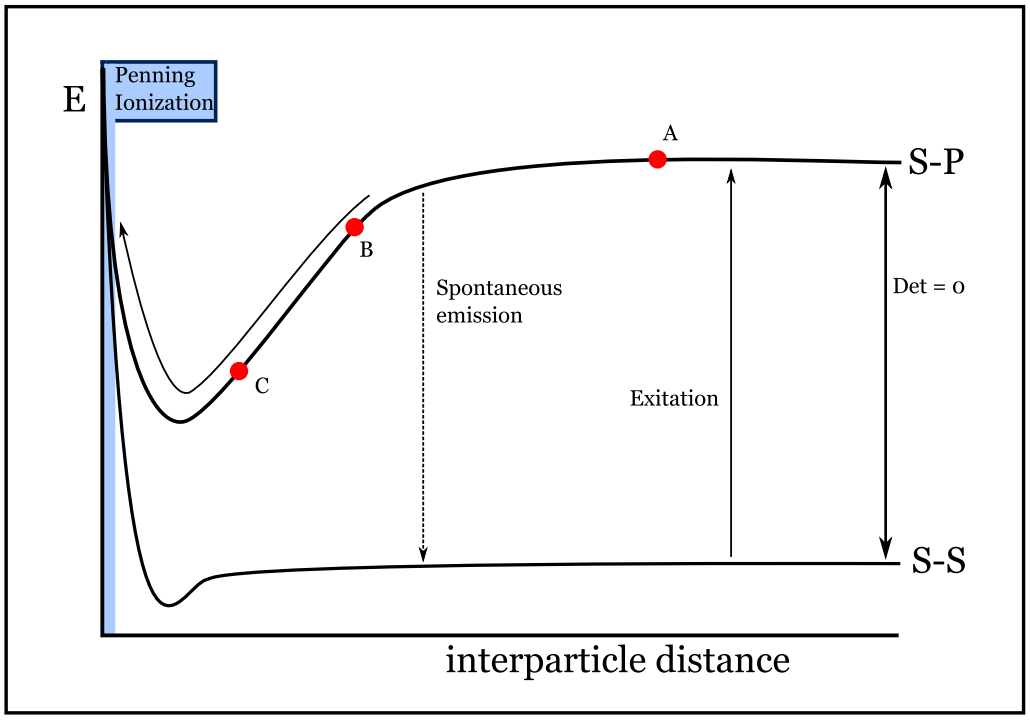

Figure 4.1: Basic explanation of trap losses due to light assisted collisions. One of the (metastable) ground state atoms gets excited into the higher state. The energy difference depends on the inter particle distance, so one can choose the place of excitation by changing the frequency of the light. If the atoms get close enough together, as shown in the gray zone named 'Penning Ionization', they can ionize and will not be trapped anymore. The atom has a chance to fall back into the ground state by spontaneous emission before reaching this distance (dotted arrow) if it is exited too far from the other atom (spot A). If the atom gets excited to close to the next one, it will not have enough energy to overcome the repulsion barrier (spot C). Only by balancing these two effects (for example spot B), atoms will get ionized.

dependent on the frequency of the light, as the population of the excited state is dependent on it. Furthermore, by changing this frequency one can tune at which inter-atomic distance one excites the atom into the 2^3P state. The chance of ionization is dependent on this distance. If the atom is excited too far away (Spot A in figure 4.1), it will fall back into the metastable ground state through spontaneous emission before it can interact with another atom. If the atom is excited too close to the other atom (Spot C in figure 4.1) there will not be enough energy to ionize the atoms. In between those two spots (for example spot B in figure 4.1), ionization will be possible, and there will be a probability distribution depending on inter atomic distance, or in other words, on the frequency of the photons.

From this simple model, we expect a peaked distribution dependance on the frequency of the light. Exactly at which frequency the peak should occur is difficult to say, to calculate this one would need a very detailed atomic potential, which is difficult at short distances due to the molecular character of the excitation.
Previous experiments have reached differing conclusions on whether the the peak exists or not [141, 143, 144].
The losses are also expected to depend linearly on the intensity of the light at low intensities, and to saturate as the transition saturates at higher intensities $I > I_{sat}$.

4.2.2 Light Induced Collisions in a MOT of Metastable Helium

These light induced losses are a problem for those working with He* or other metastable ultra cold atoms. The loss of atoms due to Penning collisions is much larger than the light induced losses in alkali gases and in the case of metastables, the density of a MOT is limited by these losses. Knowledge of these interactions, like the rate at which the collisions occur and how this depends on the frequency and intensity of the light can be very useful.

From equation 4.2 we know that the losses from the trap due to light induced collisions are dependent on the density, as you need two metastable atoms to ionize one of them, while the other decays into the ground state and both are lost from the trap. The rate equation is as follows:

$$\frac{dn}{dt} = R - \frac{n}{\tau} - \beta n^2 \tag{4.4}$$

With R the loading rate of the trap, τ the lifetime of the gas due to collisions with the background atoms present in the vacuum.
In a situation where the loading of the trap has been switched of the peak density of the cloud evolves as [155]:

$$n_0(t) = \frac{n_0(0)}{\left(1 + \frac{\beta n_0(0)\tau}{2\sqrt{2}}\right) e^{t/\tau} - \frac{\beta n_0(0)\tau}{2\sqrt{2}}} \tag{4.5}$$

The lifetime τ can be measured independently in the magnetic trap where there are no light-induced losses. We find a value of 11 s for τ and will use this as a fixed

parameter in the fitting process.

In the experiments done in the late eighties and early nineties, the loss rate β was measured by either measuring the ions lost from the trap [141, 142], or measuring the absorption by [75] or the fluorescence of [143] the trapped atoms with a photo diode. The rate of ion production is indeed also dependent on the density of the gas, when detecting the decay in a trap in that way it is therefore also described by equation 4.5.
However, the latter two methods do not monitor the density, in fact by measuring the fluorescence they are monitoring the number of atoms in the trap. They make up for this by substituting in the rate equation n_0 by N/V_{eff}, with V_{eff} an independent measurement of the volume of the cloud, usually done with a CCD camera. Following this the volume is assumed to stay constant during the process, or the change to be so minimal that it does not influence the fit of β [143].

We propose to get an accurate determination of β by switching off the loading and monitoring the subsequent decay of the density with the InGaAs camera (described in appendix B), which can be tested on the above model.

4.3 The Experiment

4.3.1 Decay Experiments

The study of the light induced collisions begins with loading the MOT of metastable helium as described in the previous two chapters. We allow the trap to load for 2 s and after that we switch off the transverse optical molasses that collimate the atomic beam, the Zeeman beam that slows it and place a mechanical shutter in the way of the atomic beam itself. The shutter is closed to reduce the pressure in the science chamber, prolonging the lifetime of the trapped gas, which we have measured to be $\tau = 11$ s.
The light induced ionization creates losses dependent on the population of the excited state and the density of the atoms. When we stop the loading in the trap, this means that the trap depletes faster than the exponential loss from collisions with the background. After a certain time, of the order of $t \sim 1/\beta n_0$ (this only holds if τ is significantly longer than this time t), the density will decrease to the point where the losses from the light induced collisions become much smaller than the losses due to the background, and we therefore expect that at longer times the losses in the MOT go back to being just exponential. The exact value of τ determines when the regime changes from one to the other.
The frequency of the MOT light is varied, but the magnetic field gradient is kept constant throughout the experiment at 9.4 G/cm. In the same regard the intensity of the MOT light is kept at $I/I_{sat} > 100$. We expect β to vary with the frequency and the intensity. Since we do a separate measurement of π_p which takes into account the changes in intensity and frequency, K_{sp} should be independent of them.
The fact that we load the MOTs in different situations (with different frequency of the light) means that there will be a different number of equilibrium atoms for each detuning. As the fitting of n_0 to find β takes this into account, we do not think this is an issue.

Besides looking at the decay rate, one can also look at the loading rate, which will also exhibit behavior related to the light induced collisions, which are dependent on the increasing density in this case. We are loading the trap so fast that it is difficult to extract quantitative and precise information about the losses. We could artificially lower the loading rate in several ways, such as purposfully misaligning the Zeeman slower or the transverse optical molasses, however we choose to not explore option unless forced to.

The equilibrium number of atoms and density is also dependent of β, and one could determine the loss rate in this way, if all the other parameters were kept the same. However, as soon as we change the frequency of the light, the conditions of the MOT change and the equilibrium number of atoms is different and not just because β has changed.
A way around this problem has been proposed [158], where one uses always the same conditions to load the MOT, but by the use of an extra, very low intensity laser, whose detuning is a variable, one can increase or decrease the losses and from this get β. This measurement can be done with the equilibrium number of atoms, but

also with looking at the decay of the trapped cloud.
We have briefly tried to use this method, but we have found that even at the lowest possible intensities where we can see an effect on β, the catalysis laser has an influence on the atoms in the MOT. A MOT with the light at a detuning of 50 MHz with the catalysis laser at a fraction of the intensity but with a detuning of 5 MHz will exhibit a sort of double structure in its shape, effectively making the cloud trapped in two MOTs at the same time, with the same magnetic field gradient but with two different lasers at different detunings. An observation that is related to the dependence of the MOT size to the detuning, see equation 3.15 and the consequent results shown in chapter 3.
This effect was not reported in the rubidium experiments, we suspect it is different for helium due to the absence of sub Doppler effects and multiple scattering, which cause the strong change in size with the detuning. Because of these issues we were not able to use the catalysis laser method and we have chosen instead to accept the different starting conditions we get from loading the atoms in a MOT with different detuned light every time. Given that our fitting of n_0 accounts for those starting conditions, we expect to obtain an accurate reading of the light induced collision loss rate β.

Experimental Sequence

We monitor the cloud in situ with the InGaAs camera, taking a picture with an exposure time of 20 ms of the atoms, one picture every 50 ms. The exposure time is necessarily this long to make sure we collect enough photons and have a decent signal-to-noise ratio. The time between pictures is limited by the data transfer trough USB from the camera to the computer.

The 2D pictures are collected for a little over 6 s, after which for all but the largest frequencies the number of atoms has reduced to below what we can detect with the camera. We blow the atoms away with an on-resonance pulse of light and take a background picture devoid of atoms. The pictures are being sent to the computer in real time, after which they are fitted with a two-dimensional Gaussian with MatLab. In figure 4.2 a typical loss curve is shown, for a situation where β is relatively large (at 5 MHz detuning), and one where it is relatively small (at 40 MHz detuning). The influence of the light induced losses is clear from the faster than exponential decay at the start of the curve. When the light induced losses are mostly absent, the curve is predominantly exponential. Only data points for which the signal-to-noise ratio is larger than 1.8, a number chosen by eye as a good cutoff below which the fitting program is unable to make a fit, are shown.
We take these curves for different detunings of the MOT light, while the magnetic field gradient the same, to keep the same situation for all measurements. The intensity of the light is slightly different for each detuning, as the AOM will have different efficiencies for different frequencies, but the differences will be minimal. However minimal, they might be of influence on the measurement of β, but the different intensities for different detunings will be incorporated into the measurement of π_p and will therefore be accounted for when determening K_{sp}.

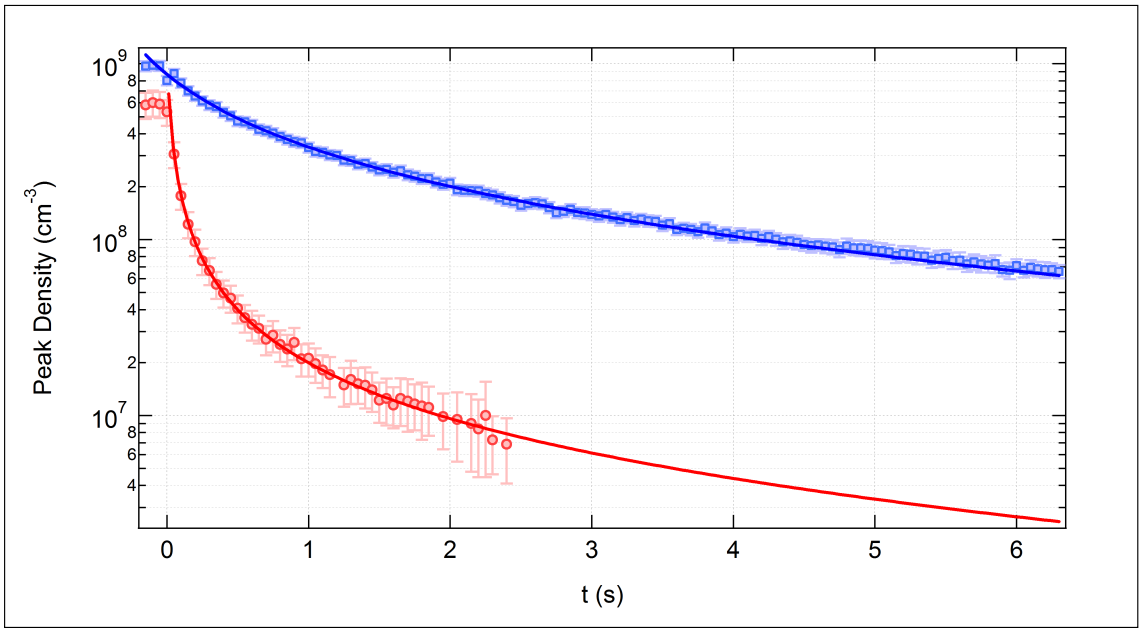

Figure 4.2: Decay curves for the peak density of metastable helium in a MOT. For a detuning of 40 MHz (blue squares) and 4 MHz (red circles). Even though the starting densities are comparable, the decay at the smaller detuning is much faster due to light induced collisions.

Curves like 4.2 are taken for detunings of the laser light ranging from 4 MHz to 40 MHz.

4.3.2 The constant loss coefficient

When fitting the density to obtain β we get a different value depending on the experimental parameters, like the detuning and the intensity of the light. The value of K_{sp} should be independent of these. To obtain K_{sp} from β we need to have acces to the population of the excited state π_p, as from equation 4.3.

We determine π_p by measuring the fluorescence emitted by the MOT and comparing it to a situation in which we are sure that the transition is fully saturated and $\pi_p = 0.5$, as seen in reference [144].
To get these numbers, we take 5 pictures of the fluoresence of the MOT in situ, and after a time of flight of 1.5 ms (a small enough time so we are absolutely sure all the atoms are still present, but we are also sure the magnetic field is turned off) we illuminate the expanded cloud with a powerfull, on-resonance pulse, of which we are sure that it saturates the transition. The ratio of the fluorescence per time unit for the two situations gives us π_p:

$$\frac{F_{MOT}}{F_{Sat}} = 2\pi_p \tag{4.6}$$

With F_{MOT} the fluorescence of the MOT in situ and F_{Sat} the fluorescence where we saturate the transition.

From the scattering rate equation we also know that in theory:

$$\frac{F_{Sat}}{F_{MOT}} = \frac{C_2}{C_1} + \frac{1 + 4\frac{\delta^2}{\Gamma^2}}{C_1}\frac{I_{Sat}}{I} \tag{4.7}$$

Where we assume the phenomenological coefficients to be $C_1 = C_2 = 1$ for now. Note that as long as $I >> I_{Sat}$, π_p is not very dependent on the precise value of I.

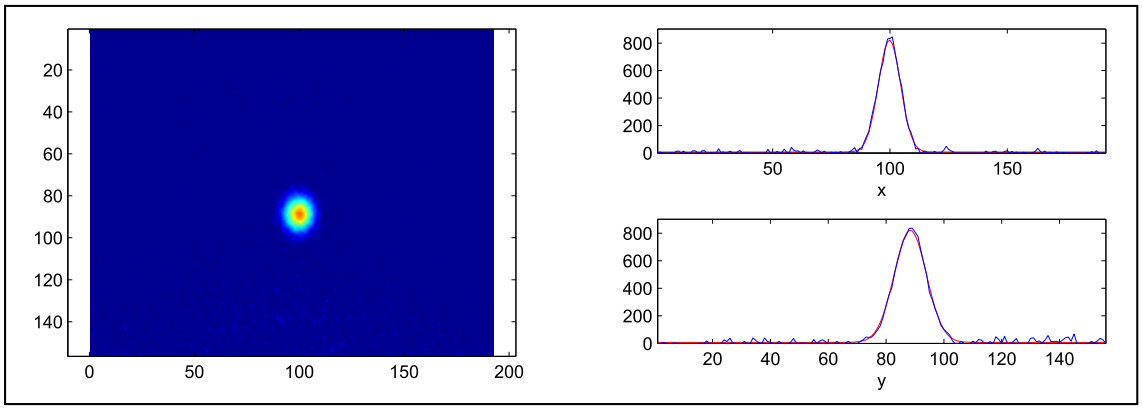

Figure 4.3: Left: A typical 2D picture of a MOT after just switching off the loading of the trap. Right: The intersections at the middle of the peak for both directions, shown is the data and the gaussian fit. This picture is of the data set for the detuning of 20 MHz.

4.4 Results

4.4.1 The Loss Rate

We know that we obtain curves like the decay curves shown previously in figure 4.2 by looking at 2D pictures taken by the InGaAs camera. In figure 4.3 such a 2D picture is shown. A shot like this has an exposure time of 20 ms, and there is a picture taken every 50 ms until there is nothing left to see on the camera.
From pictures like this we fit a two dimensional gaussian and we obtain the total number of atoms present in the trap, as well as the volume of the cloud. The size in the direction in which we integrate is assumend to be the same as the y-direction in figure 4.3. As we have seen in chapter 3 the size of the cloud is determined by the magnetic field gradient, which is symmetric around the coil axis.

To be able to compare our results to older experiments we not only find β by monitoring the density as given in equation 4.5, but we also look at the total number of atoms only. We do this by taking from the 2D Gaussian fit the total fluorescence and assuming constant volume during the decay. In this way we can compare the two methods.

Comparing the two methods

In figure 4.4 the result for the fits of β is shown. Firstly, we see that there is indeed a distribution dependent on the frequency of the MOT light. For the lower frequencies the loss rate is much higher than for large frequencies and the loss rate does not drop significantly during the lowest detunings ($4-6$ MHz), which is consistent with the model. Putting aside the behaviour as a function of the detuning, there is a noticeable difference between the fitting method we have used, and the older usage of the total number of atoms.

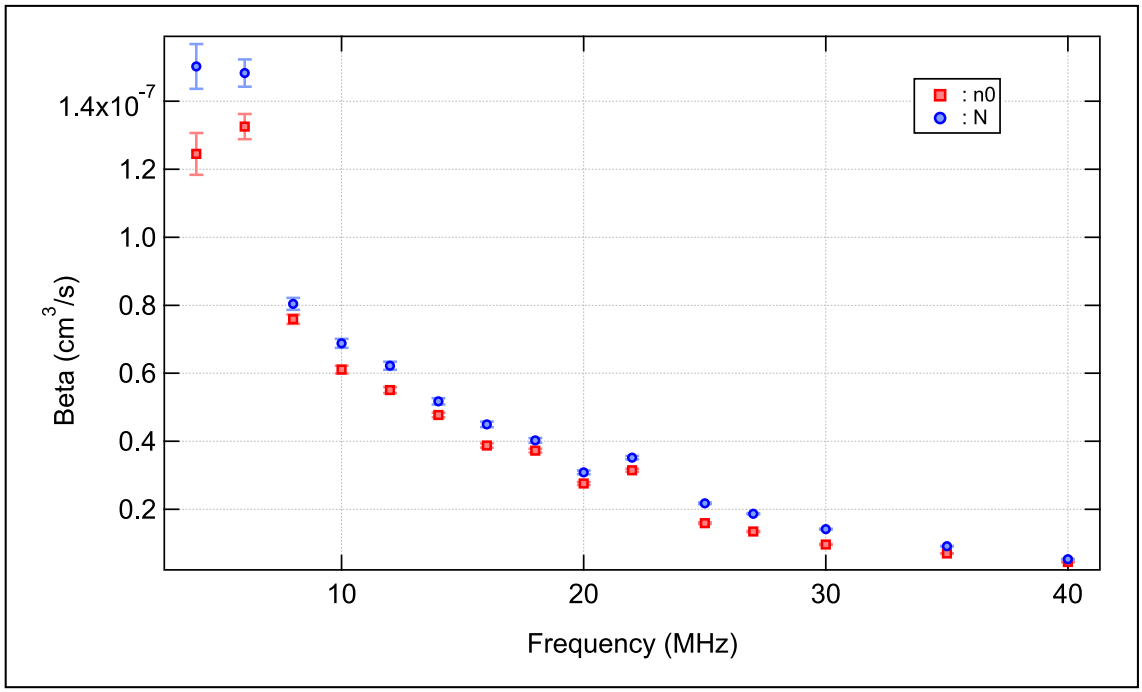

Figure 4.4: The loss rate β as a function of the detuning of the MOT light. The data has been fitted both on the total number of atoms N (blue circles) and the peak density n_0 (red squares).

The difference between using the density and using the total number of atoms needs to be investigated. The model calls for the use of the former over the latter but let us look whether this is true. For this we test the goodness of the fits of the two. To find the goodness of the fit we evaluate the χ^2 which is defined as:

$$\chi^2 = \sum \left(\frac{y - y_i}{\sigma_i} \right)^2 \tag{4.8}$$

With y the fitted value for the data point y_i and σ_i the corresponding standard deviation. The smaller χ^2, the better the fit fits to the data. Since we are fitting sets of data taken in one run, the points are correlated, and it is not possible to obtain the reduced χ^2 and to give a quantitative meaning to the value of χ^2.
In figure 4.5 the χ^2 for the fits with N and n_0 are shown. To be able to compare the two, the graph is in logarithmic scale. The goodness of the fits using the density n_0 is an order of magnitude larger than the χ^2 of the fits with the number of atoms N. When $\delta \to \infty$ the results converge. This shows us that clearly the change in volume is necessary to take into account when fitting β.
Now we know that fitting the density decay rather that the decay of the total number of atoms fits better to the model, we shall have a closer look at the evolution of the volume during the decay process. To find the loss rate from the total number of atoms, it has sofar been assumed that the volume stays constant. Since we see that this assumption leads to a mismatch with the model, let us investigate the volume.

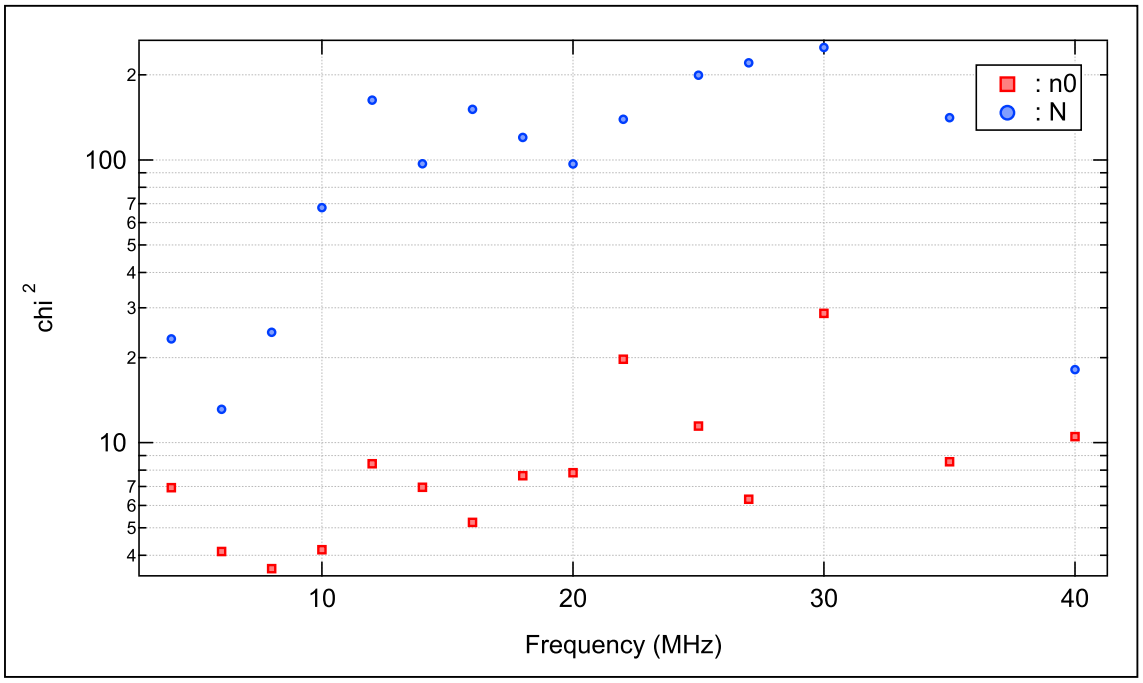

Figure 4.5: The goodness of the fits for the number of atoms N (blue circles) and the mean density n_0 (red squares) for the datasets corresponding to the given detuning of the MOT light.

4.4.2 Volume

The difference between our measurements and previously done experiments lie in the opportunities that the new InGaAs camera provides. We can monitor the 2D profile of the cloud while the loading is switched off and the trap is decaying. In earlier experiments it has been assumed that during the decay the volume of the trap does not change, but no one has been able to confirm or discredit this. This assumption is under investigation in this section.
At the start we give a quick report on an interesting feature we have found involving the Zeeman light. This is of no influence on the fitting of β, we look at the change of volume due to the loss of atoms afterwards.

Influence of the Zeeman beam

We start to monitor the volume of the cloud after we switch off the loading of the trap. As mentioned before, we stop the loading by switching off the Zeeman beam and we physically stop the atomic beam by closing a mechanical shutter. The optical molasses are also switched off, making sure that no atoms at all will be captured by the MOT.

The first thing that we noticed when monitoring the volume during the decay is that there is a huge drop in volume as soon as the Zeeman light is switched off. In figure 4.6 an example is shown, but the effect is present and of equal proportion in all

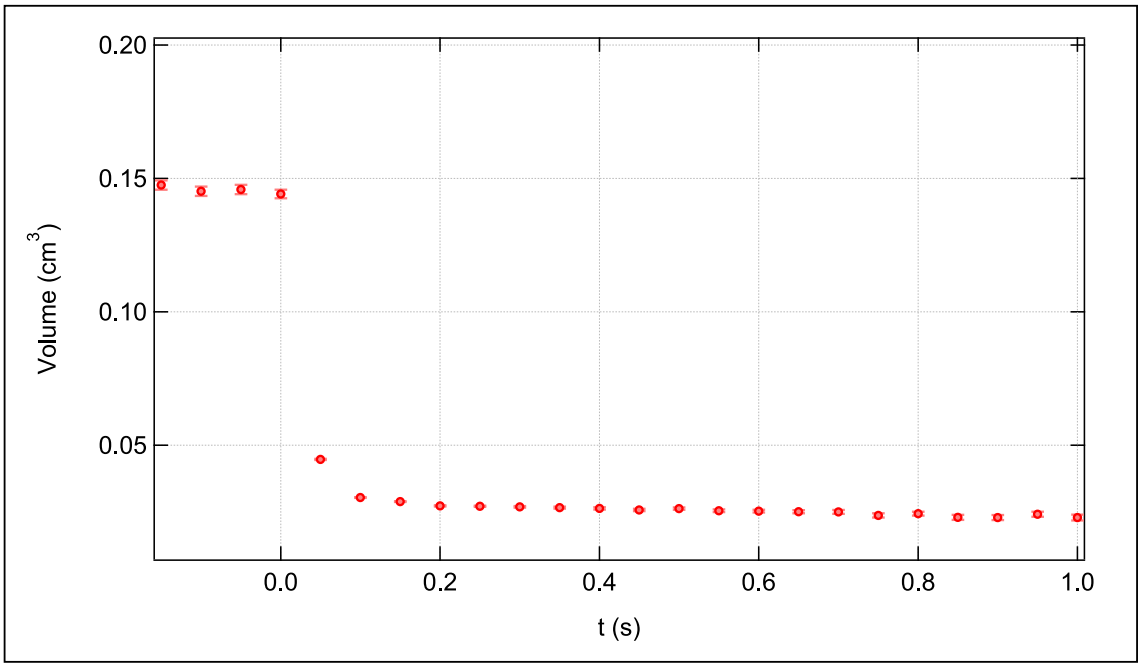

Figure 4.6: The volume change of the trapped cloud during the switching off of the Zeeman light. The Zeeman light is switched off at $t = 0$ s. This curve is for a detuning of 27 MHz, but is characteristic for all detunings.

experimental circumstances, not depending on the rate of light induced ionization losses. We think this effect comes from the light shift introduced by the Zeeman beam, the shift is of the order of 0.16 MHz. There is around 100 mW of power in the beam, and even though it is far off resonance (350 MHz), it clearly has a big influence. Multiple scattering that could be responsible for extra radiation pressure is of the order of ~ 4 kHz.

When operating the MOT, this increase of volume due to the Zeeman beam is in fact a welcome addition. As it does not affect the number of trapped atoms as far as we can tell, since it is too far off-resonance to incite a relevant rate of light induced ionization losses, but it does artificially decrease the density. This decreased density means that the light induced losses from the MOT light will be lower, and we will have a larger number of atoms in equilibrium in the trap.

For determining the decay rate, we make sure to not take into account this decrease in volume as it has nothing to do with the light induced losses. The fitting is started at the first data point where we know that the volume decrease due to the switching off of the Zeeman beam has finished.

Change of volume due to loss of atoms

Since the focus of our investigation is our ability to monitor the volume of the decaying cloud in situ, let us have a look at how the volume behaves during this time. It

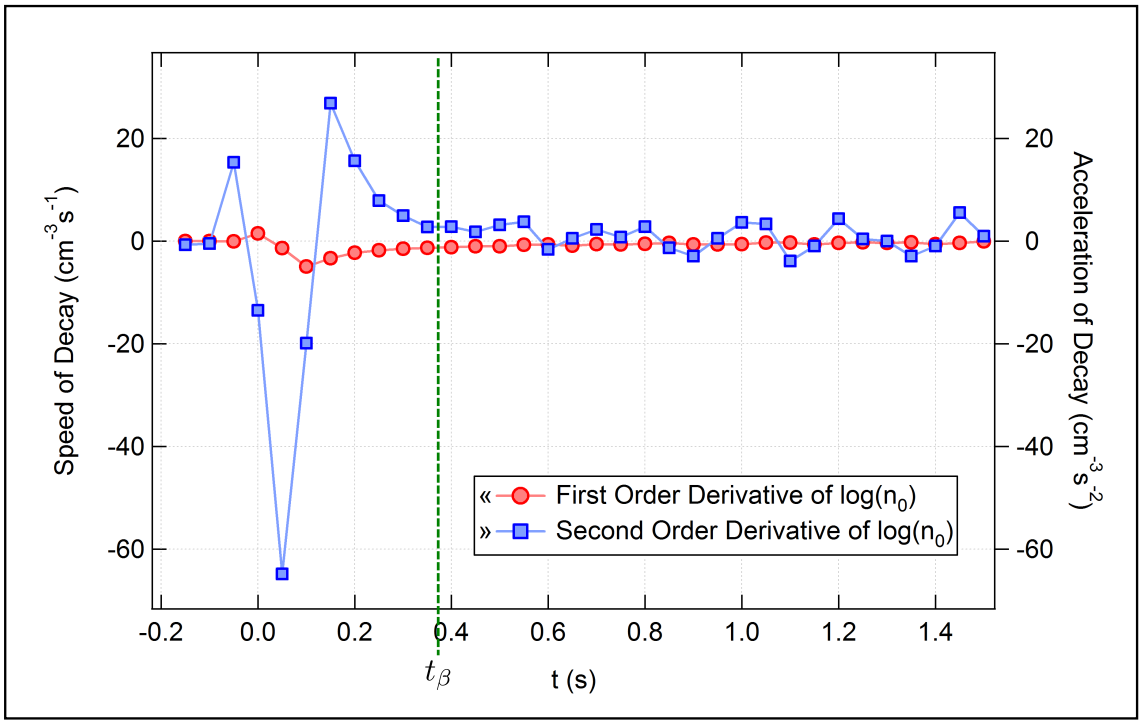

Figure 4.7: The first order (red circles) and second order (blue squares) derivatives of $\log n_0$. This specific data set it from $\delta_L = 20$ MHz. We take t_β when $\frac{d^2}{dt^2} \log n_0(t)$ approaches zero.

has previously been assumed [143, 155, 144] that the volume stays constant during the decay.

To adequately judge the change in volume the decay curve is separated in a part where the influence of the light induced losses is largest, and the flat tail, where the losses are dominated by collisions with the background.
To separate these two regimes, we take the second order derivative of the logarithm of the decay curves. The decay first speeds up when we shut off the loading, and slows down again when the density starts dropping. We take as a cutoff between the two regimes the point where the second order derivative stops decreasing fast and goes into the exponential tail associated with τ and $\frac{d^2}{dt^2} \log n_0(t) = 0$. We can see the first and second order derivative in figure 4.7.
We call this point in time t_β, and in practice it is between 0.4 s for low detunings and up to 1 s for the largest detunings. Since our data is taken in intervals of 50 ms, our resolution for determining t_β is not great. The distribution of t_β is shown in figure 4.8. There is an increase in t_β that coincides with the increase of the initial density which increases the losses, see the inset of the figure. The subsequent decline is associated with the decline of β that reduces again the light induced losses.
Figure 4.9 shows how much the volume changes in the time from the stop of the loading and t_β and from t_β until the end of the measurement. The change in volume is given as a relative change per time unit, so they can be compared. It is clear that the during the time before t_β the relative change in volume is larger than after. For

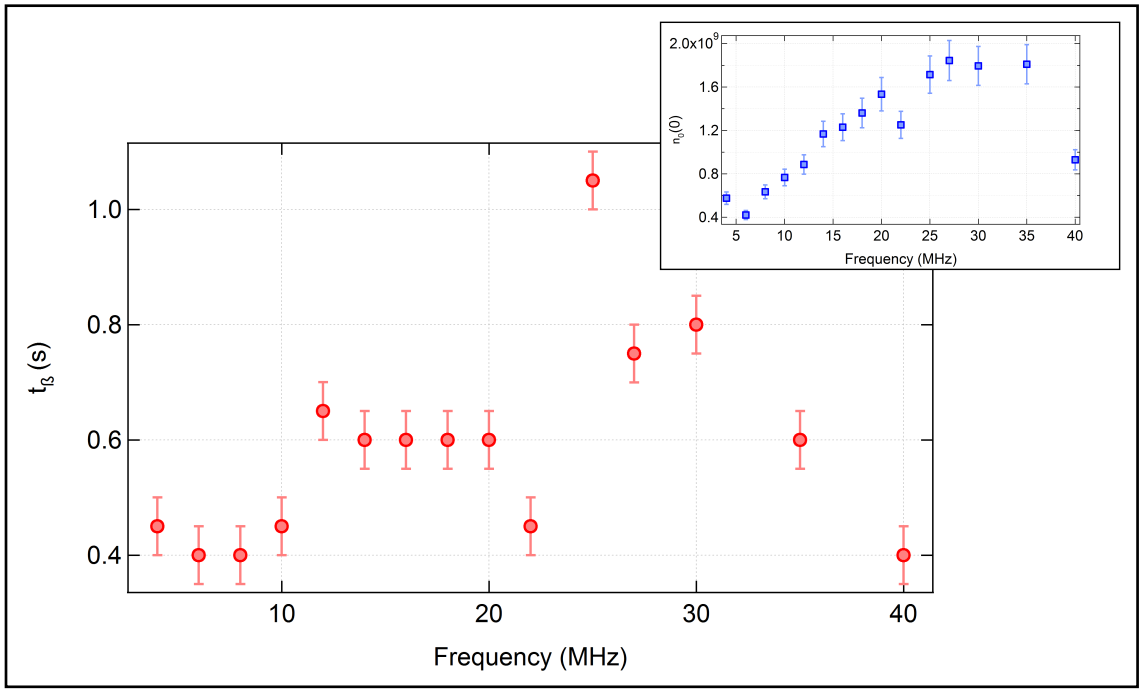

Figure 4.8: The evolution of t_β found by taking the second derivative of $\log n_0$ as a function of the frequency of the MOT light. The increase of t_β comes from the increase of $n_0(0)$, see insert, whereas the decrease at higher detunings is associated with the decrease of β at these frequencies.

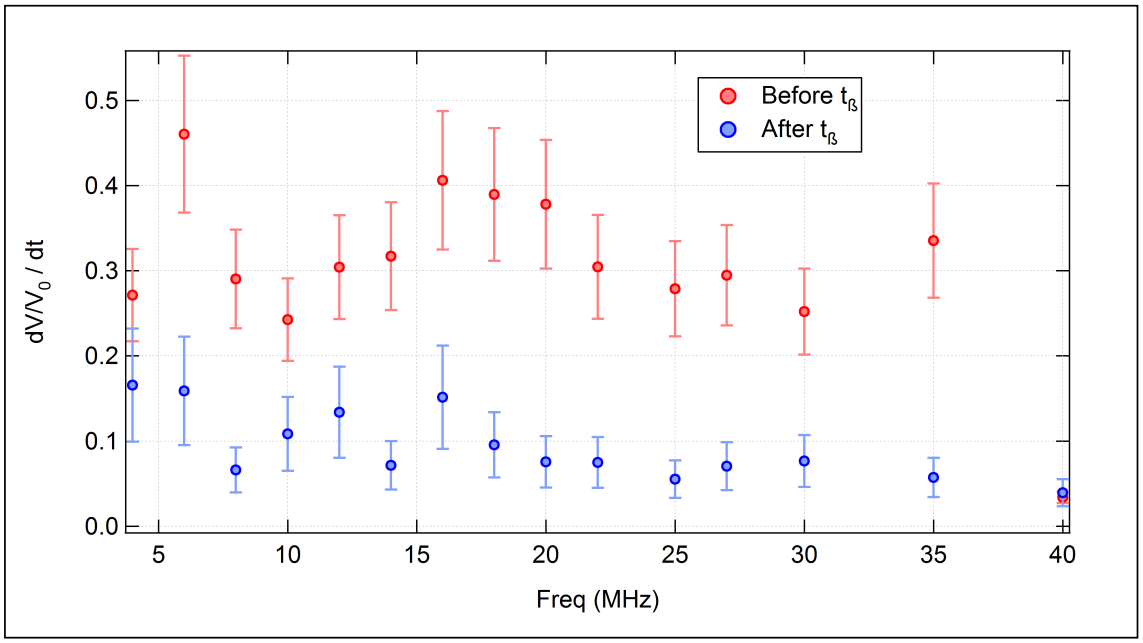

Figure 4.9: The relative change per second as a function of the detuning of the MOT light. The relative change during the period in which the light induced losses are dominant (red circles) is three times higher than the relative change during the rest of the decay (blue triangles).

this regime, the average change per second is 30 %/s, whereas for the regime where τ is the largest loss factor, the change is only 10 %/s.
There is clearly a stronger decrease in volume during the time that the light induced ionization losses are of the largest influence. However, the relative change in volume is still within the range that was assumed in [143] and which was taken into account in their error analysis.

To check whether the change in fitted β found in the previous section is due to the changing volume, we compare the relative difference between the two methods with the relative change in volume in the time up to t_β (where the light induced losses are dominant) for every data set. The results, shown in figure 4.10, show that indeed, the change in β between assuming constant volume and not, is in all cases very similar to the relative change in volume that has to be taken into account.
Let us now continue our analysis and investigate the constant loss coefficient K_{sp} and whether the found difference in β due to the volume change is of influence.

4.4.3 The Constant Loss Coefficient

To compare our results to older experiments, we need to convert our measurement of β to a measurement of K_{sp}, as this is a value that is expected to be independent of experimental parameters such as detuning and intensity of the light.
To obtain values for K_{sp} we need to know what the population of the excited state is for each measurement of β. We find π_p by comparing a situation in which we are

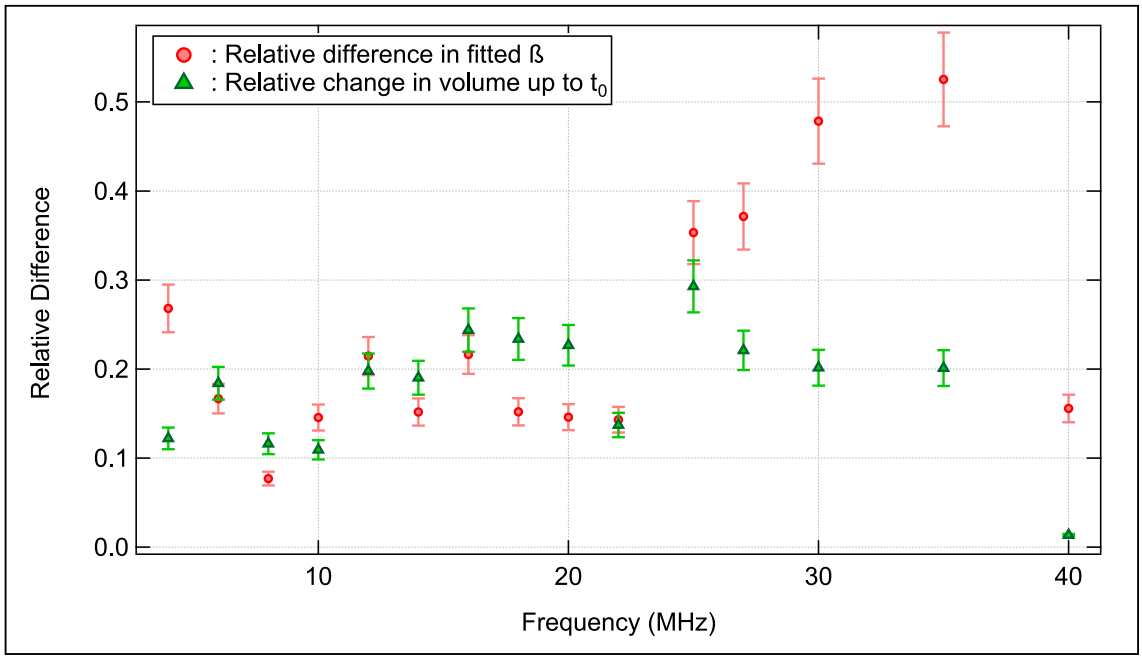

Figure 4.10: The relative difference between β for assuming constant volume and not (red circles), compared to the relative change in volume up to t_0 (green triangles).

sure that $\pi_p = 1/2$, when we saturate the transition with a powerful on-resonance pulse, to the situation in the MOT, with the light at the detuning and intensity with which we take the decay data.
Unfortunately the in situ MOT pictures taken in the same run as the decay curves are saturating the camera and the 2D gaussian fits of these images are bad.
We take a separate measurement a few months later of both the saturated and the MOT fluorescence. This is not an ideal situation, as there has been work done on the experiment in this time and the situation will not be exactly the same as the one in which the original measurements were done. We are confident though that the two most important things, the light detuning and intensity are the same for both measurements. The biggest change will be that the MOT beams are better aligned, something that will only result in more atoms, not in a difference in π_p.

Measurement of π_p

The fraction of the atoms that are in the excited state as a function of the detuning can be found in figure 4.11. The results from the experiment as well as the theoretical value from equation 4.7 for $I/I_{sat} = 100$. The two are as compatible as can be expected as the intensity will in practice not be constant over the whole range of frequencies.
The camera saturation had the largest effect at lower detunings, where we see the biggest difference between the two measurements. As our newest measurement is not saturating the camera and is closest to the calculation, we can say for sure that the older data should not be used for the deduction of π_p. Further comparing the calculated fraction to the measured one, shows that the measurement falls off a bit

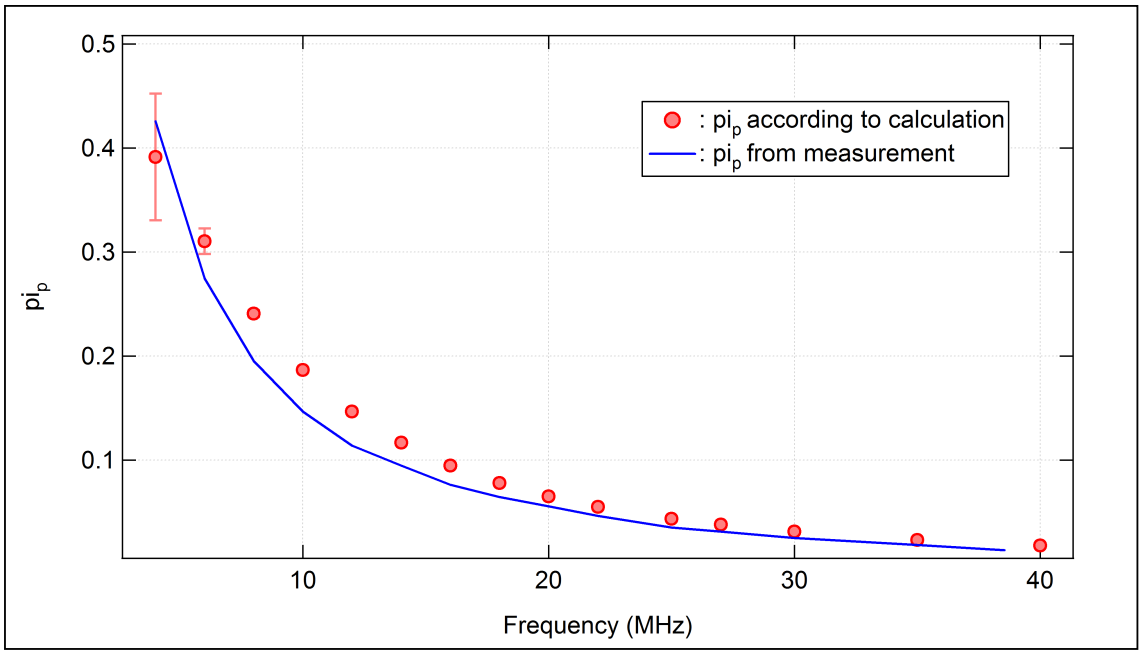

Figure 4.11: The population of the excited state as a function of the detuning of the MOT light, with constant magnetic field gradient, according to measurements (red circles). Also shown is the theory for $I/I_{sat} = 100$, as according to our experimental parameters (solid line).

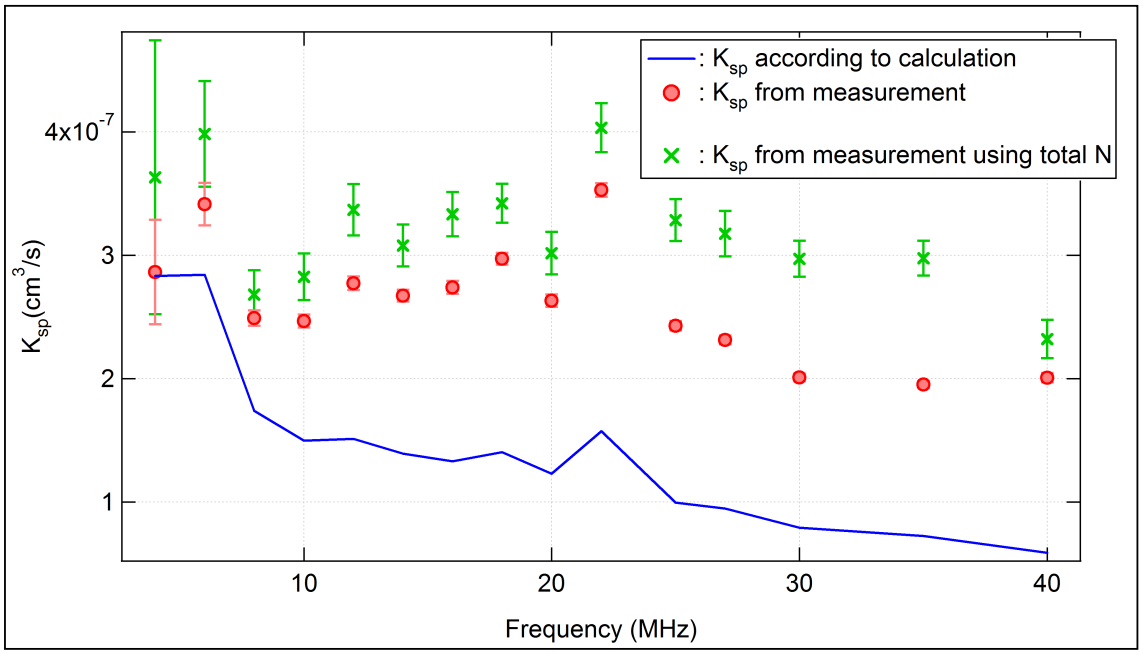

Figure 4.12: The constant loss coefficient K_{sp} as a function of the detuning of the MOT light. The coefficient is given for the loss rates β obtained with fitting the peak density (red cicrles) and with the number of atoms (green cross) to find β. When using a calculated π_p (solid line) the distribution is no longer constant.

quicker with the detuning, indicating that perhaps the intensity of the light does get a bit lower at higher detunings. Since this is incorporated into π_p, we do not have to worry about it.

We combine the measurements of β and π_p to obtain the information about K_{sp} that we want, to be able to compare our results to older ones. We take:

$$K_{sp} = \frac{1}{2}\frac{\beta}{\pi_p(1-\pi_p)} \tag{4.9}$$

For using β from the density and the number of atoms, and using π_p from the measurements as well as from the calculations, the results are shown in figure 4.12. The measured K_{sp} is nicely constant over most of the detunings of the light, only slightly wavering at the largest frequencies, where the loss parameter β is very small. The lower K_{sp} for the largest detunings can also be an indication of the process illustrated in figure 4.1, where the detuning is too large to excite any atoms into the excited state (according to our measurement $\pi_p = 0.02 \pm 0.001$).
As we see, using the calculated π_p for obtaining K_{sp} does not behave as expected, as the distribution is no longer constant.
Taking the average of the first ten data points where the value is constant gives us $K_{sp} = (2.8 \pm 0.4) \times 10^{-7}$ cm^3/s.

4.4.4 Discussion

Our measurement of $K_{sp} = (2.8 \pm 0.4) \times 10^{-7}$ cm^3/s is higher than previous measurements of the constant rate coefficient. Earlier experiments gave a range of $K_{sp} = (1.0 \pm 0.4) \times 10^{-7}$ cm^3/s (*Dos Santos et al.* [144]) and $K_{sp} = (8.3 \pm 2.5) \times 10^{-8}$ (*M. Kumakura and N. Morita* [142]), although for this last measurement is based on a single detuning only and there has not been a separate measurement of π_p. Other experiments have as well not measured π_p separately [75, 141, 143] and give only their obtained values of β. Since β is dependent on experimental parameters, we prefer to compare only K_{sp}.

In [144], the excited fraction π_p has been measured in the same way as we have done here, with the addition that they have also taken π_p as a function of I_{sat}/I (which we have taken from our known parameters), something that increases the experimental accuracy. However, we think that it is not possible that a factor 3 can be explained just by a difference in π_p, it seems highly unlikely to us that we misinterpret the fluorescence by a factor 3, as it is a well understood process, as evidenced by the results of chapter 3.

To explain the difference in our measurements with the older ones, if the problem is not with the measurement of the excited fraction, it is with the measurement of β (either ours or theirs), and there are two explanations. First there is the issue of the different fitting processes. We see that, although there is a difference in whether you assume constant volume or not, and although the fitting is much better if you do not, the absolute difference is not big and does not explain the difference with

older experiments. However, there are other differences. A typical measurement for example of [144] lasted only a couple hundred microseconds. The measurements were short because of a short vacuum lifetime, but mostly because of the low efficiency of the photodiode.
It is therefore very possible that any difference between the two measurements can be in fact explained by our larger span of time in which we are able to take data. However, when we try to fit our data using also only the first few hundred microseconds, we do not get much different results, mostly the error bars and χ^2 just increase. On the one hand this confirms our belief that the most information about β is found right at the beginning of the measurement.
On the other hand, it shows us that merely fitting over a smaller region of interest is not by itself a reason for assuming a wrong answer. It points us in another direction though. If we recall, the decay of the trap depends on the loss rate β, but also on the lifetime of the trapped gas due to collisions with the background τ.
In the range of our measurement, our lifetime is so long it could almost be infinite. In fact, forcing by hand τ to be in the order of several hours (instead of the measured 11 s) has little to no influence on the fit value of β. What this tells us is that in the time range where we determine β, the losses from collisions with the background are negligible. In [144] the same thing is claimed, however the background pressure reported there is about one order of magnitude larger than ours (6.7×10^{-10} mBar vs 6.6×10^{-11} mBar).
It is hard to say whether their assumption to ignore τ is justified as the data does not reach into the regime where one can actually test τ. However we can say that if they ignore τ (as was done in [144]) when it is not warranted it could explain a discrepancy in β. Whether it would cause one to under- or overestimate the loss rate is hard to say as it depends on the actual shape of the data.

Another possibility which can influence the determination of β is the measurement of the volume of the cloud. Disregarding whether one assumes the volume to be constant or not, an overestimation will lead to an overestimation in β in both cases. We have done a very precise analysis of our imaging system and are confident in the pixel size estimation. It seems therefore very unlikely that we are overestimating the volume. Whether past experiments have underestimated the volume is not for us to say, although when addressing the issue *Dos Santos et al.* imply they rather assume that they are more likely to overestimate than underestimate the measured volume.
One thing we should remark is that due to a much lower efficiency of the CCD camera, there is a possibility that a high noise level obscures proper measurement of the spatial size of the cloud.

The last thing we could consider is that due to the trap size there might be some spontaneous evaporation, which would increase the loss rate at the start of the decay and the rate of which would be dependent on the detuning and magnetic field gradient.

In the end we cannot say with certainty what is the cause of the (small) discrepancy

between our results and results obtained by earlier experiments, since we cannot recreate the difference by artificial means such as assuming constant fitting, or reducing the fitting range.

4.5 Conclusion

In this chapter we have discussed a measurement on the loss rate due to light induced ionization in a Magneto Optical Trap of metastable helium. We have measured this loss rate β by stopping the loading and monotoring the decay. We are able to monitor the volume of the cloud during the decay, something that has not been attempted in previous experiments.

We have found that taking into account the change of volume during the losses leads to data that is in closer accordance with the model as the goodness of the fits are much better than when one assumes constant volume. The improved measurements leads however not to a great differences in the value of the loss rate, in fact the difference is in accordance with the relative change in volume during the time when the two-body losses are largest, of the order of 20 %.

The population of the excited state of the atoms in the MOT is found by comparing the fluorescence to a situation in which we are sure to saturate the transition and the population is 1/2. Combining this information with the above found β gives us a determination of the constant loss coefficient K_{sp}, which we determine to be $(2.8 \pm 0.4) \times 10^{-7}$ cm^3/s. The rate is constant over a broad range of experimental parameter, as expected.
The found value is a factor 3 higher than values found in the literature. The difference is not explained by artificially reconstructing possible limitations of older experiments. We discuss several possible explanations for the discrepancy, such as an overestimation of the lifetime of the cloud due to background gas, or an underestimation of the volume of the cloud.

Chapter 5

Conclusion

This manuscript has been the first thesis describing the work done on the new helium experiment at the IOGS in Palaiseau.

A good experimental physics project is like a puzzle where all the pieces fit perfectly together. Indeed, one does not embark on such a mission (and spend so much money) before knowing it can be done.
In the introduction I have laid out the reasons for which this experiment was conceived. When working at it's full capacity the apparatus will be used as a quantum simulator for complex condensed matter systems, as well as a tool for investigating fundamental quantum mechanics.

After having given you a description of how the finished puzzle is going to look in the introduction, the first piece of the puzzle has been presented in chapter 1. The internal energy of the metastable helium atom allows for single atom detection with micro channel plates. Thus allowing for precise measurements of the second (and third etc) order correlations. The detection system is therefore perfectly matched with the use of metastable helium, they are two pieces of the puzzle that fit together.

We have done a study to improve both the efficiency and the accuracy of the MCP detection system, it has been described in chapter 1. We have experimented with adding a gold layer on the top of the input plate, something that we have found increases the efficiency but also decreases the accuracy.
The addition of a voltage between the two stacked plates has been shown to both raise the efficiency and improve the accuracy in non-coated MCPs.
The results found in the study that was described in chapter 1 are of importance to anyone using MCPs as detectors for neutral atoms. For us, who are building a new experiment, it has given us the opportunity to get our feet wet, to get a feeling of how to work with these kind of detectors. The results we obtained have influenced our decisions regarding the final configuration for the detectors, as we have declined to use gold covered MCPs, but have decided to implement the interplate voltage. The increased efficiency and accuracy will be very will be detrimental come the time of the correlation studies.

The detectors are a principle part of the puzzle, but an even bigger part is the atoms they detect. A big part of this thesis has been dedicated to the description of the construction of the experimental apparatus that produces and cools clouds of metastable helium. In chapter 2 we deliver the engineering piece of the puzzle. This part is important as it facilitates everything else, and the physics behind the different components is as fascinating as it was 40 years ago.
The vacuum system and the laser setup, as well as the transverse collimation and the longitudinal slowing of the atoms have been described in detail. At the end of the second chapter everything is in place to produce a slow enough atomic beam that can be trapped in a MOT. The first MOT on this experiment was created in June of 2013, quite an achievement.

The MOT that was created, afterwards optimized and characterized, has been the focus of the studies done in chapters 3 and 4
We have seen that metastable helium is a good system in which to study pure two-level Doppler cooling, as there are no sub Doppler mechanisms at play and there is no additional heating from non-degenerate ground states when working in molasses. We have been able to show the correspondence to theory for our system. The results presented in 3 are the first time that pure three-dimensional two-level Doppler has been shown.
In cold atoms nowadays, Doppler cooling is usually seen as a necessary, but not too interesting anymore step towards more interesting physics. Sub Doppler cooling mechanisms are still the subject of investigation. Having a system that very well matches with the relatively easy two photon Doppler theory is remarkable and well worth the investigation. The fact that this atomic physics theory works so well is comforting and the chapter ends with the implementation of a red molasses phase, leaving us with a well understood and cold cloud of metastable helium.

Finally a separate experiment on light induced collisions in a MOT of metastable helium has been executed, and reported in 4. These collisions determine in big ways how we deal with metastable helium, as they dictate how we set our experimental conditions. Laser light with a low detuning from the resonance has a higher chance to induce these losses, and the density of the cloud is as well limited by them.
We have been able to for the first time monitor the volume of the cloud and the density in situ, instead of just the total atom number. We have found that the constant loss rate has been underestimated up until now.

This thesis is the document of a long journey, one that has culminated in the creating of a MOT of metastable helium, and several experiments done in this MOT.

5.1 Outlook

The story has ended so far with us reaching Doppler temperature with the use of a red molasses stage after collecting the atoms in a MOT. As outlined in the introduction this is not the final stage of the experiment, in fact it is only the first.

In the last months the team has been working on a molasses stage on the blue side of the transition, a so-called grey molasses. In this system sub-Doppler temperatures of around 5 times the recoil temperature have been measured and results will be published in time. One can use blue molasses due to the sign flip in α at high intensities of the light, which at red detuning prohibits you from increasing the capture range by increasing the intensity. An preliminary example can be seen in figure 5.1. We see that the temperature indeed decreases with increasing detuning, a clear signal of sub-Doppler processes at work.

The further experimental steps towards Bose-Einstein condensation have been briefly discussed in section 3.5.2. After the grey molasses the atoms will be transferred into a magnetic trap, while optically pumping them to ensure the transfer of as many atoms as possible. The temperature of the atoms in the magnetic trap is not changed, therefore it is important that the cloud is as cold as possible before the transfer.

It is also possible to transfer the atoms directly from the blue molasses into the dipole trap. This might mean there are less atoms in the final dipole trap, as the overlap between the two is relatively small.
A lot has already been done on the design and testing of the 30 W laser (at 1500 nm) and the optics have been installed on the experiments, and the first experiments on loading the optical trap are already underway. At the moment we are limited by Penning collisions in the dipole trap, which prohibit us from reaching high enough densities so we could proceed with evaporative cooling. We are aiming to polarize the atoms in the trap, so the collisions will be much less. More about this can also be read in J. Simonet's thesis [159].
The next step is to aim for condensation in this optical dipole trap. It is difficult

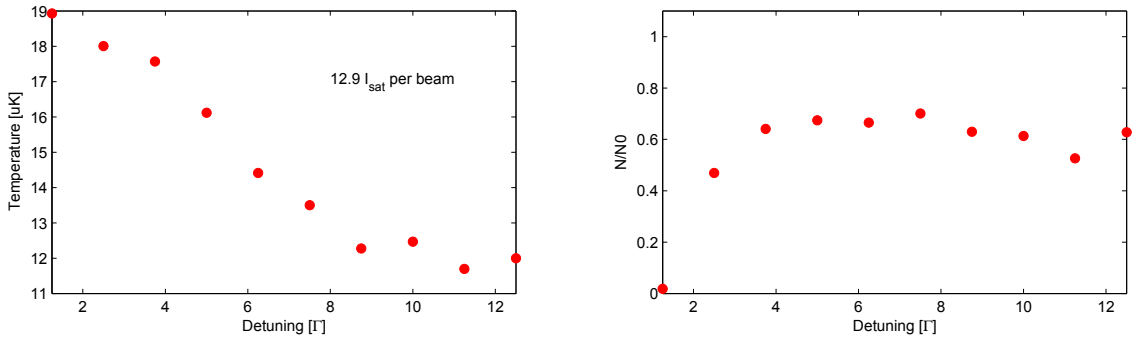

Figure 5.1: The temperature (left) and the fraction of atoms remaining (right) after a blue molasses stage.

to put a timeframe on this as cold atoms experiments can be very fragile things. The chances look favourably though and without doubt there will soon be more to report on this subject.

As told in the introduction, there will be a 3D optical lattice implemented as well on the gas, giving us many opportunities for interesting experiments. The laser and optics have been bought, but not brought out to be tested yet. Some examples of possible avenues of research have already been discussed, but really, the sky is the limit.

Appendix A

2D Magneto Optical Trap

To increase the capture rate of the MOT, which not only depends on a low enough final velocity but also on a not too large transverse velocity spread (since the MOT beams have a finite size), we want to have a 2D MOT stage between the exit of the second Zeeman slower. A 2D MOT is different from optical molasses as it has a position dependent force and therefore actually transversely cools the atoms in addition to collimating them [87].
For a more detailed description of the way a MOT works (as a 2D MOT is really just the same as a 3D MOT only in two dimensions instead of in three) see section 3.2.

In figure A.1 we see the design of the optics of the 2D MOT we plan to install. Besides these optics one also needs coils to create the magnetic field gradient.
Unfortunately the glass chamber that was supposed to go between the slower and the science chamber broke when we tried to install in on the experiment. We then decided to not continue this path at the moment and forego the 2D MOT. One can keep in mind that it is a possibility to install one in the future, if it is the loading rate of the MOT that is limiting the experiment.

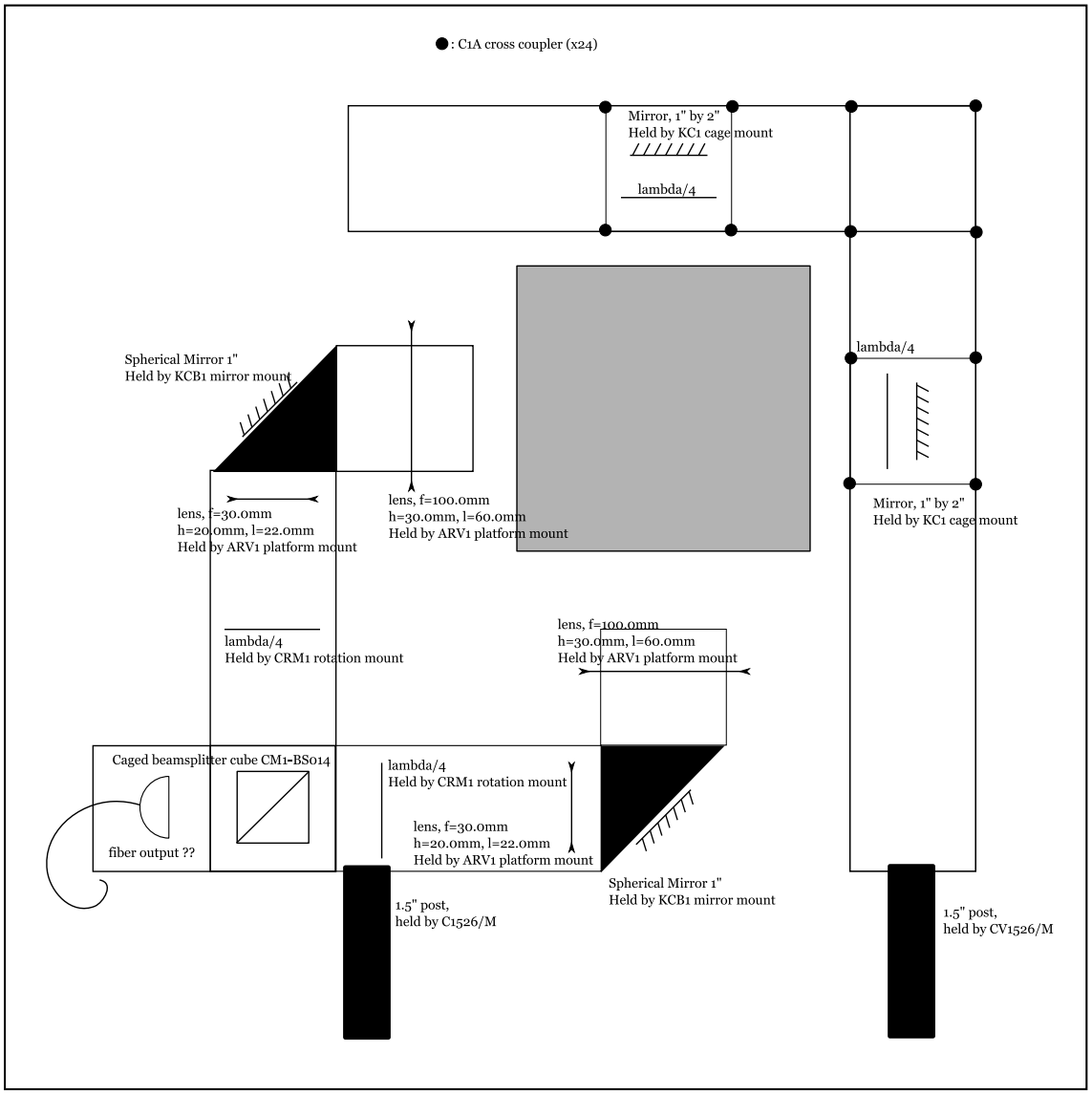

Figure A.1: The optics designed for the 2D MOT between the Zeeman slower and the Science chamber, which will transversely cool the atoms and consequently increase the capture rate of the 3D MOT.

Appendix B

Camera

As we have discussed in the introduction, the primary reason for choosing to work with metastable helium is the internal energy that makes single atom imaging possible, and we have discussed in detail the detection method that is used to do time of flight (TOF) single atom, three dimensional detection by using microchannel plates (MCP) in chapter 1. To get most out of the MCP detection, the plates should be far enough from the trapped atoms to ensure that one is in the far field regime, meaning that we are only looking at momentum space and that any information about initial position is no longer relevant. Since we aim to use the MCP detectors for the detection dilute ultra cold gases, the position of our MCP is going to be far from the trap position.
However elegant, this detection method is lacking for in situ imaging. To detect fluorescence from helium metastables at 1083 nm, people have used photodiodes [72] or CCD cameras [73][74]. The photodiode method has the downside that one only has access to the total number of photons detected and knows nothing about the spatial distribution of the atoms. The CCD camera has a quantum efficiency of 1.6 % at 1083 nm.

Since a relatively short time however, thermoelectrically cooled InGaAs cameras for scientific application have become available, which are much more efficient than other kinds of silicon based cameras [76] in the infrared. These cameras are specifically developed for working at short wave infrared (SWIR) wavelengths. For those working with fluorescence at 1083 nm, these kind of InGaAs cameras are a great new tool for imaging, and they allow us to gain access to knowledge about the atoms that was previously more difficult to access. The camera is a Xenics Infrared Solutions and is a Xeva-1.7-320 SWIR camera. The pixel size is 30 μm^2, in an array of 256 by 320 pixels, and is operational from 0.9 μm to 1.7 μm. The chip has a quantum efficiency of 80 % and can operate in a high gain (signal to noise ratio (snr) 60 dB) and a low gain (snr 68 dB) regime [77]. It is thermoelectrically cooled down to 263 K and connects through USB 2.0 to a computer.

We have tested the gain of the camera, for both high and low gain models. We aim to find the number of photons per ADU (the output unit of the camera). We do this by shining a beam of light of carefully calibrated power on the camera and

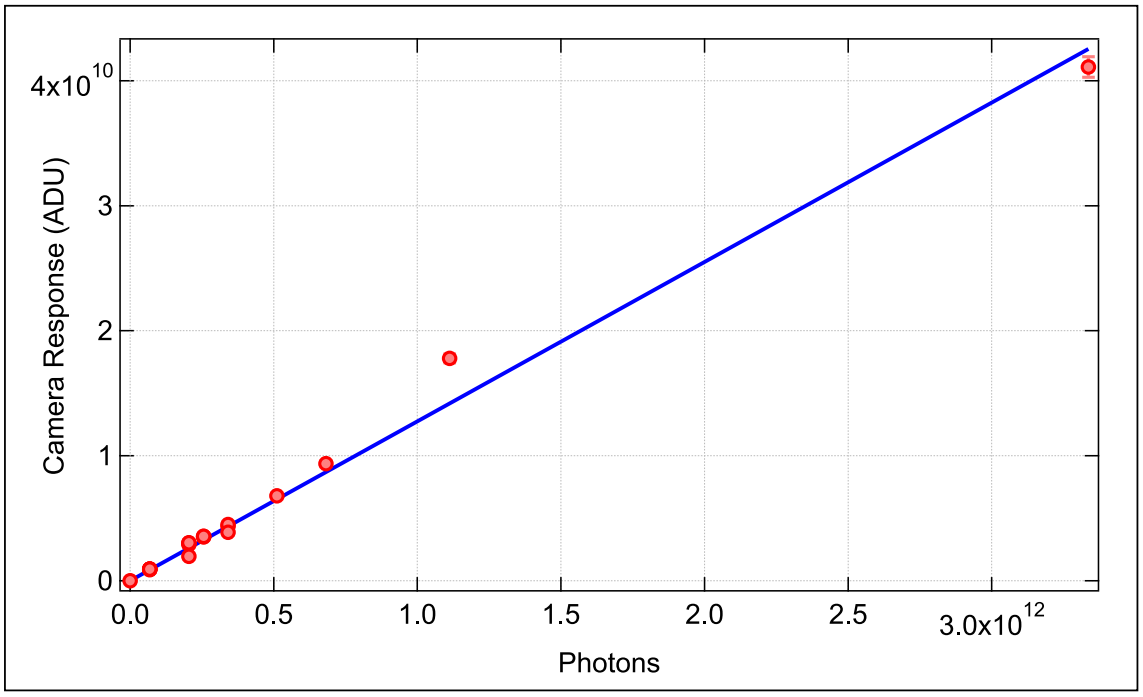

Figure B.1: The calibration of the camera: ADU per photon for the high gain regime. When one fits a linear fit to the data, there are 78 ± 2 photons for each registered ADU.

registering the response. Results of the calibration for the high gain regime can be seen in figure B.1. When the camera is in this mode, it takes 78 ± 2 photons to get one ADU. For the low gain mode the calibration comes to 1410 ± 3 photons per ADU.

Appendix C

Cicero - A GUI Based Time Sequencer

To run an ultra cold atom experiment a very precise time controller is needed to sequence the events. Magnetic coils, switches and AOMs have to be switched on and off with a very high accuracy and in a very short time. I will in this section give a description on the relatively new computer sequence control system named Cicero Word Generator. This is a program that is developed in the MIT Center for Ultra Cold Atoms and is specifically designed for cold atom experiments [100][101]. This section is based on a report written by Y. Fang during his time at the Institut d'Optique as a visiting student [102].
The system is based on a client-server architecture, the server is called Atticus and the client Cicero. Both apply a Graphic User Interface (GUI) approach to the design of time sequences. This makes it very easy to develop new sequences and to troubleshoot as it is a very visual way of working. First we look at the hardware we need to use Cicero.

C.1 Hardware

Cicero Word Generator is designed to work with a National Instruments (NI) PXI system. The PXI system consists of a chassis, with modules to place in it, a controller and usually also software, such as LabView. We have substituted here our own software, Cicero.
The controller is embedded in the chassis, we have chosen a NI PXIe-8101 [103]. This controller has an Intel 2.0 GHz processor, 2 GB of RAM and 250 GB harddrive.
For the time generation we have a FPGA device from Opal Kelly [104]. Furthermore there are two analog cards [105], two digital cards [106] and a function generator [107] that can create 40 MHz sine and square signals and 5 MHz ramp and triangle signals.
This configuration gives us in total 64 digital channels and 16 analog channels.

C.2 Software

Atticus is the program that talks to the hardware, to the cards installed in the PXI. Cicero is the client interface in which we can construct the sequences for our experiments. Atticus translates the sequences that we make in Cicero to an output buffer that the hardware will understand. In principle Cicero can have several different Atticus programs it can work with at the same time, however we are not doing this. Details on how to use the program and a troubleshoot guide can be found in [102]. In figure C.1 a screenshot of the program is shown. With Cicero, you make a sequence consisting out of several timesteps. For each timestep you set the time and you can for each digital channel decide whether the channel is on or off. For the analog channels you can set a function, the program has several such as step and sine installed, but it is also possible to write your own. Everything is then visualized for an easy overview of the whole sequence. Any value, such as time duration of a timestep or a variable in an analog function can be set as a list of variables, through which can be looped in order or randomly. For the digital channels Cicero has the option to execute slightly before or slightly after the timestep, for example to open the switch for an AOM before turning it on.

The main interesting point about using Cicero is that one has control over the resolution of the time. When you set a timing to a step, you also set a resolution, meaning that you tell the sequencer what is base timing signal is. In usual sequence controllers, the time resolution is always the same. This is unnecessary and it takes up a lot of buffering space. With Cicero, for time steps that take some time, such as loading, or time of flight, one can set the resolution to a much larger value then when doing manipulations that have to be controlled to the microsecond.

The user interface of Cicero is extremely visually oriented and once the program is installed and configurated correctly, anyone can design or alter an experimental time sequence with relative ease, as no knowledge of any specific programming language is needed.

With Cicero and Atticus installed and configurated we can control our experiment.

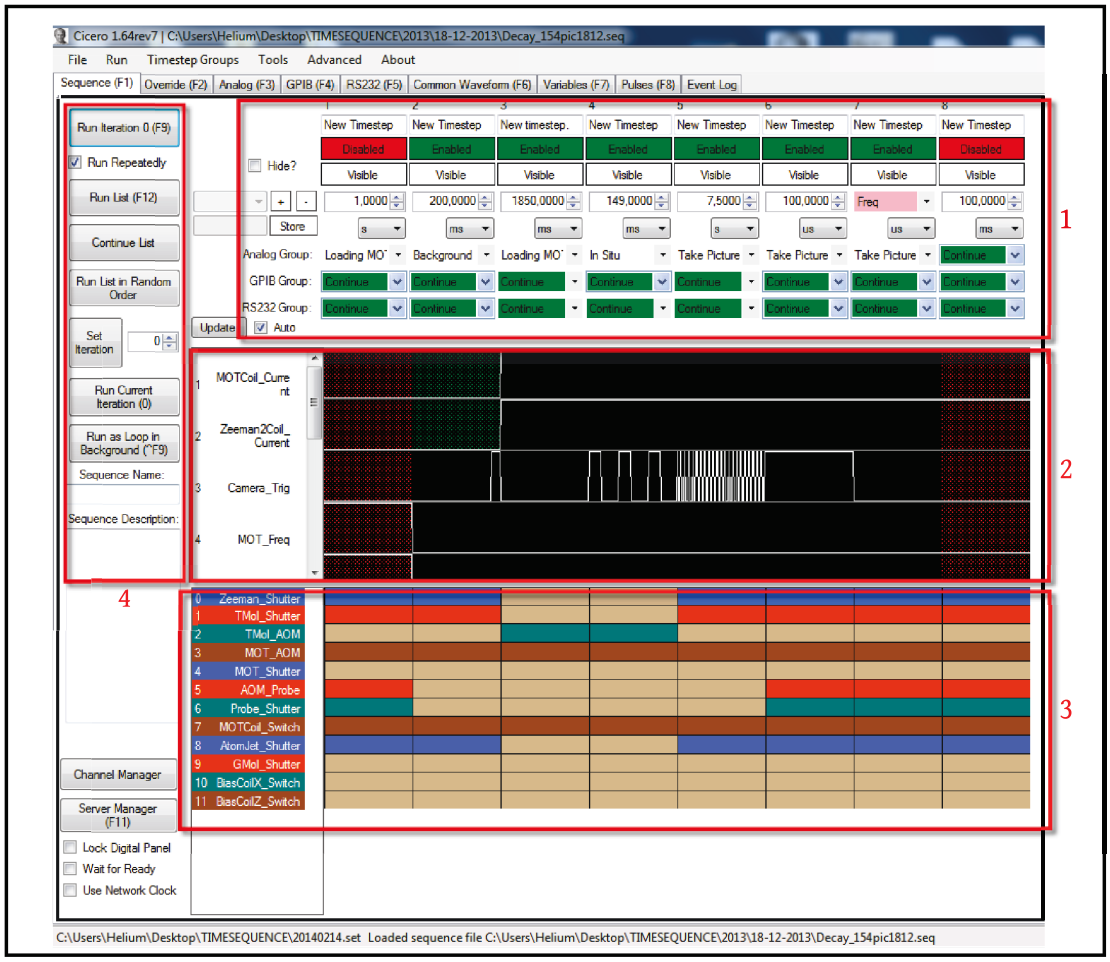

Figure C.1: A screenshot from the Cicero interface, for a sequence that monitors the decay of a MOT in situ. (1) The basic control over the timesteps. Steps can be added and removed, and the time duration can be set. Preprogrammed sequences can be assigned to analog channels per timestep. (2) The visualization of the analog channels. (3) Control and visualization of the digital timesteps. (4) Control over the run and the iterations.

Appendix D

Published Papers

A. L. Hoendervanger, D. Clément, A. Aspect, C. I. Westbrook, D. Dowek, Y. J. Picard, and D. Boiron, *Influence of gold coating and interplate voltage on the performance of chevron micro-channel plates for temporally and spatially resolved single particle detection*, Review of Scientific Instruments, vol. 84, no. 2, p. 023307, Feb. 2013.

F. Moron, A. L. Hoendervanger, M. Bonneau, Q. Bouton, A. Aspect, D. Boiron, D. Clément, and C. I. Westbrook, *An oscillator circuit to produce a radio-frequency discharge and application to metastable helium saturated absorption spectroscopy*, Review of Scientific Instruments, vol. 83, no. 4, p. 044705, Apr. 2012.

R. Chang, A. L. Hoendervanger, Q. Bouton, Y. Fang, T. Klafka, K. Audo, A. Aspect, C. I. Westbrook, and D. Clément, *Three-dimensional laser cooling at the Doppler limit*, arXiv preprint arXiv:1409.2519, 2014.

Influence of gold coating and interplate voltage on the performance of chevron micro-channel plates for temporally and spatially resolved single particle detection

A. L. Hoendervanger,[1,a)] D. Clément,[1] A. Aspect,[1] C. I. Westbrook,[1] D. Dowek,[2] Y. J. Picard,[2] and D. Boiron[1]
[1]*Laboratoire Charles Fabry, Institut d'Optique, CNRS, Université Paris-Sud, 2 Avenue Augustin Fresnel, 91127 Palaiseau Cedex, France*
[2]*Institut des Sciences Moléculaires d'Orsay, UMR 8214, Université Paris-Sud, Bat. 350, 91405 Orsay Cedex, France*

(Received 23 October 2012; accepted 10 February 2013; published online 28 February 2013)

We present a study of two different sets of Micro-Channel Plates used for time and space resolved single particle detection. We investigate the effects of the gold coating and that of introducing an interplate voltage between the spatially separated plates. We fin that the gold coating increases the count rate of the detector and the pulse amplitude as previously reported for non-spatially resolved setups. The interplate voltage also increases count rates. In addition, we fin that a non-zero interplate voltage improves the spatial accuracy in determining the arrival position of incoming single particles (by ∼20%) while the gold coating has a negative effect (by ∼30%). © *2013 American Institute of Physics*. [http://dx.doi.org/10.1063/1.4793402]

I. INTRODUCTION

Micro-Channel Plates (MCP) detectors are widely used in atomic and nuclear physics for the detection of charged particles and photons.[1,2] They are also used to detect metastable rare gas atoms[3] because the internal energy of such atoms is sufficien to produce electrons on the MCP surface. Combining these detectors with a crossed delay line anode allows one to reconstruct the full three-dimensional distribution of single particles falling with a well define velocity onto the surface of the MCP.[4] In particular second (g_2) and third (g_3) order correlation functions along the three spatial axes have been reconstructed, giving access to information related to the quantum statistics and coherence of a cold atom cloud.[5–7] In these experiments, the quantum efficien y of the MCP-Delay Line detector has been estimated to be of order 10%,[8] a rather disappointing figur which needs to be improved if one wishes to investigate quantum correlations at the two- and many-body level.[9–14] The spatial accuracy of the MCPs-Delay Line ensemble used in Ref. 8 is typically ∼150 μm, and the above mentioned experiments could benefi from an improvement in this figur as well. Efficien y of detection and spatial accuracy is crucial quantities in the context of ion studies as well and they have been the object of recent work.[15]

In this paper we will describe a study of potential ways to improve these performances. Testing different MCP-Delay Line detectors with metastable atoms directly is impractical due to the vacuum requirements set by the use of ultra-cold gases, and therefore we will attempt to simulate the response of the MCP to metastable atoms by using ultraviolet photons. The impact of a UV photon will in general only release one starting electron, as the impact of He* does, whereas for example ions might release more than one. As discussed later, we consider that, since similar and small (of the order of 10 eV) energy scales are involved, what we learn about MCP performance with UV photons carries over to metastable rare gas atoms. In addition of course, our results may be of use to workers interested in detecting photons with MCPs.

Several schemes have already been tested to improve MCP performance. Adding a special coating, for example gold, aluminium, or CsI, on the input face of the MCP has been found to increase the efficien y and the maximum count rate[16,17] for photon detection. For specifi applications which rely on pulses of larger amplitude, another scheme consists of spacing the two MCPs, unlike the common chevron stacked configuration and adding a voltage between the two slightly separated MCPs (see Fig. 1(a)). With such spaced MCPs, the additional voltage, which increases electron energy and influences their collimation in between the plates, should raise the efficien y and increase the resolution of the detector,[18,19] but not all workers have observed such improvements.[20]

Building on these ideas, we extend previous experimental investigations to the study of pairs of slightly separated MCPs using delay line anodes. We investigate both the effect of the voltage difference between the plates and the presence of a gold coating by looking at overall count rates as well as at individual electronic pulses. We discuss in detail the consequences of the different configuration on the accuracy of these detectors in the particle counting mode. We conclude that the addition of a small voltage between the two plates can slightly enhance the detection efficien y and accuracy of such a detector.

II. GENERAL CONSIDERATIONS

A. Micro-channel plates

MCPs consist of many single channels which are basically electron multipliers. To operate they need a voltage V_{mcp} between both edges of each tube (i.e., between both faces of

a)Electronic mail: Lynn.Hoendervanger@institutoptique.fr.

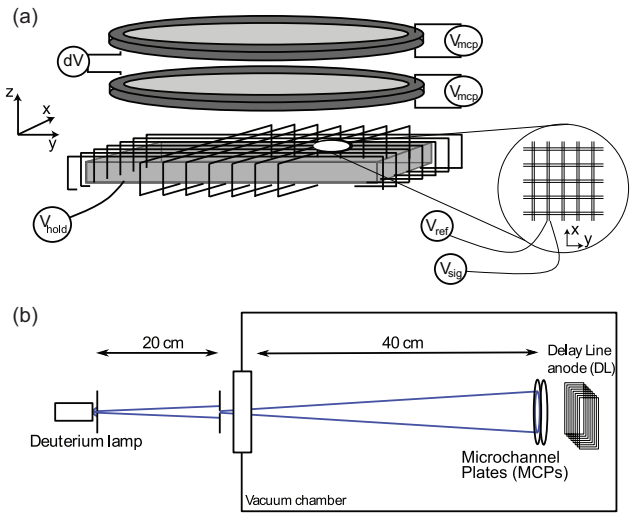

FIG. 1. Experimental setup. (a) Details of the micro-channel plate mountings. Each plate is provided with a variable voltage V_{mcp}. The output face of the second plate is set to 0 V. A variable voltage dV is applied between the two MCPs. Finally, the delay line anodes are supplied with fi ed voltages $V_{sig} = 300$ V and $V_{ref} = 250$ V for the transmission lines and $V_{hold} = 150$ V for the anode holder. (b) A deuterium lamp emitting photons in the range 185 nm–400 nm is shone onto the MCPs. The light passes through two pinholes which control the flux Inside the vacuum chamber the photons hit the MCPs.

the MCP), on the order of a kilovolt. A metal coating is therefore always evaporated on both faces of the MCP to form electrodes, such coatings being commonly mainly made from Nickel (as in Nichrome or Inconel coatings). When the voltage V_{mcp} is not high enough, there will be insufficien generation of secondary electrons when a particle hits the MCP. Raising V_{mcp} increases the ability of the MCP to start a cascade when an incident particle hits. At low V_{mcp} the gain increases exponentially with the voltage V_{mcp}. For large V_{mcp} the gain of the detector saturates and increases linearly with V_{mcp}. This happens when the presence of too many charges inside the channels screens the voltage V_{mcp}. This effect is independent of the flu of incoming particles. At a f xed discrimination level used to distinguish signal from noise, the measured count rate will saturate with V_{mcp} since the height of the pulses increases with V_{mcp} and at a certain point all of the pulses will be above the discrimination level. This picture is valid at low flux

When the flu of incoming particles is such that the arrival time between two incident particles is shorter than the time required to reestablish the electric fiel after the channel has been depleted, the second particle produces a smaller pulse. Thus, whatever the gain of the detector (even when saturated), if the flu is too high, the detector will show "flu saturation." The flu at which this happens is dependent on V_{mcp}. Adding a gold coating on the input plate can modify this behavior: the gold coated surface is more conductive than usual Ni-based coatings, thereby allowing faster replenishment of the channels and the detection of higher flu of incoming particles.[16,17]

As a function of the flu of incoming particles, one can therefore identify three regimes at large V_{mcp}: (i) at very low flu the number of counts increases linearly with the number of incoming particles with a slope define by the detection efficien y of the detector; (ii) at moderate flux the count rate increases more slowly than the number of incoming particles due to the flu saturation mentioned above; (iii) at large flux the count rate hardly evolves with the number of incoming particles and is dependent on V_{mcp}.

B. Delay line anodes

Delay lines are transmission lines that collect the electron pulses coming from the MCP. The transmission line is wound into a helical propagation line so the speed of the pulse in the relevant direction (x in Fig. 2) is much smaller than the speed of the pulse in the wire itself (see Appendix A). Dispersion ensures that the pulses created by a single electron shower in adjacent loops of the delay line overlap before reaching the end of the line[4] (see Fig. 2). This leads to a single broadened pulse at the output whose center can be precisely determined to a precision greater than the spacing between adjacent loops. Adjacent loops are separated by distances on the order of a mm and a propagation time of a few ns. Since the delay lines are built in such a way that dispersion combines the separate pulses on different loops into one larger one, pulse widths are typically a few ns. There is a delay line wound in both the x- and y-direction and from the arrival time signals obtained from both of these delay lines a spatial reconstruction can be made, and combined with the information of the arrival time on the MCP, one can reconstruct a 3D image.

C. Influence of interplate voltage *dV*

Let us now consider the situation of Fig. 1(a) with spaced MCPs when a voltage difference dV is applied between the

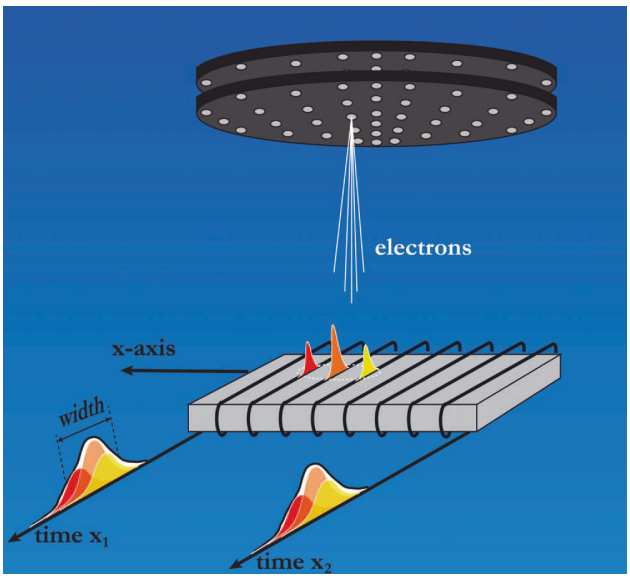

FIG. 2. An electron shower exiting the second plate of the MCP pair is accelerated towards the delay line anode. During the time-of-fligh the electron shower expands transversally and f nally excites several loops of the delay lines. After propagation in the transmission lines, the pulses from the different loops overlap due to dispersion. A single broadened pulse is observed at the output of the delay lines.

plates. We briefl comment on the electron dynamics in the interplate region[18] and during the expansion from the second MCP to the delay lines. The voltage between the plates accelerates the electrons between the two plates which otherwise travel in a zero electric fiel free space, with the result of (i) collimating the electron shower and (ii) transferring energy to the electrons. As a consequence of having a larger energy, the electrons hitting the second plate have a higher chance of inducing a cascade in the channel. The increase of the voltage dV should therefore have a positive effect on the efficien y of the detector and on the signal-to-noise ratio of the electronic pulses.

From simple arguments as put forward in Ref. 18 we can attempt to draw a picture of the behavior of the electron cloud during expansion between the second MCP and the delay line anode. At fi ed voltage difference between the bottom plate of the second MCP and the delay line (as in our experimental configuration) the number of loops where a pulse is produced by an incoming electron shower is mainly the result of two quantities: the initial size of the electron shower on the lower surface of the second MCP and the transverse expansion of the shower during the time of f ight towards the delay lines. On the one hand, the smaller the number of micro-channels excited in the second MCP (i.e., the smaller the initial size of the electron shower out of the MCP surface), the smaller the fina size of the electron shower hitting the delay line. On the other hand, the faster the electrons exiting the second plate, the greater their transverse velocity and the larger the size of the electron shower hitting the delay line (see Appendix B). Adding a non-zero voltage difference dV between the two plates clearly affects the size of the electron shower out of the second MCP (collimation of the interplate electron shower). It might also modify the energy of the electrons exiting the second plate. The net effect of dV is therefore non-trivial and it is worth being investigated.

III. EXPERIMENTAL SETUP

We study two different pairs of MCPs. Both pairs are new, Nichrome MCPs from Photonis USA, Inc. with a diameter of 1.245 in. and were matched by the manufacturer. The micro-channels have a diameter of 10 μm, a center to center spacing of 12 μm and a bias angle of 12°. All technical specification are given by the manufacturer and we have found no discrepancies in the resistances of the plates with the ones provided. One pair has a layer of 10 μm of gold deposited on the input surface of the f rst plate. In this work we have not considered the alternative mounting consisting in using the gold surface as the input one of the second plate. In the following we will refer to the non-coated MCP pair when using two Nichrome coated MCPs and to the coated pair when using the pair with the gold coating.

The setup of the experiment is shown in Fig. 1. The MCPs are placed in a vacuum chamber with a pressure of 10^{-6} mBar. Our mount has a non-conducting circular spacer with conducting surfaces between the two plates allowing us to apply an adjustable voltage difference dV (see Fig. 1(a)). In our studies there is always a spacing between the two plates, whereas in the usual chevron configuratio two MCPs are mounted directly on top of each other.

The voltage between the two MCPs (dV) can be varied from 0 V to 250 V. Below the MCPs is a delay line (Roentdek DLD80). The use of a delay line allows us to make a three-dimensional reconstruction of the signal gathered by the MCPs.[4] In all the results of this paper, the voltage supplies of the delay lines are f xed [see Fig. 1(b)]: $V_{\text{sig}} = 300$ V, $V_{\text{ref}} = 250$ V, $V_{\text{hold}} = 150$ V. The pulses from the delay line are decoupled from the reference voltage by a Roentdek FT12-TP feedthrough and decoupler which allows us to look at the pulse which is generated when a photon emitted by the source hits the MCP and triggers an electron shower. The signals are then amplifie and discriminated by a Roentdek ATR-19 Constant Fraction Discriminator (CFD)/Amplifie . The settings of the electronics are f xed throughout the article with the CFD level threshold set at 5 mV. The amplifie pulses are then processed by a Time to Digital Converter (CTNM4, IPN Orsay) with a coding step of 250 ps. For counting the pulses from the delay line we take the pulses after the CFD/Amplifie and count them with a counter.

To simulate the metastable helium atoms (He*) we use ultraviolet (UV) light source, a convenient solution since UV photons share neutral charge and similar energy as He* (the latter being 19.8 eV). Therefore, the impact of a UV photon will in general only release one starting electron, as the impact He* does, whereas for example ions might release more than one. The lamp is a Hamamatsu L6301-50 deuterium lamp with a spectrum ranging from 185 nm to 450 nm. The window through which UV photons enter the vacuum chamber is made of magnesium fluoride which has a cut-off wavelength at 100 nm. To control the incoming flu of photons on the detector we use two small pinholes, one right after the lamp and another one in front of the window of the vacuum chamber (see Fig. 1(b)). The diameter of the firs pinhole ranges from 0.5 mm to 2 mm and the second pinhole has a f xed diameter of 1 mm. We obtained a figur for the photon flu at different pinhole sizes by measuring the intensity of the lamp at 410 nm with the use of an interference filte . We then used the spectrum provided by the manufacturer to obtain absolute values for photon flu for all wavelengths.

The lamp spectrum is broad, however only a small fraction of the photons is expected to contribute noticeably to the signal. This is due to the detection efficien y of channel electron multipliers in the UV range which decreases from 10^{-5} at 180 nm to 10^{-9} at 250 nm.[21] As a matter of fact, we have operated with a Kodial glass window, with a high-pass cut-off wavelength of ∼250 nm, resulting in an almost complete suppression of the number of counts on the detector. Therefore, we are confiden that we mostly detect the highest energy photons (close to 200 nm) with energies of about 6–7 eV.

IV. EXPERIMENTAL RESULTS

A. Count rate versus flux

To study the characteristics of the two different pairs of MCPs, we f rst monitor the total number of counts from the MCPs as a function of the incoming photon flux with the

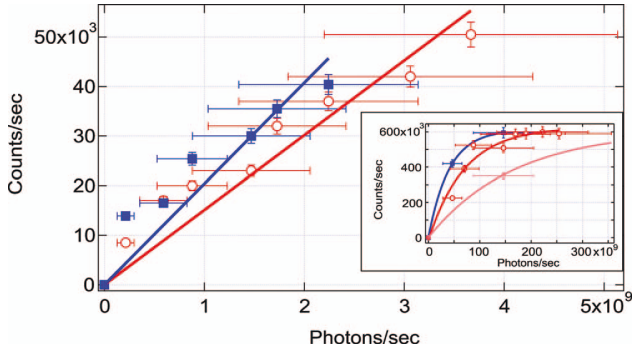

FIG. 3. The number of counts with increasing f ux. Red open circles: MCP pair without coating; blue fille squares: MCP pair with gold coating. Both pairs: $V_{mcp} = 1000$ V, $dV = 0$ V. Lines are linear fit crossing the origin. Inset: The count rate at higher f ux. The count rate for the gold coated pair (blue squares) hardly changes with dV (plotted is $V_{mcp} = 1000$ V, $dV = 25$ V). dV has a strong influenc on the non-coated pair: Light red diamond $V_{mcp} = 1000$ V, $dV = 0$ V/Red circles $V_{mcp} = 1000$ V, $dV = 25$ V. Lines are exponential fits

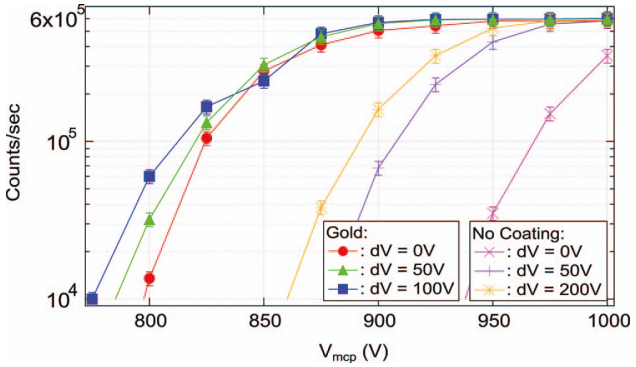

FIG. 4. Count rates as a function of V_{mcp} for the two pairs of MCPs and for different voltage differences dV. Incoming f ux $\sim 1.5 \times 10^{11}$ photons/s.

results shown in Fig. 3. The plotted number of photons hitting the active area of the MCP per second corresponds to the number of photons emitted by the lamp in a spectral range of $\sim$1 nm at the wavelength 200 nm according to our calibration. We note that this photon number slightly underestimates the total number of photons since the lamp emits a broad spectrum. For low flu (see Fig. 3) the count rate of the detectors increases linearly with the light intensity. The slope at low flu is 2.0×10^{-5} counts/photon for the gold coated MCP and 1.5×10^{-5} counts/photon for the MCP without coating. These values are comparable to those in Ref. 21 for photons with wavelengths of $\leq$200 nm.

For larger (intermediate) flu (see inset Fig. 3) the response deviates from the linear dependence, and starts to show flu saturation. In this situation the gold coated MCPs still have a better efficien y than the non-coated ones, with count rates larger by more than a factor 2, even in the presence of a non-zero dV on the plates. We relate this observation to the lower surface resistance of the gold coated plates with respect to the non-coated ones, allowing a faster replenishment of the input plate.[17] In addition, we note that the work functions for gold (5.1 eV) and nickel (4.6 eV) are similar, implying that a similar quantum efficien y on the input plate (probability for an incoming photon to excite a f rst electron) is expected for both cases and would not explain our observation. When the flu is even larger, the count rate saturates. The value of the saturation level is set by the properties of the electron channels, which we assume to be identical for both sets of plates as observed in Fig. 3.

B. Count rates versus dV and V_{mcp}

Further characterization of the MCPs is done by investigating the response of the count rate to the gradual increase of V_{mcp}. In Fig. 4 the increase in the number of counts with the total voltage over the separate MCPs (V_{mcp}) at a given photon flu of $\sim 1.5 \times 10^{11}$ photons/s is shown. We observe that the gold coated detector exhibits gain saturation at a much lower total voltage (V_{mcp}).

We now turn to a systematic investigation of the influ ence of the interplate voltage dV. The influenc of dV on the count rate of the MCPs is shown in Fig. 5. For the non-coated pair adding a voltage between the plates strongly increases the count rate of the MCPs. The effect saturates at $dV \simeq 50$ V. For the gold coated MCP, the count rate is already saturated and dV has no effect. The observed increase in count rate with dV differs with the finding by Wiza *et al.*[20] where the gain of the detector gets worse when there is a voltage between the plates. However, as demonstrated by Rogers and Malina,[18] the distance between the plates is crucial to the effect of dV. For instance when the plates are too close together the voltage may have a negative effect on the gain. Indeed we observed that tightening the MCPs too close to each other results in a drop of the count rate by a factor 5–10. By contrast the results presented here are obtained in a favorable situation with a larger distance between the plates of about $\simeq$0.2 mm. We have shown that in these circumstances one can compensate with the voltage dV for a lack of gold coating and for a lower V_{mcp} with respect to the count rate.

C. Pulse shapes

The three-dimensional reconstruction of particles falling onto the MCPs is possible thanks to recording the four

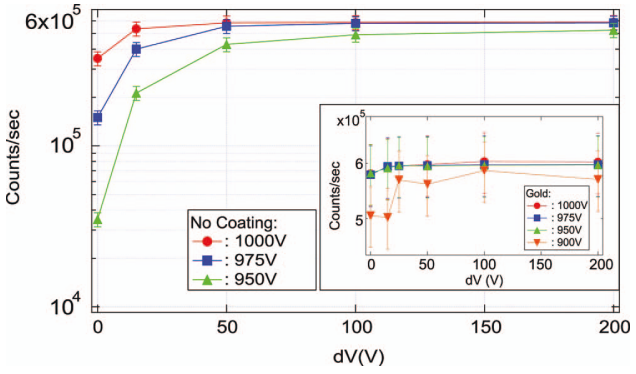

FIG. 5. Count rates measured with the non-coated MCP pair as a function of dV. Inset: Count rates measured with the gold coated MCP pair as a function of dV. Incoming f ux $\sim 1.5 \times 10^{11}$ photons/s.

arrival times of the pulses (t_{x1}, t_{x2}, t_{y1}, and t_{y2}) out of the two delay lines x and y.[4] The position of an incoming particle is extracted from the quantities $t_{x1} - t_{x2}$ and $t_{y1} - t_{y2}$. Since the position of the particle is determined from the timing signals, the ability of the detector to correctly extract this position can depend on the amplitude and width of the pulses recorded from the delay lines. We thus pay attention to those quantities, in particular to understand in further details the influenc of dV on the timing signals.

1. Amplitude

We plot the amplitude measurements in Figs. 6(a) and 6(b). First, we note that in the absence of voltage between the plates ($dV = 0$ V), the pulse amplitude on the input plate is larger with the gold coating, which is consistent with the higher count rates observed for the gold coated plate. The effect on the pulse amplitude is observable on the delay line signal as well. As a consequence and for a fi ed level of the CFD, the number of counts is larger for the coated plate (see Fig. 4). Second, we clearly observe an effect of dV on the pulse amplitude, as the electrons gain energy by being accelerated between the plates. We see that the amplitude of the pulses from the front increases as dV increases and then saturates, whereas the pulses from the delay line have a maximum at ∼25 mV. As anticipated in Sec. II, we believe that in the delay lines measurement two competing effects contribute:

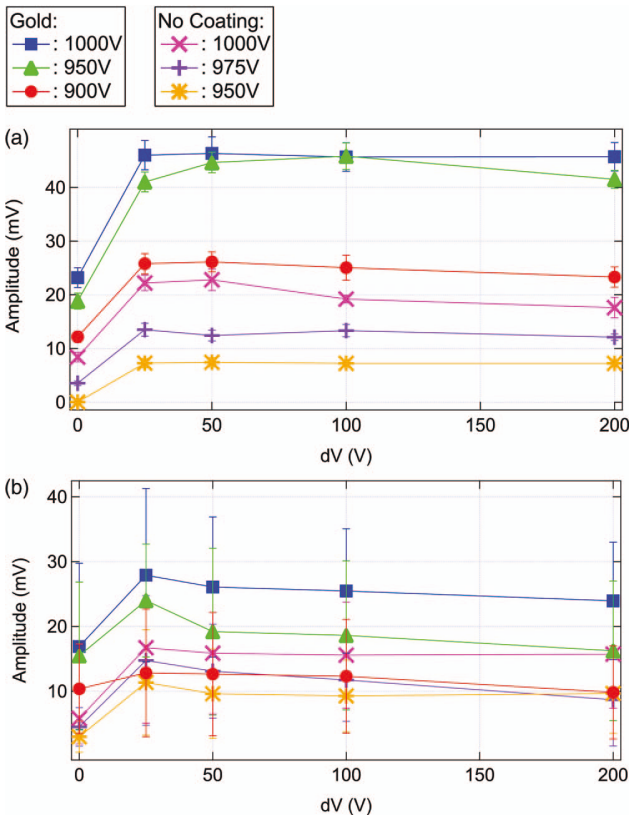

FIG. 6. (a) The amplitude of the pulse from the input plate, for non-coated and gold coated micro-channel plates. (b) The amplitude of the pulses from the delay line, averaged over all four channels.

faster electrons have a higher probability to fir a channel of the second MCP but, then, they also extend over a larger area during the expansion time to the delay line. We will discuss this interplay in more detail below.

2. Width

The recorded widths of the timing signals are plotted in Fig. 7 for different experimental situations. As predicted above, the typical width of the pulses is of the order of 5 ns, due to dispersion in the transmission lines (see Sec. II). At $dV = 0$ V (see inset Fig. 7) the width of the pulses depends on the value V_{mcp} (see Fig. 7): for both coated and non-coated MCPs the larger V_{mcp} (i.e., the higher the electron velocity) the larger the width of the delay line pulses. This corresponds with our assumption that the electrons exiting the second plate will have a larger velocity when V_{mcp} is larger, therefore increasing their spatial extent at the delay lines (see Appendix B for details).

Increasing dV to a (small) non-zero value has the effect of collimating and accelerating the electron beam which hits the second micro-channel plate, possibly resulting in a smaller width thanks to a better electron beam collimation (see Sec. II). Experimentally, tuning dV up to 25 V–50 V diminishes the delay line pulse width (see Fig. 7) while further increasing dV leads to a slight increase of this quantity. Since the width is dominated by dispersion in the transmission lines, its decrease with dV can only be of order of several percent, as it is observed experimentally (about 10%). The optimal situation might be to work with dV of the order of 25 V. In order to confir this statement, we study below the spatially-resolved two-dimensional images extracted from our detector and we measure the resolution in configuration identical to that of Fig. 7.

D. Spatial accuracy

As mentioned previously in Sec. II, the position of a single incoming particle is extracted from the timing signals out of the delay line anode. For this reason it is related to the pulse amplitude and width studied in Sec. IV. We now investigate

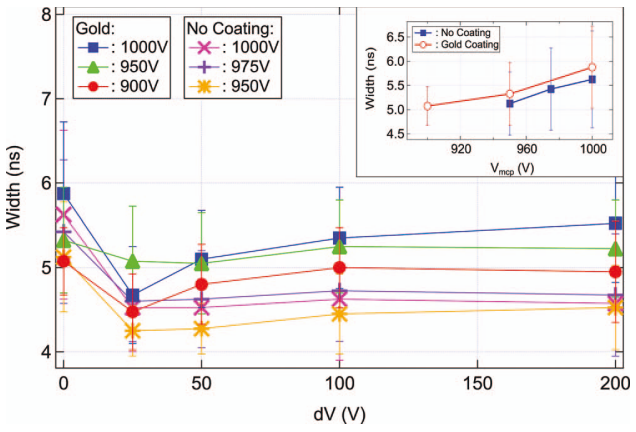

FIG. 7. The width of the pulses from the delay line, averaged over all four channels. Inset: The width of the pulses at $dV = 0$ V for increasing V_{mcp}.

the accuracy to which such a position can be reconstructed and how this quantity varies with the MCP coating and the interplate voltage dV.

A measurement of the accuracy with which the position of a single incoming particle is detected can be obtained as follows from the four arrival times t_{x1}, t_{x2}, t_{y1}, and t_{y2}, the fluctuation of which limit the detector accuracy. We consider the quantity D define as

$$D = (t_{x_1} + t_{x_2}) - (t_{y_1} + t_{y_2}). \quad (1)$$

Here, $t_{x1} + t_{x2} - 2t_0$ and $t_{y1} + t_{y2} - 2t_0$ are equal to the propagation time from one end to the other in the two orthogonal delay lines with t_0 the arrival time of the incoming particle on the delay lines. For identical delay lines, these two quantities are equal and $D = 0$. In practice the situation is more complicated. On the one hand, the total lengths of the two delay lines are not strictly equal, leading to an offset for D (we note that in the experiment this offset depends on the actual position we are looking at on the delay line). On the other hand, the quantity D fluctuate from one detected event to the other, leading to a broadening of the distribution of D around its mean value (see inset in Fig. 8). We defin the accuracy of our detector from the standard deviation σ_D of the statistical distribution of D. In spatial units, the accuracy is given by (see Appendix C for details), with c the speed of light:

$$d_x = \frac{\sigma_D}{2\sqrt{2}} \frac{c}{300}. \quad (2)$$

In Fig. 8 we plot the mean spatial accuracy d_x as a function of dV and for different configurations At a fi ed flu of incoming particles, we observe that the detector without coating has a better spatial accuracy than the MCP with gold coating. Also, the accuracy of the gold coated detector is better when the flu is lower. This effect may be related to the changes in the pulse height distribution as a function of the flu and discussed in Ref. 16: at higher detected flu the pulse height distribution may broaden, leading to a smaller signal-to-noise ratio. We do not observe a great difference between different voltages V_{mcp}.

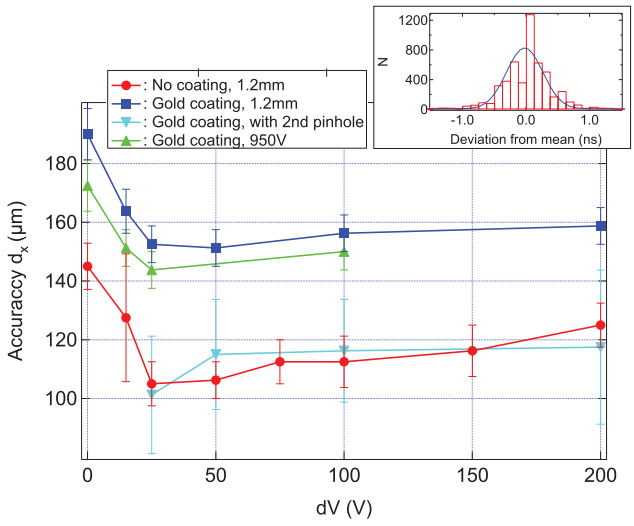

FIG. 8. Spatial accuracy d_x (as define in Eq. (2)) of the detectors as a function of dV and for different experimental configurations Inset: Typical histogram of the centered distribution of D values measured in the experiment and from which σ_D is obtained.

Finally, we observe that the accuracy of the detector decreases at low voltage values dV and seems optimal for $dV \simeq 25$ V. This optimum dV value for the accuracy corresponds to the optimum values for both the amplitude and the width of the pulses as reported in the previous paragraphs. Nevertheless we believe the pulse amplitude—leading to an improved signal-to-noise ratio—to have a much larger effect on the accuracy than the pulse width as we shall explain now. First, the decrease in the accuracy (typically ∼20%) is much larger than that observed for the width (see Fig. 7) while compatible with the increase in the pulse amplitude (see Fig. 6). Second, in order to identify the underlying mechanism of our observations we have mounted an MCP pair with a voltage difference dV on top of a phosphor screen (instead of a delay line anode). We observed that increasing dV from 0 V to ∼100 V slowly collimates the electron beam, to finall reach excitation of almost a single channel in the second plate. On the other hand, the spot intensity on the phosphor screen strongly increases for dV in the range 0 V–50 V (electrons accelerated in between MCPs having a higher probability of exciting secondary electrons in the second MCP, see Sec. II) to slightly decrease for values of $dV \geq 100$ V. From these complementary studies and our observations on the pulse amplitude and width, we conclude that the main effect for the observed smaller accuracy comes from a better signal-to-noise ratio rather than from the interplate spatial collimation (even though the latter should have a small positive effect as well).

We attribute the latter increase of d_x for $dV > 50$ V to two origins: (i) the signal-to-noise ratio slightly worsens as the pulse amplitude decreases with increasing dV; (ii) the increase in the electron beam velocity with dV broadens the spot of the electron shower on the delay line anodes (see Appendix B).

V. CONCLUSION

In this work we have made a detailed investigation of the effect of a microlayer of gold on the input layer of a MCP and adding a voltage between two slightly separated plates. We fin that the detector with the gold layer exhibits larger count rates than the detector without coating, confirmin the results of Ref. 17. In addition, pulses extracted from the front of the MCP and pulses obtained from the delay lines show that the gold coated plate yields larger electron showers, leading to a better quantum efficien y. However, we demonstrate here that the gold layer has a negative effect on the spatial accuracy, which is crucial for the 3D reconstruction of particles falling onto the detector. At a given flu of incoming particles the detector with the gold coating has an accuracy of 30% worse than the one without gold. We fin that a voltage difference dV between the plates both increases the height of the pulses and reduces the width of the pulses on the delay line, by collimating the electron beam in between the two plates and increasing the energy of the electrons. Obviously, such behavior is very dependent on the distance between the two plates. The addition of dV results in an increase of 20% in accuracy for both the coated and non coated plates, an effect coming

from an improved signal-to-noise ratio. Our results demonstrate that using a voltage difference possibly combined with a gold coated plate, leads to improved performance of MCPs used in conjunction with delay line anodes. The improvement in the accuracy with the interplate voltage will probably allow more accurate 3D reconstruction of single particle, metastable atoms detectors, whereas the improvement in the efficien y due to the gold layer could allow easier detection at lower incoming flu es.[5–7]

ACKNOWLEDGMENTS

We thank P. Roncin and R. Sellem for discussions. Our collaboration was made been possible thanks to the Triangle de la Physique through the grant DETAMI. We acknowledge support from the LUMAT Federation, the Triangle de la Physique (Contract No. 2010-062T), the IFRAF Institute, the ANR and the ERC (Grant No. 267 775) Quantatop.

APPENDIX A: SPEED OF THE ELECTRONIC PULSE ALONG THE POSITION AXIS

As sketched in Fig. 2, the spatial position x of the incoming particle is encoded perpendicularly to the current propagation in the delay line wires. As a result the effective velocity along the position axis x is smaller than the signal speed, the later being close to light speed in vacuum ($v \simeq c/3$).

This effective velocity is equal to the ratio of the distance between two adjacent loops and the time the signal needs to propagate through one loop. In the case of our Roentdek DLD80, the effective velocity is close to $v_x = v/100 = c/300$.

APPENDIX B: TIME-OF-FLIGHT BETWEEN MCPS AND DELAY LINE ANODES

The size of the electron shower hitting the delay line strongly depends on the kinetic energy of the electrons. On the one hand, a larger longitudinal velocity at a f xed transverse velocity implies a smaller time-of-fligh between the MCPs and the delay lines, therefore leading to a smaller size of the shower on the delay lines. On the other hand, a larger transverse velocity at a f xed longitudinal one leads to a larger size of the shower on the delay lines.

When electrons are further accelerated while propagating through the MCPs (either by increasing the voltage V_{mcp} or dV), both the longitudinal and transversal kinetic energy of the electron shower exiting the channel plates increase.[22] The net effect of such an acceleration on the size of the electron shower on the delay lines is not straightforward as there is a competition between a smaller time-of-fligh and a larger transverse expansion. The following simple argument corroborates the statement that the spot size actually increases with the kinetic energy of the electrons exiting the MCPs.

We take V_g the voltage difference and d the spatial distance between the lower face of the MCP and the delay line. We note eV_n and eV_t, respectively, the longitudinal and transverse electron energies at the output of the lower MCP face. From the electrostatic force applied onto the electrons we derive the time of f ight between MCPs and the delay lines,[18]

$$t_{tof} = \sqrt{\frac{2m}{e}}\,\frac{d}{V_g}\,(\sqrt{V_n + V_g} - \sqrt{V_n}). \tag{B1}$$

The transverse spatial expansion of the electron shower on the delay lines is then approximately given by

$$\Delta_t = \sqrt{\frac{2eV_t}{m}}\,t_{tof}. \tag{B2}$$

Assuming that V_n and V_t increases the same way with the voltage V_{mcp} applied on the MCPs, one find that the larger the voltage V_{mcp} the larger the electron shower size Δ_t on the delay lines.

APPENDIX C: RELATING THE TIME ACCURACY OF THE DELAY LINE TO THE SPATIAL ACCURACY ON THE MCPs

Let us defin L the length of the wire of one delay line. It takes a time L/v for an electronic pulse to travel from one end to the other at the speed v.

The origin of spatial coordinates is set at the center of the delay lines and position is encoded perpendicularly to the wire of the transmission line. As explained in Appendix A, the effective velocity v_x of pulses along the position axis x is smaller than that (v) of propagation in the wire. Writing t_0 the arrival time on the delay line of the electronic shower from the MCP and x_0 its spatial coordinate, electronic pulses arrive at the end of the delay line wire at times:

$$t_{x,1} = t_0 + \frac{L}{2v} - \frac{x_0}{v_x}, \tag{C1}$$

$$t_{x,2} = t_0 + \frac{L}{2v} + \frac{x_0}{v_x}. \tag{C2}$$

Therefore the spatial coordinate x_0 can simply be extracted from $t_{x,1}$ and $t_{x,2}$ as $x_0 = (t_{x,2} - t_{x,1})v_x/2$. Assuming uncorrelated errors on the measurement of time $t_{x,1}$ and $t_{x,2}$ and equal standard deviation (namely $\sigma_{t_{x,1}} = \sigma_{t_{x,2}} = \sigma_t$), we can write the standard deviation of x as $\sigma_x^2 = v_x^2\sigma_t^2/2$. This quantity σ_x define what we refer to as the spatial accuracy of our detector. Under these assumptions for both axes of the delay line, the quantity D, define in Eq. (1), has a standard deviation of the form $\sigma_D^2 = 4\sigma_t^2$. Combining the last two equations allows us to relate the error on coordinate x to the distribution of D values as

$$\sigma_x = \frac{\sigma_D\, v_x}{2\sqrt{2}} = \frac{\sigma_D}{2\sqrt{2}}\,\frac{c}{300}. \tag{C3}$$

[1] J. L. Wiza, Nucl. Instrum. Methods **162**(1–3), 587–601 (1979); G. W. Fraser, Nucl. Instrum. Methods **221**, 115 (1984).
[2] M. Barat, J. C. Brenot, J. A. Fayeton, and Y. J. Picard, Rev. Sci. Instrum. **71**, 2050 (2000).
[3] W. Vassen, C. Cohen-Tannoudji, M. Leduc, D. Boiron, C. Westbrook, A. Truscott, K. Baldwin, G. Birkl, P. Cancio, and M. Trippenbach, Rev. Mod. Phys. **84**, 175 (2012).
[4] O. Jagutzki, V. Mergel, K. Ullmann-Pfl ger, L. Spielberger, U. Spillmann, R. Döirner, and H. Schmidt-Böcking, Nucl. Instrum. Methods Phys. Res. A **477**, 244 (2002).

[5]T. Jeltes, J. M. McNamara, W. Hogervorst, W. Vassen, V. Krachmalnicoff, M. Schellekens, A. Perrin, H. Chang, D. Boiron, A. Aspect, and C. I. Westbrook, Nature (London) **445**, 402–405 (2007).
[6]M. Schellekens, R. Hoppeler, A. Perrin, J. V. Gomes, D. Boiron, A. Aspect, and C. I. Westbrook, Science **310**, 648 (2005).
[7]S. S. Hodgman, R. G. Dall, A. G. Manning, K. G. H. Baldwin, and A. G. Truscott, Science **331**, 1046–1049 (2011).
[8]J.-C. Jaskula, M. Bonneau, G. B. Partridge, V. Krachmalnicoff, P. Deuar, K. V. Kheruntsyan, A. Aspect, D. Boiron, and C. I. Westbrook, Phys. Rev. Lett. **105**, 190402 (2010).
[9]E. Altman, E. Demler, and M. D. Lukin, Phys. Rev. A **70**, 013603 (2004).
[10]S. Fölling, F. Gerbier, A. Widera, O. Mandel, T. Gericke, and I. Bloch, Nature (London) **434**, 481 (2005).
[11]M. Greiner, C. A. Regal, J. T. Stewart, and D. S. Jin, Phys. Rev. Lett. **94**, 110401 (2005).
[12]T. Rom, Th. Best, D. van Oosten, U. Schneide, S. Fölling, B. Paredes, and I. Bloch, Nature (London) **444**, 733 (2006).
[13]V. Guarrera, F. Fabbri, L. Fallani, C. Fort, K. M. R. van der Stam, and M. Inguscio, Phys. Rev. Lett. **100**, 250403 (2008).
[14]T. Kitagawa, A. Aspect, M. Greiner, and E. Demler, Phys. Rev. Lett. **106**, 115302 (2011).
[15]See for example E. Liénard, M. Herbane, G. Ban, G. Darius, P. Delahaye, D. Durand, X. Fléchard, M. Labalme, F. Mauger, A. Mery, O. Naviliat-Cuncic, and D. Rodriguez, Nucl. Instrum. Methods Phys. Res. A **551**, 375–386 (2005).
[16]G. W. Fraser, M. T. Pain, J. E. Lees, and J. F. Pearson, Nucl. Instrum. Methods Phys. Res. A **306**, 247–260 (1991).
[17]A. S. Tremsin, J. F. Pearson, G. W. Fraser, W. B. Feller, and P. White, Nucl. Instrum. Methods Phys. Rev. A **379**, 139–141 (1996).
[18]D. Rogers and R. F. Malina, Rev. Sci. Instrum. **53**, 1438 (1982).
[19]C. Firmani, E. Ruiz, C. W. Carlson, M. Lampton, and F. Paresce, Rev. Sci. Instrum. **53**, 570 (1982).
[20]J. L. Wiza, P. R. Henkel, and R. L. Roy, Rev. Sci. Instrum. **48**, 1217 (1977).
[21]F. Paresce, Appl. Opt. **14**(12), 2823–2824 (1975).
[22]E. H. Eberhardt, Appl. Opt. **18**(9), 1418 (1979).

An oscillator circuit to produce a radio-frequency discharge and application to metastable helium saturated absorption spectroscopy

F. Moron, A. L. Hoendervanger, M. Bonneau, Q. Bouton, A. Aspect,
D. Boiron, D. Clément,[a] and C. I. Westbrook
Laboratoire Charles Fabry, Institut d'Optique, CNRS, Univ Paris Sud,
2 Avenue Augustin Fresnel, 91127 Palaiseau Cedex, France

(Received 16 February 2012; accepted 7 April 2012; published online 26 April 2012)

We present a rf gas discharge apparatus which provides an atomic frequency reference for laser manipulation of metastable helium. We discuss the biasing and operation of a Colpitts oscillator in which the discharge coil is part of the oscillator circuit. Radiofrequency radiation is reduced by placing the entire oscillator in a metal enclosure. © *2012 American Institute of Physics*. [http://dx.doi.org/10.1063/1.4705999]

INTRODUCTION

At present, all laser cooling and trapping of noble gas atoms is performed using atoms in excited, metastable states.[1] An important part of such manipulation experiments is an absolute optical frequency reference to maintain the laser frequency at appropriate values. Such a reference is typically provided by an auxiliary low pressure gas cell in which a plasma discharge produces metastable atoms and in which saturated absorption spectroscopy can provide a spectroscopic signal to lock a laser on a desired atomic transition. Such discharge cells have employed both direct current)[2,3] and radiofrequency (rf) (Refs. 4–7) techniques. Radiofrequency discharges are appealing because they lend themselves to the use of sealed glass cells[5–7] with no internal metal parts. On the other hand, they have the drawback of radiating rf power into a laboratory in which many other sensitive electrical measurements are being performed, rf evaporation in a magnetic trap, for example.[8] In addition, when rf power is generated by an external oscillator and amplifie , impedance matching to the discharge coil is important and mismatch can result in substantial losses.[5]

In this work, we describe an efficient low cost apparatus which provides good spectroscopic signals in a rf-discharge cell of helium. To avoid impedance matching problems, we use a Colpitts oscillator design in which the discharge coil is included as part of the oscillator circuit.[9] We describe a biasing method which allows us to easily vary the rf amplitude during operation. This feature is important because the voltage necessary to strike the discharge is much higher than that necessary to maintain it or that which optimizes the saturated absorption signal. The entire apparatus can operate in a metal enclosure, thus limiting rf interference in the laboratory.

RADIO-FREQUENCY COLPITTS OSCILLATOR

The oscillator we use to generate the rf signal is a *LC* oscillator circuit in the Colpitts configuratio [9] (see Fig. 1). The resonant frequency f_0 is close to 21 MHz before the plasma turns on in the cell. Our approach shares features with the work of Ref. 10 where the *LC* oscillator circuit is in the Hartley configuration In both circuits, the resonant frequency is set by the inductance of the coil wrapped around the glass cell (as well as by the capacitors *C*4 and *C*5 of Fig. 1), therefore avoiding any problem of impedance matching between the oscillator and the load.[5] Below we discuss our circuit in more detail and emphasize the differences with the work of May and May,[10] especially with regard to the possibility to start the plasma without the need for an additional Tesla coil.

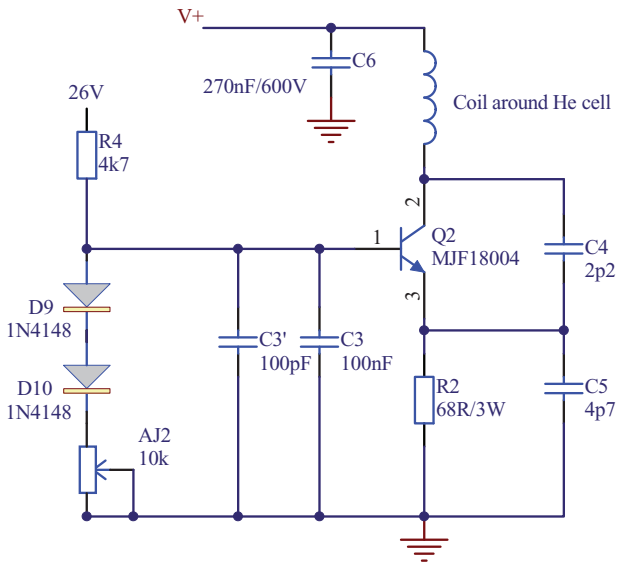

FIG. 1. Colpitts oscillator generating a rf signal in the frequency range of 12–21 MHz with varying amplitude V_+ (160–360 V) in the coil which is wrapped around a sealed glass cell containing about 1 mbar of He gas.

[a]Author to whom correspondence should be addressed. Electronic mail: david.clement@institutoptique.fr.

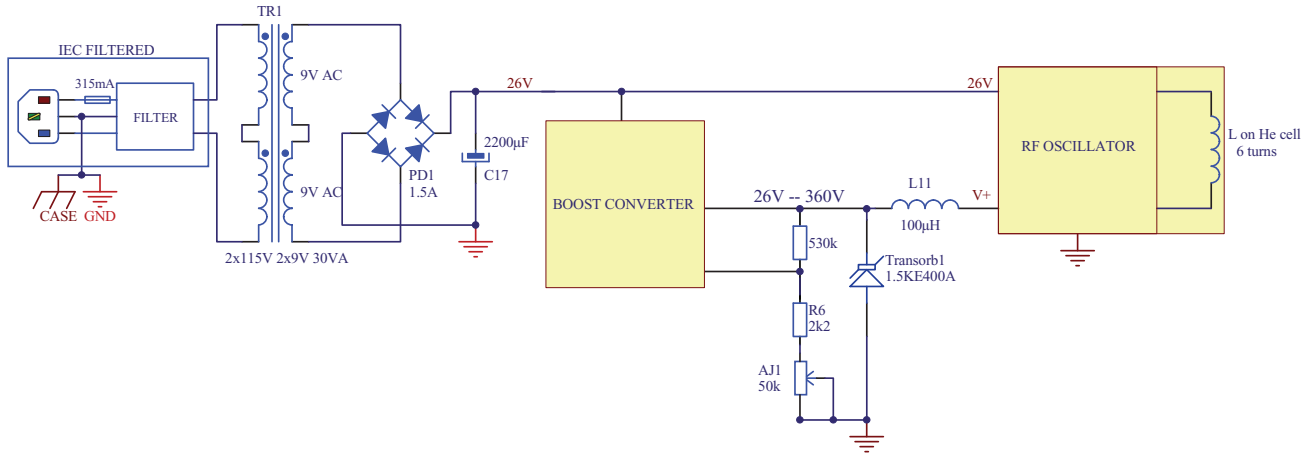

FIG. 2. Schematic of the electronic circuit located inside the box (see details in the Appendix). The potentiometer *AJ*1 controls the voltage V_+ and can be seen on the side of the box in the picture of Fig. 3.

Starting a plasma discharge requires much more power than maintaining one. For this reason, in addition to the supply which generates the steady state power, a Tesla coil is often used to strike the discharge.[10] To avoid the Tesla coil, we supply the Colpitts circuit with a varying voltage V_+ allowing a high enough power to start the plasma (up to 30 W with $V_+ = 360$ V). V_+ is given by a boost converter the details of which can be found later in the text (see Fig. 2). Once the plasma is on, we reduce V_+ to a value which optimizes our spectroscopic observations (see text below and Fig. 4). The need to tune V_+ made us choose the scheme described in Fig. 1 where the base bias of the transistor $Q2$ is connected to a constant positive voltage of 26 V, unlike common base Colpitts oscillators. This solution has two advantages. First, it allows us to solve the problem of adjusting the circuit to obtain an oscillation. Indeed, oscillation of the Colpitts circuit is critical[9] and requires adjustment of the potentiometer *AJ*2 (see Fig. 1) to adapt the transistor base current. In the common base Colpitts configuration the tuning of V_+ would require adjusting *AJ*2 every time V_+ is modified Having a constant base bias voltage (and thus a constant transistor base current) allows a single adjustment of *AJ*2. Second, electrical consumption is much reduced with the constant 26 V voltage compared to that using V_+.

Because the inductance of the circuit depends on the state of the plasma, the resonant frequency of the circuit changes with the applied voltage V_+. In our circuit, the resonant frequency with the plasma on varies from ~12 MHz at $V_+ = 140$ V to ~20 MHz at $V_+ = 360$ V. In practice, we start the plasma discharge at 21 MHz with full rf power ($\simeq$ 30 W with $V_+ = 360$ V) and then we reduce the rf amplitude to a working point where the resonant frequency happens to be 14 MHz ($\simeq$ 7 W with $V_+ = 170$ V).

ELECTRONICS INSIDE THE CLOSED BOX

The oscillator is supplied by a boost converter as depicted in Fig. 2 (see Fig. 5 for a more detailed diagram). The use of a boost converter is motivated by its efficien power production and its compactness. The converter provides enough power to start the plasma inside the cell and it allows us to later diminish the electrical power (through the potentiometer *AJ*1) in order to control the metastable atom density in the cell and thus the amount of absorption of the laser light propagating through the cell (see Fig. 4).

Two frequency f ltering elements have been placed in the electrical circuit. An inductance of 100μH (inductance L11 in Fig. 2) decouples the Colpitts oscillator from the boost converter. As the box is directly plugged onto the electrical network at 50 Hz, a line f lter prohibits any leak rf signal from propagating in the electrical network.

All components shown in Fig. 2 are placed in an aluminum box of thickness 3 mm to reduce the rf signal radiated into the laboratory. For such a box, the skin depth for a 10 MHz rf signal is 35 μm, corresponding to an enormous attenuation over 3 mm. However, the holes (of diameter 5 mm)

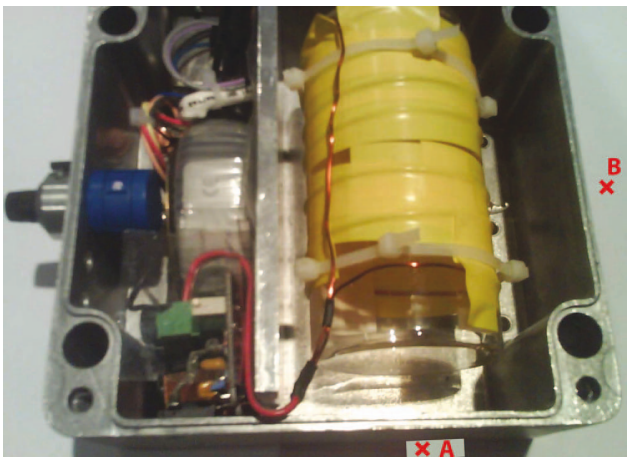

FIG. 3. View inside the box with the rf-discharge cell. The box has dimensions 160 mm × 160 mm × 90 mm. A metal shield separates the transformer and the electronic circuit from the glass cell and the coils. Points A and B are the positions where we measure the current induced by the radiated magnetic fiel in a 5 cm-loop. Point A lies in front of the 5 mm hole to allow the laser beam to enter the cell.

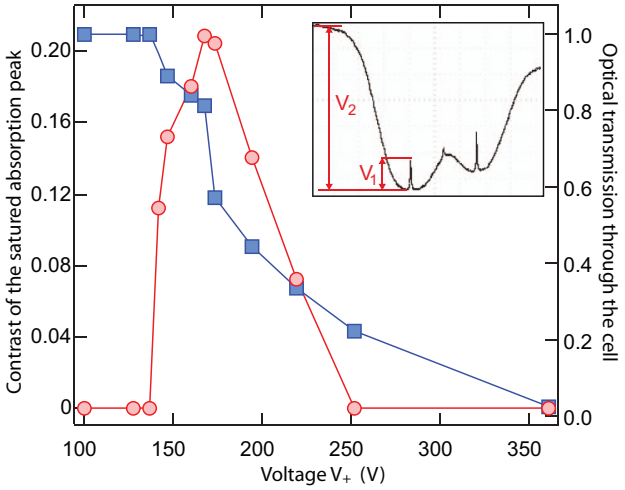

FIG. 4. Contrast of the saturated absorption peak (red circles, left scale) and optical transmission of the laser through the glass cell (blue squares, right scale) as a function of the voltage V_+. The minimum voltage to maintain the plasma is $V_+ = 130$V. Data points below this value are taken without plasma on. Lines are guides to the eyes. Inset: picture of the saturated absorption spectrum of metastable helium. The ratio of voltages V_1/V_2 define the contrast of the saturated absorption peak of the $2^3S_1 - 2^3P_2$ transition. The other absorption peak visible corresponds to the transition $2^3S_1 - 2^3P_1$.

required for letting the laser beam propagate through the cell will limit the attenuation of the radiated rf signal in the laboratory. The picture in Fig. 3 shows a view inside the box. The electrical circuit of Fig. 2 is on the left-hand side and the He glass cell wrapped with the coil is on the right-hand side of the picture. Having rf signals confine inside the box avoids both problems of rf radiation from the coil wrapped around the cell as well as rf radiation through cables that would connect an external rf generator.[5]

Ignition of the plasma is more difficul with the box closed, presumably because of parasitic capacitive coupling to the box walls. Indeed, the initial version of the boost converter did not provide enough power (maximum value $V_+ \simeq 280$ V instead of 360 V) to start the discharge with the box closed. Using a more powerful boost converter as described here, permits ignition of the plasma with the box closed in a few seconds. We emphasize that the conditions for ignition of the plasma are related to the properties of the coil, the box, and of the sealed glass cell (*e.g.,* the gas pressure, about 1 mbar in our case).

MEASUREMENT OF rf ATTENUATION

To test the attenuation of the radiated rf signal when the box is closed, we have measured the voltage amplitude of the signal picked up by a loop of copper wire with a diameter of 5 cm similar to that of the glass cell. The induced current in the loop is proportional to the rf magnetic fiel and the measured voltage amplitude is therefore proportional to the amplitude of the radiated rf field We have repeated this measurement at point A, in front of the hole made in the box (just in front of the glass cell) and at point B, on the side of the glass cell, both with the box closed and opened. The attenuation of the magnetic fiel amplitude at point A is ∼100 while it is ∼300 at point B. This difference is expected as point A lies in front of the small hole made in the box for the laser beam to propagate. In this respect point B is more representative of the attenuation on the radiated rf magnetic fiel in the lab room.

ABSORPTION SPECTROSCOPY SIGNAL

We have used our device to lock a laser to the atomic transition $2^3S_1 - 2^3P_2$ at 1083nm of metastable He. Our laser source is a fibe -laser with 2 W output power. A small part of the laser power is double-passed in an acousto-optic modulator to produce a 10 kHz frequency modulation (FM) of the laser frequency. The FM laser beam is sent through the cell in a saturated absorption spectroscopy configuration

When the plasma is on, optical transmission goes to zero with increasing V_+ as the density of metastable helium atoms increases. In Fig. 4, we plot a measurement of the optical transmission through the glass cell as a function of the voltage V_+. The transmission is unity for voltages below the minimum for maintaining the plasma (130 V). To choose the working point we monitor the amplitude of the saturated absorption peak. The contrast of this peak, plotted in Fig. 4, is define as the ratio of the voltage amplitude of the saturated absorption peak to that of the total absorption (as sketch in the inset of Fig. 4). The optimum value for V_+ corresponds to the deepest saturated absorption feature. It happens to be $V_+ \simeq 170$ V, well below the ignition point of the plasma and just above the minimum voltage to maintain the plasma. Finally, an error signal is obtained from the demodulated absorption signal.[11] We easily obtain stable locking with a few mW of laser power delivered to the cell. Thanks to the use of a toroidal transformer (TR1 in Fig. 2), we observe no 50 Hz oscillations in the absorption signal.

CONCLUSION

With the exception of the glass cell, all the components of our device are inexpensive and readily available. The attenuation provided by the metal box seems to be adequate for continuous use in our laboratory. The design should be easily adaptable to other metastable species.

ACKNOWLEDGMENTS

We acknowledge support from the Triangle de la Physique—Contract No. 2010-062T, the IFRAF Institute, the ANR and the ERC—Grant No. 267 775 Quantatop.

APPENDIX

See Fig. 5.

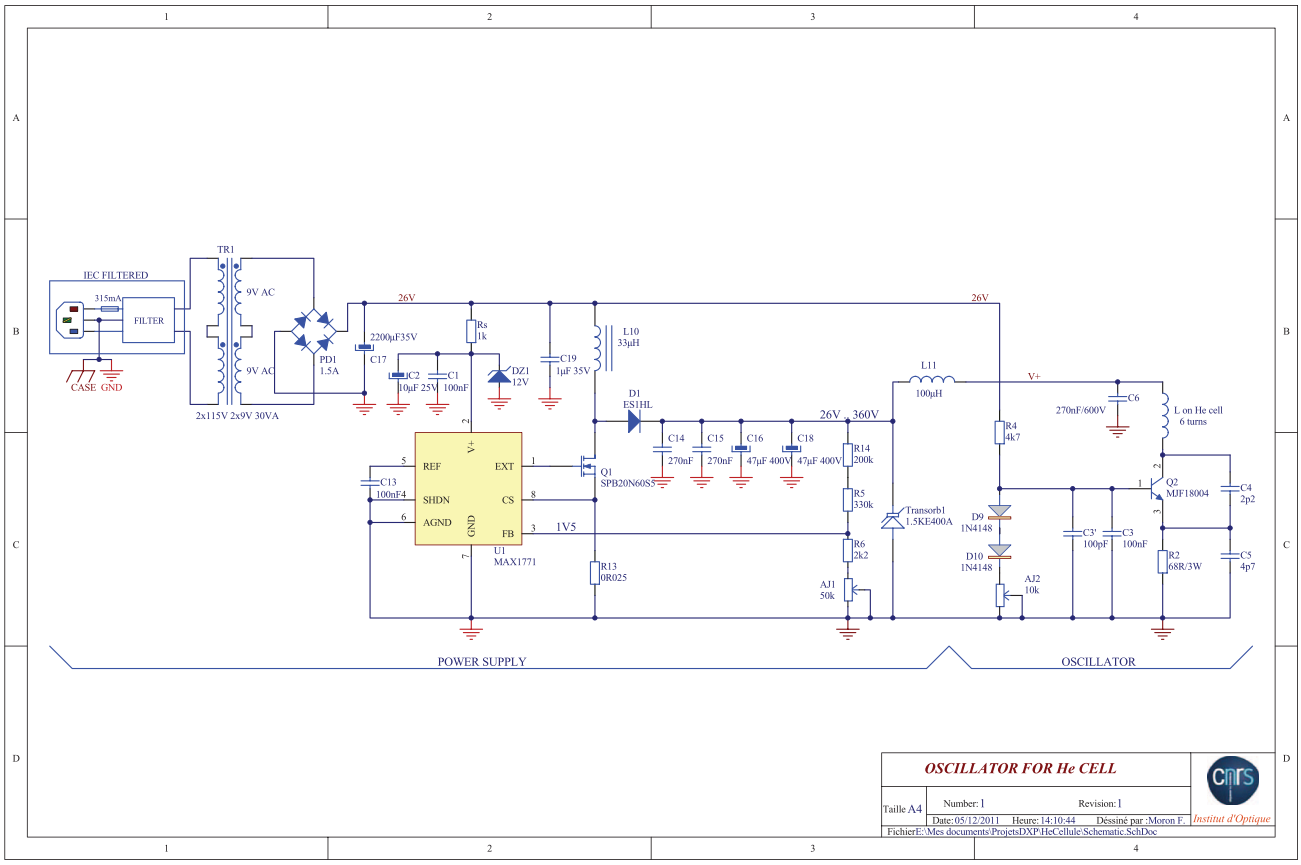

FIG. 5. Complete schematic diagram of the electronics.

[1]W. Vassen *et al.*, Rev. Mod. Phys. **84**, 175 (2012).
[2]W. Lu, D. Milic, M. D. Hoogerland, M. Jacka, K. Baldmwin, and S. J. Buckman, Rev. Sci. Instrum. **67**, 3003 (1996).
[3]J. E. Lawler, A. Siegel, B. Couillaud, and T. W. Hansch, J. Appl. Phys. **52**, 4375 (1981).
[4]C. Y. Chen, K. Bailey, Y. M. Li, T. P. O'Connor, Z.-T. Lu, X. Du, L. Young, and G. Winkler, Rev. Sci. Instrum. **72**, 271 (2001).
[5]C. I. Sukenik and H. C. Busch, Rev. Sci. Instrum. **73**, 493 (2002).
[6]D. I. Hoult and C. M. Preston, Rev. Sci. Instrum. **63**, 1927 (1992).
[7]J. C. J. Koelemeij, W. Hogervorst, and W. Vassen, Rev. Sci. Instrum. **76**, 033104 (2005).
[8]A. Browaeys, A. Robert, O. Sirjean, J. Poupard, S. Nowak, D. Boiron, C. I. Westbrook, and A. Aspect, Phys. Rev. A **64**, 034703 (2001).
[9]A. E. Clifford and A. H. Wing, *Electronic Circuits and Tubes* (McGraw-Hill, New York, 1947).
[10]R. D. May and P. H. May, Rev. Sci. Instrum. **57**, 2242 (1986).
[11]N. Vansteenkiste, C. Gerz, R. Kaiser, C. Salomon, and A. Aspect, J. Phys. II **1**, 1407–1428 (1991).

Three-Dimensional Laser Cooling at the Doppler limit

R. Chang,[1] A. L. Hoendervanger,[1] Q. Bouton,[1] Y. Fang,[1,2] T. Klafka,[1] K. Audo,[1] A. Aspect,[1] C. I. Westbrook,[1] and D. Clément[1]

[1] *Laboratoire Charles Fabry, Institut d'Optique, CNRS, Univ. Paris Sud, 2 Avenue Augustin Fresnel 91127 PALAISEAU cedex, France*

[2] *Quantum Institute for Light and Atoms, Department of Physics, State Key Laboratory of Precision Spectroscopy, East China Normal University, Shanghai, 200241, China*

Many predictions of Doppler cooling theory of two-level atoms have never been verified in a three-dimensional geometry, including the celebrated minimum achievable temperature $\hbar\Gamma/2k_B$, where Γ is the transition linewidth. Here, we show that, despite their degenerate level structure, we can use Helium-4 atoms to achieve a situation in which these predictions can be verified. We make measurements of atomic temperatures, magneto-optical trap sizes, and the sensitivity of optical molasses to a power imbalance in the laser beams, finding excellent agreement with the Doppler theory. We show that the special properties of Helium, particularly its small mass and narrow transition linewidth, prevent effective sub-Doppler cooling with red-detuned optical molasses.

I. INTRODUCTION

The seminal proposals for Doppler cooling in 1975 [1, 2] prompted the realization of the first optical molasses in the 1980's [3], a major landmark in the field of laser cooling and trapping of atoms [4–6]. The physical concepts behind the Doppler cooling mechanism are both simple and elegant, and predict the achievement of very low temperatures. They remain to this day the starting point of most courses on laser cooling and degenerate gases [7]. It is thus ironic that not only, to our knowledge, quantitative predictions of this simple model have not been experimentally validated, but moreover, experimental studies have found results quantitatively and even qualitatively different from the predictions of the model [8–11].

Today, it is well known that for most atoms with a degenerate ground state manifold, the complex multilevel structure gives rise to new mechanisms which come to dominate the cooling process, yielding ultimate temperatures far below those predicted by Doppler theory [7, 12, 13]. Accounting for these sub-Doppler mechanisms allows one to understand the qualitative and quantitative experimental observations. In contrast, three-dimensional laser cooling of an atomic sample in agreement with the celebrated Doppler model is still lacking [14]. Recent work with alkaline-earth and rare-earth atoms, which exhibit a non-degenerate ground state, have provided natural candidates to study cooling in a purely Doppler regime. Yet, to our knowledge, all experiments with these atoms have found temperatures above the expected Doppler limit in magneto-optical traps (MOTs) [16–28]. This discrepancy has been attributed to the presence of additional heating mechanism [29, 30].

Here we report the three-dimensional laser cooling of metastable Helium-4 gases in the Doppler regime. We monitor the temperature of the gas as a function of the laser detuning δ, as shown in Fig. 1, finding excellent agreement with Doppler theory. The temperature reaches a minimum for a detuning $\delta = -\Gamma/2$ (where Γ is the transition linewidth), while increasing with $|\delta|$, in contrast with sub-Doppler molasses. In addition, the

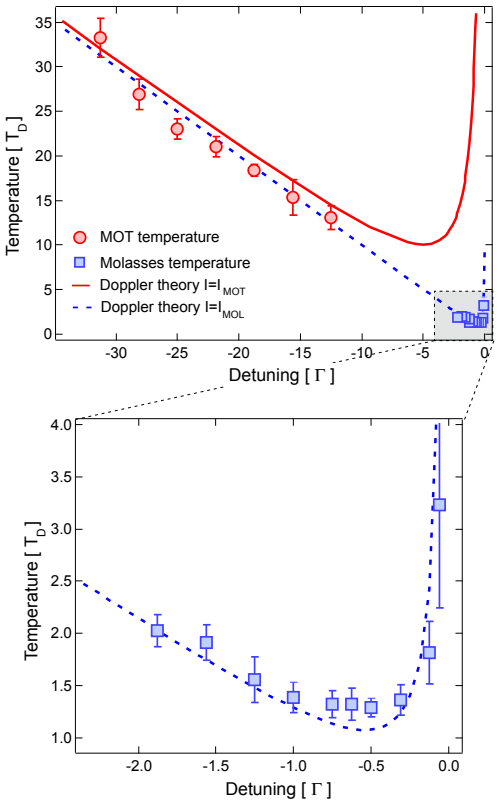

FIG. 1. Temperature in magneto-optical trap and optical molasses as a function of the detuning of the laser cooling beams. Temperatures are extracted from monitoring time-of-flight expansion of the gas. Error bars (one standard deviation) reflect the error from fitting. The total intensity (sum of the six beams) used in the experiment are respectively $I_{\mathrm{MOT}} = 100\ I_{\mathrm{sat}}$ and $I_{\mathrm{MOL}} = I_{\mathrm{sat}}/10$. The lines are the results of Doppler theory of Eq. 7, for intensities I_{MOT} (solid line) and I_{MOL} (dashed line).

drift velocities of optical molasses with unbalanced power between counter-propagating beams are far larger than those expected of sub-Doppler molasses [9]. We use the $2^3S_1 \rightarrow 2^3P_2$ transition of Helium-4, which allows in principle for sub-Doppler cooling, and yet our results show no evidence for such effects. We present a physical argument showing that the special properties of metastable Helium (^{4}He*) strongly inhibit sub-Doppler cooling in the experimental configuration we probe.

II. THEORETICAL CONSIDERATIONS

A. Laser cooling mechanisms

Laser cooling of an atomic gas relies upon the exchange of momentum between the atoms and the near-resonant light field, resulting in a mechanical force F on the atoms. For small velocities, the equilibrium temperature T of these cooling schemes is given by the ratio of a momentum-space diffusion constant $\mathcal{D}$ (given by the fluctuations of the force) to the velocity-damping coefficient α. In the following we will first recall the main theoretical results for laser Doppler cooling of a two-level atom, then proceeding to discuss a multi-level atom where sub-Doppler mechanisms may appear.

The mechanical interaction of a near-resonant light beam (frequency $\omega/2\pi$) with a two-level atom (atomic resonance frequency $\omega_0/2\pi$) is dominated by the radiation pressure effect and its associated force [9]. This light-matter interaction is characterised by the laser detuning from resonance $\delta = \omega - \omega_0$, the laser intensity I, the natural linewidth of the transition Γ, and the saturation intensity of the transition I_{sat}. A convenient physical quantity is the generalized saturation parameter

$$s = \frac{s_0}{1 + 4\delta^2/\Gamma^2}, \tag{1}$$

which characterizes the excited state population in a 2-level atom. Here $s_0 = I/I_{sat} = 2\Omega^2/\Gamma^2$ is the on-resonance saturation parameter, and Ω is the Rabi frequency.

At low saturation of the atomic transition $s \ll 1$ and small velocities $|kv| \ll |\delta|$, the average force acting on a two-level atom moving at velocity v takes the form $F_{2\text{level}} = -\alpha_{2\text{level}} v$ with

$$\alpha_{2\text{level}} = -4\hbar k^2 \frac{2\delta/\Gamma \; 2\Omega^2/\Gamma^2}{(1 + 2\Omega^2/\Gamma^2 + (2\delta/\Gamma)^2)^2}. \tag{2}$$

Here k is the photon wavevector, and $\hbar$ the reduced Planck's constant. The force $F_{2\text{level}}$ is plotted in Figure 2 (dashed line) for the typical experimental parameters of optical molasses.

Calculating the diffusion constant $\mathcal{D}_{2\text{level}}$ for the two-level atom, one can obtain the equilibrium temperature $k_B T_{2\text{level}} = \mathcal{D}_{2\text{level}}/\alpha_{2\text{level}}$, where k_B is Boltzmann's constant. Following the generalization to cooling in 3D [9], the temperature of a 3D molasses formed by three orthogonal pairs of counter-propagating laser beams is,

$$k_B T_{2\text{level}} = \frac{\hbar\Gamma}{2} \frac{1 + I_{\text{tot}}/I_{\text{sat}} + (2\delta/\Gamma)^2}{4|\delta|/\Gamma}, \tag{3}$$

where the $I_{\text{tot}} = 6I$ is the total intensity resulting from all six laser beams. In the Doppler regime, the minimum possible temperature is achieved for a detuning $\delta = -\Gamma/2$ and vanishing intensity. This minimum is commonly referred to as the Doppler limit, $T_D = \hbar\Gamma/2k_B$.

We now turn the discussion to an atom with several ground-state levels where sub-Doppler mechanisms of cooling may be involved [9, 10, 12]. For this discussion we restrict ourselves to the atomic structure of the ^{4}He* atom on the $2^3S_1 \rightarrow 2^3P_2$ transition (see Fig. 2a), and the laser configuration used in the experiment: counter-propagating laser beams with opposite circular polarization (configuration $\sigma^+ - \sigma^-$) along three orthogonal axes.

Consider first a single axis of the system. Following the derivation from [31] an explicit formulation of the semi-classical force F on a moving atom can be obtained. This approach takes into account atomic coherence effects up to second-order in absorption-emission processes. In Fig. 2 we plot this force F along with that exerted on a two-level atom $F_{2\text{level}}$. In the low-velocity region (see Fig. 2c) the cooling force on the multi-level atom exhibits a sharp feature with an associated damping coefficient α significantly larger than that of a two-level atom. This feature arises from the presence of atomic coherences and two-photon processes, and is the signature of sub-Doppler cooling mechanisms. Since the momentum-space diffusion coefficient hardly changes, the new damping coefficient would lead one to expect sub-Doppler cooling.

In this configuration, the additional cooling results from a motion-induced population difference between the ground-state levels, and is referred to as $\sigma^+ - \sigma^-$ polarization gradient cooling. In a 3D configuration, it is well known that Sisyphus cooling can also occur due to spatially dependent light shifts of the atomic ground-state levels. The electric field from laser beams along orthogonal axes interfere, resulting in a modulation of the intensity, which in turn may lead to Sisyphus cooling as in a one-dimensional lin $\perp$ lin configuration. Within the parameter range of interest ($|\delta| \sim \Gamma$), both sub-Doppler effects result in similar velocity capture ranges and equilibrium temperatures [9, 10, 12].

The comparison between a 2-level and a multi-level atom presented in Fig. 2 suggests two important conclusions. On the one hand the two-photon structure occurs only in a small range close to zero velocity (see Fig. 2c). In particular, for typical experimental parameters with Helium-4 atoms this velocity range is smaller than the recoil velocity $v_R = \hbar k/m$, where m is the particle's mass. This implies that sub-Doppler cooling is highly ineffective in a red molasses of ^{4}He* since the velocity capture range for such processes is much smaller than the lowest velocity achievable through Doppler cooling. On the

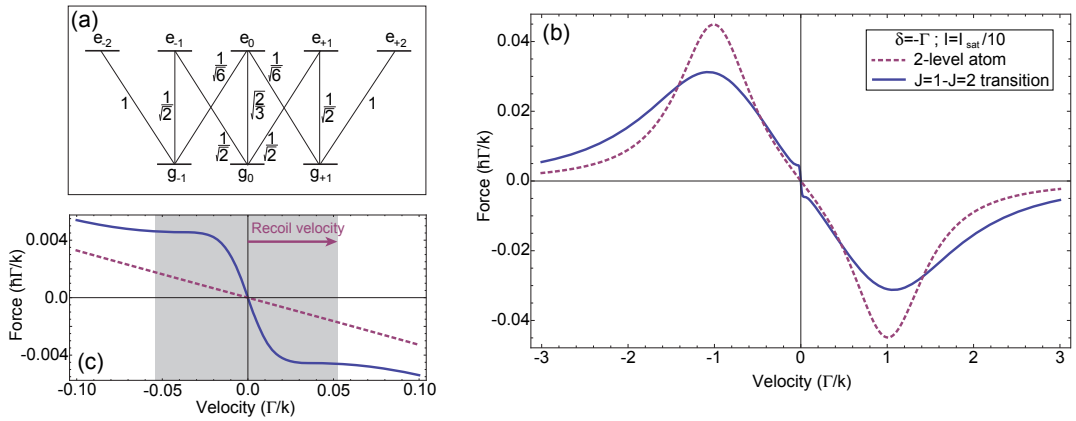

FIG. 2. **(a)** Atomic structure of a multi-level atom on a $J = 1 \to J' = 2$ transition. **(b)** Semi-classical force for a moving Helium atom in a $\sigma^+ - \sigma^-$ standing wave in the case of a two-level atom (dashed line, calculated as in [9]) and in that of a multi-level atom on a $J = 1 \to J' = 2$ transition (solid line, calculated as in [31]). Detuning and intensity correspond to typical values used in the experiment for optical molasses. **(c)** Expanded view of the low velocity region of the semi-classical forces, high-lighting the narrow range of the sub-Doppler feature. In both calculations, $s = 0.02$.

other hand, on a larger velocity range corresponding to Doppler velocities the friction coefficient for the multi-level atom is close to that of an effective two-level atom. In the following section, we will study the sub-Doppler capture velocity range in greater detail, showing that indeed ^{4}He* occupies a special place in the study of laser cooling mechanisms.

B. Capture range of sub-Doppler cooling

The velocity capture range for Doppler cooling is $v_c^D \simeq |\delta|/k$, directly reflecting the largest Doppler effect that can be compensated with a detuning δ from resonance. Similarly, the capture range for sub-Doppler cooling reflects the new physical mechanisms involved. For Sisyphus cooling (lin $\perp$ lin) to be effective, a ground-state atom should have a high probability of being optically pumped into a different ground-state atom on a wavelength distance [7]. In the semi-classical regime, this yields a condition on the atomic velocity $v \ll \Gamma'/k$, where Γ' is the optical pumping rate from one ground-state level to another ground-state level. The capture velocity is thus estimated to be $v_c^\perp \simeq \Gamma'/k$. In the case of $\sigma^+ - \sigma^-$ polarization gradient cooling, the capture velocity is given by the pumping rate at small detunings $\delta \sim -\Gamma$, $v_c^\sigma \simeq \Gamma'/k$ [31], while it is set by the light shift δ' of the ground-state levels at large detuning $|\delta| \gg \Gamma$, and is defined in the same way to be $v_c^\sigma \simeq |\delta'|/k$, [7]. The optical pumping rate and the light shift can be expressed conveniently as [7]

$$\Gamma' = \frac{\Gamma}{2}\frac{2\Omega^2/\Gamma^2}{1+2\Omega^2/\Gamma^2+(2\delta/\Gamma)^2} = \frac{\Gamma}{2}\frac{s}{1+s}$$
$$\delta' = \frac{\delta}{2}\frac{2\Omega^2/\Gamma^2}{1+2\Omega^2/\Gamma^2+(2\delta/\Gamma)^2} = \frac{\delta}{2}\frac{s}{1+s} \tag{4}$$

A large capture velocity range for sub-Doppler cooling requires a large Γ' and/or δ'. These two quantities are decreasing functions of the detuning δ when $|\delta| \gg \Gamma$ and δ' is maximum for $|\delta| = \Gamma/2$. The Doppler temperature (see Eq. 7) is minimum in the same range of detuning δ. In the following, we will therefore concentrate on laser detuning $|\delta|$ of the order of Γ, the most favorable situation to observe signatures of sub-Doppler cooling (although not the lowest temperature). The capture velocities for both sub-Doppler mechanisms are then of the same order,

$$v_c^\perp \simeq v_c^\sigma = v_c = \frac{\Gamma}{2k}\frac{s}{1+s}. \tag{5}$$

For the parameters represented in Fig. 2 ($s = 0.02$) and using Eq. 5, we find $v_c \simeq 0.01\Gamma/k$ in agreement with the numerical calculation of the force shown in Fig. 2. Identifying a root-mean-square (RMS) velocity v_D of a 3D gas at the Doppler temperature T_D, $\frac{1}{2}mv_D^2 = \frac{3}{2}k_BT_D$, we find

$$\frac{v_c}{v_D} = \sqrt{\frac{1}{6}\frac{T_D}{T_R}}\frac{s}{1+s}, \tag{6}$$

where T_R is the temperature associated with the recoil energy $k_BT_R = \hbar^2k^2/2m$. The capture velocity for sub-Doppler cooling is proportional to Γ (via v_D) and the square-root of the ratio T_D/T_R. Both these quantities are

Species	T_D/T_R	$v_c^{\rm up}/v_D$
^{4}He*	18.8	0.59
^{7}Li	39.4	0.85
^{23}Na	196	1.90
^{40}K	348	2.54
^{87}Rb	808	3.87
^{133}Cs	1413	5.12

TABLE I. Ratio T_D/T_R and estimated maximum capture velocity $v_c^{\rm up}/v_D$ ($s_{max} = 1/2$) for several commonly laser-cooled atoms.

small in the case of ^{4}He* as compared to other species. In the Table I we present a comparison of the ratio T_D/T_R for several atomic species commonly used in laser-cooling experiments.

Eq. 6 indicates that the capture velocity v_c/v_D increases with saturation parameter s, approaching the limit $\sqrt{T_D/6T_R}$. However, s can not be increased arbitrarily. For red-detuned optical molasses, the friction coefficient α is known to change sign at large saturation parameter [32]. This change of sign occurs when the contribution of multi-photon processes to the force becomes large enough to modify the excited state decay rate, and typically occurs at $s \sim 1$. Supposing a maximum saturation parameter $s_{max} = 1/2$, we estimate an upper limit on the capture velocity v_c^{up}/v_D. The values for v_c^{up}/v_D are given in Table I. It is clear that Helium, and to a lesser extent Lithium, is special with respect to other alkali atoms since the capture range for sub-Doppler cooling is smaller than the range of velocities achievable with Doppler cooling. This statement applies both to the $\sigma^+ - \sigma^-$ and lin $\perp$ lin configurations. Thus we conclude that sub-Doppler cooling is not expected to play a role on the $2^3S_1 \rightarrow 2^3P_2$ transition of Helium-4. Indeed, in the experiment we do not observe any signatures of sub-Doppler cooling. The semi-classical arguments we have presented above highlight the special place that Helium occupies among laser cooled species. A precise and quantitative condition for the appearance of efficient sub-Doppler cooling would require a fully quantum, three-dimensional computation and is beyond the scope of this paper.

C. Equilibrium temperature for a multi-level atom in the Doppler regime

From the above arguments, sub-Doppler effects on metastable Helium on the $2^3S_1 \rightarrow 2^3P_2$ transition are expected to be negligible. We will therefore compare the temperature measurements in 3D gases to the predictions of Doppler theory [9]. To account for the multi-level atomic structure in the 3D Doppler theory we take a weighted sum over all possible one-photon transitions, where the weights are given by the square of the Clebsch-Gordan coefficients (see Fig. 2a). This leads to a rescaling of the saturation intensity $I_0 = 9/5\ I_{sat}$, and an equilibrium temperature

$$k_B T = \frac{\hbar\Gamma}{2}\frac{1 + I_{tot}/I_0 + (2\delta/\Gamma)^2}{4|\delta|/\Gamma}. \qquad (7)$$

where I_{tot} is the total intensity in the 6 beams. A similar approach has been used in [33].

III. DESCRIPTION OF THE EXPERIMENTAL APPARATUS

A. ^{4}He* Magneto-Optical traps

Our measurements are performed with an apparatus which cools and traps metastable Helium atoms in a MOT. ^{4}He* atoms are produced in a hot plasma (dc-discharge) and slowed down to trappable velocities on the order of several tens of meters per second with a 2.5 m long Zeeman slower. The slowed atoms enter the science chamber where three orthogonal pairs of counter-propagating laser beams are shone onto the atoms in the presence of a quadrupole magnetic field. The cooling light, which addresses the $2^3S_1 \rightarrow 2^3P_2$ transition, is derived from a Koheras AdjustiK Y10 fiber laser from NKT Photonics with a manufacturer stated linewidth < 10 kHz. During the MOT phase, the typical intensity per beam is $\sim 20 I_{sat}$ at a detuning $\delta_{MOT} = -50$ MHz $\simeq -31\Gamma$ from the atomic transition, where the transition linewidth is $\Gamma = 2\pi \times 1.6$MHz. The magnetic field gradient along the coil axis is $B'_x = 24$ G/cm. Under these conditions, 8×10^8 atoms at a temperature of 1.5(1) mK are loaded within 2 seconds.

Detection of the gas is performed using a thermo-electrically cooled InGaAs camera (XEVA type from Xenics company – 256×320 pixels with a pixel size of 30×30 μm). This technology is suited to image metastable Helium atoms with a quantum efficiency of ~ 80 % at 1083 nm. The camera collects the fluorescence of the atoms from the probe beams. The latter are made of the six beams we use to make a MOT which are tuned onto resonance of the atomic transition during the imaging pulse. The duration of the imaging pulse is 100 μs and the total intensity is about 175 I_{sat}, where $I_{sat} = \pi hc\Gamma/3\lambda^3 \simeq 0.165$ mW/cm^2 is the saturation intensity of the $J = 1 \rightarrow J' = 2$ cycling transition. Sizes and temperature of the ^{4}He* clouds are extracted by monitoring the time-of-flight expansion of the initially trapped gases and fitting the imaged 2D density profiles with a Gaussian function.

B. Optical molasses

After the MOT phase we implement an optical molasses on the $2^3S_1 \rightarrow 2^3P_2$ transition, as we shall now describe. At the end of the MOT phase we ramp the

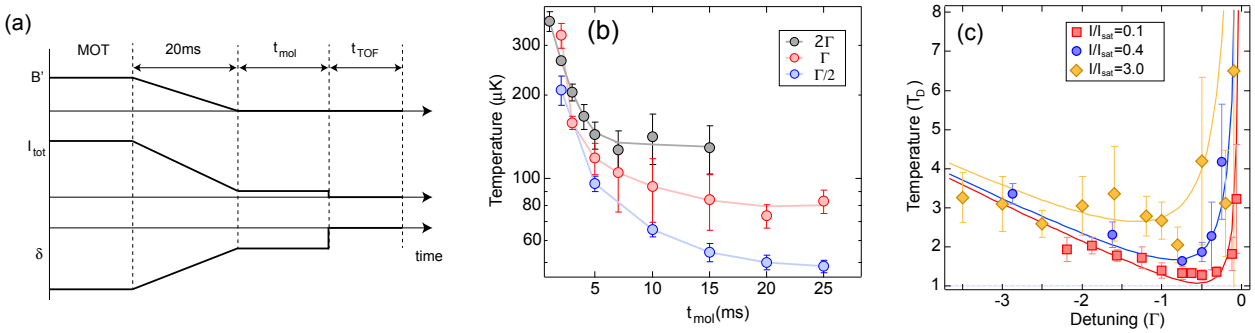

FIG. 3. **(a)** Sketch of the experimental cycle to probe optical molasses. After the MOT phase, the magnetic field gradient B', the beam intensity I_{tot} and the detuning δ are ramped over 20 ms. A molasses phase at constant parameters lasts t_{mol}. After switching off the molasses beams, fluorescence pictures are taken after a time-of-flight t_{TOF}. **(b)** Temperature of optical molasses as a function of the duration t_{mol} of the second stage of molasses. Solid lines are guide to the eye. **(c)** Temperature of optical molasses as a function of the laser detuning. Comparison with Doppler theory for laser cooling multi-level atoms of Eq. 7 (solid lines). The different sets correspond to different intensity in the cooling beams.

magnetic field gradient to zero and ramp both the detuning and intensity of the laser beams from the MOT values to those of the molasses within 20 ms (see Fig. 3a). This ramp of the parameters allows us to capture and cool half of the atoms ($N = 4 \times 10^8$) in the molasses. The polarization of the light beams during the molasses stage is identical to that of the MOT. We then wait for a variable time t_{mol} at fixed final intensity and detuning of the laser beams to reach thermal equilibrium. We monitor the time-of-flight expansion of the optical molasses cloud to extract its temperature.

IV. RESULTS

A. Temperature

In Fig. 1 we present the results of the temperature measurements performed on the MOT and on the optical molasses by recording the TOF expansion of the atomic clouds. Temperature is plotted as a function of the laser detuning δ. We observe a minimum temperature at a detuning $\delta = -\Gamma/2$ as predicted by Doppler cooling theory. The minimum measured temperature $T = 1.3(1)\ T_D$ is close to the expected Doppler limit, which occurs for vanishingly small light intensity. In addition we compare our temperature measurements to the Doppler prediction of Eq. 7 and we find excellent agreement over the entire range of detunings studied in the experiment. For the high-temperature measurements, the confining potential provided by the MOT is necessary to reach thermal equilibrium on the timescale of the experiment. On the other hand, the low-temperature measurements are performed on an optical molasses (see Figs. 1 and 3c), since otherwise density-dependent Penning collisions would severely reduce the number of trapped atoms [34].

B. Equilibration time for 3D optical molasses

In Fig. 3b we plot the time evolution of the atom cloud temperature during the molasses phase. On a short timescale of $t_{mol} \sim 1$ ms, we observe a rapid decrease of the temperature. However, reaching the equilibrium temperature requires durations even longer. Close to the Doppler limit T_D ($\delta = -\Gamma/2$ and $I_{tot}/I_{sat} = 1/10$), the molasses temperature reaches equilibrium on a timescale $t_{mol} \simeq 10$ ms. We have observed that the equilibration time can vary drastically in the presence of uncompensated bias magnetic fields and power imbalances between counter-propagating beams. As we will see in Section IV D, the equilibirum molasses state is also very sensitive to such technical issues.

In Doppler theory, the timescale to reach the equilibrium temperature is directly related to the velocity damping coefficient, predicting an expected cooling time of $\tau_{cool} = m/2\alpha$ [9]. For the low value of the saturation parameter $s \simeq 0.05$ and detuning $|\delta| \sim \Gamma$ used in the data presented in Fig. 3, the expected Doppler cooling time is $t_{cool} \simeq 0.5$ ms. Although this timescale is similar to that of the observed initial rapid decrease in temperature, for the above stated reasons we can not use this measurements to estimate α.

C. MOT sizes

The Penning collision rate in non-polarized ^{4}He* is relatively high [34], limiting the atomic density of laser-cooled Helium clouds to $\sim 10^9$ cm^{-3}. As a result, photon re-scattering effects, which can result in heating of the atom cloud in other species, are typically negligible for Helium [35]. As a consequence, the equilibrium of metastable Helium MOTs is reached in the absence of both multiple scattering and sub-Doppler cooling. In this

simple regime, the equilibrium temperature is given by Eq. 7 and the MOT sizes derive from the equipartion theorem at the Doppler temperature. The force acting onto the MOT can be written $\vec{F} = -\alpha\vec{v} - \kappa_x\vec{x} - \kappa_y\vec{y} - \kappa_z\vec{z}$ at low velocities and close to the trap center. The expected RMS cloud size σ_i of MOT is then given by

$$\frac{1}{2}\kappa_i\sigma_i^2 = \frac{1}{2}k_BT, \tag{8}$$

with the three-dimensional equilibrium temperature T calculated from Eq. 7 and index i referring to the different coordinate axis, $i = \{x, y, z\}$. The one-dimensional spring constants κ_i are given by

$$\kappa_i = -\alpha_{2\text{level}}\frac{\mu B_i'}{\hbar k} \tag{9}$$

where B_i' is the magnetic field gradient along direction i and $\mu = 3\mu_B/2$ is an average magnetic moment for the multi-level atom on the the $2^3S_1 \rightarrow 2^3P_2$ transition (Landé factors are $g_J(2^3S_1) = 2$ and $g_J(2^3P_2) = 3/2$). From this model we calculate the expected MOT sizes from the known experimental parameters.

We have measured the RMS MOT sizes as a function of both the axial magnetic-field gradient B_x' and the detuning δ of the MOT beams. We plot in Fig. 4 the experimental measurements along with the theoretical predictions in the Doppler cooling regime. The behavior of the MOT sizes with both the magnetic field gradient and the laser detuning are in good agreement with the prediction from Eq. 8 with no adjustable parameters, further demonstrating the validity of the Doppler model. We emphasize that the scaling of the MOT size with the detuning is different in the sub-Doppler regime where the temperature scales inversely proportional to $|\delta|$ [33]. As expected the MOT temperature is independent of B', as shown in the inset of Fig. 4a. Previous studies of MOT sizes were either conducted in sub-Doppler regime of cooling [37–39] or with alkaline-earth-metal atoms where high diffusion coefficients and multiple scattering prevent observations similar to ours [25, 40].

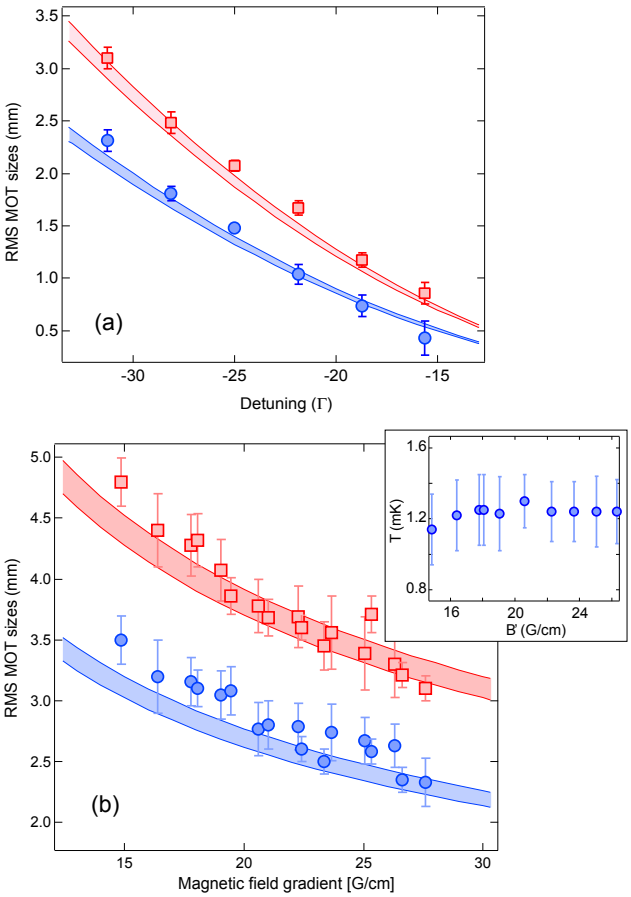

FIG. 4. RMS sizes of the MOT clouds σ_x, σ_y (blue, red) as a function of the laser detuning (a) and as a function of the magnetic field gradient (b). The lines result from numerical calculation (no adjustable parameter) of the expected sizes in the regime of Doppler cooling (see text), accounting for a 5% error on the calibration of the light intensity. Inset in (b) : temperature of the MOT as a function of the magnetic field gradient B'.

D. Stability of Doppler molasses and drift velocity

One experimental observation that puzzled researchers in the very first experiments with laser cooling was the long lifetime of the optical molasses [3, 9]. These measurements were associated with an unexpected robustness of the laser-cooling against an intensity imbalance between counter-propagating laser beams. The additional decay rate induced by this imbalance was measured to be 10 to 20 times lower than that predicted for Doppler molasses. This discrepancy was soon after explained by the presence of sub-Doppler cooling mechanisms [9, 12].

We have investigated the stability of the Helium molasses against intensity imbalance between counter-propagating laser beams. Following [9], we define the imbalance parameter ϵ by $P_1 = (1+\epsilon)P_2$, where P_1 (P_2) is the power in the forward-propagating (counter-propagating) beam along one given axis. We measure the drift velocity v_d of the molasses cloud along this axis in the following way. We repeat experimental cycle with varying molasses time t_{mol}, taking fluorescence pictures after a fixed and short time-of-flight $t_{TOF} = 0.1$ ms. Recording the time evolution of the center of the molasses cloud, we extract a drift velocity v_d. In Fig. 5 we plot the drift velocity as a function of the power imbalance between the two laser beams.

Following the derivation of the Doppler force valid in the limit of low intensity $s_0 \ll 1$ [9], we derive the net force in the case of an unbalanced beam intensity. In this case, the scattering forces from counter-propagating beams balance at a non-zero velocity v_d. Although we

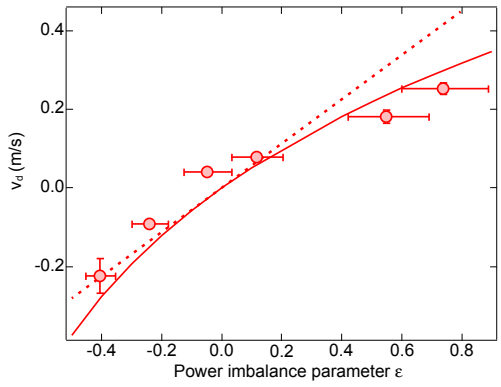

FIG. 5. Drift velocity v_d of the molasses cloud as a function of the power imbalance between two-counter propagating laser beams. For this measurement, we use $\delta = -\Gamma$ and $I/I_{sat} \simeq 1/40$. The dashed line is the prediction of [9] which is first order in ϵ. The solid line is the full prediction of Doppler theory, valid in the low-intensity limit.

obtain an analytical formula for v_d under those circumstances, we express the result in orders of the imbalance ϵ to elucidate the physical content,

$$v_d = \frac{\epsilon\Gamma}{8k}\frac{1+4\delta^2/\Gamma^2}{2|\delta|/\Gamma} - \frac{\delta\epsilon^2}{8k}\frac{1+4\delta^2/\Gamma^2}{4\delta^2/\Gamma^2} + \dots \qquad (10)$$

In particular, the first order term of Eq. 10 is found to be consistent with that reported in [9] and results from writing the force $F = -\alpha_{2level} v$ with α_{2level} being expressed from Eq. 2.

We plot in Fig. 5 the results of the predictions for the intensity and detuning used in the experiment. The good agreement of the measurements with the Doppler prediction without adjustable parameters is an additional confirmation that the red optical molasses we manipulate are indeed in the regime of Doppler cooling, and that sub-Doppler cooling mechanisms are ineffective on the $2^3S_1 \rightarrow 2^3P_2$ transition of ^{4}He*. Lastly, we note that similar behavior is observed for an imposed bias magnetic field.

V. CONCLUSION

In this paper we have reported on the first experimental observation of three-dimensional laser cooling at the Doppler limit with Helium-4 atoms. We have found quantitative agreement with the Doppler theory of (i) the temperature dependence as a function of the laser detuning, (ii) the MOT sizes and (iii) the velocity drift in optical molasses with unbalanced power between counter-propagating light beams. In particular we find the celebrated minimum Doppler temperature of $T_D = \hbar\Gamma/2k_B$ at a laser detuning of $\delta = -\Gamma/2$, as predicted in the simple picture of Doppler laser cooling. We have shown that this behavior arises due to the special properties of metastable Helium atoms

The reported absence of sub-Doppler mechanism is related to the limited capture range allowed by the relatively low intensities required in red-detuned molasses. On the contrary, in blue-detuned molasses there is no such restriction, and high intensities can be used to extend the capture range of sub-Doppler cooling [41, 42]. This paves the way for the investigation of possible sub-Doppler cooling on the blue-detuned side of the $2^3S_1 \rightarrow 2^3P_1$ transition with Helium-4.

ACKNOWLEDGMENTS

We acknowledge fruitful discussions with D. Boiron, T. Bourdel, C. Cohen-Tanoudji and L. Sanchez-Palencia. We thank A. Guilbaud, F. Moron, F. Nogrette and A. Villing, along with all members of the Atom Optic group at LCF, for technical help during the building of the experimental apparatus. We acknowledge financial support from the Région Ile-de-France (DIM Daisy), the RTRA Triangle de la Physique (Junior Chair to D. C.), the European Research Council (senior grant Quantatop) and the Institut Francilien de Recherche sur les Atomes Froids (IFRAF). LCF is a member of IFRAF.

[1] T.W. Hänsch and A.L. Schawlow, *Cooling of Gases by Laser Radiation*, Opt. Commun. **13**, 68 (1975).
[2] D. Wineland and H. Dehmelt, *Proposed* 10^{14} $\Delta\nu/\nu$ *Laser Fluorescence Spectroscopy on* TI^+ *Mono-Ion Oscillator*, Bull. Am. Phys. Soc. **20**, 637 (1975).
[3] S. Chu, L. Hollberg, J.E. Bjorkholm, A. Cable and A. Ashkin, *Three-Dimensional Viscous Confinement and Cooling of Atoms by Resonance Radiation Pressure*, Phys. Rev. Lett. **55**, 48 (1985).
[4] C. Cohen-Tannoudji, *Nobel Lecture: Manipulating Atoms With Photons*, Rev. Mod. Phys. **70**, 707 (1998).
[5] S. Chu, *Nobel lecture: The Manipulation of Neutral Particles*, Rev. Mod. Phys. **3**, 685 (1998).
[6] W. D. Phillips, *Nobel Lecture: Laser Cooling and Trapping of Neutral Atoms*l, Rev. Mod. Phys. **70**, 721 (1998).
[7] C. Cohen-Tannoudji, in *Fundamental Systems in Quantum Optics*, Les Houches, Session LIII, 1990, ed. by J. Dalibard, J.M. Raimond and J. Zinn Justin, pp. 1-164 (Elsevier Science Publisher B.V., 1992).
[8] P. D. Lett, R. N. Watts, C. I. Westbrook, W. D. Phillips, P. L. Gould and H. J. Metcalf, *Observation of Atoms Laser Cooled below the Doppler Limit*, Phys. Rev. Lett. **61**, 169 (1988).
[9] P. D. Lett, W. D. Phillips, S.L. Rolston, C. E. Tanner, R. N. Watts and C. I. Westbrook, *Optical Molasses*, J Opt. Soc. Am. B **6**, 2084 (1989).

[10] D.S. Weiss, E. Riis, Y. Shevy, P.J. Ungar and S. Chu *Optical Molasses and Multilevel Atoms: Experiment* J. Opt. Soc. Am. B **6**, 2072 (1989).

[11] C. Salomon, J. Dalibard, W. D. Phillips, A. Clairon and S. Guellati, *Laser Cooling of Cesium Atoms Below 3 μK*, Europhys. Lett. **12**, 683 (1990).

[12] J. Dalibard and C. Cohen-Tanoudji, *Laser Cooling below the Doppler Limit by Polarization Gradients: Simple Theoretical Models*, J. Opt. Soc. Am. B **6**, 2023 (1989).

[13] P. J. Ungar, D. S. Weiss, E. Riis, and S. Chu, *Optical Molasses and Multilevel Atoms: Theory*, J. Opt. Soc. Am. B **6**, 2058 (1989)

[14] Agreement with the Doppler model has only been reported for experiments in one-dimension [10, 15].

[15] M. Chalony, A. Kastberg, B. Klappauf and D. Wilkowski, *Doppler Cooling to the Quantum Limit*, Phys. Rev. Lett. **107**, 243002 (2011).

[16] G. Zinner, T. Binnewies and F. Riehle, *Photoassociation of Cold Ca Atoms*, Phys. Rev. Lett. **85**, 2292 (2000).

[17] E. A. Curtis, C. W. Oates and L. Hollberg, *Quenched Narrow-Line Laser Cooling of ^{40}Ca to Near the Photon Recoil Limit*, Phys. Rev. A **64**, 031403(R) (2001).

[18] J. Grünert and A. Hemmerich, *Optimizing the Production of Metastable Calcium Atoms in a Magneto-Optical Trap*, Appl. Phys. B **73**, 815 (2001).

[19] U. Dammalapati, I. Norris, L. Maguire, M. Borkowski and E. Riis, *A Compact Magneto-Optical Trap Apparatus for Calcium*, Meas. Sci. Technol. **20**, 095303 (2009).

[20] T. Binnewies, G. Wilpers, U. Sterr, F. Riehle, J. Helmcke, T. E. Mehlstäubler, E. M. Rasel and W. Ertmer, *Doppler Cooling and Trapping on Forbidden Transitions*, Phys. Rev. Lett. **87**, 123002 (2001).

[21] Th. Kisters, K. Zeiske, F. Riehle and J. Helmcke, *High-Resolution Spectroscopy With Laser-Cooled and Trapped Calcium Atoms*, Appl. Phys. B **59**, 89 (1994).

[22] K. Sengstock, U. Sterr, J. H. Müller, V. Rieger, D. Bettermann and W. Ertmer. *Optical Ramsey Spectroscopy on Laser-Trapped and Thermal Mg Atoms*, Appl. Phys. B **59**, 99 (1994).

[23] M. Riedmann, H. Kelkar, T. Wubbena, A. Pape, A. Kulosa, K. Zipfel, D. Fim, S. Ruhmann, J. Friebe, W. Ertmer, and E. Rasel, *Beating the Density Limit by Continuously Loading a Dipole Trap from Millikelvin-Hot Magnesium Atoms*, Phys. Rev. A **86**, 043416 (2012).

[24] H. Katori, T. Ido, Y. Isoya and M. Kuwata-Gonokami, *Magneto-Optical Trapping and Cooling of Strontium Atoms down to the Photon Recoil Temperature*, Phys. Rev. Lett. **82**, 1116 (1999).

[25] X. Xu, T. H. Loftus, M. J. Smith, J. L. Hall, A. Gallagher and J. Ye, *Dynamics in a Two-Level Atom Magneto-Optical Trap*, Phys. Rev. A **66**, 011401R (2002).

[26] T. Kuwamoto, K. Honda, Y. Takahashi and T. Yabuzaki, *Magneto-Optical Trapping of Yb Atoms Using an Intercombination Transition*, Phys. Rev. A **60**, R745(R) (1999).

[27] T. Loftus, J. R. Bochinski and T. W. Mossberg. *Probing Magneto-Optic Trap Dynamics Through Weak Excitation of a Coupled Narrow-Linewidth Transition*, Phys. Rev. A **61**, 061401 (2000).

[28] S. Dorscher, A Thobe, B. Hundt, A. Kochanke, R. Le Targat, P. Windpassinger, C. Becker and K. Sengstock, *Creation of Quantum-Degenerate Gases of Ytterbium in a Compact 2D-/3D-Magneto-Optical Trap Setup*, Rev. Sci. Instrum. **84**, 043109 (2013).

[29] S. K. Choi, S. E. Park, J. Chen, and V. G. Minogin, *Three-Dimensional Analysis of the Magneto-Optical Trap for (1+3)-Level Atoms*, Phys. Rev. A **77**, 015405 (2008).

[30] T. Chaneliere, J. Meunier, R. Kaiser, C. Miniatura, and D. Wilkowski, *Extra-Heating Mechanism in Doppler Cooling Experiments*, J. Opt. Soc. Am. B **22**, 1819 (2005).

[31] S. Chang, T. Y. Kwon, H. S. Lee, and V. G. Minogin, *Two-Photon Laser-Cooling Mechanism in Multilevel Interaction Schemes*, Phys. Rev. A **60**, 3148 (1999).

[32] V. G. Minogin and O. T. Serimaa, *Resonant Light Pressure Forces in a Strong Standing Laser Wave*, Opt. Commun. **30**, 373 (1979).

[33] C. G. Townsend, N. H. Edwards, C. J. Cooper, K. P. Zetie, C. J. Foot, A. M. Steane, P. Szriftgiser, H. Perrin and J. Dalibard, *Phase-Space Density in the Magneto-Optical Trap*, Phys. Rev. A **52**, 1423 (1995).

[34] G. V. Shlyapnikov, J. T. M. Walraven, U. M. Rahmanov and M. W. Reynolds, *Decay Kinetics and Bose Condensation in a Gas of Spin-Polarized Triplet Helium*, Phys. Rev. Lett. **73**, 3247 (1994).

[35] The maximum density that can be reached in the presence of multiple scattering [36] is $\sim 10^{12}$ cm^{-3} for the MOT parameters, a value which exceeds than three orders of magnitude the measured densities ($\sim 10^{9}$ cm^{-3}).

[36] T. Walker, D. Cesko and C. Wieman, *Collective behavior of optically trapped neutral atoms*, Phys. Rev. Lett. **64**, 408 (1990).

[37] C. D. Wallace, T. P. Dinneen, K. Y. N. Tan, A. Kumarakrishnan, P. L. Gould and J. Javanainen, *Measurements of Temperature and Spring Constant in a Magneto-Optical Trap*, J. Opt. Soc. Am. B **11**, 703 (1994).

[38] P. Kohns, P. Buch, W. Süptitz, C. Csambal and W. Ertmer, *On-Line Measurement of Sub-Doppler Temperatures in a Rb Magneto-optical Trap-by-Trap Centre Oscillations*, Europhys. Lett. **22**, 517 (1993).

[39] A. Höpe, D. Haubrich, G. Müller, W. G. Kaenders and D. Meschede, *Neutral Cesium Atoms in Strong Magnetic-Quadrupole Fields at Sub-Doppler Temperatures*, Europhys. Lett. **22**, 669 (1993).

[40] F. Y, Loo, A. Brusch, S. Sauge, M. Allegrini, E. Arimondo, N. Andersen and J. W. Thomsen, *Investigations of a Two-Level Atom in a Magneto-Optical Trap Using Magnesium*, J. Opt. B: Quantum Semiclass. Opt. **6**, 81 (2004).

[41] A. Aspect, J. Dalibard, A. Heidmann, C. Salomon and C. Cohen-Tannoudji, *Cooling Atoms with Stimulated Emission*, Phys. Rev. Lett. **57**, 1688 (1986).

[42] A. T. Grier, I. Ferrier-Barbut, B. S. Rem, M. Delehaye, L. Khaykovich, F. Chevy and C. Salomon, Λ*-Enhanced Sub-Doppler Cooling of Lithium Atoms in D1 Gray Molasses*, Phys. Rev. A **87**, 063411 (2013).

Bibliography

[1] R. P. Feynman, *Simulating physics with computers*, Int J Theor Phys, vol. 21, no. 67, pp. 467488, Jun. 1982.

[2] G. G. Batrouni, R. T. Scalettar, and G. T. Zimanyi, *Quantum critical phenomena in one-dimensional bose systems*, Physical review letters, vol. 65, no. 14, pp. 17651768, 1990.

[3] R. T. Scalettar, G. G. Batrouni, and G. T. Zimanyi, *Localization in interacting, disordered, Bose systems*, Phys. Rev. Lett., vol. 66, no. 24, pp. 31443147, Jun. 1991.

[4] W. Krauth and N. Trivedi, *Mott and Superfluid Transitions in a Strongly Interacting Lattice Boson System*, EPL, vol. 14, no. 7, p. 627, Apr. 1991.

[5] W. Krauth, N. Trivedi, and D. Ceperley, *Superfluid-insulator transition in disordered boson systems*, Phys. Rev. Lett., vol. 67, no. 17, pp. 23072310, Oct. 1991.

[6] G. G. Batrouni and R. T. Scalettar, *World-line quantum Monte Carlo algorithm for a one-dimensional Bose model*, Phys. Rev. B, vol. 46, no. 14, pp. 90519062, Oct. 1992.

[7] A. Kitaev and J. Preskill, *Topological Entanglement Entropy*, Phys. Rev. Lett., vol. 96, no. 11, p. 110404, Mar. 2006.

[8] I. Bloch, J. Dalibard, and S. Nascimbène, *Quantum simulations with ultracold quantum gases*, Nat Phys, vol. 8, no. 4, pp. 267276, Apr. 2012.

[9] M. H. Anderson, J. R. Ensher, M. R. Matthews, C. E. Wieman, and E. A. Cornell, *Observation of Bose-Einstein Condensation in a Dilute Atomic Vapor*, Science, vol. 269, no. 5221, pp. 198201, Jul. 1995.

[10] C. C. Bradley, C. A. Sackett, J. J. Tollett, and R. G. Hulet, *Evidence of Bose-Einstein Condensation in an Atomic Gas with Attractive Interactions*, Phys. Rev. Lett., vol. 75, no. 9, pp. 16871690, Aug. 1995.

[11] K. B. Davis, M.-O. Mewes, M. R. Andrews, N. J. van Druten, D. S. Durfee, D. M. Kurn, and W. Ketterle, *Bose-Einstein Condensation in a Gas of Sodium Atoms*, Phys. Rev. Lett., vol. 75, no. 22, pp. 39693973, Nov. 1995.

[12] B. DeMarco and D. S. Jin, *Onset of Fermi Degeneracy in a Trapped Atomic Gas*, Science, vol. 285, no. 5434, pp. 17031706, Sep. 1999.

[13] A. G. Truscott, K. E. Strecker, W. I. McAlexander, G. B. Partridge, and R. G. Hulet, *Observation of Fermi Pressure in a Gas of Trapped Atoms*, Science, vol. 291, no. 5513, pp. 25702572, Mar. 2001.

[14] F. Schreck, L. Khaykovich, K. L. Corwin, G. Ferrari, T. Bourdel, J. Cubizolles, and C. Salomon, *Quasipure Bose-Einstein Condensate Immersed in a Fermi Sea*, Phys. Rev. Lett., vol. 87, no. 8, p. 080403, Aug. 2001.

[15] H. Feshbach, *A unified theory of nuclear reactions. II*, Annals of Physics, vol. 19, no. 2, pp. 287313, Aug. 1962.

[16] S. Inouye, M. R. Andrews, J. Stenger, H.-J. Miesner, D. M. Stamper-Kurn, and W. Ketterle, *Observation of Feshbach resonances in a BoseEinstein condensate*, Nature, vol. 392, no. 6672, pp. 151154, Mar. 1998.

[17] D. Jaksch, C. Bruder, J. I. Cirac, C. W. Gardiner, and P. Zoller, *Cold Bosonic Atoms in Optical Lattices*, Phys. Rev. Lett., vol. 81, no. 15, pp. 31083111, Oct. 1998.

[18] J. Dalibard, F. Gerbier, G. Juzeliūnas, and P. Öhberg, *Colloquium: Artificial gauge potentials for neutral atoms*, Rev. Mod. Phys., vol. 83, no. 4, pp. 15231543, Nov. 2011.

[19] M. P. A. Fisher, P. B. Weichman, G. Grinstein, and D. S. Fisher, *Boson localization and the superfluid-insulator transition*, Phys. Rev. B, vol. 40, no. 1, pp. 546570, Jul. 1989.

[20] D. Jaksch, H.-J. Briegel, J. I. Cirac, C. W. Gardiner, and P. Zoller, *Entanglement of Atoms via Cold Controlled Collisions*, Physical Review Letters, vol. 82, pp. 19751978, Mar. 1999.

[21] M. Greiner, O. Mandel, T. Esslinger, T. W. Hänsch, and I. Bloch, *Quantum phase transition from a superfluid to a Mott insulator in a gas of ultracold atoms*, Nature, vol. 415, no. 6867, pp. 3944, Jan. 2002.

[22] I. Bloch, *Ultracold quantum gases in optical lattices*, Nat Phys, vol. 1, no. 1, pp. 2330, Oct. 2005.

[23] M. Lewenstein, A. Sanpera, and V. Ahufinger, *Ultracold Atoms in Optical Lattices: Simulating quantum many-body systems*, Oxford University Press, 2012.

[24] I. Bloch and W. Zwerger, *Many-body physics with ultracold gases*, Reviews of Modern Physics, vol. 80, no. 3, pp. 885964, Jul. 2008.

[25] G. G. Batrouni, V. Rousseau, R. T. Scalettar, M. Rigol, A. Muramatsu, P. J. H. Denteneer, and M. Troyer, *Mott Domains of Bosons Confined on Optical Lattices*, Phys. Rev. Lett., vol. 89, no. 11, p. 117203, Aug. 2002.

[26] V. A. Kashurnikov, N. V. Prokofev, and B. V. Svistunov, *Revealing the superfluidMott-insulator transition in an optical lattice*, Phys. Rev. A, vol. 66, no. 3, p. 031601, Sep. 2002.

[27] S. Wessel, F. Alet, M. Troyer, and G. G. Batrouni, *Quantum Monte Carlo simulations of confined bosonic atoms in optical lattices*, Phys. Rev. A, vol. 70, no. 5, p. 053615, Nov. 2004.

[28] S. Stellmer, B. Pasquiou, R. Grimm, and F. Schreck, *Laser Cooling to Quantum Degeneracy*, Phys. Rev. Lett., vol. 110, no. 26, p. 263003, Jun. 2013.

[29] A. Robert, O. Sirjean, A. Browaeys, J. Poupard, S. Nowak, D. Boiron, C. I. Westbrook, and A. Aspect, *A Bose-Einstein Condensate of Metastable Atoms*, Science, vol. 292, no. 5516, pp. 461464, Apr. 2001.

[30] F. Pereira Dos Santos, J. Léonard, J. Wang, C. J. Barrelet, F. Perales, E. Rasel, C. S. Unnikrishnan, M. Leduc, and C. Cohen-Tannoudji, *Bose-Einstein Condensation of Metastable Helium*, Phys. Rev. Lett., vol. 86, no. 16, pp. 34593462, Apr. 2001.

[31] D. M. Stamper-Kurn, A. P. Chikkatur, A. Grlitz, S. Inouye, S. Gupta, D. E. Pritchard, and W. Ketterle, *Excitation of Phonons in a Bose-Einstein Condensate by Light Scattering*, Phys. Rev. Lett., vol. 83, no. 15, pp. 28762879, Oct. 1999.

[32] C. A. Müller and C. Gaul, *Condensate deformation and quantum depletion of BoseEinstein condensates in external potentials*, New J. Phys., vol. 14, no. 7, p. 075025, Jul. 2012.

[33] K. Xu, Y. Liu, D. E. Miller, J. K. Chin, W. Setiawan, and W. Ketterle, *Observation of Strong Quantum Depletion in a Gaseous Bose-Einstein Condensate*, Phys. Rev. Lett., vol. 96, no. 18, p. 180405, May 2006.

[34] A. L. Hoendervanger, D. Clément, A. Aspect, C. I. Westbrook, D. Dowek, Y. J. Picard, and D. Boiron, *Influence of gold coating and interplate voltage on the performance of chevron micro-channel plates for temporally and spatially resolved single particle detection*, Review of Scientific Instruments, vol. 84, no. 2, p. 023307, Feb. 2013.

[35] J. Ladislas Wiza, *Microchannel plate detectors*, Nuclear Instruments and Methods, vol. 162, no. 13, pp. 587601, Jun. 1979.

[36] G. W. Fraser, *X- and -ray imaging using microchannel plates*, Nuclear Instruments and Methods in Physics Research, vol. 221, no. 1, pp. 115130, Mar. 1984.

[37] M. Barat, J. C. Brenot, J. A. Fayeton, and Y. J. Picard, *Absolute detection efficiency of a microchannel plate detector for neutral atoms*, Review of Scientific Instruments, vol. 71, no. 5, pp. 20502052, May 2000.

[38] W. Vassen, C. Cohen-Tannoudji, M. Leduc, D. Boiron, C. I. Westbrook, A. Truscott, K. Baldwin, G. Birkl, P. Cancio, and M. Trippenbach, *Cold and trapped metastable noble gases*, Reviews of Modern Physics, vol. 84, no. 1, pp. 175210, Feb. 2012.

[39] O. Jagutzki, V. Mergel, K. Ullmann-Pfleger, L. Spielberger, U. Spillmann, R. Dörner, and H. Schmidt-Bcking, *A broad-application microchannel-plate detector system for advanced particle or photon detection tasks: large area imaging, precise multi-hit timing information and high detection rate*, Nuclear Instruments and Methods in Physics Research Section A: Accelerators, Spectrometers, Detectors and Associated Equipment, vol. 477, no. 13, pp. 244249, Jan. 2002.

[40] M. Schellekens, R. Hoppeler, A. Perrin, J. V. Gomes, D. Boiron, A. Aspect, and C. I. Westbrook, *Hanbury Brown Twiss Effect for Ultracold Quantum Gases*, Science, vol. 310, no. 5748, pp. 648651, Oct. 2005.

[41] T. Jeltes, J. M. McNamara, W. Hogervorst, W. Vassen, V. Krachmalnicoff, M. A. Perrin, H. Chang, D. Boiron, A. Aspect, and C. I. Westbrook, *Comparison of the Hanbury BrownTwiss effect for bosons and fermions*, Nature, vol. 445, no. 7126, pp. 402405, Jan. 2007.

[42] S. S. Hodgman, R. G. Dall, A. G. Manning, K. G. H. Baldwin, and A. G. Truscott, *Direct Measurement of Long-Range Third-Order Coherence in Bose-Einstein Condensates*, Science, vol. 331, no. 6020, pp. 10461049, Feb. 2011.

[43] J.-C. Jaskula, M. Bonneau, G. B. Partridge, V. Krachmalnicoff, P. Deuar, K. V. Kheruntsyan, A. Aspect, D. Boiron, and C. I. Westbrook, *Sub-Poissonian Number Differences in Four-Wave Mixing of Matter Waves*, Phys. Rev. Lett., vol. 105, no. 19, p. 190402, Nov. 2010.

[44] E. Altman, E. Demler, and M. D. Lukin, *Probing many-body states of ultracold atoms via noise correlations*, Phys. Rev. A, vol. 70, no. 1, p. 013603, Jul. 2004.

[45] S. Fölling, F. Gerbier, A. Widera, O. Mandel, T. Gericke, and I. Bloch, *Spatial quantum noise interferometry in expanding ultracold atom clouds*, Nature, vol. 434, no. 7032, pp. 481484, Mar. 2005.

[46] M. Greiner, C. A. Regal, J. T. Stewart, and D. S. Jin, *Probing Pair-Correlated Fermionic Atoms through Correlations in Atom Shot Noise*, Physical Review Letters, vol. 94, p. 110401, Mar. 2005.

[47] T. Rom, T. Best, D. van Oosten, U. Schneider, S. Fölling, B. Paredes, and I. Bloch, *Free fermion antibunching in a degenerate atomic Fermi gas released from an optical lattice*, Nature, vol. 444, no. 7120, pp. 733736, Dec. 2006.

[48] V. Guarrera, N. Fabbri, L. Fallani, C. Fort, K. M. R. van der Stam, and M. Inguscio, *Noise Correlation Spectroscopy of the Broken Order of a Mott Insulating Phase*, Phys. Rev. Lett., vol. 100, no. 25, p. 250403, Jun. 2008.

[49] T. Kitagawa, A. Aspect, M. Greiner, and E. Demler, *Phase-Sensitive Measurements of Order Parameters for Ultracold Atoms through Two-Particle Interferometry*, Phys. Rev. Lett., vol. 106, no. 11, p. 115302, Mar. 2011.

[50] See for example E. Liénard, M. Herbane, G. Ban, G. Darius, P. Delahaye, D. Durand, X. Fléchard, M. Labalme, F. Mauger, A. Mery, O. Naviliat-Cuncic, and D. Rodríguez, *Performance of a micro-channel plates position sensitive detector*, Nuclear Instruments and Methods in Physics Research Section A: Accelerators, Spectrometers, Detectors and Associated Equipment, vol. 551, no. 23, pp. 375386, Oct. 2005.

[51] G. W. Fraser, M. T. Pain, J. E. Lees, and J. F. Pearson, *The operation of microchannel plates at high count rates*, Nuclear Instruments and Methods in Physics Research Section A: Accelerators, Spectrometers, Detectors and Associated Equipment, vol. 306, no. 12, pp. 247260, Aug. 1991.

[52] A. S. Tremsin, J. F. Pearson, G. W. Fraser, W. B. Feller, and P. White, *Microchannel plate operation at high count rates: new results*, Nuclear Instruments and Methods in Physics Research Section A: Accelerators, Spectrometers, Detectors and Associated Equipment, vol. 379, no. 1, pp. 139151, Sep. 1996.

[53] E. H. Eberhardt, *Gain model for microchannel plates*, Applied Optics, vol. 18, no. 9, p. 1418, May 1979.

[54] Roentdek DLD-100 Manual

[55] D. Rogers and R. F. Malina, *Optimization of the performance of a tandem microchannel plate detector as a function of interplate spacing and voltage*, Review of Scientific Instruments, vol. 53, no. 9, pp. 14381441, Sep. 1982.

[56] Thesis M. Schellekens, *Université Paris XI*, 2007.

[57] C. Firmani, E. Ruiz, C. W. Carlson, M. Lampton, and F. Paresce, *Highresolution imaging with a twodimensional resistive anode photon counter*, Review of Scientific Instruments, vol. 53, no. 5, pp. 570574, May 1982.

[58] J. L. Wiza, P. R. Henkel, and R. L. Roy, *Improved microchannel plate performance with a resistive anode encoder*, Review of Scientific Instruments, vol. 48, no. 9, pp. 12171218, 1977.

[59] F. Paresce, *Quantum efficiency of a channel electron multiplier in the far ultraviolet*, Appl. Opt., vol. 14, no. 12, pp. 28232824, Dec. 1975.

Chapter 2 :

[60] Pfeiffer Vacuum Turbo Pumps Data Sheet

[61] M. Prentiss, E. L. Raab, D. E. Pritchard, A. Cable, J. E. Bjorkholm, and S. Chu, *Atomic-density-dependent losses in an optical trap*, Opt. Lett., vol. 13, no. 6, pp. 452454, Jun. 1988.

[62] J. E. Bjorkholm, *Collision-limited lifetimes of atom traps*, Phys. Rev. A, vol. 38, no. 3, pp. 15991600, Aug. 1988.

[63] Koheras AdjustiK Spec Sheet (Koheras AdjustiK-$Y10-120711$)

[64] Keopsys CYFA-BO Series Spec Sheet

[65] F. Moron, A. L. Hoendervanger, M. Bonneau, Q. Bouton, A. Aspect, D. Boiron, D. Clément, and C. I. Westbrook, *An oscillator circuit to produce a radio-frequency discharge and application to metastable helium saturated absorption spectroscopy*, Review of Scientific Instruments, vol. 83, no. 4, p. 044705, Apr. 2012.

[66] W. Lu, D. Milic, M. D. Hoogerland, M. Jacka, K. G. H. Baldwin, and S. J. Buckman, *A practical direct current discharge helium absorption cell for laser frequency locking at 1083 nm*, Review of Scientific Instruments, vol. 67, no. 9, pp. 30033004, Sep. 1996.

[67] J. E. Lawler, A. Siegel, B. Couillaud, and T. W. Hänsch, *A hollow cathode for dopplerfree spectroscopy*, Journal of Applied Physics, vol. 52, no. 7, pp. 43754378, Jul. 1981.

[68] J. C. J. Koelemeij, W. Hogervorst, and W. Vassen, *High-power frequency-stabilized laser for laser cooling of metastable helium at 389 nm*, Review of Scientific Instruments, vol. 76, no. 3, p. 033104, Feb. 2005.

[69] C. I. Sukenik and H. C. Busch, *A rf discharge cell for saturated absorption spectroscopy of metastable argon*, Review of Scientific Instruments, vol. 73, no. 2, pp. 493494, Feb. 2002.

[70] D. I. Hoult and C. M. Preston, *Inexpensive plasma discharge source for molecular emission spectroscopy with application to 15N analysis*, Review of Scientific Instruments, vol. 63, no. 3, pp. 19271931, Mar. 1992.

[71] Thesis A. Broweays, *Université Paris VI*, 2000.

[72] A. Browaeys, J. Poupard, A. Robert, S. Nowak, W. Rooijakkers, E. Arimondo, L. Marcassa, D. Boiron, C. I. Westbrook, and A. Aspect, *Two body loss rate in a magneto-optical trap of metastable He*, Eur. Phys. J. D, vol. 8, no. 2, pp. 199203, Jan. 2000.

[73] A. Tychkov, T. Jeltes, J. McNamara, P. Tol, N. Herschbach, W. Hogervorst, and W. Vassen, *Metastable helium Bose-Einstein condensate with a large number of atoms*, Physical Review A, vol. 73, no. 3, Mar. 2006.

[74] F. P. Dos Santos, J. Léonard, J. Wang, C. J. Barrelet, F. Perales, E. Rasel, C. S. Unnikrishnan, M. Leduc, and C. Cohen-Tannoudji, *Bose-Einstein condensation of metastable helium*, Physical Review Letters, vol. 86, no. 16, p. 3459, 2001.

[75] P. J. J. Tol, N. Herschbach, E. A. Hessels, W. Hogervorst, and W. Vassen, *Large numbers of cold metastable helium atoms in a magneto-optical trap*, Phys. Rev. A, vol. 60, no. 2, pp. R761R764, Aug. 1999.

[76] D. Sacchet, J. Moreau, P. Georges, and A. Dubois, *Simultaneous dual-band ultra-high resolution full-field optical coherence tomography*, Opt. Express, vol. 16, no. 24, pp. 1943419446, Nov. 2008.

[77] Xenics Xeva Camera Spec Sheet

[78] Pfeiffer Gas Dosing Valve EVN 116 Data Sheet

[79] N. Vansteenkiste, C. Gerz, R. Kaiser, L. Hollberg, C. Salomon, and A. Aspect, *A frequency-stabilized LNA laser at 1.083nm: application to the manipulation of helium 4 atoms*, Journal de Physique II, vol. 1, no. 12, pp. 14071428, Dec. 1991.

[80] W. Rooijakkers, W. Hogervorst, and W. Vassen, *An intense collimated beam of metastable helium atoms by two-dimensional laser cooling*, Optics Communications, vol. 123, no. 13, pp. 321330, Jan. 1996.

[81] Thesis G. Labeyrie, *Université Paris XI*, 1998.

[82] W. D. Phillips and H. Metcalf, *Laser Deceleration of an Atomic Beam*, Phys. Rev. Lett., vol. 48, no. 9, pp. 596599, Mar. 1982.

[83] Nobel prize in physics press release, 1997

[84] M. Zhu, C. W. Oates, and J. L. Hall, *Continuous high-flux monovelocity atomic beam based on a broadband laser-cooling technique*, Phys. Rev. Lett., vol. 67, no. 1, pp. 4649, Jul. 1991.

[85] W. Ketterle, A. Martin, M. A. Joffe, and D. E. Pritchard, *Slowing and cooling atoms in isotropic laser light*, Phys. Rev. Lett., vol. 69, no. 17, pp. 24832486, Oct. 1992.

[86] V. S. Letokhov, V. G. Minogin, and B. D. Pavlik, *Cooling and trapping of atoms and molecules by a resonant laser field*, Optics Communications, vol. 19, no. 1, pp. 7275, Oct. 1976.

[87] T. G. Tiecke, S. D. Gensemer, A. Ludewig, and J. T. M. Walraven, *High-flux two-dimensional magneto-optical-trap source for cold lithium atoms*, Phys. Rev. A, vol. 80, no. 1, p. 013409, Jul. 2009.

[88] T. W. Hänsch and A. L. Schawlow, *Cooling of gases by laser radiation*, Optics Communications, vol. 13, no. 1, pp. 6869, Jan. 1975.

[89] D. Wineland and H. Dehmelt. *Proposed: Laser Fluorescence Spectroscopy of tl+ Mono-Ion Oscillator III*, Bull. Am. Phys. Soc. 637 (1975).

[90] E. L. Raab, M. Prentiss, A. Cable, S. Chu, and D. E. Pritchard, *Trapping of Neutral Sodium Atoms with Radiation Pressure*, Phys. Rev. Lett., vol. 59, no. 23, pp. 26312634, Dec. 1987.

[91] J. Dalibard and C. Cohen-Tannoudji, *Laser cooling below the Doppler limit by polarization gradients: simple theoretical models*, Journal of the Optical Society of America B, vol. 6, no. 11, p. 2023, Nov. 1989.

[92] P. D. Lett, W. D. Phillips, S. L. Rolston, C. E. Tanner, R. N. Watts, and C. I. Westbrook, *Optical molasses*, J. Opt. Soc. Am. B, vol. 6, no. 11, pp. 20842107, Nov. 1989.

[93] S.-K. Choi, S. E. Park, J. Chen, and V. G. Minogin, *Three-dimensional analysis of the magneto-optical trap for (1+3)-level atoms*, Phys. Rev. A, vol. 77, no. 1, p. 015405, Jan. 2008.

[94] T. Chanelière, J.-L. Meunier, R. Kaiser, C. Miniatura, and D. Wilkowski, *Extra-heating mechanism in Doppler cooling experiments*, J. Opt. Soc. Am. B, vol. 22, no. 9, pp. 18191828, Sep. 2005.

[95] J. Lawall, S. Kulin, B. Saubamea, N. Bigelow, M. Leduc, and C. Cohen-Tannoudji, *Three-Dimensional Laser Cooling of Helium Beyond the Single-Photon Recoil Limit*, Phys. Rev. Lett., vol. 75, no. 23, pp. 41944197, Dec. 1995.

[96] C. Cohen-Tannoudji, *Fundamental systems in quantum optics*. Ecole des Houches. Amsterdam: North-Holland (1992): 1-164.

[97] S. Chang, T. Yong Kwon, H. Seong Lee, and V. G. Minogin, *Two-photon laser-cooling mechanism in multilevel interaction schemes*, Phys. Rev. A, vol. 60, no. 4, pp. 31483159, Oct. 1999.

[98] V. G. Minogin and O. T. Serimaa, *Resonant light pressure forces in a strong standing laser wave*, Optics Communications, vol. 30, no. 3, pp. 373379, Sep. 1979.

[99] NEXTorr Pumps Data Sheet Saes Group

[100] A. Keshet and W. Ketterle, *A Distributed GUI-based Computer Control System for Atomic Physics Experiments*. arXiv preprint arXiv:1208.2607, 2012.

[101] A. Keshet, *Cicero Word Generator Technical and User Manual*, June 7, 2008

[102] Y. Fang, *Cicero Word Generator*, Internal Use, 6 Jan. 2014

[103] NI PXIe-8101 Data Sheet

[104] XEM 3001 FPGA Opal Kelly Data Sheet

[105] National Instruments PXI-6713 Analog I/O Card Data Sheet

[106] National Instruments PXIe-6535 Digital I/O Card Data Sheet

[107] National Instruments PXI-5406 Function Generator Card Data Sheet

[108] H. J. Metcalf and P. van der Straten, *Laser Cooling and Trapping*, Springer, 1999.

[109] W. Demtröder, *Laser Spectroscopy*, Springer, 2003

[110] Nobel prize in physics press release, 1997

[111] S. Chu, L. Hollberg, J. E. Bjorkholm, A. Cable, and A. Ashkin, Three-dimensional viscous confinement and cooling of atoms by resonance radiation pressure, Phys. Rev. Lett., vol. 55, no. 1, pp. 4851, Jul. 1985.

[112] B. J. Garrison, W. H. Miller and H. F. Schaefer, *Penning and Associative Ionization of Triplet Metastable Helium Atoms*, Journal of Chemical Physics, vol. 59, no. 6, 15 Sept. 1973.

[113] Schäfter Kirchhoff Fiber Port Cluster Manual

[114] Schäfter Kirchhoff Fiber Collimator Manual

[115] R. Boddeda, *Bose Einstein condensation of metastable Helium in an optical dipole trap*, MSc Thesis École Polytechnique, June 2012.

[116] X. Xu, T. H. Loftus, M. J. Smith, J. L. Hall, A. Gallagher, and J. Ye, *Dynamics in a two-level atom magneto-optical trap*, Phys. Rev. A, vol. 66, no. 1, p. 011401, Jul. 2002.

[117] T. W. Hodapp, C. Gerz, C. Furtlehner, C. I. Westbrook, W. D. Phillips, and J. Dalibard, *Three-dimensional spatial diffusion in optical molasses*, Appl. Phys. B, vol. 60, no. 23, pp. 135143, Feb. 1995.

[118] P. D. Lett, R. N. Watts, C. I. Westbrook, W. D. Phillips, P. L. Gould, and H. J. Metcalf, *Observation of Atoms Laser Cooled below the Doppler Limit*, Phys. Rev. Lett., vol. 61, no. 2, pp. 169172, Jul. 1988.

[119] D. W. Sesko, T. G. Walker, and C. E. Wieman, *Behavior of neutral atoms in a spontaneous force trap*, J. Opt. Soc. Am. B, vol. 8, no. 5, pp. 946958, May 1991.

[120] C. G. Townsend, N. H. Edwards, C. J. Cooper, K. P. Zetie, C. J. Foot, A. M. Steane, P. Szriftgiser, H. Perrin, and J. Dalibard, *Phase-space density in the magneto-optical trap*, Phys. Rev. A, vol. 52, no. 2, pp. 14231440, Aug. 1995.

[121] C. Gabbanini, A. Evangelista, S. Gozzini, A. Lucchesini, A. Fioretti, J. H. Müller, M. Colla, and E. Arimondo, *Scaling laws in magneto-optical traps*, EPL, vol. 37, no. 4, p. 251, Feb. 1997.

[122] A. Vorozcovs, M. Weel, S. Beattie, S. Cauchi, and A. Kumarakrishnan, *Measurements of temperature scaling laws in an optically dense magneto-optical trap*, J. Opt. Soc. Am. B, vol. 22, no. 5, pp. 943950, May 2005.

[123] P. J. Ungar, D. S. Weiss, E. Riis, and S. Chu, *Optical molasses and multilevel atoms: theory*, J. Opt. Soc. Am. B, vol. 6, no. 11, pp. 20582071, Nov. 1989.

[124] M. Walhout, J. Dalibard, S. L. Rolston, and W. D. Phillips, σ_+-σ_- *Optical molasses in a longitudinal magnetic field*, J. Opt. Soc. Am. B, vol. 9, no. 11, pp. 19972007, Nov. 1992.

[125] Y.-J. Lin, A. R. Perry, R. L. Compton, I. B. Spielman, and J. V. Porto, *Rapid production of R87b Bose-Einstein condensates in a combined magnetic and optical potential*, Phys. Rev. A, vol. 79, no. 6, p. 063631, Jun. 2009.

[126] J. Weiner, V. S. Bagnato, S. Zilio, and P. S. Julienne, *Experiments and theory in cold and ultracold collisions*, Rev. Mod. Phys., vol. 71, no. 1, pp. 185, Jan. 1999.

[127] A. Gallagher and D. E. Pritchard, *Exoergic collisions of cold Na*-Na*, Physical review letters, vol. 63, no. 9, pp. 957960, 1989.

[128] P. S. Julienne and F. H. Mies, *Collisions of ultracold trapped atoms*, J. Opt. Soc. Am. B, vol. 6, no. 11, pp. 22572269, Nov. 1989.

[129] P. S. Julienne and J. Vigué, *Cold collisions of ground- and excited-state alkali-metal atoms*, Phys. Rev. A, vol. 44, no. 7, pp. 44644485, Oct. 1991.

[130] M. Prentiss, E. L. Raab, D. E. Pritchard, A. Cable, J. E. Bjorkholm, and S. Chu, *Atomic-density-dependent losses in an optical trap*, Opt. Lett., vol. 13, no. 6, pp. 452454, Jun. 1988.

[131] L. Marcassa, V. Bagnato, Y. Wang, C. Tsao, J. Weiner, O. Dulieu, Y. B. Band, and P. S. Julienne, *Collisional loss rate in a magneto-optical trap for sodium atoms: Light-intensity dependence*, Phys. Rev. A, vol. 47, no. 6, pp. R4563R4566, Jun. 1993.

[132] D. Sesko, T. Walker, C. Monroe, A. Gallagher, and C. Wieman, *Collisional losses from a light-force atom trap*, Phys. Rev. Lett., vol. 63, no. 9, pp. 961964, Aug. 1989.

[133] A. Fioretti, J. H. Müller, P. Verkerk, M. Allegrini, E. Arimondo, and P. S. Julienne, *Direct measurement of fine-structure collisional losses from a Cs magneto-optical trap*, Phys. Rev. A, vol. 55, no. 6, pp. R3999R4002, Jun. 1997.

[134] D. Hoffmann, P. Feng, R. S. Williamson, and T. Walker, *Excited-state collisions of trapped Rb85 atoms*, Phys. Rev. Lett., vol. 69, no. 5, pp. 753756, Aug. 1992.

[135] C. D. Wallace, T. P. Dinneen, K.-Y. N. Tan, T. T. Grove, and P. L. Gould, *Isotopic difference in trap loss collisions of laser cooled rubidium atoms*, Phys. Rev. Lett., vol. 69, no. 6, pp. 897900, Aug. 1992.

[136] S. D. Gensemer, V. Sanchez-Villicana, K. Y. N. Tan, T. T. Grove, and P. L. Gould, *Trap-loss collisions of 85Rb and 87Rb: Dependence on trap parameters*, Phys. Rev. A, vol. 56, no. 5, pp. 40554063, Nov. 1997.

[137] R. S. Williamson and T. Walker, *Magneto-optical trapping and ultracold collisions of potassium atoms*, J. Opt. Soc. Am. B, vol. 12, no. 8, pp. 13931397, Aug. 1995.

[138] J. Kawanaka, K. Shimizu, H. Takuma, and F. Shimizu, *Quadratic collisional loss rate of a Li7 trap*, Phys. Rev. A, vol. 48, no. 2, pp. R883R885, Aug. 1993.

[139] N. W. M. Ritchie, E. R. I. Abraham, Y. Y. Xiao, C. C. Bradley, R. G. Hulet, and P. S. Julienne, *Trap-loss collisions of ultracold lithium atoms*, Phys. Rev. A, vol. 51, no. 2, pp. R890R893, Feb. 1995.

[140] M. S. Santos, P. Nussenzveig, L. G. Marcassa, K. Helmerson, J. Flemming, S. C. Zilio, and V. S. Bagnato, *Simultaneous trapping of two different atomic species in a vapor-cell magneto-optical trap*, Phys. Rev. A, vol. 52, no. 6, pp. R4340R4343, Dec. 1995.

[141] H. C. Mastwijk, J. W. Thomsen, P. van der Straten, and A. Niehaus, *Optical Collisions of Cold, Metastable Helium Atoms*, Phys. Rev. Lett., vol. 80, no. 25, pp. 55165519, Jun. 1998.

[142] M. Kumakura and N. Morita, *Laser Trapping of Metastable ^{3}He Atoms: Isotopic Difference in Cold Penning Collisions*, Phys. Rev. Lett., vol. 82, no. 14, pp. 28482851, Apr. 1999.

[143] A. Browaeys, J. Poupard, A. Robert, S. Nowak, W. Rooijakkers, E. Arimondo, L. Marcassa, D. Boiron, C. I. Westbrook, and A. Aspect, *Two body loss rate in a magneto-optical trap of metastable He*, Eur. Phys. J. D, vol. 8, no. 2, pp. 199203, Jan. 2000.

[144] F. P. D. Santos, F. Perales, J. Léonard, A. Sinatra, J. Wang, F. S. Pavone, E. Rasel, C. S. Unnikrishnan, and M. Leduc, *Penning collisions of laser-cooled metastable helium atoms*, Eur. Phys. J. D, vol. 14, no. 1, pp. 1522, Apr. 2001.

[145] H. Katori and F. Shimizu, *Laser-Induced Ionizing Collisions of Ultracold Krypton Gas in the 1s5 Metastable State*, Phys. Rev. Lett., vol. 73, no. 19, pp. 25552558, Nov. 1994.

[146] K. J. Matherson, R. D. Glover, D. E. Laban, and R. T. Sang, *Absolute metastable atom-atom collision cross section measurements using a magneto-optical trap*, Review of Scientific Instruments, vol. 78, no. 7, p. 073102, Jul. 2007.

[147] H. C. Busch, M. K. Shaffer, E. M. Ahmed, and C. I. Sukenik, *Trap loss in a dual-species Rb-Ar* magneto-optical trap*, Phys. Rev. A, vol. 73, no. 2, p. 023406, Feb. 2006.

[148] M. Walhout, U. Sterr, C. Orzel, M. Hoogerland, and S. L. Rolston, *Optical Control of Ultracold Collisions in Metastable Xenon*, Phys. Rev. Lett., vol. 74, no. 4, pp. 506509, Jan. 1995.

[149] F. M. Penning, *Über Ionisation durch metastabile Atome*, Naturwissenschaften, vol. 15, no. 40, pp. 818818, Oct. 1927.

[150] J. Dalibard, *Collisional dynamics of ultra-cold atomic gases*, in Proceedings of the International School of Physics-Enrico Fermi, 1999, vol. 321.

[151] C. J. Joachain, *Quantum collision theory*, Originating Research Org. not identified, Jan. 1975.

[152] M. W. Müller, A. Merz, M.-W. Ruf, H. Hotop, W. Meyer, and M. Movre, textitExperimental and theoretical studies of the Bi-excited collision systems He*(23 S) + He*(23 S, 21 S) at thermal and subthermal kinetic energies, Z Phys D - Atoms, Molecules and Clusters, vol. 21, no. 2, pp. 89112, Jun. 1991.

[153] K.-A. Suominen, K. Burnett, and P. S. Julienne, *Role of off-resonant excitation in cold collisions in a strong laser field*, Phys. Rev. A, vol. 53, no. 3, pp. R1220R1223, Mar. 1996.

[154] K.-A. Suominen, *Theories for cold atomic collisions in light fields*, J. Phys. B: At. Mol. Opt. Phys., vol. 29, no. 24, p. 5981, Dec. 1996.

[155] F. Bardou, O. Emile, J.-M. Courty, C. I. Westbrook, and A. Aspect, *Magneto-Optical Trapping of Metastable Helium: Collisions in the Presence of Resonant Light*, EPL, vol. 20, no. 8, p. 681, Dec. 1992.

[156] V. Venturi, I. B. Whittingham, P. J. Leo, and G. Peach, *Close-coupled calculation of collisions of magnetostatically trapped metastable helium atoms*, Phys. Rev. A, vol. 60, no. 6, pp. 46354646, Dec. 1999.

[157] V. Venturi and I. B. Whittingham, *Close-coupled calculation of field-free collisions of cold metastable helium atoms*, Phys. Rev. A, vol. 61, no. 6, p. 060703, May 2000.

[158] M. G. Peters, D. Hoffmann, J. D. Tobiason, and T. Walker, *Laser-induced ultracold Rb(5S1/2)+Rb(5P1/2) collisions*, Phys. Rev. A, vol. 50, no. 2, pp. R906R909, Aug. 1994.

[159] J. Simonet, *Optical traps for Ultracold Metastable Helium atoms*, Universit Pierre et Marie Curie - Paris VI, 2011

Abstract

This thesis describes the work done over the past three and a half years on the new metastable helium experiment at the Institut d'Optique in Palaiseau.
In the first chapter it describes a study to improve both the efficiency and the accuracy of the Micro-channel Plate (MCP) detection system. We have experimented with adding a gold layer on the top of the input plate, something that we have found increases the efficiency but also decreases the accuracy. The addition of a voltage between the two stacked plates has been shown to both raise the efficiency and improve the accuracy in non-coated MCPs.
The second chapter is devoted to the construction of the experimental apparatus. Here the excitation of ground state helium to its metastable state is described, as well as the subsequent collimation and cooling by Zeeman slower of the resulting hot atomic beam. The slowed beam is then captured in a Magneto-Optical Trap, in which we have captured 8×10^8 atoms.
In the third chapter an original study on three-dimensional Doppler cooling in a red-detuned molasses and in the Magneto-Optical trap is presented. The metastable helium system is unique as there is no multiple scattering of photons and there are no sub-Doppler effects. This allows for a never before seen experimental realisation of pure Doppler cooling theory.
The fourth chapter describes a study on collisions in a magneto-optical trap of metastable helium. Light-induced Penning collisions are responsible for high trap losses at high intensities and at frequencies close to the transition frequency. We measure the constant rate coefficient to $K_{sp} = 2.8 \pm 0.4 \times 10^{-7}\ cm^3/s$.

Keywords : Metastable Helium, Doppler Cooling, Michrochannel Plates, Penning Collisions, Magneto-Optical Trap, Cold Atoms

Résumé

Cette thèse décrit le travail accompli au cours des trois dernières années sur la nouvelle expérience d'Hélium métastable de l'Institut d'Optique à Palaiseau.
Le premier chapitre décrit une étude visant à améliorer à la fois l'efficacité et la précision du système de détection par galettes à micro-canaux (MCP). Nous avons fait des mesures avec des galettes recouvertes d'une couche d'or sur la face avant, obtenant un accroissement de l'efficacité de détection mais également une réduction de la précision. L'ajout d'une tension intermédiaires entre les deux galettes empilées a au contraire améliorer à la fois l'efficacité et la précision des MCP, en l'absence d'une couche d'or.
Le deuxième chapitre est consacré à la construction de l'appareil expérimental pour le refroidissement et le piégeage d'atomes. L'excitation de l'état fondamental de l'Hélium à l'état métastable est décrite, ainsi que la collimation et le refroidissement ultérieur par Zeeman lent du faisceau atomique chaud résultant. Le faisceau ralenti est alors capturé dans un piège magnéto-optique (PMO), dans lequel nous avons capturé 8×10^8 atomes.
Dans le troisième chapitre une étude originale du refroidissement Doppler tridimensionnel dans un PMO et une mélasse désaccordée vers le rouge de la transition atomique est discutée. L'atome d'Hélium métastable est unique et ses propriétés ont permis une telle étude. En effet, les faibles densités atomiques impliquent qu'il n'y a pas de diffusion multiple de photons d'une part, et la faible masse et la faible largeur de la transition $2^3S_1 \rightarrow 2^3P_2$ rend inefficace les processus de refroidissement sous la limite Doppler. Ces conditions nous ont permis d'observer pour la première fois à trois dimensions un gaz refroidit dans le régime Doppler.
Le quatrième chapitre présente une étude sur les collisions dans un piège magnéto-optique d'Hélium métastable. Les collisions Penning induites par la lumière, en particulier à des intensités élevées et à des fréquences proches de la fréquence de transition, sont responsables de pertes élevées d'atomes piégés. Nous mesurons le coefficient de taux associé à ces pertes, $K_{sp} = 2.8 \pm 0.4 \times 10^{-7}\ cm^3/s$.

Mots-Clés : L'hélium métastable, refroidissement Doppler, galette micro-canaux, collisions Penning, piège magnéto-optique, atomes froids